



MONASH University

Novel hole transporting materials for perovskite solar cells

Iacopo Benesperi

*A thesis submitted for the degree of Doctor of Philosophy at
Monash University in 2017
School of Chemistry*

To Leone

Copyright notice

© Iacopo Benesperi 2017.

I certify that I have made all reasonable efforts to secure copyright permissions for third-party content included in this thesis and have not knowingly added copyright content to my work without the owner's permission.

Abstract

The harvest of solar energy is going to play a key role in human energy production in the near future and new solar cell technologies are being developed to complement existing silicon wafer technology – the current market standard. In the past five years, hybrid organic-inorganic perovskite solar cells (PSCs) have emerged as a very promising technology due to their low cost, ease of fabrication and high energy conversion efficiency. PSCs belong to the family of excitonic *p-i-n* junctions and – to achieve high performances – they require the presence of charge selective contacts at both ends in order to generate free charges from the excitons. Concerning the hole selective contact, many hole transporting materials (HTMs) have been synthesised for the use with perovskite light absorbers. Thus far, an HTM possessing all the key qualities in concert to bring PSCs closer to the market – affordability, stability and good electrical conductivity – has not been found. The aim of this thesis is to contribute to the knowledge of HTMs for PSCs, not only by synthesising novel HTMs with the aforementioned qualities in mind but also by analysing fundamental aspects of these compounds to provide insights for future developments.

In chapter 2, a new class of HTMs is presented for the first time. The studied compound is a transition metal complex with a Fe(II/III) metal centre, a polypyridyl hexadentate ligand – 6,6'-bis(1,1-di(pyridin-2-yl)ethyl)-2,2'-bipyridine (bpyPY4) – and trifluoromethanesulfonate (OTf⁻) as a counter-ion. While a few other metal complex HTMs based on planar and highly conductive ligands such as phthalocyanines have previously been reported, the present study introduces for the first time a non-planar metal complex as a hole transporter for application in PSCs. The conductivity for this compound is provided by the redox transformation of the metal centre rather than charge hopping within the ligand.

In chapter 3, the influence of counter-ions in a metal complex HTM on the charge transport properties of the material is examined. In this study, two complexes based on a Co(II/III) metal centre are compared. One features the same bpyPY4 ligand employed in chapter 2 and OTf⁻ counter-ions, while the other is based on two 2,5-(dipyridin-2-yl)-pyrrole tridentate ligands with no counter-ion for the Co(II) centre and only one OTf⁻ ion for the Co(III) centre. Comparison of mixed cation PSCs fabricated with the two HTMs show that the efficiency of those featuring the metal complex with a reduced number of counter-ions is more than two-fold higher compared to those produced using the metal complex based on the bpyPY4 ligand.

In chapter 4, a novel organic HTM (3,3'-dimethyl-4,4',5,5'-tetrakis-(*p*-(*N,N*-di-*p*-methoxyphenylamino)phenyl)-2,2'-bithiophene) is presented. This compound features the same four triphenylamine branches of the state-of-the-art 2,2',7,7'-tetrakis-(*N,N*-di-*p*-methoxy-phenylamino)-9,9'-spirobifluorene (spiro-OMeTAD) but the expensive spiro core is replaced with a more economical bithiophene one. The new HTM is compared – both experimentally and using density functional theory calculations – to two similar hole conductors reported in the literature, to probe the effect of molecular geometry on hole

transport properties. The comparison suggests that organic hole conductors with a flatter molecular geometry, which facilitates π -stacking, perform better as HTM in PSCs.

Publications during enrolment

F. Huang, Y. Dkhissi, W. Huang, M. Xiao, I. Benesperi, S. Rubanov, Y. Zhu, X. Lin, L. Jiang, Y. Zhou, A. Gray-Weale, J. Etheridge, C. R. McNeill, R. A. Caruso, U. Bach, L. Spiccia and Y.-B. Cheng, “Gas-assisted preparation of lead iodide perovskite films consisting of a monolayer of single crystalline grains for high efficiency planar solar cells”, *Nano Energy*, vol. 10, pp. 10–18, 2014. DOI: <https://doi.org/10.1016/j.nanoen.2014.08.015>

Y. Dkhissi, H. Weerasinghe, S. Meyer, I. Benesperi, U. Bach, L. Spiccia, R. A. Caruso and Y.-B. Cheng, “Parameters responsible for the degradation of CH₃NH₃PbI₃-based solar cells on polymer substrates”, *Nano Energy*, vol. 22, pp. 211–222, 2016. DOI: <https://doi.org/10.1016/j.nanoen.2016.02.015>

A. R. Pascoe, S. Meyer, W. Huang, W. Li, I. Benesperi, N. W. Duffy, L. Spiccia, U. Bach and Y.-B. Cheng, “Enhancing the Optoelectronic Performance of Perovskite Solar Cells via a Textured CH₃NH₃PbI₃ Morphology”, *Adv. Funct. Mater.*, vol. 26, no. 8, pp. 1278–1285, 2016. DOI: <https://doi.org/10.1002/adfm.201504190>

M. K. Kashif,⁺ I. Benesperi,⁺ R. A. Milhuisen, S. Meyer, J. Hellerstedt, D. Zee, N. W. Duffy, B. Halstead, M. S. Fuhrer, J. Cashion, Y.-B. Cheng, L. Spiccia, A. N. Simonov and U. Bach, “Polypyridyl Iron Complex as a Hole-Transporting Material for Formamidinium Lead Bromide Perovskite Solar Cells”, *ACS Energy Lett.*, vol. 2, pp. 1855–1859, 2017. DOI: <https://doi.org/10.1021/acsenergylett.7b00522>

Thesis including published works declaration

I hereby declare that this thesis contains no material which has been accepted for the award of any other degree or diploma at any university or equivalent institution and that, to the best of my knowledge and belief, this thesis contains no material previously published or written by another person, except where due reference is made in the text of the thesis.

This thesis includes one original paper published in the ACS Energy Letters peer reviewed journal. The core theme of the thesis is the synthesis and characterisation of novel hole transporting materials for perovskite solar cells. The ideas, development and writing up of all the papers in the thesis were the principal responsibility of myself, the student, working within the School of Chemistry under the supervision of Prof. Leone Spiccia, Prof. Udo Bach, Prof. Yi-Bing Cheng and Dr. Alexandr N. Simonov.

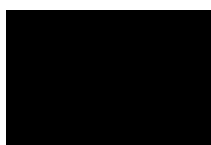
(The inclusion of co-authors reflects the fact that the work came from active collaboration between researchers and acknowledges input into team-based research.)

In the case of chapter two my contribution to the work involved the following:

Thesis Chapter	Publication Title	Status	Nature and % of student contribution	Co-authors names Nature and % of co-authors' contribution	Co-authors, Monash student Y/N
2	Polypyridyl Iron Complex as a Hole-Transporting Material for Formamidinium Lead Bromide Perovskite Solar Cells	Published	32% contribution. Ligand and complex synthesis; FABr synthesis; cell fabrication and characterisation; sc-XRD of Fe(III) complex sample preparation; Mössbauer sample preparation; cyclic voltammetry; PESA; UPS sample preparation; fluorescence quenching; perovskite XRD; perovskite UV-Vis; SEM sample preparation; manuscript preparation.	Muhammad K. Kashif 32% contribution. Original idea; complex synthesis; conductivity sample preparation and measurements; sc-XRD of Fe(II) complex; XRD of complex films.	N
				Rebecca A. Milhuisen 9% contribution. Complex synthesis; conductivity sample preparation and measurements; XRD of complex films; manuscript preparation.	Y
				Steffen Meyer 2% contribution. SEM imaging; device encapsulation.	N
				Jack Hellerstedt, Michael S. Fuhrer 1% contribution. Low temperature conductivity measurements.	N
				David Zee 9% contribution. Ligand synthesis.	N
				Noel W. Duffy 1% contribution. Interpretation of impedance measurements	N
				Barry Halstead 1% contribution. GAXRD measurements.	N
				John Cashion 2% contribution. Mössbauer analysis and interpretation.	N
Yi-Bing Cheng, Leone Spiccia, Alexandr N. Simonov, Udo Bach 10% contribution. Directing the study, data analysis, manuscript preparation.	N				

I have renumbered sections of the submitted paper in order to generate a consistent presentation within the thesis.

Student signature:



Date: 06/09/2017

The undersigned hereby certify that the above declaration correctly reflects the nature and extent of the student's and co-authors' contributions to this work. In instances where I am not the responsible author I have consulted with the responsible author to agree on the respective contributions of the authors.

Main Supervisor signature:



Date: 06/09/2017

Acknowledgements

The first and biggest thanks goes to the late Leone Spiccia, who brought me to Monash and allowed me to pursue my PhD studies. Unfortunately, he fell sick only a few months after my arrival in Melbourne and I did not have the chance to get to know him as much as I would have liked to. Nevertheless, right from the start he encouraged me to find and follow my own path and agreed to let me work on the thesis' subject of my choice. For this, I will always be grateful.

The second and equally big thank you is for my family and parents. They have supported me both morally and financially throughout my studies, allowing me to focus on them and letting me reach this stage. They have always been there when I needed their help and have always supported my decisions, including reaching the other end of the world for four years. I would not be writing this thesis now, without their unconditional love.

A big thanks goes to Dr. Steffen Meyer and Dr. Sebastian Fürer – fellow synthetic chemists in a lab of engineers – for guiding me through some of the experimental procedures, sharing their knowledge with me and especially for patiently receiving all my ranting about things not working as they were supposed to, sometimes to the point of being ridiculous. There was never a shortage of that. I would also like to thank Dr. Jinbao Zhang for his general kindness and for helping me out in the nick of time, when I needed it the most.

I would like to acknowledge Prof. Udo Bach and Prof. Yi-Bing Cheng, my co-supervisors, who have stepped in the supervision role to fill Leone's gap after his sickness. I have been considered and treated like a member of both their research groups during all my PhD and they have been always available when I had a question or a doubt about my research, doing much more than what was expected from them. A big thank you also goes to Dr. Alexandr Simonov, for stepping in as my main supervisor after Leone's passing away. He had a lot to deal with but managed greatly, being also very responsive in terms of feedback on the paper manuscript and this thesis.

Thanks to Alex, Anuradha, Askhat, Dijon, Dorota, Julia, Julian, Katharina, Kira, Max, Shannon, Tom (both) and Yasmina for all the lunches, barbecues and fun time together; you've made my period in Melbourne a most enjoyable one. A toast to all the people in Gold Club, it's been nice to share a beer and some conversation at the end of long weeks. A big thank you to all my housemates in these three and a half years, Christina, Fred, Han, Hieu, Rodrigo, Thian, Will and to my landlords Phillip and Halina – you've made me feel at home, away from home.

I would like to acknowledge all the people who have worked and are still working in the Renewable Energy Laboratory and the Spiccia research group at Monash University. It's been a pleasure working with you all and you have all contributed in creating a pleasant and friendly working environment. I hope to cross your paths again in the future.

A last thank you goes to Leila, for all the proof reading and English polishing work done for the introduction and the conclusions. It's been a big help, for all the other chapters as well.

A final acknowledgement goes to Arnott's Tim Tams, which have brought some sweetness in our working days for many years.

No words of praise will be given to the blindfolded goddess (the one without scales), who has never bothered to show up for the past four years. I hope to meet you in the future.



This thesis should be enjoyed in its electronic format. All required hard copies were printed using 100% recycled paper, as should be done for all printed copies of this thesis.

Table of contents

Copyright notice.....	i
Abstract.....	ii
Publications during enrolment.....	iv
Thesis including published works declaration.....	iv
Acknowledgements.....	vii
Nomenclature.....	xi
1. Introduction.....	1
1.1. Solar energy production overview.....	1
1.2. Working principles of a silicon solar cell.....	6
1.3. Third generation solar cells overview.....	7
1.4. Perovskite solar cells overview.....	10
1.4.1. Perovskite solar cells early history.....	10
1.4.2. Perovskite's unique properties.....	11
1.4.3. Perovskite deposition and solar cell architecture.....	11
1.4.4. Different perovskite materials.....	12
1.4.5. Overview of other components of a perovskite solar cell.....	14
1.4.6. The hysteresis conundrum.....	15
1.5. Hole transporting materials overview.....	16
1.5.1. Key parameters for efficient hole transporting materials.....	17
1.5.2. Organic small molecular hole conductors.....	20
1.5.3. Polymeric hole conductors.....	32
1.5.4. Inorganic hole conductors.....	36
1.5.5. Transition metal complex hole conductors.....	38
1.5.6. Solid-state redox-active metal complexes as hole conductors for ssDSSCs.....	40
1.6. Introduction summary & Aims of the thesis.....	41
2. Polypyridyl iron complex hole transporter.....	45
2.1. The long journey there.....	45
2.2. Published article.....	46
2.3. Supporting Information.....	51
3. Influence of the counter-ion on the hole transporting properties of metal complexes.....	71
3.1. The long journey there.....	71
3.2. Introduction.....	72
3.3. Results and discussion.....	73
3.3.1. Ligands and complexes synthesis and characterisation.....	73
3.3.2. Electronic properties and conductivity.....	75
3.3.3. Solar cell characterisation.....	78
3.3.4. Influence of the counter-ion.....	81
3.4. Conclusions.....	82
4. Bithiophene core-based organic hole transporter.....	83
4.1. The long journey there.....	83
4.2. Introduction.....	84
4.3. Results and discussion.....	85
4.3.1. Computational analysis.....	85
4.3.2. Synthesis of bithi-MeOMeTPA.....	89
4.3.3. Comparison of the properties of bithi-MeOMeTPA, KTM3 and H112.....	90
4.3.4. Comparison of bithi-MeOMeTPA-, KTM3- and H112-based solar cells.....	96
4.4. Conclusions.....	101

5. Conclusions and perspective.....	104
6. Experimental section.....	108
6.1. Materials.....	108
6.2. Syntheses.....	108
6.3. Fabrication of devices.....	112
6.4. Characterisation.....	115
Appendix A – Solar cell measurement techniques.....	118
<i>J-V</i> curve measurement.....	118
Steady-state measurement.....	121
Incident photon-to-electron conversion efficiency measurement.....	121
Appendix B – Detailed crystallographic information.....	124
Complete single crystal XRD data refinement for [Fe(bpyPY4)](OTf) ₂	124
Complete single crystal XRD data refinement for [Fe(bpyPY4)](OTf) ₃	132
Complete single crystal XRD data refinement for [Co(py ₂ pz) ₂].....	141
Complete single crystal XRD data refinement for [Co(py ₂ pz) ₂](OTf).....	151
Bibliography.....	161

Nomenclature

List of abbreviations

AM1.5G	Reference solar spectral irradiance according to ASTM G-173-03
ASTM	American Society for Testing and Materials
BHJ	Bulk heterojunction
BIPV	Building integrated photovoltaics
bpyPY4	6,6'-bis(1,1-di(pyridin-2-yl)ethyl)-2,2'-bipyridine
CB	Conduction band
CBZ	Chlorobenzene
cps	Counts per second
c-TiO ₂	Compact TiO ₂
CV	Cyclic voltammetry
DCM	Dichloromethane
DFT	Density functional theory
DMF	<i>N,N</i> -dimethylformamide
dmp	2,9-dimethyl-1,10-phenanthroline
DOS	Density of states
DSC	Differential scanning calorimetry
DSSC	Dye-sensitised solar cell
ETL	Electron transporting layer
EtOAc	Ethyl acetate
EtOH	Ethanol
FA	Formamidinium, CH(NH ₂) ₂ ⁺
FB	Forward bias
Fc ^{0/+}	Ferrocene/Ferrocenium redox couple
FTO	Fluorine-doped tin oxide
HOMO	Highest occupied molecular orbital

HTM	Hole transporting material
IPCE	Incident photon-to-electron conversion efficiency
ITO	Indium tin oxide
LCOE	Levelised cost of electricity
LiTFSI	Lithium bis(trifluoromethylsulfonyl)imide
LUMO	Lowest unoccupied molecular orbital
MALDI	Matrix-Assisted Laser Desorption/Ionization
MA	Methylammonium, CH_3NH_3^+
MeCN	Acetonitrile
MeOH	Methanol
MLCT	Metal-to-ligand charge transfer
mp-TiO ₂	Mesoporous TiO ₂
NHE	Normal hydrogen electrode
NMR	Nuclear magnetic resonance
NREL	National Renewable Energy Laboratory
OPV	Organic photovoltaics
OTf ⁻	Trifluoromethanesulfonate anion
PB	Petroleum benzene
PCE	Solar-to-electrical power conversion efficiency
PESA	Photoelectron spectroscopy in air
PL	Photoluminescence
PLD	Pulsed laser deposition
ppm	Parts per million
PSC	Perovskite solar cell
PV	Photovoltaic
QDSC	Quantum dot solar cell
RH	Relative humidity
rpm	Revolutions per minute

RT	Room temperature
sc	Single crystal
SC	Short circuit
SEM	Scanning electron microscopy
ssDSSC	Solid-state dye sensitised solar cell
tBP	4- <i>tert</i> -butylpyridine
TCO	Transparent conductive oxide
TEGDME	Tetraethylene glycol dimethyl ether
TFSI ⁻	Bis(trifluoromethane)sulfonamide anion
THF	Tetrahydrofuran
TOF	Time of flight
triflate	Trifluoromethanesulfonate anion
UV	Ultraviolet
VB	Valence band
Vis	Visible
XRD	X-ray diffraction spectroscopy

List of symbols

δ	Chemical shift
θ	Diffraction angle
ε	Molar extinction coefficient
μ_h	Hole mobility
ρ_h	Hole density
σ	Electrical conductivity
e	Elementary charge ($1.6021766208(98) \times 10^{-19}$ C)
$E_{1/2}$	Mid-point potential
E_{CB}	Conduction band edge energy
E_F	Position of the Fermi level

E_g	Band gap
E_{VB}	Valence band edge energy
FF	Fill factor
i	Intrinsic semiconductor (light absorber)
I	Current
I_{P_m}	Current at the maximum power point
J	Current density
J_{sc}	Short circuit current density
n	n -type (electron accepting) semiconductor
p	p -type (hole accepting) semiconductor
P_m	Cell's maximum power point
R_s	Series resistance
R_{sh}	Shunt resistance
T	Temperature
T_g	Glass transition temperature
V	Voltage
V_{P_m}	Voltage at the maximum power point
V_{OC}	Open circuit voltage

1. Introduction

The world's energy demand is steadily increasing every year. The main driving force for this increase is the rapid development of new economies like China and India but a general higher energy demand is present in all industrialised countries due to the uptake of new technologies. In 2017, the majority of the energy being produced on Earth to fulfil this demand is derived from fossil fuels. However, the climate change resulting from their use is pushing our planet to a point of no return. Considering the broader picture – the role of fossil fuels in the greenhouse effect,^[1] the likely damage inflicted by the extraction of the last reserves^[2] and the international tensions and open conflicts generated across the world by the fossil fuel industry – it is clear that we have to eliminate our reliance on them as fast as possible. Indeed, in the next two decades our society will have to completely rethink the way it produces and consumes energy, in order to avoid major planetary catastrophes.^[3] This compels a move away from waste intensive, fossil fuel-based energy technologies towards cleaner energy production, more energy efficient appliances and mandated reuse and recycling of waste. In terms of energy production, nuclear energy is often considered a clean and viable alternative. However, even leaving aside the radioactive waste produced, accidents such as Chernobyl and Fukushima remind us that when something fails in the nuclear field, the consequences are simply too severe to withstand. These facts lead inevitably to the conclusion that renewable energies are the only truly viable option to preserve the Earth for the future. Governments worldwide have started to make modest steps in this direction, such as the Paris agreement signed at the Cop21 conference in 2015. However, policies alone cannot be enough to achieve the targets: technology advancements must be developed by scientists and engineers to support these sweeping changes to our energy sector. In the sphere of energy production, these advances will correspond mostly to improvements in solar panels and wind turbines technologies, as the high availability of these two renewable energy sources means efforts here will have maximum impact.

1.1. Solar energy production overview

At the time of writing less than one per cent of the world's energy production (about 2% of the total electricity production) is supplied by solar energy.^[4] Despite this, it will be a crucial technology to enable humankind to address its looming energy demand problems. As an example, in 2016 86% of the new power generation capacity installed in the European Union was based on renewable sources.^[5] Essentially, the Sun provides an enormous amount of energy to the Earth surface. Even conservative estimates – including energy irradiated on emerged lands only and allowing a 65% energy loss due to atmospheric interference – show that the Sun irradiates about 23 000 TWy every year. For reference, the global energy demand in 2015 was approximately 18.5 TWy.^[6] In other words, the Sun provides enough energy to the Earth in seven hours to fulfil the entire global human energy demand for a year. Efficiently harvesting even a tiny fraction of this energy may solve our energy problems for the years to come. A general overview of energy availability in terms of

different renewable and fossil sources, which shows the great potential of solar energy, is depicted in Figure 1.

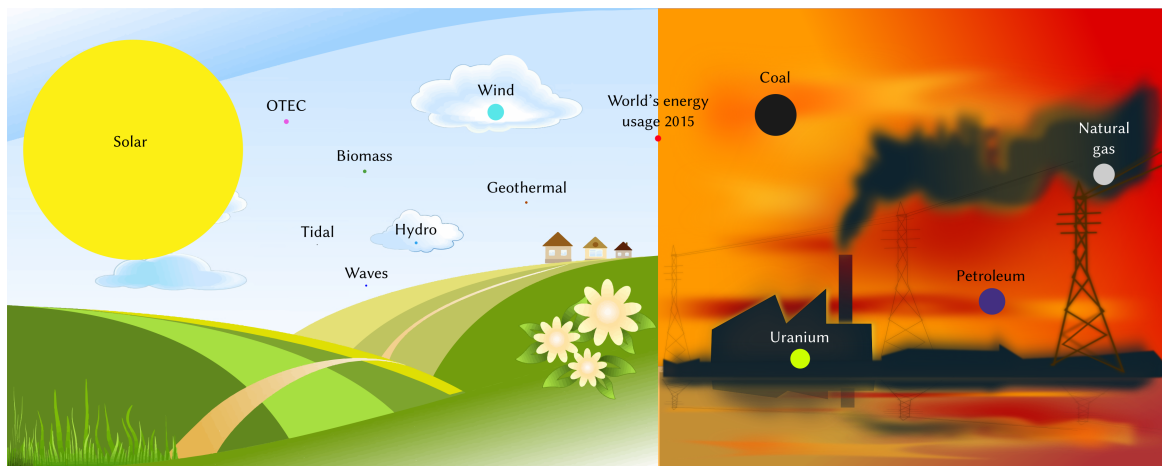


Figure 1. Total energy availability from renewable and fossil sources compared to annual energy consumption, adapted from Ref. [6]. Renewable sources are per year, fossil sources are the total amount known on Earth.

To date, solar energy production is dominated by panels comprised of silicon solar cells, either single- or multi-crystalline. Silicon technology is well established and mature, integrating forty years of laboratory research together with consolidated industrial production methods. Already, the most efficient solar panel in the market – produced by SunPower – can reach 22% solar-to-electrical power conversion efficiency (PCE), with the market average being about 17%. It is possible to estimate how many solar panels would be required to fulfil electricity and total energy requirements for two first-world countries like Germany (taken as a reference of central Europe) and Australia (the country with the highest solar irradiation in the world). The estimate is based on current technologies (20% PCE solar panel), using the data of electricity and total energy consumption per capita provided by the International Energy Agency and the solar irradiance data provided by Solargis. As a starting point for the comparison, Germany has both a lower energy consumption per capita and a lower Sun irradiation power throughout the year, compared to Australia. In Germany, 29 m²/person of solar panels would be required to meet the national electricity demand, while 180 m²/person would be required to meet the overall national energy demand. By contrast, Australia would require 26 m²/person and 164 m²/person, respectively, with its higher energy use more than compensated by its access to higher solar irradiation. In fact, this calculation is already tempered, based on the lower solar irradiance in the densely populated cities rather than the sunny but remote deserts. Looking at the numbers – and absent any other energy source – it is clear that the current technology might be sufficient to meet the *electricity* demand of an industrialised country but that it is still inadequate to meet its *overall energy* demand. Furthermore, the evident rise of electric cars replacing combustion engines will further increase the world's electricity demand, making efficient solar panels increasingly vital.

Other than panel efficiency and land usage, price is the other key factor that affects the uptake of solar energy in the market. It is increasingly clear that solar energy is gaining

momentum as a price competitive option. There are two prices relevant for solar energy: one is the price of the solar panel and the other is the levelised cost of electricity (LCOE), which is the ratio between the total cost of an energy production plant and the amount of energy that it will produce, both estimated over the plant lifetime. As shown in Figure 2, solar panel prices have decreased dramatically over recent years, from about 76.7 US\$ W⁻¹ of year 1997 to the 0.3 US\$ W⁻¹ of year 2015, with prices continuing in this downward trend over the last two years.

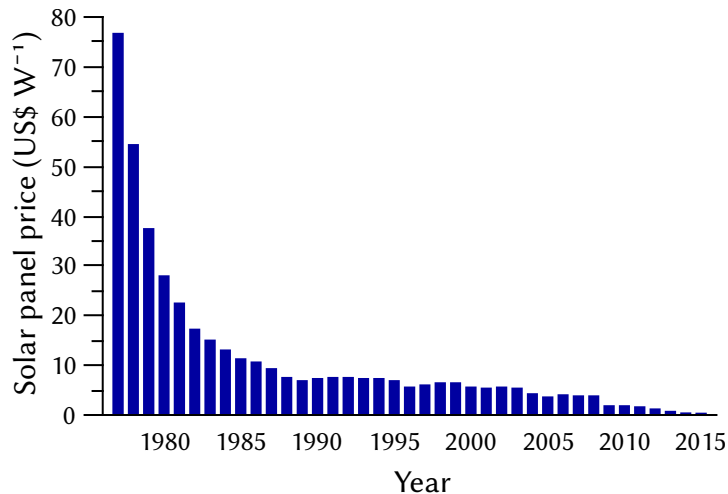


Figure 2. Solar panel price history. Data are taken from Bloomberg New Energy Finance up to year 2013 and from pv.energytrend.com for years 2014-15.

Solar panels have become so inexpensive that, in fact, they no longer represent the major cost of a PV installation anymore, although their contribution varies significantly when taking into account a small rooftop system or a large utility as a solar farm. A report on PV costs written by the U.S. National Renewable Energy Laboratory (NREL)^[7] found that the cost of the solar panel only accounts for 22.3% of the total cost for a rooftop PV system up to 45.3% for a large scale utility (Figure 3).

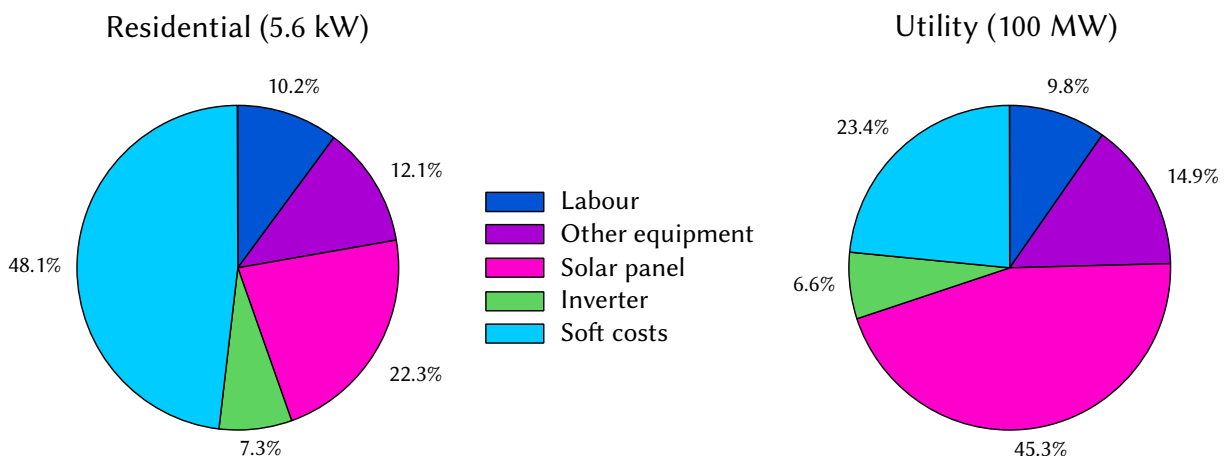


Figure 3. Breakdown of the various cost items of the LCOE for solar installations. Data taken from Ref. [7].

There is not a single method to calculate the LCOE of an energy technology that has found consensus in the market and unfortunately, results differ greatly depending on the method

chosen. One commonly used approach is to use a strict LCOE for a certain technology, without taking into account any external factor. Another one is to include in the LCOE the government subsidies for each technology (which, counter-intuitively, benefits fossil sources, as they are now more heavily subsidised than renewable sources worldwide). A third one is to include in the LCOE all the hidden costs of a certain technology, such as environmental impacts and direct and indirect health costs: a study by Epstein *et al.* in 2011 estimated that these hidden costs may reach \$500 billion per year in the U.S.^[8] When considering the latter method (which, in the writer's opinion, should always be preferred), renewable energy sources are revealed as being much less costly than fossil sources. Nevertheless, the first two methods remain in favour to calculate energy prices. Renewable sources, however, are not less costly than fossil ones only when considering all hidden costs. A report published by Lazard investment bank at the end of 2016^[9] demonstrates that – even disregarding subsidies and carbon impacts – renewable sources are already less costly than fossil ones even in this scenario. In the Lazard report, unsubsidised LCOE values varies between 46 and 61 US\$ MWh⁻¹ for utility-scale PV systems, between 88 and 222 US\$ MWh⁻¹ for rooftop PV systems, between 32 and 62 US\$ MWh⁻¹ for wind farms, between 60 and 143 US\$ MWh⁻¹ for coal plants and between 48 and 78 US\$ MWh⁻¹ for gas combined cycle plants. Indeed, some of the bids in the electricity market in late 2016 and early 2017 have been won by renewable energy suppliers with incredibly low prices. Energy production by renewable sources is no longer merely a private or a political choice, it has become and will continue as a strongly market-driven choice due to its low cost.

Despite the fact that renewable sources are now cost effective, the large scale transition of our electricity supply system away from fossil fuels will require huge effort, cost and time. There are two key drivers behind this, which are correlated: the nature of the energy source itself and legacy issues associated with existing design of our electrical infrastructure. Renewable sources are highly intermittent – the wind does not always blow, nor does it blow with the same intensity or from the same direction. The Sun does not shine overnight and even during the day its intensity varies depending on the location and the weather. This intermittence couples badly with our need for steady energy and so – in order for renewable energies to become predominant in our supply chain – efficient energy storage solutions must be developed and implemented. This will allow us to accumulate the excess of energy produced in peak times and inject it into the grid when production is outpaced by demand. It will also be important to rely on a variety of renewable energy sources – for example a combination of wind and solar – as diversification will help to balance this intermittence, giving an overall more stable production. While a fossil fuel power plant can be designed and built almost anywhere, in the case of renewable sources, plants must be built where the resource is abundant, which may well be far away from where the energy will actually be consumed. For example, in Germany most of the wind electricity is produced close to the North and Baltic seas and most of the PV electricity is produced in the southern regions, but the majority of consumption occurs in the central regions. This necessitates long, powerful

and efficient transmission lines, to transport the electricity from where it is produced to where it is used. Thus, this new energy production model will require that our grids are redesigned and demonstrates why these systems are currently under such significant pressure. Presently, our grids are designed with fossil fuels plants in mind as energy sources: a single point of input in a region that acts as a centre for electricity distribution. These plants supply a steady and known amount of energy at all times. As a result, our grids are reliable but are also very stiff and ill suited to adapt to the intermittency of the renewable sources and their more dispersed energy production model. A good example of this stiffness is the fact that on the 8th of May 2016, in Germany, for a few hours the electricity price in the national market went down to a negative value – customers were actually paid to consume electricity – due to an excess of renewable energy production that the grid was not able to manage. A diffuse energy production fuelled by renewable sources is certainly the future of energy production on Earth and renewable energy plants – at parity of costs – create many more jobs compared to fossil fuel plants as most of the money is spent on installation and maintenance of the system rather than on purchase of fuel, which is also beneficial for the larger society. Despite this, the complete redesign and adaptation of our electricity grids to accommodate an increasing reliance on renewable energy production will demand a significant investment of resources, money and time. Above all, it cannot be forgotten that the time required to implement these changes lies in stark contrast with the time available before the irreversible ravages of climate change render the continuation of our way of life impossible.

Based on the analysis above, it is possible to outline which technological improvements in solar technology will be most immediately critical to enable it to meaningfully supplement our energy needs. First of all, to provide a sufficient generation footprint, solar technology needs to greatly expand the range of locations and light conditions where panels can be installed and effectively operate. At a logical extreme, it might be said that every non-natural surface that is not capable of producing energy from light, is a wasted surface. Second, solar energy prices will need to go further down. This will mainly be achieved not by producing less expensive solar panels but by producing more efficient ones, achieving a better energy production over surface area ratio. Lowering the price of the panel, in fact, will only provide for a reduction of the solar panel cost item in the LCOE. By contrast, manufacturing a more efficient solar panel, even if this increases its price, will not only reduce the amount of active surface needed to produce a given amount of energy but, since the LCOE is calculated as a price per unit of energy produced, increasing the panel efficiency will uniformly lower every single cost item of the LCOE, providing a much greater reduction of the figure. This is where third generation solar cells, which are the subject of this thesis and which will be described in greater details in section 1.3, can play a key role in the shape of the energy technology of tomorrow. Although relatively efficient and well established, in fact, silicon solar cells are disadvantaged by being relatively expensive (due to their high energy fabrication process) and by their low efficiency in

indirect sunlight. By contrast, third generation cells can potentially be fabricated from low-energy solution processes, can be built on flexible substrates and work well in diffuse light. All these characteristics allow them to be much more versatile than silicon solar cells, for example in wearables, building integrated photovoltaics (BIPV), object surface treatments and many more. They are not only much less expensive than silicon cells but they will also enable ubiquitous PV energy production. Furthermore, given their relative ease of fabrication and different light absorption profiles compared to silicon cells, it is possible to use them in conjunction with silicon cells to create stacked devices (tandem solar cells). This – at a relatively small cost increase – will allow the manufacture of panels with much greater efficiency than silicon cells alone. Despite the fact that some of these solar cells have already entered the market, there is still a lot of research work to be done to push their efficiency and fabrication methods to the limit. Indeed, most of the technologies that comprise the third generation cells family are still only in their laboratory research phase.

1.2. Working principles of a silicon solar cell

Before introducing third generation solar cells, it is useful to explain in detail the working principles of a silicon solar cell. Some principles are in fact shared between the two classes, while others are better explained by contrast with the other. Silicon is a semiconductive material; that is – a material in which there is an energy gap (called band gap, E_g) between its valence and conduction bands. The valence band (VB) is the energy band where the electrons in their ground state (bound to the crystal lattice) reside, while the conduction band (CB) is the high energy band in which electrons are free to move throughout the material. Another important parameter to take into account is the Fermi level (E_F) of a material, which describes the total chemical potential for electrons of the material and it expresses the work required (obtained) to add (remove) an electron to (from) it. A single material can only have one Fermi level and in the case of a perfect semiconductor it sits in the middle of the band gap.

A silicon solar cell (also called photodiode) is what is called a *p-n* junction. In a silicon *p-n* junction two oppositely-doped (p-type, *p* and n-type, *n*) silicon materials are fused together. This creates an active region that is able to convert absorbed sunlight into electric current. A *p* silicon is a silicon crystal in which some of the lattice positions have been replaced by a boron atom. Boron possesses one *fewer* electron in its outer shell compared to silicon and its presence produces an electron vacancy (called a hole) in the crystal. This vacancy moves the E_F very close to the VB, as little work will now be required to add an electron to the crystal. By contrast, an *n* silicon is a silicon crystal in which some of the lattice positions have been replaced by a phosphorous atom. Phosphorous possesses one *more* electron in its outer shell compared to silicon and its presence produces an excess of electron density in the crystal. The result is that the E_F is moved very close to the CB, as little work will be now gained by removing an electron from the crystal, due to the excess of the electron density. When a *p* and an *n* silicon are fused together in a bigger single crystal the E_F of each half will align, as

there can be only one E_F per crystal. From a practical point of view, the excess of electrons in the n part of the crystal will migrate to fill the holes in the p part of the crystal, creating an accumulation of charges resulting in a net electric field at the interface. Due to the E_F alignment, both the VB and the CB will bend in the area where the electric field is present (called depletion region), generating a difference in energy potential and, hence, a driving force to physically separate photo-generated holes and excited electrons. A scheme of the depletion region is depicted in Figure 4.

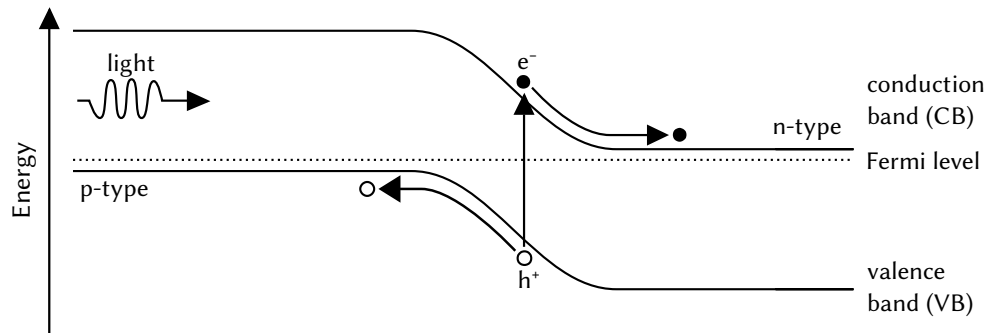


Figure 4. Scheme of the depletion region of a silicon solar cell (p-n junction).

When the energy of a photon is absorbed inside the depletion region, an electron is excited into the CB, creating an electron-hole pair. Both the excited electron and the resulting hole in the VB respond to the presence of the electric field and move toward a space in the crystal with a lower energy – as shown in Figure 4 – becoming spatially separated. Electric contacts on the two surfaces of the cell carry the charges across a circuit before they can recombine. The depletion region is not the only area where charges can be generated. The full active region of a silicon solar cell is, in fact, much larger than the length of the electric field at the p - n interface. Although electron-hole pairs generated outside of the depletion region cannot be immediately separated, through diffusion they can move towards the depletion region and become separated by its electric field. Silicon wafers for solar cells are cut thinly enough to be comprised of the active region only. The length of the active region is related to the diffusion length of the charge carriers, which is the total distance that an electron-hole pair can travel before recombination occurs. The thickness of the wafer needs to be small compared to the diffusion length of the charge carriers, to avoid excessive recombination in the region dominated by the diffusion process.

1.3. Third generation solar cells overview

The term “third generation solar cells” is a very broad umbrella that covers a multitude of research efforts to produce better or more efficient solar cells compared to silicon (1st generation) and thin film (2nd generation) solar cells. The term can either refer to techniques, such as tandem cells, concentrated PV, down-conversion and hot carriers,^[10] aimed at overcoming the Shockley-Queisser limit^[11] (the theoretical efficiency limit for a single band gap solar cell) or to actual solar cell technologies, that are characterised by being comprised of thin films of inexpensive, abundant and (usually) non-toxic materials.^[12,13] Examples of

these technologies are dye-sensitised (DSSC), organic (OPV), quantum dot (QDSC) and perovskite (PSC) solar cells.

Unlike silicon solar cells, in which the absorbed light generates free electron-hole pairs, all the aforementioned third generation solar cells are excitonic in nature.^[14] In excitonic solar cells, the absorbed light generates an exciton, rather than a free electron-hole pair. Excitons are still comprised of an electron-hole pair but these charges are much more tightly bound to each other compared to a $p-n$ junction. They are also much shorter lived and need to be physically separated at an interface in order to become independent. In the context of silicon solar cells the terms p or n indicate a lack or an excess of electron density in a crystal, by contrast in the case of excitonic cells p or n indicates a material which is capable of donating or receiving an electron, respectively. The driving force for the movement of charges is no longer generated by a bending of the bands and an internal electric field. In excitonic cells, charges move with a hopping process due to the energy mismatch at the various interfaces between the VBs or CBs – in the case of bulk materials – or the highest occupied (HOMO) or lowest unoccupied (LUMO) molecular orbitals – in the case of small molecules. While some of the third generation cells can still be considered $p-n$ junctions (e.g. in the case of OPV), more commonly they belong to the class of $p-i-n$ junctions, where i (the intrinsic material) is the light absorber where the excitons are generated. The intrinsic material is sandwiched between the p and n materials and in it, the two opposite charges remain bound together, becoming separated only when they reach their respective selective contacts. A scheme of the charge movements in a $p-i-n$ cell is depicted in Figure 5.

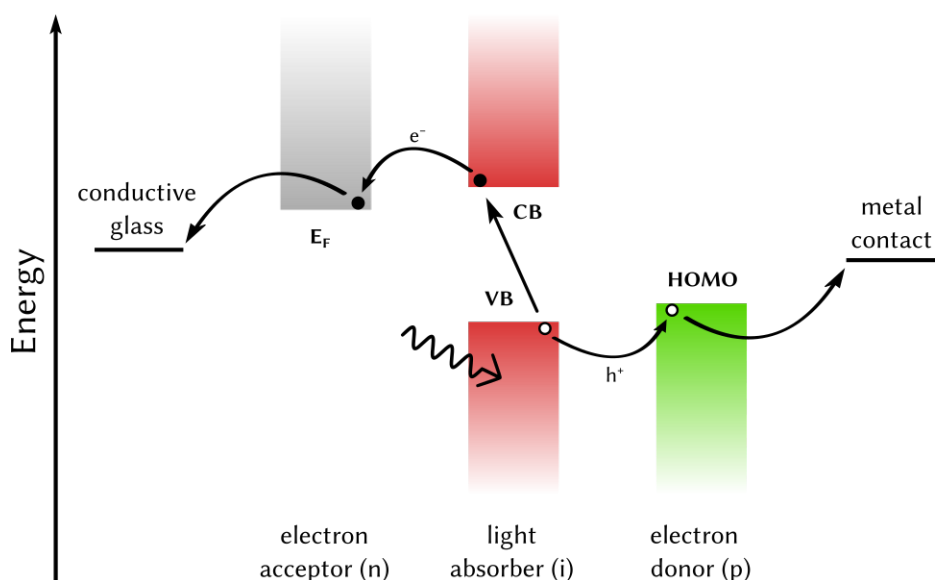


Figure 5. Scheme of the charge movements in a $p-i-n$ solar cell.

In the case of OPV, two organic small molecules or polymers are brought into contact and the p material is usually the light absorber. Excitons in OPV are very short lived and possess a carrier diffusion length (the distance that the exciton can travel before the charges recombine) of about 20 nm. Given the short exciton lifetime, it is impossible to build OPV cells by sequentially depositing layers of the p and n materials, as the amount of light

absorbed by a 20 nm layer would be too little. Instead, OPV cells are comprised of bulk heterojunctions (BHJ), where a blend of both the *p* and *n* materials is deposited as a film with a thickness varying between a few hundred nanometers and 1-2 μm ; the BHJ is deposited between selective contacts. The ideal structure of the BHJ would be one of two intertwined combs, ensuring a high contact area between the two materials and an efficient charge transport toward the respective selective contact in each material. In practice, it is not easy to control the morphology of BHJs and there are always “dead” zones inside them, either because the thickness of a material in a particular area is larger than the carrier diffusion length or because a certain domain of a material is not connected to its selective contact.

DSSCs are a classic example of a *p-i-n* solar cell. In *n*-type DSSCs (Figure 6), a mesoporous layer of titania nanoparticles (mp-TiO₂, which acts as the *n* material) is sintered on a thin conductive oxide (TCO) glass. This electrode (called photoanode) is then immersed in a solution containing a dye (the *i* material), which infiltrates the mesoporous structure and gets chemisorbed as a single layer on the titania surface. The electrode is then sealed using another TCO glass on the back – coated with platinum or graphite to act as a cathode – and the space in between is filled with a solution containing a redox couple (the *p* material; the most common couple is I⁻/I₃⁻) before the cell is sealed. In such a structured cell, a photon is absorbed by the dye, which promotes an electron from the ground state to an excited state; the electron is injected in the E_F of the titania and the reduced species of the redox couple is oxidised, donating an electron to the dye. To close the circuit, the oxidised species of the redox couple is regenerated at the cathode.

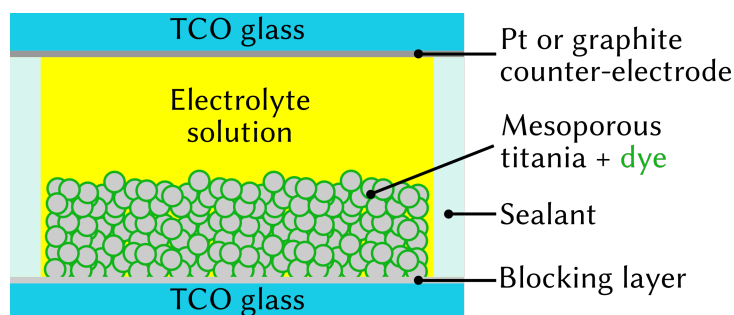


Figure 6. Scheme of a *n*-type solution-based DSSC.

DSSCs work best (relatively speaking) in diffuse light and at lower light intensities, rather than in full direct sunlight; furthermore, they are very colourful and transparent. These characteristics makes them perfect for BIPV applications, either as coloured windows capable of generating electricity or as functional, decorative elements within a building. The main disadvantage of DSSCs is the liquid solution inside, which can leak or evaporate if the sealing is compromised. The causes for sealing failure can be either physical – due to mechanical stress or imperfect fabrication – or chemical – when the sealing material is not able to withstand the action of the usually corrosive redox couple. In order to overcome this issue, fully solid state DSSCs (ssDSSC) have been developed, in which the redox couple in

solution is replaced with a solid state small molecule or polymer, which takes the name of hole transporting material (HTM, hole conductor). Despite removing the risk of a leakage or evaporation, the introduction of an HTM generates a different set of problems and as a result ssDSSCs are usually less efficient than their liquid counterparts.

QDSCs have the same structure as a DSSC but in these the dye molecule is replaced by quantum dots. PSCs are the subject of this thesis and will be analysed in more detail in the following section.

1.4. Perovskite solar cells overview

Perovskite solar cells have attracted a lot of interest in the past few years, due to their inexpensive materials, ease of fabrication and the fact that they have reached a remarkable 23% certified PCE^[15] in merely five years of research. The term “perovskite” does not represent a single material but a crystal structure typical of materials with an ABX_3 composition, where A is a cation with a large ionic radius, B is a cation with a small ionic radius and a charge double than that of A and X is an anion with the same charge of A. The first compound to be classified as perovskite was $CaTiO_3$, so named by its discoverer in honour of a minister of the Russian Imperial Court. The perovskite crystal is comprised of octahedra of B and X, with each X anion being shared by two B cations; the A cations are placed in the interstices between the octahedra. The material composition of the perovskite absorber in a solar cell can vary but they all share the same crystal structure (although with a different degree of distortion) and the same category name. In a perovskite cell, A is usually a small organic cation – such as methylammonium ($CH_3NH_3^+$, MA) or formamidinium ($CH(NH_2)_2^+$, FA) – or an alkali metal – such as Cs^+ or Rb^+ ; B is almost always Pb^{2+} and X is a halogen (I^- or Br^- ; Cl^- is sometimes used in small quantities). A perovskite crystal of $MAPbI_3$ is depicted in Figure 7.^[16]

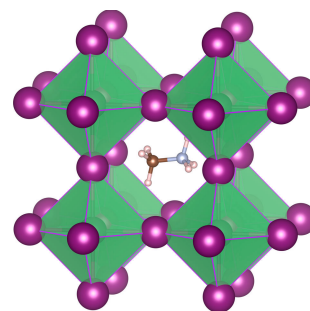


Figure 7. $MAPbI_3$ perovskite crystal. Image taken from Ref. [16].

1.4.1. Perovskite solar cells early history

The perovskite absorber was first used as a dye in DSSCs. Indeed, the first PSC fabricated by Miyasaka and co-workers in 2009^[17] was very similar to a DSSC, since the perovskite was deposited on top of a mesoporous titania layer with a redox couple in an electrolyte solution used to regenerate the light absorber. This cell, while reaching a remarkable PCE of 3.8%, was extremely unstable, degrading in less than an hour due to the liquid electrolyte dissolving the organometal halide perovskite. Perovskites were re-discovered in 2012, when Snaith and co-workers^[18] and Park and co-workers^[19] replaced the liquid electrolyte with a solid-state HTM. In contrast to ssDSSCs – which are less efficient than their solution-based counterparts – the presence of an HTM boosted the cell efficiency to about 10% and its stability to weeks. Furthermore, Snaith discovered that, unlike a DSSC dye, the perovskite

absorber does not need a mesoporous titania layer to work properly and that the perovskite crystal was able to carry the electrons to the electrode when deposited on a mesoporous alumina layer (which is an insulator). This finding suggested that the perovskite was more than a mere light absorber for DSSCs and indeed a year later Snaith and co-workers fabricated the first planar PSC,^[20] possessing a remarkable 15% PCE. In this cell the perovskite was deposited over a compact layer of titania (c-TiO₂, also called blocking layer, to act as an *n* contact) without the need of any mesoporous scaffold. These two findings established PSCs as a solar cell technology in their own right, rather than just a kind of DSSC.

1.4.2. Perovskite's unique properties

The fact that it is possible to fabricate an efficient planar device demonstrated the uniqueness of perovskite light absorbers. In the discussion about third generation cells above, it was shown that OPV needs a BHJ to fabricate efficient cells due to its short exciton lifetime. In the case of perovskites, since the very beginning – when deposition methods were not yet fully optimised – it was already shown that these materials possessed remarkable carrier diffusion lengths *e.g.* length exceeding 100 nm for MAPbI₃ films^[21] and even longer, exceeding 1 μm, for chlorine-doped films of MAPbI_{3-x}Cl_x.^[22] More recent studies on single crystals of MAPbI₃ show carrier diffusion lengths reaching values above 175 μm under full sun illumination and 3 mm in low sun intensity^[23] with very low trap state densities (in the order of 10⁹-10¹⁰ cm⁻³), which is comparable to the value for silicon solar cells.^[24] These extraordinary carrier diffusion lengths are achieved thanks to the peculiarities of the perovskite crystal structure and film formation. Density functional theory (DFT) theoretical computations on perovskite crystals^[25,26] show that the perovskite materials possess a high molar extinction coefficient (ϵ) in the order of 10⁴ M⁻¹ cm⁻¹. This allows high light absorption even in thin films (~300 nm); small effective masses for both electron and holes; high energy formation for deep level defects (leading to the absence of trap states inside the band gap) and intrinsic benign grain boundaries, which do not generate trap states, allowing a polycrystalline film to perform almost like a single crystal.

1.4.3. Perovskite deposition and solar cell architecture

The first major problem of PSC fabrication has been the deposition of a uniform and continuous perovskite film from solution. The perovskite crystal growth rate, in fact, is much higher than its nucleation rate and the perovskite crystal tends to grow with a dendritic structure. This produces layer gaps on the substrate surface which eventually lead to a short circuit of the final device. Three methods have been developed and are currently used to overcome this problem; each having been first developed for the MAPbI₃ perovskite. The first method involves a two-step sequential deposition and was developed by Burschka *et al.*^[27] In the first step, a solution of PbI₂ is spin-coated on the substrate: PbI₂ deposits as a relatively uniform and amorphous film. In the second step, the substrate is immersed in a solution of MAI in 2-propanol for 20 s: the MAI infiltrates and reacts with the PbI₂ film

producing a uniform perovskite layer. With this technique, the formation of dendrites is inhibited due to the close packing achieved with the PbI_2 pre-coating. The other two methods utilise a single step for the deposition and in each the goal is to increase the crystal nucleation rate as compared to the growth rate. The first of these was developed in parallel by Jeon *et al.*^[28] and by Xiao *et al.*^[29] and involves the introduction of an anti-solvent during the spin-coating of the perovskite solution. In practice, a few seconds after the spin-coating process commences, an anti-solvent (typically chlorobenzene, CBZ) is pipetted on the substrate, inducing a fast precipitation of the perovskite material. This also results in a uniform perovskite film, because the film is precipitated (with a high nucleation rate) before the formation of dendrites can begin. The final method was developed by Huang *et al.*^[30] and it is based on the same concept. In this method, the anti-solvent is replaced with a stream of inert gas (either N_2 or Ar) which removes the perovskite solution solvent more quickly, again inducing a fast precipitation, before dendrite formation occurs.

In terms of device fabrication, perovskites are very flexible materials and the majority of the research community utilise three main device architectures. The first of these is the mesoporous structure, in which the perovskite infiltrates a mesoporous scaffold of either titania or alumina, with or without a perovskite capping layer on top of the mesoporous one. The second is the planar structure, in which the perovskite is directly deposited on top of a blocking layer. The third architecture is the inverted structure (which can be either mesoporous or planar) and involves the perovskite being deposited on top of the HTM rather than the electron transporting layer (ETL). Schemes of the three device architectures are depicted in Figure 8.

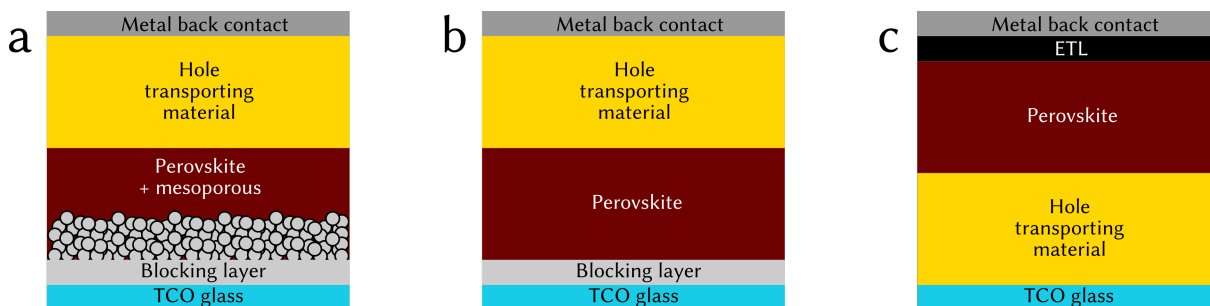


Figure 8. Scheme of the (a) mesoporous, (b) planar and (c) inverted PSC architectures. Layer heights are not in scale.

1.4.4. Different perovskite materials

As discussed previously, the term perovskite does not refer to a single material, but to a class of materials sharing the same crystal structure. Perovskite materials for solar applications present a highly symmetric cubic structure, in which the halogen ions occupy the vertices of octahedra with the metal bivalent cation in the centre, while the monovalent cation is hosted in the cuboctahedral cavities formed by the connecting octahedra. Goldschmidt developed an equation for a tolerance factor in perovskite crystals, which describes the level of distortion of the cubic symmetry of a crystal and the point at which

the crystal loses its cubic symmetry due to distortion and adopts a different, lower energy structure.^[31] The equation for the tolerance factor t is the following:

$$t = \frac{r_A + r_X}{\sqrt{2}(r_B + r_X)}, \quad (1)$$

where r_A , r_B and r_X are the ionic radii of the ions A, B and X, respectively. The perovskite structure is perfectly cubic when t is equal to 1, so from equation 1 it derives that the A cation needs to be larger than the B cation. In general, the cubic symmetry is retained for values of t between 0.8 and 1.^[32] Although geometrical considerations alone are not sufficient to predict the formation of a perovskite crystal – chemical stability and bond valence are other important factors for example – the tolerance factor is a good indicator to predict if a set of different materials will be able to form a perovskite crystal. Indeed, in the very first paper on perovskites, Miyasaka and co-workers were already presenting two different perovskite materials: MAPbI₃ and MAPbBr₃.^[17]

Different perovskite materials present different characteristics, such as different band gap, VB and CB energy levels, phase transition and, ultimately, solar cell efficiency and stability. Noh *et al.*^[33] and Eperon *et al.*^[34] show how mixing iodide and bromide halides in MAPbI_{3-x}Br_x and FAPbI_{3-x}Br_x, respectively, can produce perovskite layers with different colours ranging from yellow-orange to brown-black. This is due to the fact that the density of states (DOS) at the edge of both the VB and the CB is dominated by the orbitals of the lead cation and the halide anion and by the angle of their bond:^[35] substituting the halide anion changes the DOS at the edges of the bands and therefore, the band gap.

While the composition of the X ion is important to tune the energy properties, the major role of the A ion is to control phase transitions, as A is the ion sitting in the octahedra interstices, preventing them from collapsing. As an example, MAPbI₃ undergoes two phase transitions which are attributed to different levels of disorder of MA caused by temperature change. At higher temperatures the orientation of MA inside the interstices is highly disordered due to the high thermal energy; at lower temperatures this disorder is reduced, affecting the average shape of the molecule and hence its ionic radius. Unfortunately, one of the phase transitions occurs in the working temperature range of a solar cell (at about 60 °C)^[36] and the constant phase change may well lead to quicker degradation of the perovskite film. Perovskites based on the FA cation present a higher temperature phase transition and are therefore potentially more stable during operation.^[37,38]

Halide ions are not the only ions that can be mixed in a single perovskite material – all ions can be mixed at the same time, providing opportunities to tune the band gap and the geometrical stability of the perovskite material. As an example, the third most efficient existing perovskite cell (there is no disclosed information regarding the current record cell) – developed by Saliba *et al.*^[39] – employs a highly mixed perovskite material with general formula Cs_x(MA_{0.17}FA_{0.83})_(1-x)Pb(I_{0.83}Br_{0.17})₃ and it reaches efficiencies up to 21%, with a long-

term stability of 250 h at 18% PCE. Attempts to replace lead as the B cation with a non-toxic material – such as germanium^[40] or tin^[41] – have also been made but both Ge and Sn have a more stable and energetically favoured (IV) oxidation state compared to the (II) oxidation state. For this reason, cells fabricated with these are usually short-lived due to the oxidation of the metal cation and the loss of the perovskite structure.

1.4.5. Overview of other components of a perovskite solar cell

Perovskite solar cells are usually fabricated by solution process, depositing the perovskite precursor solution on a substrate to form a film. The substrate is acting as an electrode for the solar cell and therefore, it needs to be both transparent (in order for the light to reach the perovskite film) and conductive. The most common substrate for PSC fabrication is a glass sheet (or a plastic sheet for flexible devices) coated with a thin layer of conductive oxide. The two most commonly employed TCOs are indium tin oxide (ITO) and fluorine-doped tin oxide (FTO). The latter shows poorer performances – both in terms of conductivity and transmittance – but it is also much less expensive and overcomes the problem of indium scarce availability, which would fast become an issue in the case of mass production of TCO glasses.

The nature of the blocking layer or of the ETL varies depending on the architecture of the PSC. In the standard architecture, the blocking layer is deposited directly on top of the TCO and can be deposited at a high temperature. In this case, the layer is usually comprised of a semiconducting oxide, most typically TiO_2 . ZnO has been used in some earlier work but this oxide induces quick perovskite degradation^[42] and it has therefore been abandoned. More recently, SnO_2 has been proposed as an efficient blocking layer with a lower deposition temperature compared to TiO_2 .^[43] When using an inverted cell architecture, metal oxides cannot be used as ETLs due to the high temperature required for their deposition. Thus, fullerene is commonly used as an alternative electron selective contact.^[44]

At the other end of the perovskite layer, HTMs can vary greatly and studies exist on organic small molecules, polymers, metal complexes and inorganic salts or oxides. A more comprehensive overview on HTMs follows below.

The back electrode of a PSC can be comprised of a variety of materials. In the standard architecture, gold is usually thermally evaporated on top of the HTM. Silver is also used but – despite the presence of the HTM – it tends to react with the iodide of the perovskite layer to form AgI , reducing the long-term stability of the cell.^[45] When metal evaporation is not feasible, graphite is also considered a good electrode.^[46] In the case of inverted structure cells, gold is usually replaced with aluminium as its work function is more suitable.^[47] When solar cell transparency is important and it is not possible to deposit a thin metal layer as a back electrode, metal nanowires^[48] or TCOs^[49] are employed.

One of the peculiarities of perovskites is that they can transport electrons and holes equally well,^[50] that is – they are ambipolar in nature. This characteristic of the perovskite allows

the fabrication of devices with good efficiency where one of the selective contacts, either n ^[51] or p ^[52] is missing. Despite this, the highest efficiencies are only attained when good n and p materials are both present in the cell.

1.4.6. The hysteresis conundrum

Among the peculiarities of perovskites – most of which make them wonderful materials – one – the so-called hysteresis problem – is a source of trouble. Unlike every other solar cell, PSCs give a different efficiency value depending on the scan speed and direction of the current density-voltage (J - V) curve (refer to appendix A for the methods employed to perform electrical characterisation of a solar cell). This problem was first discovered by Snaith *et al.*^[53] in 2014 and since then it has become common practice in the perovskite field to report results in both scanning directions. An example of the hysteretic behaviour of a PSC is depicted in Figure 9.

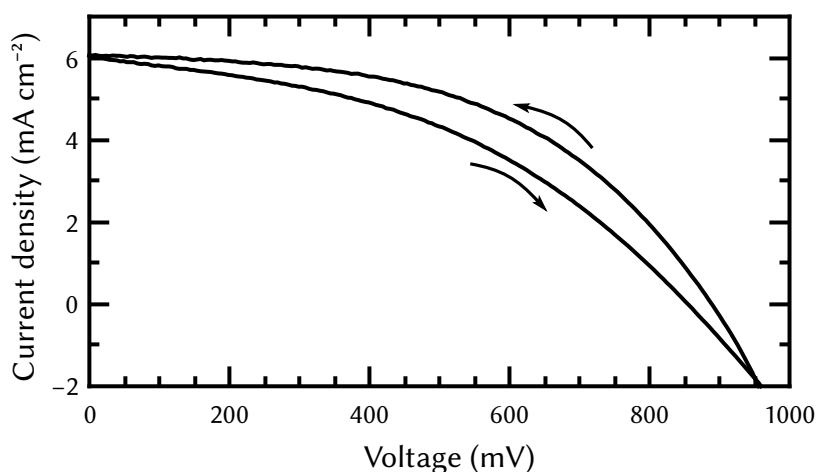


Figure 9. Hysteretic behaviour of a PSC. The arrows indicate the scan direction.

Since Snaith's first paper, a lot of research efforts have been spent in trying to understand the nature of the hysteresis in PSCs.^[54] A definitive understanding of this problem is yet to be reached but the main theories regarding its source initially related to slow transient capacitive currents, dynamic trapping and de-trapping processes of charge carriers, band bending due to ion migration and/or band bending due to ferroelectric polarization of perovskites. Recent experiments are proving that the hysteresis is not due to the ferroelectric nature of perovskites^[55] and are instead supporting the ion migration hypothesis.^[56] Compared to planar PSCs, little to no hysteresis is shown in PSCs comprised of a mesoporous titania layer^[57] or in inverted structure PSCs^[58] – where fullerene is the ETL.^[59] In the case of mesoporous titania it is believed that the high surface contact area between the perovskite and the n material is the cause of the hysteresis reduction, due to an increased electron injection despite the relatively poor contact between the materials.^[60] In the case of inverted cells, it is hypothesised that fullerene has the dual advantage of passivating defects in the perovskite grain boundaries by infiltrating them and of creating a better contact with the perovskite in general. The hysteresis is not only due to the contact

with the n material: a different p material on top of the same $n-i$ structure can also significantly influence the hysteresis.^[46,61] Many researchers believe that hysteresis in PSCs is an intrinsic problem to be solved. It is my opinion that hysteresis is not a problem *per se*, as the problem it poses merely impacts on the ability to quickly and reliably measure the efficiency of a solar cell. A more time-consuming steady state or maximum power point tracking measurement would yield the correct solar cell efficiency regardless of how large its hysteresis may be. The hysteresis is an easy way of studying and understanding charge transport mechanisms in PSCs and provides a good indicator of the quality of the contact between the different materials. Thus, it is important to recognise the “hysteresis problem” as it reflects the quality of contacts between the materials. However, if a hypothetical PSC was highly efficient and stable but with a large hysteresis, it is my opinion that the large hysteresis should not itself be regarded as a problem to solve for that particular cell, unless doing so would improve its efficiency.

1.5. Hole transporting materials overview

Research on ETLs is dominated by a few metal oxides – due to their good conductive properties, low cost and consolidated knowledge derived from the DSSC field – and by fullerenes, which are very well known in the OPV field. Research on HTMs, on the other hand, remains very open and a leading category of compounds is yet to be found. The first HTM employed by both Snaith and Park and their teams in 2012 was 2,2',7,7'-tetrakis-(N,N -di- p -methoxyphenylamino)-9,9'-spirobifluorene (spiro-OMeTAD, Figure 10), which is the HTM that Bach *et al.*^[62] used for the first time in ssDSSCs with high efficiencies. Despite all the research efforts on new HTMs, to date spiro-OMeTAD is still the molecule of choice for the p material in PSCs and almost all newly developed HTMs are tested against it.

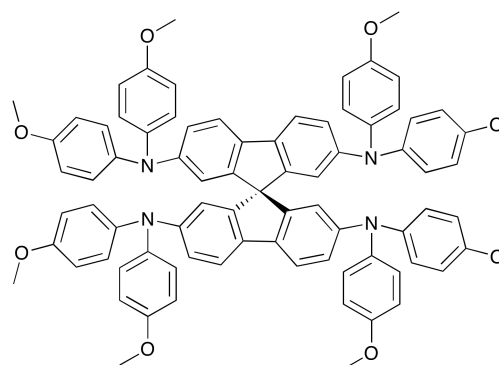


Figure 10. Spiro-OMeTAD.

While spiro-OMeTAD is capable of achieving high PCEs in laboratory-scale devices, it also entails several drawbacks that prevent its use in large-scale device production and a suitable alternative will need to be found before PSCs can enter the market. The first hurdle for spiro-OMeTAD is economical in nature: to date, the price of spiro-OMeTAD is in the order of AU\$300 per gram, which makes it five times more expensive than gold. Although the resultant economy of scale would reduce this problem in mass production, the complexity of the synthesis and purification required to obtain a solar-grade material would keep the price unfeasibly high. The second drawback is related to the electrical conductivity of spiro-OMeTAD, which is very low in its pristine form. In order to achieve conductivities high enough to be efficiently employed as an HTM in solar cells, spiro-OMeTAD needs to be mixed with additives which facilitate its oxidation either chemically or upon light exposure

and which introduce ions in the film to facilitate charge movements.^[63] These additives are very hygroscopic and facilitate the ingress of moisture in the device, which is detrimental to the perovskite lifetime. PSCs employing spiro-OMeTAD also demonstrate the so-called fatigue behaviour, which severely hampers the solar cell performance in real operational conditions.^[64] The same problem does not occur when other HTMs are employed.^[65] Due to all the aforementioned reasons, research efforts have focused on developing novel HTMs for PSCs that are more economically viable, more stable and/or more conductive than spiro-OMeTAD, to avoid the use of additives. More than a hundred compounds have been synthesised and tested, most of which have been the subject of recent reviews.^[66–69] In the following section the main key parameters for an efficient hole conductor will be discussed, followed by a review of the most promising compounds of each category: organic small molecules, polymers, inorganic salts or oxides and metal complexes.

1.5.1. Key parameters for efficient hole transporting materials

When designing an efficient HTM for solar cell applications, many parameters – some physical, some chemical – need to be considered. From a physical perspective, the most important properties for an HTM are its HOMO and LUMO energy levels and its conductivity, σ (or hole mobility, μ_h). From a chemical point of view, the most critical consideration is the different moieties which comprise a given compound. These moieties and their position in the molecule, in fact, affect parameters such as the quality of the contacts with other materials, the spatial position of the HOMO and LUMO in the molecule and the geometry of the molecule itself. The molecule's geometry, in turn, affects film-forming properties such as the degree of crystallinity and the film's glass transition temperature (T_g). Furthermore, the HTM should be chemically stable and compatible with the perovskite of choice, to avoid the degradation of the light absorber.

The task of the HTM in a PSC is to receive a hole from the perovskite and to transport it to the counter electrode (or, if viewed from the opposite side, to donate an electron to the perovskite and then to obtain it back from the counter electrode). In order to achieve this, charges need to hop from one molecule to the other across the thickness of the HTM layer. For this reason, it is important for a hole conductor to feature at least one moiety on a side that possesses a high electron density and whose cationic form is stable enough to avoid fast recombination. The most common functional groups with these characteristics involve the presence of a nitrogen atom (that has a lone electron pair) bonded to aromatic rings in order to distribute the positive charge resulting from the electron donation and stabilise the cation. The triphenylamine group is the one most employed in HTMs^[66,70] but carbazoles,^[71–73] (triazol)truxenes,^[74,75] *S,N*-heteroacenes,^[76,77] diketopyrrolopyrroles,^[78] *N*-phenylindoles,^[79] or their combinations^[80] are also used. The molecular structures of these moieties are depicted in Figure 11. These side moieties have a strong influence on the hole conductor's HOMO energy level and sometimes this contribution prevents a good matching with the perovskite's energy levels. Due to the electronic configuration of these

functionalities, in fact, the resulting HOMO of the molecule might be either too deep or too shallow compared to the valence band edge (E_{VB}) of the perovskite. To tune the energy levels, these moieties are often substituted with electron donating or withdrawing groups that change the overall electronic configuration of the molecule. The most clear example is the case of the triphenylamine group, in which the two phenyl rings that are not attached to the rest of the molecule are usually substituted with a methoxy group in *para* position to destabilise the electron clouds in the rings and thus raise the energy level.

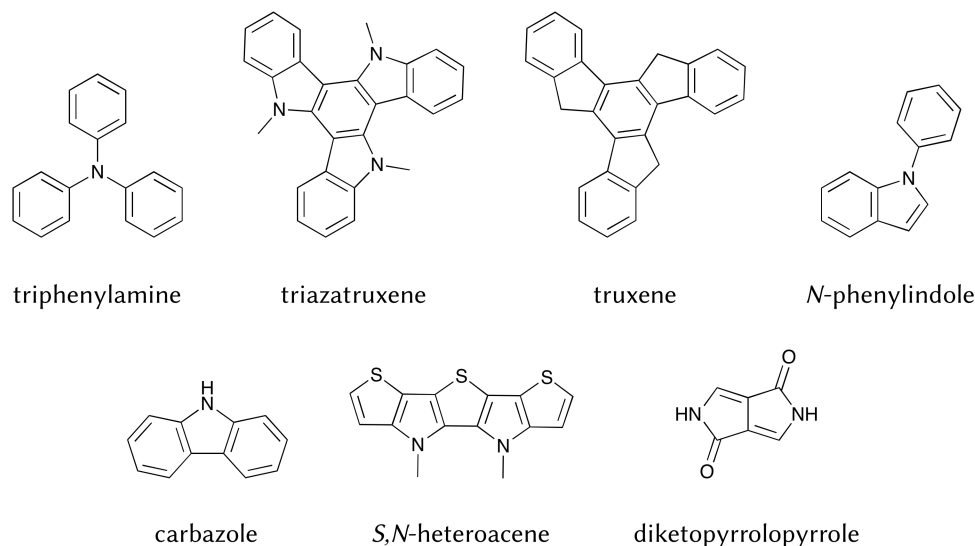


Figure 11. Common side moieties for HTMs.

The core moiety of a molecule – to which the various side groups are attached – also plays two important roles in an HTM. From an electronic perspective, it allows or blocks electron movements across the molecule and has a big influence on the position of the LUMO of the molecule. The core moiety's most important role, however, is to define the structural geometry of the molecule, from which all the film-forming properties of an HTM derive. In the case of spiro-OMeTAD, for example, the central sp^3 carbon of the spiro core has a tetrahedral geometry, making the two triphenylamine couples orthogonal to each other, giving the molecule a crossed structure. Furthermore, the same central carbon blocks electron conductivity across the molecule, so that the HOMO is localised in one of the two triphenylamine couples and the HOMO-1 in the other, both with very similar energies.^[81] As an opposite example, truxene is a very flat and large moiety without any heteroatom. Therefore, resulting molecules are mostly planar and with the HOMO and LUMO delocalised across the entire molecule.^[82] In other cases, the HOMO and the LUMO are completely separated in opposite sides of the molecule.^[83]

These considerations on geometry and orbitals shape are very important to the final performance of the HTM film, as they bring benefits that are mutually exclusive and it is important to find a good balance between them, to design an efficient HTM. For example, molecules with a more defined 3D structure like spiro-OMeTAD are more likely to form amorphous, glassy films compared to planar molecules. These glassy films usually present a

lower concentration of pinholes and defects and are, therefore, of higher quality. On the other hand, planar molecules present high π -stacking capabilities, which lead to the presence of crystalline domains in the film, with associated domain boundaries that the evaporated metal counter electrode can infiltrate, reducing the quality of electric contacts. At the same time, the various molecules inside glassy films are not in close contact with each other (at least in relative terms) and this can hinder an efficient charge transport inside the film, reducing the conductivity and increasing the charge recombination rate. On the other hand, the high π -stacking ensures good charge transport across a crystalline domain, providing a much higher conductivity compared to amorphous films. Orbital positions inside the molecule are important due to the hopping mechanism of charge transport in HTMs (except the fully inorganic ones). For the charge to move from one molecule to the other to reach the counter electrode, the relevant orbitals of the donating and receiving molecules have to be in close contact for an easy charge transfer. A final consideration is the molecular size of an HTM and the intermolecular interactions in a glassy film. Larger molecules that interact more strongly in the film, in fact, present a much higher T_g . It is important for the T_g of the HTM to be well above the maximum solar cell operation temperature, to avoid long-term degradation of the device due to molecular diffusion and re-arrangements of the HTM layer above its glass transition temperature.

Concerning the physical parameters, both the HOMO and LUMO energy levels and the conductivity/hole mobility are equally important. As already discussed in section 1.3, in third generation solar cells the driving force for the charge separation is given by the energy mismatch of the HOMO/LUMO energies of the various materials. This poses again a problem of balancing two mutually exclusive beneficial effects. On the one hand, in fact, the higher the energy mismatch, the higher the charge injection rate and the lower the recombination rate between the i and the p/n materials, until an asymptote is reached. On the other hand, the maximum open circuit voltage (V_{OC}) obtainable by a solar cell is given by the difference in potential between the HOMO/ E_{VB} of the HTM and the LUMO/ E_F of the ETL. To maximise this potential difference, it is necessary to minimise the energy mismatches between the various layers. In DSSCs the minimum amount of driving force required to efficiently regenerate the dye varies for different dye/redox couple combinations but in general, hundreds of millivolts are required.^[84] In PSCs, only tens of millivolts are required for good charge transfer,^[78,85] noting that when the driving force is very little, although there is no loss in short circuit current density (J_{sc}), there is also no gain in V_{OC} despite the larger difference in potential between the HTM and the ETL.

Conductivity (σ) and hole mobility (μ_h) are related intrinsic properties of a material. The conductivity measures the ability of a material to conduct an electric current, while the hole mobility measures the speed of a hole that moves through a material. The two properties are directly related by the following equation:

$$\sigma = \mu_h e \rho_h , \quad (2)$$

where ρ_h is the concentration of holes in a given material and e the elementary charge. The same equation applies to the relation between conductivity and electron mobility and for a material that can conduct both electron and holes the total conductivity is the sum of the two. A high conductivity is very important for a material to be employed in a solar cell. This parameter is, in fact, inversely related to the recombination rate of the charges: the faster the free charges are moved away from where they are generated, the less probable their recombination becomes. In addition to high conductivities of the materials in a solar cell, charge mobilities (for both electrons and holes) need to be well balanced throughout the various layers, to avoid accumulation of charges at an interface. Both perovskites^[86] and TiO_2 ^[87] possess high carrier mobilities, while organic hole conductors usually present much lower hole mobilities.^[88–90] In order to increase the conductivity of HTMs, additives are usually added to the precursor solution; the two most common ones are lithium bis(trifluoromethylsulfonyl)imide (LiTFSI) and 4-*tert*-butylpyridine (tBP). The role played by these additives in the HTM performance increase is not yet fully understood, although Snaith and Grätzel believe that in the case of LiTFSI the improvements are related to an increased molecular disorder in the film and a broadening of the tail of the density of states in the HTM.^[91] Another way of increasing the conductivity of the HTM is to chemically dope it. In this case, the oxidised form of a metal complex with a redox potential higher than that of the HTM is commonly added to the solution. The metal complex oxidises the hole conductor, creating an HTM^+ species while reducing itself. Cobalt complexes are usually used for this purpose,^[92–94] but an iridium complex has also been studied.^[95] Instead of using metal complexes to dope the HTM, it is also possible to mix the hole conductor with a pre-synthesised oxidised form of the HTM itself.^[96] The main role of these p dopants is to increase the density of holes in the HTM layer and thereby enhance conductivity.

1.5.2. Organic small molecular hole conductors

In the past five years of PSC research, more than a hundred organic small molecules have been synthesised and characterised as HTMs, to try to replace spiro-OMeTAD as material of choice in PSCs. Some of these materials have demonstrated similar or better performances compared to spiro-OMeTAD but have failed to gain the attention of the field and to be employed by different research groups. A full review of all these compounds would be too extensive to conduct and many exist in the literature already.^[66,68,97,98] Instead, in this section a review of the best performing HTMs or of ones that could give useful insights for future developments will be provided.

Spiro-OMeTAD is arguably the best HTM for PSCs to date. Nevertheless, it is useful to understand how modifications in the side moieties of this molecule influence its HOMO energy level and its charge transport properties. Jeon *et al.*^[99] have modified spiro-OMeTAD by varying the position of the methoxy group in four of the eight external phenyl rings. The original spiro-OMeTAD molecule was called *pp*-spiro-OMeTAD (*pp*) and the two variations were called *po*-spiro-OMeTAD (*po*, four methoxy moved to the *ortho* position) and *pm*-spiro-

OMeTAD (*pm*, four methoxy moved to the *meta* position). Hu *et al.*^[100] decided instead to substitute the eight *para* methoxy groups with either ethyl (spiro-E), *N,N*-dimethylamino (spiro-N) or methylsulfanyl (spiro-S) groups. The molecules involved in these two studies are depicted in Figure 12 and their properties are listed in Table 1.

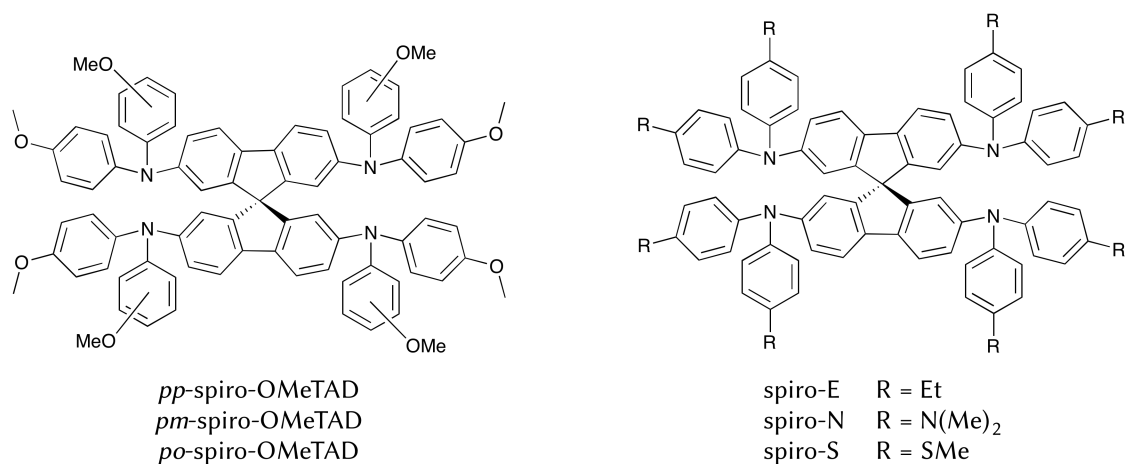


Figure 12. Modified spiro-OMeTAD molecules.

Table 1. Properties of modified spiro-OMeTAD HTMs for PSCs.

HTM	HOMO (eV)	HOMO of spiro ^a (eV)	Hole mobility (10 ⁵ cm ² V ⁻¹ s ⁻¹)	Hole mobility of spiro ^a (10 ⁵ cm ² V ⁻¹ s ⁻¹)	PCE ^b (%)	PCE with spiro ^{a,b} (%)
<i>pp</i> -spiro-OMeTAD ^[99]	-5.22	-5.22 ^c	NR ^d	NR	14.9	15.2 ^e
<i>pm</i> -spiro-OMeTAD ^[99]	-5.31	-5.22 ^c	NR	NR	13.9	15.2 ^e
<i>po</i> -spiro-OMeTAD ^[99]	-5.22	-5.22 ^c	NR	NR	16.7	15.2 ^e
spiro-E ^[100]	-4.81	-4.76	1.3 ± 0.2	1.6 ± 0.3	15.8 14.6 ± 0.7	11.6 10.4 ± 0.5
spiro-N ^[100]	-4.42	-4.76	0.25 ± 0.04	1.6 ± 0.3	11.9 11.0 ± 0.8	11.6 10.4 ± 0.5
spiro-S ^[100]	-4.92	-4.76	1.9 ± 0.4	1.6 ± 0.3	15.9 15.1 ± 0.5	11.6 10.4 ± 0.5

(a) spiro: spiro-OMeTAD. (b) When two lines are present, the first indicates the best-performing cell and the second the batch average. (c) Values based on *pp*-spiro-OMeTAD. (d) NR: not reported. (e) Cells fabricated with commercial spiro-OMeTAD.

In their work, Jeon *et al.*^[99] varied the position of the methoxy group to explore the effects of its double nature on the final properties of spiro-OMeTAD. The methoxy group, in fact, is weakly electron withdrawing via inductive effect (-I) but strongly electron donating via resonance (+M): changing its position in the ring from *para* to *meta* will change the prevalence of these two effects as the resonance is lost in the *meta* position. The *ortho* substitution is also altering the orbitals of the molecule, mostly due to steric effects. The

position variation did not overly affect the UV-Vis spectrum of the molecules, although there were slight differences in the onset wavelength and in the peak at lower wavelengths for the *po* compound. From an energy point of view, cyclic voltammetry (CV) measurements showed three oxidation peaks for each compound, with the first one of the *pm* compound at a more positive potential compared to the other two. In the solar cell, all materials showed similar performances in terms of V_{OC} and J_{SC} (noticeably, there was no V_{OC} increase for the *pm* compound despite the deeper HOMO). A big difference was instead measured in the fill factor (FF) following the order *pm* (65%) < *pp* (71%) < *po* (78%), due to large differences in series resistance (R_s).

While Jeon *et al.* only varied the position of the methoxy group in spiro-OMeTAD, Hu *et al.*^[100] decided to substitute it altogether with others having different electronic properties. In this case as well, the various substituents (ethyl, *N,N*-dimethylamino and methylsulfanyl) did not alter the position of the peaks in the UV-Vis spectra but they gave an important contribution to the peak onset. Furthermore, CV experiments showed that all the investigated molecules have three oxidation peaks, as per spiro-OMeTAD. Although the measured HOMO of spiro-OMeTAD was much higher than the value usually derived from CV analysis in the literature (-5.22 eV), these measurements provided a relative difference in energy between the various compounds, showing that all substituents have a different effect on the HOMO of the molecule. Concerning charge transfer, it is worth noting the big difference in hole mobility of the spiro-N compound compared to the other three. Hu *et al.* fabricated inverted structure cells, with the perovskite layer on top of the various HTMs and demonstrated by using scanning electron microscopy (SEM) that the resulting perovskite film was higher in quality when the hydrophobicity of the HTM (measured with the contact angle technique) was higher. In terms of solar cell parameters, the V_{OC} of spiro-N was about 100 mV lower than the V_{OC} of the other three, probably due to the much higher HOMO energy, while there was no significant difference for the other materials. The J_{SC} of spiro-N was also the lowest of the four, although in this case there were significant differences between all the various compounds (17.4 ± 0.6 , 18.4 ± 0.3 , 16.1 ± 0.5 and 18.6 ± 0.4 mA cm⁻² for spiro-OMeTAD, spiro-E, -N and -S, respectively). Unexpectedly, the FF of the spiro-OMeTAD cells was 0.15 (15%) lower than that found for the other three compounds in absolute value, while in this case spiro-N is comparable with spiro-E and -S. Both spiro-S and -E had remarkably higher PCEs when compared to spiro-OMeTAD, mostly due to the low FF of the latter. It would be interesting to verify if the efficiency trend is similar in classic configuration cells as well, in which the morphology of the perovskite layer would not be affected by the underlying HTM.

The reason for the high performance of spiro-OMeTAD is partly attributed to the spirobifluorene core, which gives the molecule a very defined and rigid structure but which is also very difficult to synthesise and therefore expensive. For this reason, several molecules with spiro cores – that are easier to synthesise than spirobifluorene – have been designed in an attempt to exploit the advantages of a twisted geometry at a lower price.

Some of these do not reach the high efficiencies of spiro-OMeTAD but others perform even better than the reference compound. SCPDT-BiT^[101] and spiro-CPDT^[102] are based on a 4,4'-spirobi[cyclopenta[2,1-*b*;3,4-*b'*]dithiophene] core. X60^[89] and SFXMeOTAD, SFXTAD, SFXTPTZ and SFXTCz^[103] are comprised of a spiro[fluorene-9,9'-xanthene] core; these HTMs were reported at the same time and X60 and SFXMeOTAD are the same molecule, giving the opportunity to verify how properties can vary when measured by different researchers. PST1^[104] features a peculiar 2*H*,2'*H*,4*H*,4'*H*-3,3'-spiro-bi[thieno[3,4-*b*][1,4]dioxepine]-6,6',8,8'-tetrayl core. FDT^[105] – with a spiro[cyclopenta[2,1-*b*;3,4-*b'*]dithiophene-4,9'-fluorene] core – is the smallest and best performing HTM of the group. Finally, SAF-OMe^[106] and CW3, CW4 and CW5^[107] are all based on a 10-phenyl-10*H*-spiro[acridine-9,9'-fluorene] core. The molecular structures of all these HTMs are depicted in Figure 13 and their properties are listed in Table 2.

SCPDT-BiT and spiro-CPDT are based on the same SCPDT core, similar to spirobifluorene but in which the four phenyl rings have been substituted with thiophenes. Except for the same core, they are very different compounds: SCPDT-BiT is comprised only of thiophenes, by attaching four bithiophene branches with an octyl side chain to the SCPDT core. Spiro-CPDT, on the other hand, features four triphenylamine side groups. Thiophene chains are good light absorbers and it is therefore not surprising that the UV-Vis spectrum of SCPDT-BiT presented a much broader absorption compared to that of spiro-OMeTAD. The absorption peak of spiro-CPDT – with a much shorter thiophene chain – was blue-shifted by about 50 nm compared to SCPDT-BiT. By contrast, the measured HOMO levels of both are very similar to that of spiro-OMeTAD, although SCPDT-BiT's is slightly higher while spiro-CPDT's is slightly lower. Differential scanning calorimetry (DSC) analyses showed that all HTMs formed amorphous films.

A very peculiar behaviour was reported for the hole mobility of SCPDT-BiT. A room temperature-prepared film of this HTM possessed a hole mobility of $4.5 \times 10^{-6} \text{ cm}^2 \text{ V}^{-1} \text{ s}^{-1}$, which could be increased by an order of magnitude to $6.0 \times 10^{-5} \text{ cm}^2 \text{ V}^{-1} \text{ s}^{-1}$ upon annealing at 100 °C for 10 min. For comparison, spiro-OMeTAD's hole mobility was measured at 1.5 and $5.4 \times 10^{-5} \text{ cm}^2 \text{ V}^{-1} \text{ s}^{-1}$ for as-prepared and annealed films, respectively. A unique hole mobility behaviour was reported for spiro-CPDT, too. An initial value of $6.0 \times 10^{-6} \text{ cm}^2 \text{ V}^{-1} \text{ s}^{-1}$ was measured for the HTM but after light-soaking the film for five minutes its hole mobility increased to $3.0 \times 10^{-5} \text{ cm}^2 \text{ V}^{-1} \text{ s}^{-1}$, while no change was found in the case of spiro-OMeTAD. The same behaviour was recorded in a full PSC, as the device required an initial light-soaking step to reach its maximum efficiency. In planar PSCs, SCPDT-BiT gave the same performance as spiro-OMeTAD in terms of V_{oc} and FF , while SCPDT-BiT's J_{sc} was significantly lower (16.5 mA cm^{-2} vs. 20.8 mA cm^{-2}). The cause for the lower J_{sc} was attributed to fast interfacial charge recombination between the perovskite and SCPDT-BiT layers. Noteworthy for spiro-CPDT is the fact that, although its efficiency in a PSC was lower compared to spiro-OMeTAD, the latter reached the maximum performance with the usual additives and *p* dopant, while the former performed best in its pristine form.

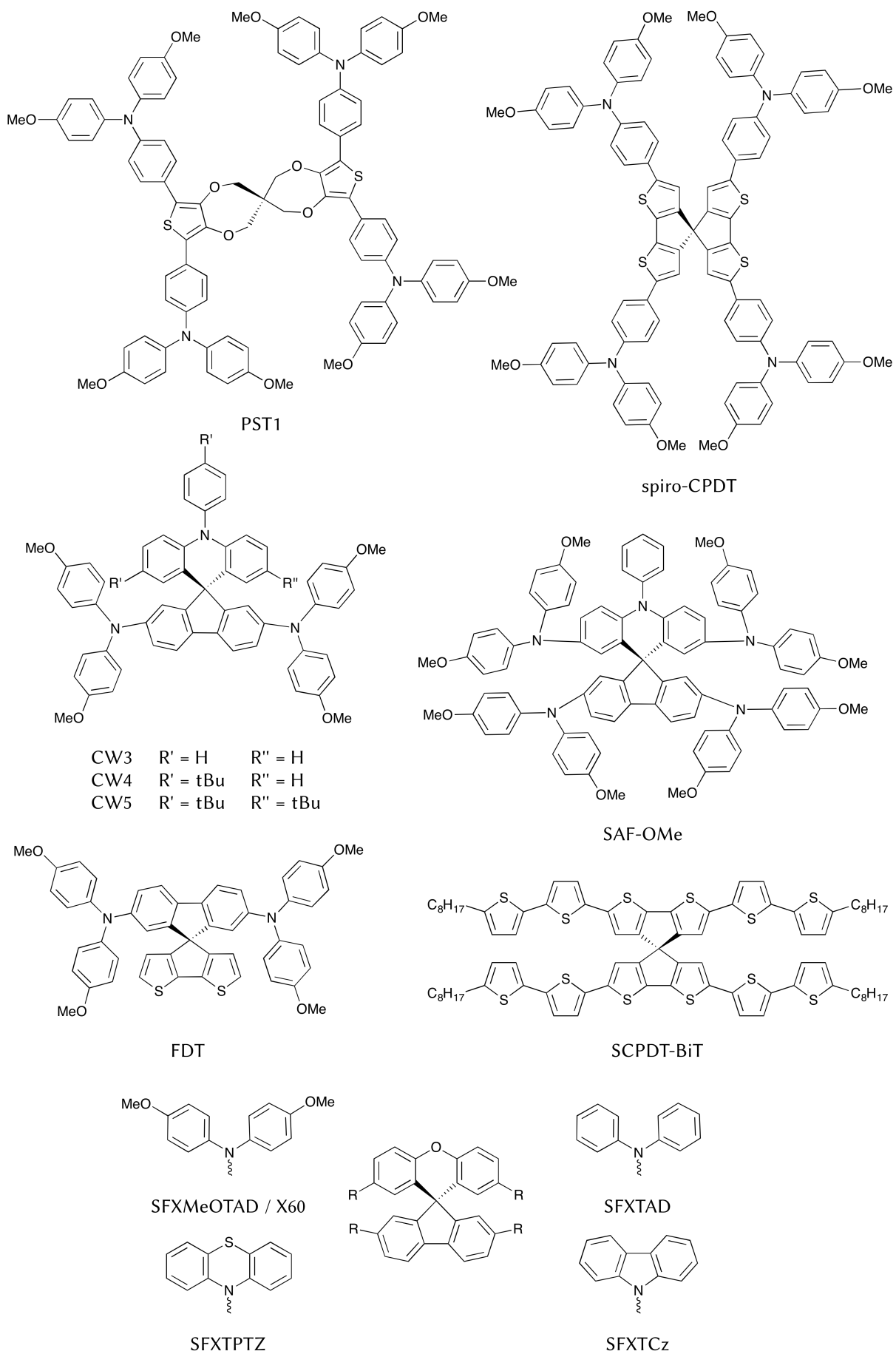


Figure 13. HTMs featuring a spiro core.

Table 2. Properties of HTMs for PSCs based on the spiro core.

HTM	T_g (°C)	T_g of spiro ^a (°C)	HOMO (eV)	HOMO of spiro ^a (eV)	Hole mobility ^b ($10^5 \text{ cm}^2 \text{ V}^{-1} \text{ s}^{-1}$)	Hole mobility of spiro ^{a,b} ($10^5 \text{ cm}^2 \text{ V}^{-1} \text{ s}^{-1}$)	PCE ^c (%)	PCE with spiro ^{a,c} (%)
SCPDT-BiT ^[101]	137	125	-5.07	-5.04	6.0	5.4	10.4	13.3
spiro-CPDT ^[102]	150	NR ^e	-5.00	-5.04	3.0	8.5	13.4 13.2 ± 0.3	15.0 14.7 ± 0.4
X60 ^[89]	NR	NR	-5.09 ^d	-5.07 ^d	19	8.1	19.8 18.8 ± 0.6	NR
SFXMeOTAD ^[103]	108	122	-5.16	-5.14	1.4×10^{-5} S cm ⁻¹	1.6×10^{-5} S cm ⁻¹	12.4 11.1 ± 0.8	13.0 11.3 ± 0.9
SFXTAD ^[103]	118	122	-5.34	-5.14	NR	NR	NR	NR
SFXTPTZ ^[103]	None	122	-5.39	-5.14	NR	NR	NR	NR
SFXTCz ^[103]	None	122	-5.70	-5.14	NR	NR	NR	NR
PST1 ^[104]	175	NR	-5.15	-5.07	NR	NR	13.4	12.2
FDT ^[105]	110	120	-5.16	-5.14	NR	NR	20.2	19.7
SAF-OMe ^[106]	126	NR	-5.07	-5.22	99	31	16.7 15.9 ± 0.5	14.8 13.7 ± 0.6
CW3 ^[107]	127	125	-4.92	-4.96	12	20	10.9	14.3
CW4 ^[107]	142	125	-4.92	-4.96	5.8	20	16.6	14.3
CW5 ^[107]	148	125	-4.93	-4.96	8.7	20	10.8	14.3

(a) spiro: spiro-OMeTAD. (b) When units of measure are reported together with the value, the number is referred to conductivity and the hole mobility was not reported. (c) When two lines are present, the first indicates the best-performing cell and the second the batch average. (d) Assuming an energy vs. vacuum of the NHE electrode of 4.44 eV.^[108] (e) NR: not reported.

Adding LiTFSI and tBP to spiro-CPDT significantly lowered the J_{SC} of the cell, while adding the cobalt complex as well lowered all cell parameters. An average efficiency of $9.6 \pm 0.6\%$ was obtained for cells including the additives and an average efficiency of $5.5 \pm 0.6\%$ for cells including the cobalt complex as well. On the contrary, pristine spiro-OMeTAD cells gave an average efficiency of $7.0 \pm 0.2\%$. The lower performance of spiro-CPDT in the presence of additives was attributed to the influence of the latter on the charge transfer properties and consequently on the hole extraction rate of the HTM.

One compound was concurrently reported by two different research groups with two different names, X60^[89] and SFXMeOTAD.^[103] Maciejczyk *et al.* extended their synthetic work to three other compounds – SFXTAD, SFXTPTZ and SFXTCz – but did not fully characterise them. Both papers highlight the inexpensive synthesis required to produce the SFX core, which is about 30 times less expensive than the spirobifluorene core. The measured HOMO levels for X60 and SFXMeOTAD are markedly different but so are the values recorded for spiro-OMeTAD. More importantly, the measured energy difference between the novel HTM and spiro-OMeTAD is the same in both cases. A similar behaviour is found for the conductivities measured in the two different studies, which vary by an order of magnitude. The value reported for X60 is $1.1 \times 10^{-4} \text{ S cm}^{-1}$, while the value reported for SFXMeOTAD is $1.4 \times 10^{-5} \text{ S cm}^{-1}$. For comparison, the values measured for spiro-OMeTAD in both papers are 1.5×10^{-4} (X60) and $1.6 \times 10^{-5} \text{ S cm}^{-1}$ (SFXMeOTAD), respectively. The novel HTM was applied to two different kinds of perovskite in the two different works. Maciejczyk *et al.* deposited SFXMeOTAD on top of a $\text{CH}_3\text{NH}_3\text{PbI}_{3-x}\text{Cl}_x$ perovskite and obtained average performances equal to the ones of spiro-OMeTAD. Xu and Bi *et al.* employed a mixed cation perovskite to test their X60. Although they did not compare X60 to spiro-OMeTAD in their work, they reported that the maximum PCE obtained with their compound, 19.8%, is very close to that reached by a similar cell with spiro-OMeTAD in a different work with a similar PSC, 20.8%.^[109] Their top-performing cell, after encapsulation, presented a reasonable stability, with a PCE of 19.6% measured after two months of ageing in a desiccator and in the dark.

PST1^[104] is comprised of a larger spiro core with four ether groups linking the sp^3 carbon to two thiophenes. In this molecule, the oxygen bond angles of the four ethers counter-balance the spiro twisting, making the final molecule mostly planar (7° distortion angle compared to 90° for spiro-OMeTAD). The UV-Vis spectrum of PST1 was similar to that of spiro-OMeTAD, although slightly red-shifted and with a broader absorption tail at higher wavelengths. The UV-Vis spectrum of PST1 in the solid state was significantly different compared to the one in solution: the main peak was 38 nm red-shifted and the absorption in the UV region higher, indicating inter-molecular interactions in the solid state. V_{OC} values for PSCs fabricated with PST1 and spiro-OMeTAD reflected their difference in HOMO energy, with 1024 mV for PST1 and 910 mV for spiro-OMeTAD. PST1 also features a higher FF (0.73 vs. 0.70) but a lower J_{SC} (17.6 vs. 18.6 mA cm^{-2}).

FDT^[105] is a relatively small HTM, with only two triphenylamine branches attached to the spiro core. Despite the lower molecular weight, its T_g is only slightly lower than that of spiro-OMeTAD, indicating a good thermal stability. The authors claim that the extra interaction of the perovskite with the two thiophenes of the HTM's core will facilitate charge transfer when compared to spiro-OMeTAD, which interacts with the perovskite only through its methoxy groups. Despite the presence of a bithiophene in the core – and contrary to what has been shown previously – the UV-Vis spectrum of FDT is very similar to that of spiro-OMeTAD.

Wang *et al.*^[106] with SAF-OMe and Li and Hsu *et al.*^[107] with CW3, CW4 and CW5 have completed complementary work on molecules with the SAF core: the former attached four diphenylamine branches to the main core, the latter only two. The UV-Vis spectrum is reported only for SAF-OMe and is comparable with that of spiro-OMeTAD. The HOMO energy level of SAF-OMe was significantly lower than that measured for spiro-OMeTAD, whilst for the other three HTMs the values were similar. The hole mobility recorded for SAF-OMe was three times higher than that of spiro-OMeTAD, while CW3, CW4 and CW5 all presented lower hole mobilities. The presence of more diphenylamine branches, therefore, seems beneficial to this particular property. PCEs of the top-performing PSCs made with spiro-OMeTAD had very similar values for Li and Hsu and Wang, which allows an easy comparison of the various SAF-based HTMs. SAF-OMe and CW4 provided very similar PCEs, while CW3 and CW5 provided lower PCEs compared to the other two, mainly due to a lower J_{sc} . Performances of SAF-OMe and CW4 were superior to that of spiro-OMeTAD. The low performances of both CW3 and CW5, on the other hand, were attributed to geometrical variations in the molecule due to the absence or to the excessive presence of the *tert*-butyl groups. These variations lead to worse morphological cover of the perovskite layer for CW3 or to worse charge hopping for CW5.

In many of the aforementioned HTMs, the spiro core was attached to thiophene moieties. Thiophenes are highly conductive groups, thanks to the presence of both an aromatic ring and an electron rich sulphur atom inside the ring. Indeed, many conductive organic polymers contain thiophene groups, as in the case of poly-3-hexylthiophene (P3HT). Thiophenes are also employed as bridges in donor- π -acceptor molecules, *e.g.* in organic dyes for solar cells.^[110] Due to their outstanding electronic properties, thiophenes can be used as core groups in HTMs. Contrary to the spiro core, thiophenes will not block electron flow across the molecule, providing extended orbitals that can potentially span across the whole molecule. Li *et al.*^[111] have synthesised a very simple HTM by attaching two triphenylamine branches to a 3,4-ethylenedioxythiophene (EDOT) core (H101). Coming from the same group at Nanyang Technological University, Krishnamoorthy *et al.*^[112] have attached four triphenylamine branches to a bithiophene core, where the two thiophenes are bonded in the 3,3' position (KTM3). Li *et al.*^[113] have also worked on a similar molecule, this time with the thiophenes bonded in the 2,2' position (H112); in the same paper, they also attach four

triphenylamine branches to a single thiophene molecule (H111). The four described HTMs are depicted in Figure 14, with their properties listed in Table 3.

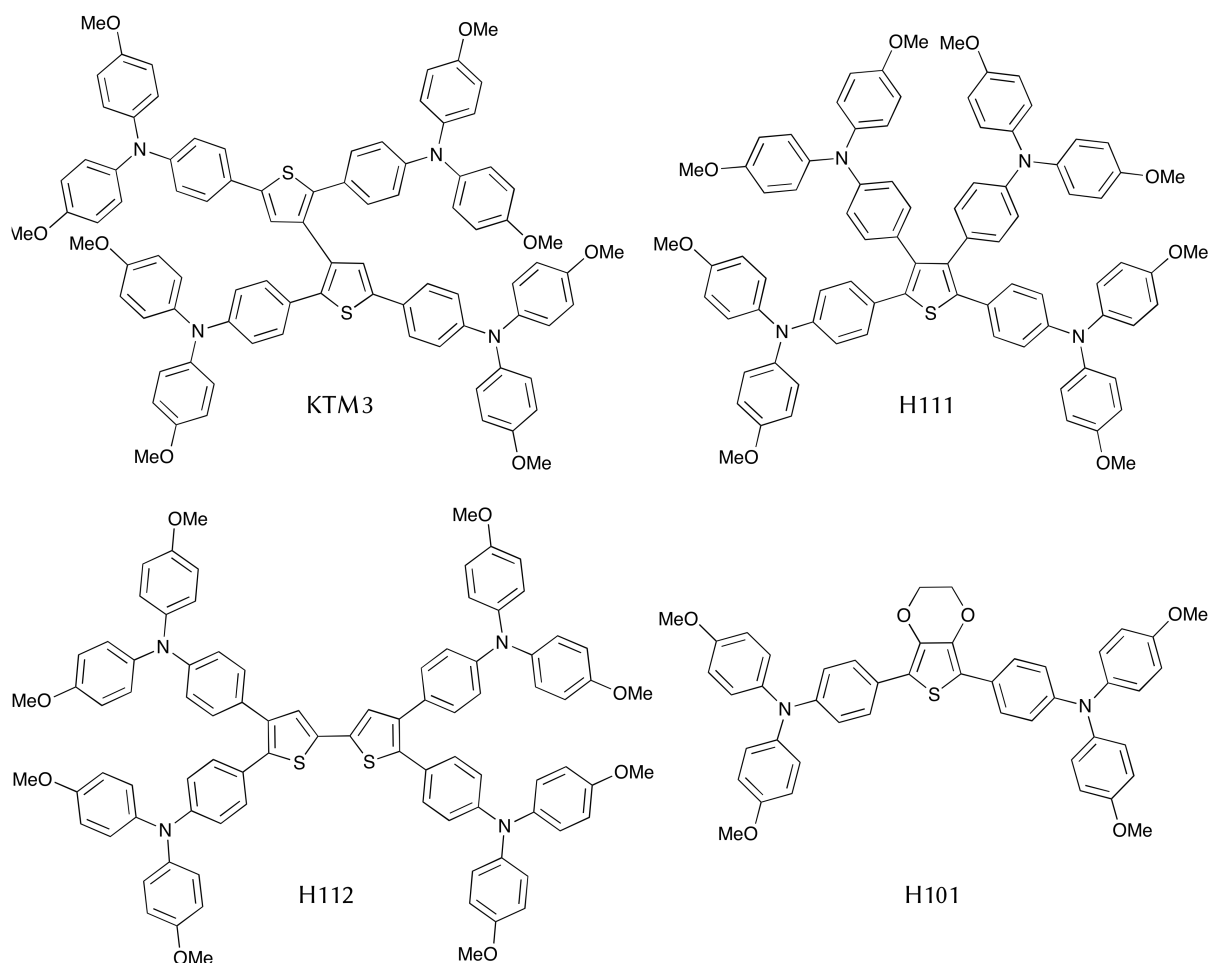


Figure 14. HTMs featuring a thiophene core.

Table 3. Properties of HTMs for PSCs based on a thiophene core.

HTM	T_g (°C)	HOMO (eV)	HOMO of spiro ^a (eV)	PCE ^b (%)	PCE with spiro ^{a,b} (%)
H101 ^[111]	73	-5.16	-5.21	13.8 13.2 ± 0.6	13.7
KTM3 ^[112]	65	-5.13 (CV) -5.29 (PESA)	-5.04 (CV) -5.22 (PESA)	11.0	11.4
H111 ^[113]	100	-5.31	-5.21	15.4 14.9 ± 0.5	14.4 14.0 ± 0.4
H112 ^[113]	120	-5.29	-5.21	15.2 14.7 ± 0.4	14.4 14.0 ± 0.4

(a) spiro: spiro-OMeTAD. (b) When two lines are present, the first indicates the best-performing cell and the second the batch average.

In their first work, Li *et al.*^[111] characterised a relatively small and simple HTM. Due to its small size, its T_g was much lower compared to that of spiro-OMeTAD. Although this lower T_g could have affected the long-term stability of the devices, an accelerated ageing test

performed by storing the perovskite cells at 70 °C over a 7-days period showed a very similar J - V response from the devices fabricated with H101 and spiro-OMeTAD. The UV-Vis absorption maximum of H101 was red-shifted compared to that of spiro-OMeTAD and with a more extended absorption tail, probably due to the thiophene functionality. PSCs fabricated with the two HTMs showed comparable results. Moving from two to four triphenylamine branches attached to a single thiophene core (H111^[113]), the T_g of the HTM increased. The UV-Vis spectrum of H111 was very different compared to that of H101 as the peak around 400 nm became a shoulder and the absorption maximum was shifted to lower wavelengths. Similarly to the results obtained with H101, PSCs made with H111 showed an efficiency close to that of spiro-OMeTAD-based devices.

The introduction of a second thiophene ring in the core (H112^[113]) did not affect the HOMO level of the HTM significantly. However, it increased the T_g of the molecule and it caused a red-shift of the UV-Vis spectrum of about 25 nm, with a much more pronounced peak around 360 nm. Solar cell performances with H112 were very similar to those achieved when using H111. When changing the bond position between the thiophenes (KTM3^[112]), the absorption peak at about 400 nm became more prominent compared to that at *ca.* 360 nm, which resulted in a shoulder. The T_g changed dramatically, with a temperature almost halved for KTM3 compared to H112. Remarkably, the T_g of KTM3 is even lower than that of H101, despite the bigger molecular size. HOMO levels for H112 and KTM3 were very similar, indicating that the different bond position within the bithiophene does not affect this particular property. Top-performing PSCs fabricated with KTM3 and spiro-OMeTAD gave comparable PCEs. Although the PCE and V_{oc} values were very similar in both cases, there was a big difference for both J_{sc} (13.0 vs. 17.2 mA cm⁻²) and FF (78 vs. 62%) of these cells.

As mentioned in the previous section, hole conductors often exhibit low hole mobility in their pristine form. To increase their performance, they necessitate the use of additives and p dopants. Sometimes HTMs are conductive enough to give good results without the need of any additive and – as seen in the case of spiro-CPDT^[102] – sometimes these additives can be detrimental. Many HTMs that work well without the presence of any additives have been synthesised: some of them perform only slightly worse than doped spiro-OMeTAD,^[77,82,114–121] while others work even better and they will be reviewed below. Kazim *et al.*^[122] have worked on a planar HTM based on a pentacene core (TIPS-pentacene). Liu *et al.*^[123] have developed a long molecule based on a benzodithiophene core with two thiophene-based branches (DOR3T-TBDT). Li *et al.*^[124] have synthesised a donor-acceptor chromophore to be used as hole conductor in PSCs (BTPA-TCNE). The molecular structures of these three HTMs are depicted in Figure 15, while their properties are listed in Table 4.

The UV-Vis spectrum of TIPS-pentacene was very broad, as expected considering the long fused chain of aromatic rings. Its T_g was 122 °C, close to that of spiro-OMeTAD (124 °C). The HOMO energy level of this HTM was recorded at -5.4 eV, very close to the E_{VB} of MAPbI₃

(-5.44 eV) – the perovskite employed by Kazim *et al.* The conductivity of pristine TIPS-pentacene was $3.5 \times 10^{-7} \text{ S cm}^{-1}$ and it raised to $1.0 \times 10^{-5} \text{ S cm}^{-1}$ after the addition of LiTFSI and tBP. Despite the higher conductivity, cells fabricated with the presence of the additives gave poorer performances, which were attributed to the introduction of trap sites and disorder in the chain packing in the HTM layer.

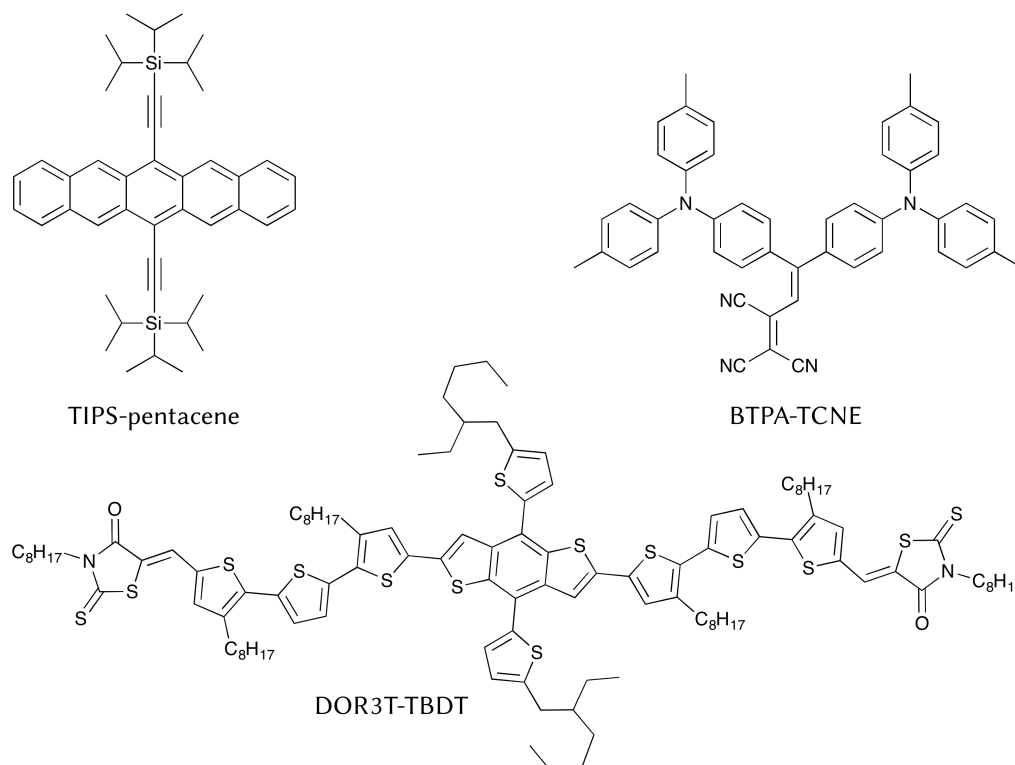


Figure 15. Molecular structures of dopant free HTMs.

Table 4. Properties of dopant free HTMs for PSCs.

HTM	HOMO (eV)	HOMO of spiro ^a (eV)	Hole mobility ^b ($\text{cm}^2 \text{ V}^{-1} \text{ s}^{-1}$)	Hole mobility of spiro ^a ($\text{cm}^2 \text{ V}^{-1} \text{ s}^{-1}$)	PCE ^c (%)	PCE with spiro ^{a,c} (%)
TIPS-pentacene ^[122]	-5.4	-5.07	$3.5 \times 10^{-7} \text{ S cm}^{-1}$	NR ^d	11.8 11.5 ± 0.3	9.8 ± 0.4
DOR3T-TBDT ^[123]	-5.1	-5.0	0.26	NR	14.9 ~12.7	14.0 ~12.0
BTPA-TCNE ^[124]	-5.30 (CV) -5.35 (UPS)	NR	3.1×10^{-5}	2.1×10^{-5}	16.9	15.7

(a) spiro: spiro-OMeTAD. (b) When units of measure are reported together with the value, the number is referred to conductivity and the hole mobility was not reported. (c) When two lines are present, the first indicates the best-performing cell and the second the batch average. (d) NR: not reported.

The work on DOR3T-TBDT^[123] was focused on optoelectronic properties. The conductivity of this new hole conductor in its pristine form was $\sim 4 \times 10^{-4} \text{ S cm}^{-1}$, compared to the $\sim 10^{-4} \text{ S cm}^{-1}$ measured for *p*-doped spiro-OMeTAD. Its hole mobility was $0.26 \text{ cm}^2 \text{ V}^{-1} \text{ s}^{-1}$, which is incredibly high for an organic hole conductor. PSCs fabricated with DOR3T-TBDT displayed a lower V_{OC} despite the deeper HOMO level but higher J_{SC} and FF values.

BTPA-TCNE^[124] is comprised of two triphenylamine moieties connected to a diene heavily substituted with cyano groups. In addition to the absorption peaks in the UV region common to many of the HTMs analysed so far, BTPA-TCNE also presented a very intense peak at about 600 nm. PSCs were fabricated with BTPA-TCNE both with and without additives. The highest PCE, 17.7%, was obtained with the presence of the additives but the PCE of solar cells with pristine BTPA-TCNE, 16.9%, was very close to that of the doped compound and higher than that of devices fabricated with doped spiro-OMeTAD, 15.7%.

In conclusion, some of the organic HTMs published in the literature have been reviewed, categorised by molecular characteristics or by the presence of additives in the final device. Many other HTMs have been published in the past five years – after the pioneer work of Snaith and co-workers^[18] and Park and co-workers^[19] – that do not fall into the categories presented in this overview. Some of them allow the fabrication of high efficiency PSCs, with performances rivalling that of spiro-OMeTAD.^[83,125–143] Nevertheless, despite the many presented HTMs, some of which outperform spiro-OMeTAD in performance and stability, the latter is still considered the HTM of choice for PSCs and the one commonly employed in works non related to the synthesis of new HTMs.

Some considerations can be made about the design of future highly efficient hole conductors. By looking at the molecular structures of the reviewed HTMs and of those outperforming spiro-OMeTAD in general, it is difficult to draw conclusions on which particular functional group will provide high performances. Some of the reviewed molecules feature the same spiro core of spiro-OMeTAD or have relatively complex 3D-structured molecular geometries. Others, on the other hand, are quite flat but very well performing, too. The triphenylamine functionality is present in many of the reviewed compounds. While this group is known to be a good electron donor, the impression is that it is so widely employed because it is the functional group present in spiro-OMeTAD, rather than because it is better performing than any other functionality. Indeed, groups like thiophene and carbazole can perform equally well. In general, the only strict requirement seems be the presence in the molecule of aromatic rings containing heteroatoms, or heteroatoms directly bonded to aromatic rings. Their lone electron pairs, in fact, are paramount to act as electron donor and the cation stabilisation given by the aromatic rings is equally important. Given the lack of a clear direction for what concerns functional groups, it is important to focus on other elements of the final HTM layer as well. It is known, in fact, that the additives commonly mixed with the hole conductor – especially LiTFSI – are very hygroscopic and facilitate the ingress of moisture in the cell, accelerating the degradation of the perovskite layer. Kim *et al.*^[144] give a very clear example of this additives-induced degradation process. It has been shown that additive-free HTMs can outperform spiro-OMeTAD in PSCs, although the final absolute PCE values were not always very high. Further studies should be undertaken to verify the performance of additive-free HTMs applied to the most efficient perovskite materials. Nevertheless, it is my opinion that a few per cent in top performance can be sacrificed in order to gain device stability in the long term, if both cannot be

achieved at the same time. For these reasons, future research efforts should be focused on the design of additive-free HTM layers.

1.5.3. Polymeric hole conductors

Semiconducting polymers play an important role in photovoltaics. Although their main use is in OPV cells – where they act as electron donors and light absorbers – they are also used as hole conductors in ssDSSCs and PSCs. Some of the polymeric HTMs, as P3HT, are directly derived from the OPV field as in both cases they act as electron donors; others have been specifically designed to be used in PSCs. Polymers are largely used in inverted structure PSCs but are also well performing in conjunction with perovskite flat surfaces in planar classical structures. Their large size, however, makes their infiltration of mesoporous cavities difficult. Polymers are usually less preferred compared to small molecules due to the more complicated purification process required to obtain optoelectronic grade products and to the batch to batch differences in terms of chain size and polydispersity index. Performances of PSCs with polymeric HTMs are usually lower than those based on small molecular hole conductors^[145–157] but there are also examples of very well performing compounds. For example, a PSC fabricated with poly(triarylamine) (PTAA, Figure 16) twice held for a period the record in the field.^[28,158] Polymers can also be mixed with highly conductive materials such as carbon nanotubes^[159,160] or with the same additives used for organic small molecules^[161] to improve their hole transport properties. An overview of the best performing polymeric HTMs reported so far is provided below.

Molecular structures of the repeating units for the reviewed polymeric HTMs for PSCs are depicted in Figure 16. Some of them, such as PEDOT,^[162] PVK,^[72] PT^[163] and PTAA^[158] are comprised of very small monomers while others, such as PDPPDBTE,^[78] PDTSTTZ and PDTSTTZ-4^[164] and TFB^[165] have much more complex structures. One, RCP,^[144] is a block copolymer of two similar monomers and two others, P3CT-Na^[166] and PhNa-1T,^[167] present a salt at the end of their side groups. Table 5 summarises the key properties of each of them.

The data presented in Table 5 show that they all possess much higher hole mobilities – by at least one order of magnitude – compared to organic small molecules. The reason for the higher conductivity is given by the long chains of aromatic rings that form the polymers, in which the charges travel more quickly and which provide more points of contact for intermolecular charge transfer between the various polymeric chains.

The inspection of the structure of the monomeric units suggests that those bigger and more complex possess long alkyl chains as side groups. These groups are needed to increase the solubility of the polymer and to tune the film morphology, to avoid the formation of big crystalline domains. While these functionalities do not influence the charge transport properties of the main chain, they do influence the final morphology of the film, playing an important role in the properties of the final polymeric layer. A clear example of this influence is given by PDTSTTZ and PDTSTTZ-4, reported by Wang *et al.*^[164] These polymers

To complete the assessment of the structure-performance correlations for polymeric HTMs, it is interesting to notice that the size of the repeating unit of the polymer does not appear to play a key role on the overall performance of the compound as HTM in PSCs. Indeed, the two best performing hole conductors reported so far are one of the smallest, PTAA,^[158] and the largest, RCP.^[144] The difference in monomer size is expected to affect the morphology of the film and especially the glass transition temperature but these parameters have not been investigated by the authors, unfortunately.

Table 5. Properties of the best performing polymeric HTMs for PSCs.

HTM	HOMO (eV)	Hole mobility ^a (cm ² V ⁻¹ s ⁻¹)	Hole mobility of spiro ^{a,b} (cm ² V ⁻¹ s ⁻¹)	PCE ^c (%)	PCE of spiro ^{b,c} (%)
PEDOT ^[162]	-5.5	5.3×10^{-1} S cm ⁻¹	NR ^d	17.0	NR
PVK ^[72]	NR	5.3×10^{-3} S cm ⁻¹	6.4×10^{-3} S cm ⁻¹ (of PEDOT:PSS)	15.8 14.4 ± 0.8	NR
PT ^[163]	-5.18	NR	NR	15.4	NR
PTAA ^[158,168]	-5.2	4×10^{-3}	NR	22.6	NR
PDPPDBTE ^[78]	-5.4	$\sim 10^{-3}$	$\sim 10^{-4}$	9.2	7.6
PDTSTTZ ^[164]	-5.1	3.6×10^{-3}	$\sim 10^{-5}$	14.4 13.4 ± 0.8	13.6 13.0 ± 0.7
PDTSTTZ-4 ^[164]	-5.0	7.8×10^{-2}	$\sim 10^{-5}$	15.8 15.2 ± 0.7	13.6 13.0 ± 0.7
TFB ^[165]	-5.3	$7 \times 10^{-3} \sim 10^{-2}$	2×10^{-5}	10.9	9.8
RCP ^[144]	-5.41	3.09×10^{-3}	$\sim 10^{-5}$	17.3	15.3
P3CT-Na ^[166]	-5.26	NR	NR	16.6 15.4	NR
PhNa-1T ^[167]	-5.2	2.6×10^{-4} S cm ⁻¹	NR	14.7 13.3	NR

(a) When units of measure are reported together with the value, the number is referred to conductivity and the hole mobility was not reported. (b) spiro: spiro-OMeTAD. (c) When two lines are present, the first indicates the best-performing cell and the second the batch average. (d) NR: not reported.

The value of the presence of a salt in the side groups, *e.g.* as found in P3CT-Na^[166] and PhNa-1T,^[167] in terms of optoelectronic properties, is not fully clear. One advantage is the possibility to dissolve these polymers in water, which removes the need for the use of organic solvents in at least one step of the device fabrication. The two aforementioned polymers were used in inverted structure PCSs. The presence of the charged species in the side groups may have been beneficial to achieve a higher wettability of the HTM layer by the perovskite solution, leading to better perovskite films. Another interesting feature of these studies is that both HTMs provided high efficiencies of the solar cells when deposited as very thin layers: 4 nm in the case of P3CT-Na and 9 nm in the case of PhNa-1T. Thicker HTM layers maintained good charge transport properties but – due to their high absorption of the incident light – the final J_{sc} of the device was greatly reduced. This fact is verifiable by

the direct correlation between the changes in the UV-Vis absorption and incident photon-to-electron conversion efficiency (IPCE) profiles at different HTM layer thicknesses in the case of P3CT-Na.

Comparatively high conductivity of the high-performing polymeric hole conductors listed in Table 5 significantly reduces charge transport imbalance between holes and electrons in a PSC. In all the papers considering this aspect, namely those reporting on the PhNa-1T,^[167] PVK,^[72] PT,^[163] PTAA^[158] and P3CT-Na^[166] hole conductors, the final solar cells exhibited minimal or no hysteresis when recording J - V characteristics. Even more importantly, the enhanced conductivity of polymeric HTMs removes the need for the use of the additives that are usually mixed with the organic small molecular HTMs to facilitate hole transport. The absence of these hygroscopic compounds has a very positive impact on the long-term stability of the PSC devices. As an example, Kim *et al.*^[144] prepared devices with RCP with and without LiTFSI and tBP and compared their long-term performance to that of solar cells made with an HTM layer containing spiro-OMeTAD and the two additives. Experiments were undertaken at 25% and 75% relative humidity (RH). After 1 400 h of storage at 25% RH, PSCs with an unmodified HTM film of RCP retained their initial efficiency, while devices with additives added to RCP and spiro-OMeTAD lost *ca.* 10 and 25% of their initial efficiency, respectively. At 75% RH and in the same amount of time RCP devices with and without additives lost *ca.* 5 and 60% of their initial efficiency, respectively, while solar cells with spiro-OMeTAD stopped working after only 900 h. A similar trend was found by Kwon *et al.*^[78] PSCs fabricated with the PDPPDBTE hole transporting material stored at 20% RH in the dark and without encapsulation did not suffer detectable degradation after 1 000 h, as did devices based on P3HT. Under the same conditions, PSCs with spiro-OMeTAD lost 28% of their initial efficiency during the same period of test. The hole conductor has an influence on device stability in an inverted structure PSC as well, despite the fact that in this case the HTM does not act as a protective layer over the perovskite. For example, solar cells fabricated with PhNa-1T^[167] as HTM performed much better compared to their PEDOT:PSS counterparts. Nevertheless, their performance loss in 300 h (25 °C, 40% RH) was still significant. A plausible reason for the observed degradation might be attributed to the higher intrinsic hygroscopicity of PhNa-1T ensuing from the presence of the ionic species.

In conclusion, polymeric hole conductors usually display worse performances compared to organic small molecules. However, they can still allow the fabrication of highly efficient perovskite solar cells with up to 22.6% PCE with a mesoporous FAPbI₃/MAPbBr₃ mixture light absorber layer, a result exceeding those of the best small molecular HTMs applied to similar perovskites. The higher conductivity of polymers compared to small molecules allows the fabrication of devices without the addition of hygroscopic additives, which has a remarkable beneficial effect on the long-term stability of devices. Nevertheless, polymers have not been extensively studied as hole conductors in perovskite solar cells yet. One possible reason for this might be the more complex synthesis required to obtain HTM-grade

polymers and the worse control over batch to batch quality compared to small molecules, which may lead to a lack of reproducibility of the results.

1.5.4. Inorganic hole conductors

Inorganic hole conductors are usually comprised of transition metal salts or oxides. The interest towards this class of HTMs arises from their stability at higher temperatures and in the long term. Their major drawback, on the other side, is related to the deposition procedures, which require the use of polar solvents and often high temperature treatment to form functioning layers. Both polar solvents and high temperatures can decompose the perovskite layer. For this reason, inorganic hole conductors are mostly employed in inverted structure PSCs, although reports on the integration of this class of HTMs into classical structure devices is also known. Unlike organic molecules and polymers – whose properties can be finely tuned and which allow the synthesis of many different compounds – there are only few inorganic compounds that possess energy levels and hole conductivities suitable to be employed in PSCs. Furthermore, apart from very few exceptions, they do not yield highly efficient devices. The inorganic compounds so far employed for the fabrication of PSCs, NiO_x, CuI, CuSCN, CuO, Cu₂O, kesterite Cu₂ZnSnS₄ (CZTS) and FeS₂ will be reviewed below. The key properties of these materials are listed in Table 6 for the best performing devices based thereon. Among the aforementioned compounds, only NiO_x, CuI and CuSCN have been extensively studied, while CuO, Cu₂O, CZTS and FeS₂ have only been investigated in the papers that are referenced in Table 6.

Table 6. Efficient inorganic HTMs used in PSCs.

HTM	E_{VB} (eV)	Conductivity (S cm ⁻¹)	Device architecture	PCE ^a (%)
NiO ^[169]	-5.2	NR ^b	Inverted	17.3
NiO(Cu) ^[170]	-5.3	1.2×10^{-3}	Inverted	17.7 17.3
NiO(Li:Mg) ^[171]	-5.25	2.3×10^{-3}	Inverted	18.3
CuI ^[172]	-5.2	NR	Inverted	16.8 16.0 ± 0.5
CuSCN ^[173]	-5.3	NR	Inverted	16.6
CuO ^[174]	-5.4	NR	Inverted	12.2 11.6 ± 0.5
Cu ₂ O ^[174]	-5.4	NR	Inverted	13.4 12.7 ± 0.3
CZTS ^[175]	NR	NR	Classical	12.8
FeS ₂ ^[176]	-5.3	NR	Classical	11.2

(a) When two lines are present, the first indicates the best-performing cell and the second the batch average.

(b) NR: not reported.

Nickel oxide – with formula NiO but often reported as NiO_x due to an unknown amount of Ni³⁺ doping in the film needed to increase its conductivity – has been used in inverted structure PSCs only. NiO_x layers have been deposited on top of the conductive glass with several methods, including spin-coating from solution,^[47,177] spray pyrolysis,^[178,179] electrodeposition,^[180] sputtering,^[179,181] sol-gel^[182] and pulsed laser deposition (PLD).^[169] Excluding the PLD method – with which respectable performances are achieved – in no other paper reported on NiO_x the final devices reached the level of 15% PCE. Furthermore, again with the exceptions of the PLD (which only required annealing at 200 °C) and sputtering (which required no annealing) methods, all the reported NiO_x deposition strategies required a high temperature annealing step, between 350 and 500 °C. It has been known for many years that pure NiO is not a good conductor^[183] and that doping with Ni³⁺ ions is necessary to achieve reasonably efficient charge transport. Alternatively, doping of NiO layers with ions of other metals, such as Cu (deposited via sol-gel^[184] and combustion^[170] processes) and Li and Mg^[171] (deposited via spray pyrolysis) has led to the fabrication of high-performing HTM layers in PSCs. With these two different doping, device efficiencies were much higher than in the case of Ni³⁺ doping alone.

CuI and CuSCN are more flexible in terms of device fabrication compared to NiO_x and devices with both inverted and classical structures can be fabricated with each of them, although inverted devices perform significantly better. The current record in PSCs for the CuI hole conductor is held by Sun *et al.*^[172] for an inverted structure device with the CuI layer deposited from solution and is the only cell reported featuring CuI with an efficiency above 15%. The second best performing device – also fabricated with an inverted structure – has a PCE of 13.6%.^[185] For CuSCN, the best device has been fabricated by Ye *et al.*,^[173] with the inorganic HTM electrodeposited on the conductive glass. This is the only paper featuring either CuI or CuSCN hole conductors in which the HTM layer has not been deposited by mechanical solution processes and the only study reporting cell efficiencies above 15% for CuSCN. From a device fabrication point of view it is of interest to review the techniques engineered to allow the fabrication of classical structure PSCs employing these HTMs, given the solubility of both CuI and CuSCN in polar solvents only, which degrade the perovskite. For CuI, both Christians *et al.*^[186] and Sepalage *et al.*^[146] used di-*n*-propyl sulfide in chlorobenzene (1:39 ratio) to dissolve CuI by stirring the solution for a long time. The presence of chlorobenzene mitigates the detrimental effects of di-*n*-propyl sulfide – which is the actual solvent for the inorganic salt – on the perovskite layer. For CuSCN, different techniques are employed. Ito *et al.*^[187] and Qin *et al.*^[188] simply dissolved CuSCN in di-*n*-propyl sulfide and used doctor blading deposition at a relatively high temperature of 65 °C to accelerate solvent evaporation and minimise the damage to the underlying MAPbI₃ layer. Chavhan *et al.*^[189] used a similar precursor solution but with a drop casting deposition technique and an even higher substrate temperature of 85 °C. Sepalage *et al.*^[190] used a more complex procedure to fabricate their CuSCN layer. Using a substrate temperature similar to that of Chavhan (90 °C), they first deposited a layer of chlorobenzene on the perovskite for

protection, then doctor-bladed the solution of CuSCN in di-*n*-propyl sulfide while applying a gentle gas flow on top. With this method, chlorobenzene induces a quick precipitation of the CuSCN material, while both high temperature and gas flow promote the quick evaporation of solvents, minimising the damage to MAPbI₃. Although the methods invented to protect the perovskite from the “harsh” conditions of inorganic HTM deposition are of scientific interest, inverted PSCs where these tricks are not needed are better in terms of performance. Furthermore, these additional procedures – required to fabricate classic structure devices – represent a hurdle from a commercialisation view point.

In conclusion, inorganic hole conductors are a viable choice when fabricating inverted structure devices. The devices based on these HTMs can reach reasonably high values depending on the deposition method, although typically they cannot compete with PCEs available with organic hole conductors. The limited amount of compounds available and the very limited possibilities to tune their properties makes inorganic HTMs not very appealing from a scientific point of view, although from a commercial perspective only one good material is really needed to commence PSC commercialisation, no matter how many other compounds belong to the same class.

1.5.5. Transition metal complex hole conductors

The first report on a transition metal complex used as hole conductor in PSCs is dated 2014^[191] but this class of materials has only really started receiving significant attention in late 2015. For the most part, these compounds belong to the class of metal phthalocyanines but there is also one report on two porphyrins^[192] as well as on two Ag-based metal complexes.^[193] Most of the reported PSCs based on phthalocyanine HTMs perform poorly, with PCEs often below 10%.^[191,194–206] In a few cases device efficiencies above 15% were reported^[207–209] and the relevant metal complexes used as HTM in these works are reviewed below along with the best-performing porphyrin and Ag-based complex. The molecular structures of the reviewed compounds are depicted in Figure 17, while Table 7 summarises the key parameters for each.

The compounds reported in Table 7 all present planar molecular structures, similar to the organic small molecules that yield high performances without the need of any additive (see end of section 1.5.2). Indeed, most of these compounds are used in their pristine form, although HT-ZnPc^[207] and CuPc-DMP^[209] have been mixed with the additives (LiTFSI and tBP) commonly used for organic small molecules. Despite the fact that they feature a metal centre, the latter is not redox active under conditions of a working PSC and the hole transport mechanism is similar to that for organic small molecules, with the charge hopping from ligand to ligand. The metal centre, in fact, is always present in its highest oxidation state and it does not play a role in the charge transport. Ligands such as phthalocyanine and porphyrin, due to their large electron clouds and high π -stacking, are very good charge transporters even without the presence of the metal centre. A work published by Dao *et al.*^[210] shows that a phthalocyanine molecule without any metal centre performs better than

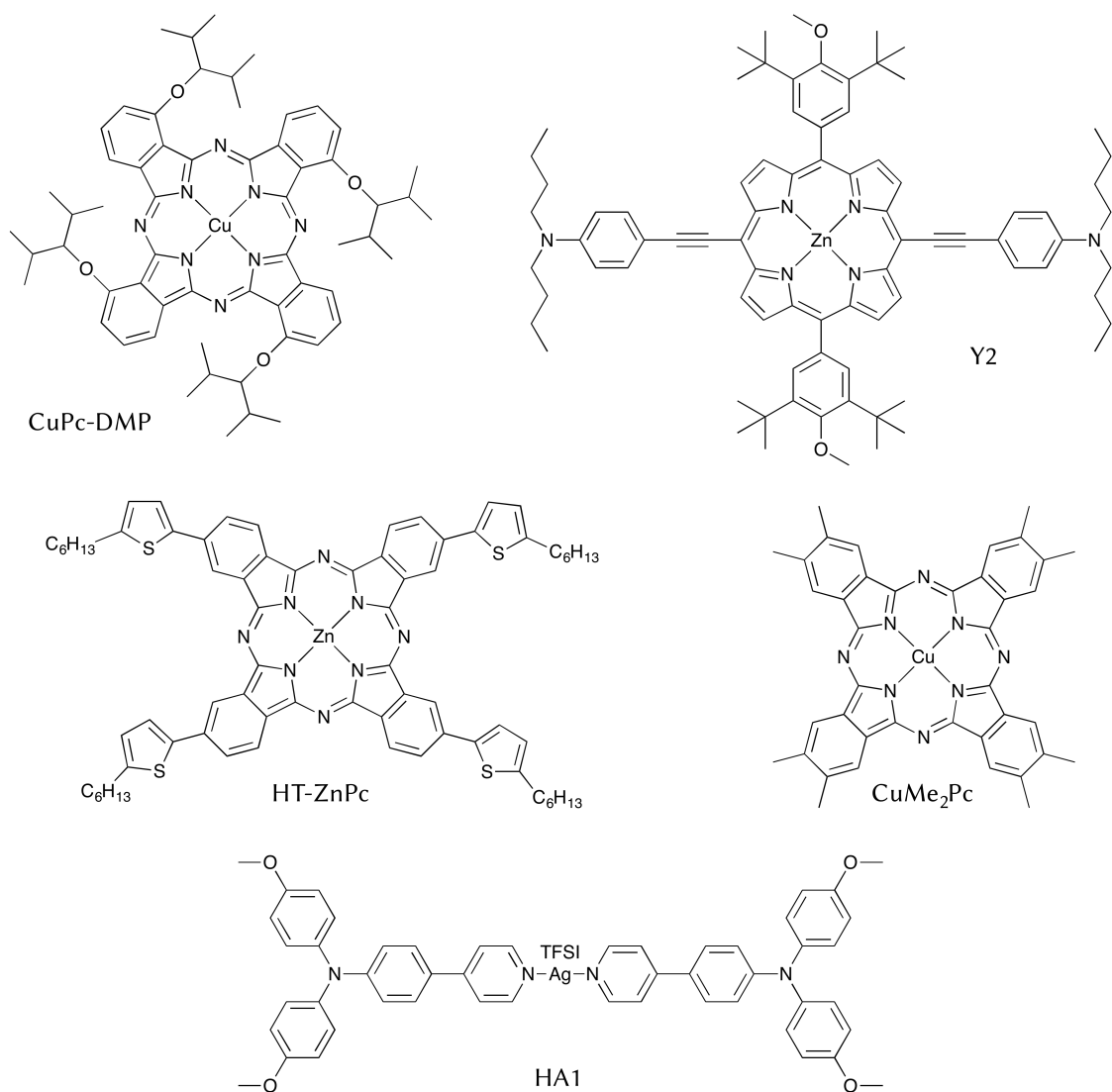


Figure 17. Best-performing transition metal complex HTMs.

Table 7. Properties of the best-performing transition metal complex HTMs for PSCs.

HTM	HOMO (eV)	Hole mobility ^a (cm ² V ⁻¹ s ⁻¹)	Hole mobility of spiro ^b (cm ² V ⁻¹ s ⁻¹)	PCE ^c (%)	PCE of spiro ^{b,c} (%)
CuPc-DMP ^[209]	-5.46	9.8×10^{-5}	4.0×10^{-5}	17.1 15.1	16.7 14.9
HT-ZnPc ^[207]	-5.19	8×10^{-5} S cm ⁻¹	NR ^d	17.1	19.1
CuMe ₂ Pc ^[208]	-5.1	4.8×10^{-2}	NR	15.7 14.3 ± 0.7	NR
Y2 ^[192]	-5.25	2.0×10^{-4}	9.5×10^{-4}	16.6 14.0 ± 0.9	18.0
HA1 ^[193]	-5.22	6.5×10^{-4}	NR	12.0	12.3

(a) When units of measure are reported together with the value, the number is referred to conductivity and the hole mobility was not reported. (b) spiro: spiro-OMeTAD. (c) When two lines are present, the first indicates the best-performing cell and the second the batch average. (d) NR: not reported.

most of the metal phthalocyanine HTMs reported. Noteworthy is the long-term stability of devices employing CuMe₂Pc as HTM. Yang *et al.*^[208] have tested their compound for 2 000 h in devices that were non encapsulated and stored at 50% RH.

At the end of the experiment, devices fabricated with CuMe₂Pc retained 95% of their initial efficiency, while devices fabricated with spiro-OMeTAD and stored under the same conditions lost 79% of their initial efficiency in the same amount of time.

In conclusion, transition metal complexes are a class of materials that has been recently started to be employed as HTMs in PSCs. While few examples of reasonably high-performing devices exist, most of the reported compounds do not allow the fabrication of highly efficient perovskite solar cells. Furthermore, this class of compounds should not be confused with metal complexes employed *e.g.* in DSSCs. In the former case, in fact, the metal centre is only present in its highest oxidation state and does not play a primary role in the charge transfer process.

1.5.6. Solid-state redox-active metal complexes as hole conductors for ssDSSCs

While there are no reports on the use of metallorganic hole transporters where conductivity is provided by a redox transformation of a metal centre in PSCs, two studies of such compounds have been recently published for ssDSSCs. One focuses on a cobalt complex featuring a polypyridyl hexadentate ligand (bpyPY4) and a trifluoromethanesulfonate (OTf⁻) counter-ion developed by Kashif *et al.*^[211] The other reports on a copper complex featuring two identical 2,9-dimethyl-1,10-phenanthroline ligands (dmp) and a mix of bis(trifluoromethane)sulfonamide (TFSI⁻) and chloride counter-ions developed by Freitag *et al.*^[212] The molecular structures of the two transition metal complexes are depicted in Figure 18, while the properties of the two compounds are listed in Table 8.

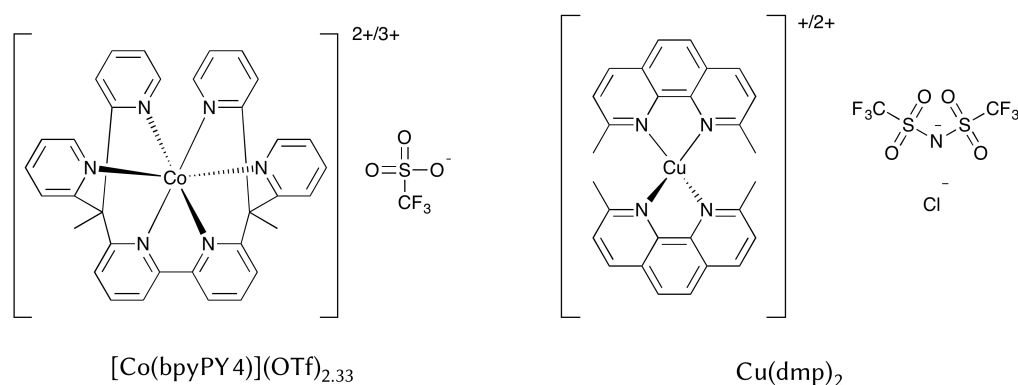


Figure 18. Solid-state redox-active metal complexes used as HTMs in ssDSSCs.

Table 8. Properties of redox-active metal complex HTMs used in ssDSSCs.

HTM	Reversible potential for $\text{M}^{n/n+1}$ (mV vs. NHE)	Conductivity (S cm^{-1})	Dye	PCE (%)
$[\text{Co}(\text{bpyPY4})](\text{OTf})_{2,33}$ ^[211]	465	3×10^{-2}	Y123	5.68 ± 0.06
$\text{Cu}(\text{dmp})_2\text{TFSI}/\text{Cl}$ ^[212]	940	(for Cu ^I)	LEG4	8.2

Both metal complexes in Figure 18 have been used in either liquid or solid-state DSSCs. In the case of $[\text{Co}^{\text{II/III}}(\text{bpyPY4})]$, a liquid DSSCs based on the MK2 dye exhibited a PCE of 8.3%.^[213] $\text{Cu}^{\text{I/II}}(\text{dmp})_2$ was tested in the liquid and solid-state in the same report, with better performances achieved in the latter case.^[212]

When deposited as solid films, both $[\text{Co}^{\text{II/III}}(\text{bpyPY4})](\text{OTf})_{2,33}$ and $\text{Cu}^{\text{I/II}}(\text{dmp})_2\text{TFSI/Cl}$ demonstrated comparatively high conductivities, which depended on the ratio of oxidised/reduced state of the metal centre. In particular, a film of $[\text{Co}^{\text{II}}(\text{bpyPY4})](\text{OTf})_2$, which contains only the reduced form, was reported to exhibit very low conductivity ($1.1 \times 10^{-10} \text{ S cm}^{-1}$). The introduction of the oxidised species, $[\text{Co}^{\text{III}}(\text{bpyPY4})](\text{OTf})_3$, enhanced the conductivity dramatically (Table 8).^[211] The conductivity measured for $\text{Cu}^{\text{I}}(\text{dmp})_2\text{TFSI}$ ($10^{-5} \text{ S cm}^{-1}$, Table 8) was five orders of magnitude higher than that for $[\text{Co}^{\text{II}}(\text{bpyPY4})](\text{OTf})_2$ and – despite the fact that the conductivity of the film employed in the final device was not measured^[212] – it is expected that the conductivity of said film would be much higher than that reported for $\text{Cu}^{\text{I}}(\text{dmp})_2\text{TFSI}$ alone. Freitag *et al.* compared the conductivity and hole mobility of a film of $\text{Cu}^{\text{I}}(\text{dmp})_2\text{TFSI}$ to those of a film of spiro-OMeTAD with additives (LiTFSI and tBP). The conductivity of $\text{Cu}^{\text{I}}(\text{dmp})_2\text{TFSI}$ is stated above, while that of the spiro-OMeTAD-based film was $2 \times 10^{-5} \text{ S cm}^{-1}$. The measured hole mobility values were 3×10^{-2} and $4 \times 10^{-3} \text{ cm}^2 \text{ V}^{-1} \text{ s}^{-1}$, respectively. Nevertheless, despite the high conductivities, the highest efficiencies of ssDSSCs based on the two redox-active metal complex HTMs reported so far could only be achieved when the latter were modified with the additives commonly employed in the organic small molecule hole transporting materials in PSCs.

In conclusion, it has been demonstrated that redox couples comprised of transition metal complexes can work efficiently as hole transporting materials in solid-state DSSCs. Since PSCs are conceptually similar to DSSCs in terms of working principles, it is plausible to expect that said redox couples can function efficiently as solid-state HTMs in perovskite solar cells as well.

1.6. Introduction summary & Aims of the thesis

In the future, an always growing share of humankind's energy production and consumption will have to be sourced from renewable energy. On the one hand, the always rising energy demand will exhaust the reserves of fossil fuels available on Earth. On the other hand – and most importantly – the pollution created by the combustion of fossil fuels is already poisoning our planet, decreasing the quality of the air that we breathe and causing a global temperature raise that is destroying natural habitats and posing a serious issue to humankind's life on the planet. Solar energy is by far the biggest and most widely spread source or renewable energy available to humankind. Without taking into account installation prices – which are nowadays economically viable in the market – with the current technologies it is already feasible, in theory, to meet the world's electricity demand with solar energy alone. In order to meet our total energy demand, however, it is necessary

to fabricate more efficient solar panels – in order to reduce the amount of surface area required per unit of power generated – and to extend the kinds of surfaces where solar panels can be installed onto.

Perovskite solar cells are an emerging technology in the renewable energy field. In only five years of development they have reached a certified solar to power conversion efficiency of more than 22% for laboratory-scale devices. Despite a yet-to-solve long term device stability issue, PSCs have the potential to become one of the leading technologies for the future generations of solar panels. Their fabrication is achieved with low-energy solution processes which – together with the low cost of the precursor materials – makes them very cost effective. The solution processing enables the fabrication of devices on flexible substrates, which – together with the fact that this light absorber works efficiently in diffused light – makes them ideal to be employed in environments where silicon solar cells do not work with a high output. Moreover, given the high efficiency and higher band gap of perovskite-based photovoltaics compared to silicon cells, it is possible to use the two technologies together to fabricate tandem devices, which can have an efficiency potentially much higher than any of the two alone. PSCs are *p-i-n* junctions and – although efficient devices without either the *p* or *n* layer are known – in order to achieve the best performances they require both an electron and a hole selective contact at either interface.

The first hole conductor used in a PSC – and the one still considered the state-of-the-art – is spiro-OMeTAD. Albeit being highly efficient, spiro-OMeTAD presents several drawbacks and many different compounds have been synthesised and characterised in order to replace it. So far, the various HTMs can be divided in four categories: organic small molecules, polymer, inorganic salts or oxides and transition metal complexes. Each of these categories has examples of high-performing compounds and some of them are more efficient than spiro-OMeTAD in terms of absolute efficiency, long term stability or both. Despite this, spiro-OMeTAD remains the HTM of choice for works on PSCs and its successor is yet to come.

The overall aim of this thesis is to widen the knowledge about hole conducting materials for perovskite solar cells, both by presenting new materials and by studying general properties that will prove useful to the research community. More specifically, the work focuses on the following scientific problems:

1. To demonstrate the feasibility of employing a solid-state redox-active metal complex as a hole transporting material in perovskite solar cells. Spawning from a work previously done in our research group on a Co(II/III) complex used as an HTM in ssDSSCs, a Fe(II/III) complex with the same hexadentate ligand is applied to PSCs featuring a FAPbBr₃ light absorber. This iron complex is comprehensively characterised, as are the solar cells based thereon.

2. To study the influence that the counter-ion has on the conductivity and general performance of redox-active metal complex HTMs, where the charge transport is provided by charge hopping through the various metal complex cations. It is postulated that anions, which are present to balance the charges, will have the side effect of spatially distancing the cations, thus hindering the charge transport process. To address the problem, the $[\text{Co}^{\text{II/III}}(\text{bpyPY4})](\text{OTf})_{2+x}$ complex previously used in ssDSSCs^[211] is now compared to a Co(II/III) complex with a negatively charged tridentate ligand in terms of their conductivity and performances as HTMs in PSCs. This second complex is neutral in its reduced form and only possesses one counter-ion in its oxidised form, reducing the number of counter-ions in the final layer from five to one per redox couple.
3. To study the effect that molecular geometry has on charge transport properties in organic small molecule HTMs. An organic hole conductor comprised of four triphenylamine branches and a bithiophene core twisted due to steric hindrance is compared to two similar hole conductors^[112,113] which lack the two methyl groups that are responsible for the twisting of the bithiophene core. The three HTMs are compared in terms of UV-Vis absorption, glass transition temperature, HOMO energy level and performances as hole conducting materials in PSCs.

2. Polypyridyl iron complex hole transporter

2.1. The long journey there

The initial idea for this project, during the last quarter of 2014, was to apply the same cobalt complex that Kashif *et al.*^[211] used as HTM in ssDSSCs to PSCs and combine the results in a single publication. Unfortunately, the Co(II) species of the complex decomposes MAPbI₃ and at the time the mixed-cation perovskite – which has been used with this complex as reported in the next chapter – had not been developed yet. Kashif proposed to replace the cobalt metal centre with iron and synthesised the first batch of the iron complex. Kashif and Milhuisen started working on the conductivity of the complex, while I focused on solar cell fabrication. From CV it was immediately clear that the iron complex had a much deeper HOMO level than the cobalt one and indeed PSCs fabricated with MAPbI₃ and the complex presented nicely-shaped *J-V* curves but the current output was negligible, due to the energy mismatch.

I decided to introduce bromide to the perovskite mixture, as it was reported that bromide, other than increasing the band gap of the light absorber material, also deepened its E_{VB} . From photoelectron spectroscopy in air measurements, it was clear that only MAPbBr₃ possessed an E_{VB} deep enough to be employed together with the iron complex. MAPbBr₃ can only be efficiently used in mesoporous devices and I started optimising their fabrication using the gas-assisted method developed in our laboratory.^[30] Despite the efforts, solar cells fabricated with this method and featuring spiro-OMeTAD as HTM only reached about 2.5% PCEs. In that period, Sheng *et al.* published a paper reporting on the fabrication of MAPbBr₃ devices with a vapour-assisted deposition technique and up to 9% efficiency.^[214] My efforts to reproduce Sheng's work, however, only yielded devices with about 3.5% PCEs. Sheng could not reproduce her own results in our laboratory when she came as a visiting student, despite the use of her own chemicals, while she was able to fabricate another batch of efficient devices once back at the University of New South Wales. This very unexpected irreproducibility can be attributed to slightly different fabrication procedures (*e.g.* in terms of cell ageing environment) and cell architecture and design (*e.g.* different active area, for which there was a lack of suitable metal evaporation and *J-V* characterisation masks) used at the Monash Renewable Energy Laboratory. This additionally emphasises the extraordinarily high sensitivity of PSCs performances on their fabrication method. Considering my poor results with MAPbBr₃, I decided to look into different kind of perovskite light absorbers.

While searching for fully bromide perovskites, I found a paper by Hanusch *et al.*^[215] reporting on planar devices using FAPbBr₃ as light absorber. At the time that was the only paper showing solar cells made with this material and results were reasonable with a two-step deposition method. I started optimising devices using the gas-assisted method and the final results have been presented in a manuscript published in the ACS Energy Letters journal, which is the body of this chapter.

Polypyridyl Iron Complex as a Hole-Transporting Material for Formamidinium Lead Bromide Perovskite Solar Cells

Muhammad K. Kashif,^{†,+} Iacopo Benesperi,^{‡,+} Rebecca A. Milhuisen,^{†,§} Steffen Meyer,[‡] Jack Hellerstedt,^{||,⊥,#} David Zee,^{∇,○} Noel W. Duffy,[◆] Barry Halstead,[◆] Michael S. Fuhrer,^{||,⊥,#} John Cashion,^{||} Yi-Bing Cheng,[†] Leone Spiccia,^{‡,||} Alexandr N. Simonov,^{*,‡,||} and Udo Bach^{*,§,◆,⊥,Ⓢ,Ⓣ}

[†]Department of Materials Science and Engineering, Monash University, 20 Research Way, Clayton, Victoria 3800, Australia

[‡]School of Chemistry, Monash University, 17 Rainforest Walk, Clayton, Victoria 3800, Australia

[§]ARC Centre of Excellence in Exciton Science, Monash University, Clayton, Victoria 3800, Australia

^{||}School of Physics and Astronomy, Monash University, 19 Rainforest Walk, Clayton, Victoria 3800, Australia

[⊥]Monash Centre for Atomically Thin Materials, Monash University, Clayton, Victoria 3800, Australia

[#]Center for Nanophysics and Advanced Materials, University of Maryland, College Park, Maryland 20742-4111, United States

[∇]Department of Chemistry, University of California, Berkeley, 420 Latimer Hall, Berkeley, California 94720, United States

[○]Materials Sciences Division, Lawrence Berkeley National Laboratory, 1 Cyclotron Road, Berkeley, California 94720, United States

[◆]CSIRO, Research Way, Clayton, Victoria 3168, Australia

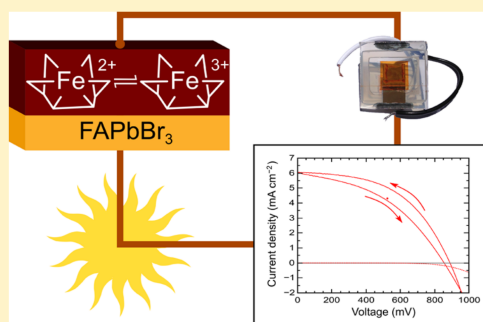
^{||}ARC Centre of Excellence for Electromaterials Science, Monash University, Clayton, Victoria 3800, Australia

[Ⓢ]Melbourne Centre for Nanofabrication, 151 Wellington Road, Clayton, Victoria 3168, Australia

[Ⓣ]Department of Chemical Engineering, Monash University, Clayton, Victoria 3800, Australia

Supporting Information

ABSTRACT: An efficient hole-transporting material (HTM) is indispensable for high-performing perovskite solar cells (PSCs), which have recently emerged as a breakthrough photovoltaic technology. Here, we demonstrate the capacity of the transition metal complex (6,6'-bis(1,1-di(pyridin-2-yl)ethyl)-2,2'-bipyridine)-iron(II/III) trifluoromethanesulfonate ($[\text{Fe}(\text{bpyPY4})](\text{OTf})_{2+x}$) to act as an additive-free, solution-processable HTM in PSCs based on the formamidinium lead bromide absorber. State-of-the-art physical methods have been employed to characterize $[\text{Fe}(\text{bpyPY4})](\text{OTf})_{2+x}$ and, in particular, to demonstrate its significantly higher conductivity compared to that of the conventional HTM spiro-OMeTAD. A maximum power conversion efficiency of 2.2% was obtained for a device employing $[\text{Fe}(\text{bpyPY4})](\text{OTf})_{2+x}$, which is the first evidence of the applicability as a HTM in a PSC of a solid material in which conductivity is provided by a redox transformation of a transition metal.



The first ever reported perovskite solar cell (PSC) by Miyasaka and co-workers in 2009¹ employed a redox couple in solution to scavenge holes from the perovskite light absorber. In 2012, a major breakthrough in the PSC field was made by Park and co-workers² and Snaith and co-workers,³ who independently developed the first all-solid-state device with 2,2',7,7'-tetrakis(*N,N*-di-*p*-methoxyphenylamine)9,9'-spiro-bifluorene (spiro-OMeTAD) as a hole-transporting material (HTM), which eventually enabled massive improvements in the power conversion efficiency

(PCE). The significance of this development for high-performing PSCs became immediately evident, leading to a plethora of research aimed to design new, efficient solid-state HTMs.^{4–7}

Among other HTMs, work has recently started on hole-conducting metal complexes, with an exclusive focus on planar

Received: June 16, 2017

Accepted: July 14, 2017

Published: July 14, 2017

molecules with high π -stacking capacity like phthalocyanines^{8–11} and other extended π -conjugated molecules.^{12,13} As a matter of fact, organic ligands in these complexes exhibit high conductivity even without a coordinated metal cation.¹⁴ When present, the latter was in its highest oxidation state and most probably did not play a key role in the hole transport process. At the same time, the capability of transition metal ions to adopt multiple oxidation states ensures low kinetic barriers for self-exchange reactions within a network of complexes of said metal cations and thereby provides a highly efficient mechanism for charge transfer.¹⁵ The feasibility of this concept has been recently demonstrated for solid-state dye-sensitized solar cells with nonplanar Cu^{I/II} and Co^{II/III} complexes as HTMs where conductivity was attributed to the redox transformations of the metal center.^{16,17} To date, HTMs of this class have not been applied in PSCs.

Here, we introduce a nonplanar iron complex based on a hexadentate polypyridyl ligand as a solid-state, solution-processable, additive-free HTM in a PSC. We employ a blend of [Fe^{II}(bpyPY4)](OTf)₂ and [Fe^{III}(bpyPY4)](OTf)₃ (hereinafter, [Fe(bpyPY4)](OTf)_{2+x}, x is the Fe^{III} fraction), where bpyPY4 is 6,6'-bis(1,1-di(pyridin-2-yl)ethyl)-2,2'-bipyridine (Figure 1a) and OTf⁻ is the trifluoromethanesulfonate

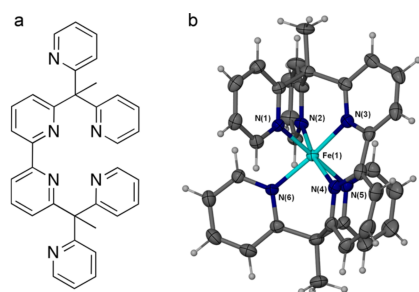


Figure 1. (a) 6,6'-Bis(1,1-di(pyridin-2-yl)ethyl)-2,2'-bipyridine (bpyPY4) ligand. (b) Structure of [Fe(bpyPY4)]³⁺ inferred by single-crystal X-ray analysis with 50% thermal ellipsoids.

anion. The electronic configuration of this iron complex (vide infra) necessitated the use of a perovskite material with a sufficiently low valence band edge energy (E_{VB}), namely, formamidinium lead bromide (FAPbBr₃) perovskite,^{18,19} to maximize the open-circuit voltage of the resulting devices. Despite the lower photovoltaic efficiency of full bromide perovskites compared to their iodide-containing counterparts, the wider band gap (E_g) FAPbBr₃ light absorber can find its niche in promising tandem solar cell applications.²⁰

[Fe(bpyPY4)](OTf)_{2+x} was synthesized by adopting the procedure previously developed for the [Co^{II/III}(bpyPY4)] complexes,^{17,21} which is detailed in the Supporting Information (SI) along with the outcomes of the elemental, mass, and structural analyses and ¹H NMR, UV–vis, and Mössbauer spectroscopic characterization. Figures 1b and S1 feature the molecular structures of [Fe^{III}(bpyPY4)]³⁺ and [Fe^{II}(bpyPY4)]²⁺, as derived from single-crystal XRD data. The refinement of these data suggests a triclinic lattice with a $P\bar{1}$ space group for the Fe^{II}-based complex and a monoclinic lattice with a $P2_1/n$ space group for the Fe^{III}-based complex (Figure S1). XRD patterns of the thin, mixed [Fe(bpyPY4)](OTf)_{2+x} films obtained by drop-casting and spin-coating did not depend on the deposition strategy and

could be well fitted using the single-crystal data, showing crystallite sizes ranging from 30 nm to subnanometer scale (Figure S2). The Mössbauer spectrum for [Fe(bpyPY4)](OTf)₂ (Figure S3a) suggests the presence of one Fe^{II} population and a small impurity. Mössbauer analysis of [Fe(bpyPY4)](OTf)₃ shows that the compound is dominated by the Fe^{III} complex (single population) with a minor (7.8 atom %) admixture of Fe^{II} (Figure S3b). On this basis, this compound is further referred to as [Fe(bpyPY4)](OTf)_{2.9}. In the absorption spectra, three major peaks resulting from one ligand-based transition (320–325 nm) and two metal-to-ligand charge-transfer transitions (440–450 and 560–570 nm) were identified for both [Fe(bpyPY4)](OTf)₂ and [Fe(bpyPY4)](OTf)_{2.9} (Figure S4). Maximum extinction coefficients were 18600 (321 nm) and 12000 M⁻¹ cm⁻¹ (324 nm) for $x = 0$ and 0.9, respectively.

Electrical conductivity is a critical parameter for a material to be employed as a HTM and is directly proportional to the density of charge carriers. As previously reported by our group,¹⁷ this property can be controlled by tuning the ratio of oxidized to reduced molecular species. Here, two-probe interdigitated array (IDA) microelectrodes were used to assess the conductivity of the drop-cast [Fe(bpyPY4)](OTf)_{2+x} films with $0 \leq x \leq 0.9$. Linear current–voltage dependencies were obtained for all blends, demonstrating ideal ohmic contact with the gold electrodes, while the iron-free ligand molecule showed very little conductivity (Figure S5). Even a small addition of [Fe(bpyPY4)](OTf)₃ to [Fe(bpyPY4)](OTf)₂ increased the conductivity by more than 2 orders of magnitude, while further enhancements at $x > 0.1$ were not that significant (Figure 2). A

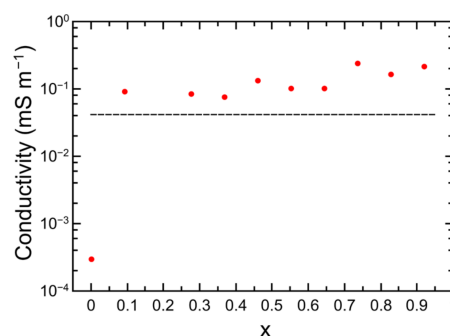


Figure 2. Room-temperature conductivity of various blends of the [Fe(bpyPY4)](OTf)₂ and [Fe(bpyPY4)](OTf)₃ thin films. For comparison, the conductivity of the 10% oxidized spiro-OMeTAD thin film is shown as a dashed line.

maximum room-temperature conductivity of 0.24 mS m⁻¹ was achieved with 74 mol % [Fe(bpyPY4)](OTf)₃, which is almost 5-fold higher than 0.051 mS m⁻¹ measured under the same conditions for the reference organic HTM, namely, 10% oxidized spiro-OMeTAD. Conductivity measurements undertaken for [Fe(bpyPY4)](OTf)_{2.7} at different temperatures (210–300 K range) demonstrated Arrhenius behavior (Figure S6), which is typical for semiconducting materials with thermally activated hopping as the dominant mode of charge transport. As expected, the 10% oxidized spiro-OMeTAD also followed similar semiconducting behavior. The corresponding activation energies derived from the linear fits to the experimental data were 0.36 eV for [Fe(bpyPY4)](OTf)_{2.7}

and 0.31 eV for the 10% oxidized spiro-OMeTAD thin films. The latter value is consistent with the one found in literature.²²

Electronic structure is another key property of a prospective HTM that must be considered to enable appropriate alignment of the energy levels in the solar cell. The highest occupied molecular orbital (HOMO) energy level for the Fe-based HTM was first derived from the cyclic voltammetric analysis of [Fe(bpyPY4)](OTf)₂ in CH₃CN (0.1 M *n*-Bu₄PF₆), where the compound undergoes chemically reversible oxidation with a midpoint potential of 0.54 V vs ferrocene^{0/+} attributed to the Fe^{II/III} transition (Figure S7). Further, ultraviolet photoelectron spectroscopy (UPS) and photoelectron spectroscopy in air (PESA) measurements on the [Fe(bpyPY4)](OTf)_{2.5} films were undertaken (Figures S8, S9). This particular HTM composition was used in these studies as it provided the highest PCE of the solar cells (vide infra). Thus, the measured HOMO for [Fe(bpyPY4)](OTf)_{2.5} varied slightly between −5.46 and −5.67 eV depending on the technique employed (Table S1). The same set of methods was used to determine that the HOMO for spiro-OMeTAD lies between −5.14 and −4.69 eV, while E_{VB} for FAPbBr₃ falls within the −5.83 to −5.62 eV range as measured by UPS and PESA (Table S1). Analysis of the Tauc plot for the perovskite provided a band gap of 2.28 eV (Figure S10). These results agree well with the literature^{18,23} and are summarized along with the new data for [Fe(bpyPY4)](OTf)_{2.5} in Figure 3a. Inspection of the constructed

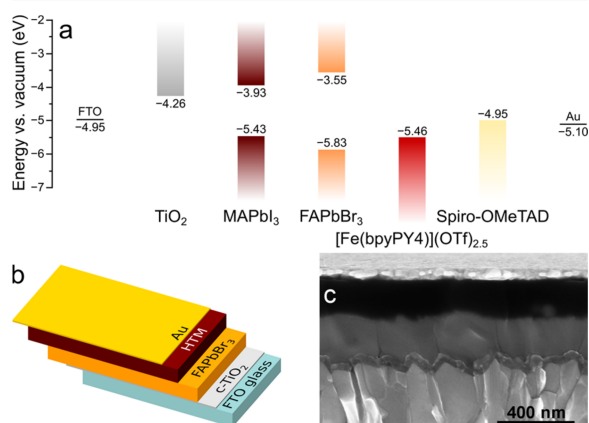


Figure 3. (a) Energy level diagram of the materials employed for solar cell fabrication; data for MAPbI₃² are shown for comparison. (b) Scheme of the solar cell arrangement. (c) Cross-sectional SEM image of the device based on the [Fe(bpyPY4)](OTf)_{2.5} HTM.

energy level diagram suggests compatibility of FAPbBr₃ with the new HTM introduced here but clearly demonstrates unfavorable band alignment with a light absorber having a more positive E_{VB} like CH₃NH₃PbI₃ (MAPbI₃). Highly efficient charge injection from FAPbBr₃ into [Fe(bpyPY4)](OTf)_{2.5} was

further proven by fluorescence quenching measurements, which demonstrated more than 99% intensity suppression when the perovskite film was modified with the Fe-based HTM (Figure S11).

Finally, a set of solar cells with a planar FTO/c-TiO₂/FAPbBr₃/HTM/Au architecture (FTO—glass covered with fluorine-doped tin(IV) oxide; c-TiO₂—compact titania blocking layer) was fabricated (schematic structure shown in Figure 3b). Devices based on the MAPbI₃ light absorber were also fabricated and tested, but those demonstrated negligible photocurrent density, as expected. [Fe(bpyPY4)](OTf)_{2+x} is poorly soluble in the relatively nonpolar solvents commonly employed for HTM deposition in PSCs. This problem was addressed here by using nitromethane to prepare the Fe-based HTM deposition solutions. Importantly, this solvent does not dissolve or damage the FAPbBr₃ or MAPbI₃ layers, thus enabling the use of more polar HTMs in solution-processed PSCs. A scanning electron microscopic (SEM) cross-sectional image of the [Fe(bpyPY4)](OTf)_{2.5}-based device featuring ~250 nm thick HTM and perovskite layers is shown in Figure 3c. The employed FAPbBr₃ deposition method allowed for the formation of a compact, void-free layer of single grains (Figures 3c and S12), which, however, contained small amounts of isolated PbBr₂ particles as inferred by energy dispersive X-ray analysis (Figure S13). Importantly, PbBr₂ could not be detected by XRD on the films, confirming its very low amount and segregation to the perovskite surface (Figure S14). An increase of the FAPbBr₃ content in the perovskite precursor solution removed the PbBr₂ grains but resulted in lower device efficiencies. All devices were encapsulated under an inert atmosphere before being tested to avoid degradation in air and under illumination. Full solar cell fabrication details are provided in the SI.

Initial tests on PSCs based on [Fe(bpyPY4)](OTf)_{2+x} with 0 ≤ *x* ≤ 0.9 have shown that the HTM must contain at least a small amount of Fe^{III} to enable reasonable photovoltaic performance, which is most probably due to the very low conductivity of [Fe(bpyPY4)](OTf)₂. Furthermore, the PCE peaked at *x* = 0.5, though differences in solar cell efficiencies at higher Fe^{III}:Fe^{II} ratios were not significant. Thus, detailed device performance studies reported below were undertaken for *x* = 0.5.

A summary of the photovoltaic parameters for a representative population of the FAPbBr₃ solar cells with [Fe(bpyPY4)](OTf)_{2.5} or spiro-OMeTAD as the HTM is reported in Table 1. The current density vs potential (*J*–*V*) curves for both scan directions and incident photon to current conversion efficiency (IPCE) spectra are exemplified in Figure 4. The quasi-steady-state measurements at maximal power potentials for the [Fe(bpyPY4)](OTf)_{2.5} devices (Figure S15) produced PCE values that were close to those derived from the short-circuit to forward bias sweeps of the *J*–*V* curves (Figure 4a). An opposite trend was found for all solar cells based on the

Table 1. Photovoltaic Parameters^a of the FAPbBr₃ PSCs with Different HTMs under 1 Sun AM1.5G Irradiation

HTM	V_{OC} (mV)	J_{SC} (mA cm ⁻²)	FF (%)	PCE (%)
spiro-OMeTAD	1290 ± 40	6.3 ± 0.4	61 ± 6	4.9 ± 0.4
[Fe(bpyPY4)](OTf) _{2.5}	760 ± 60	6.1 ± 0.3	42 ± 2	2.0 ± 0.3

^aDerived from the *J*–*V* curves (scan rate = 10 mV s⁻¹) for seven spiro-OMeTAD-based (forward bias to short-circuit sweeps) and 15 [Fe(bpyPY4)](OTf)_{2.5}-based (short-circuit to forward bias sweeps) devices. V_{OC} , open-circuit voltage; J_{SC} , short-circuit current density; FF, fill factor. See Table S2 for the complete set of *J*–*V* data.

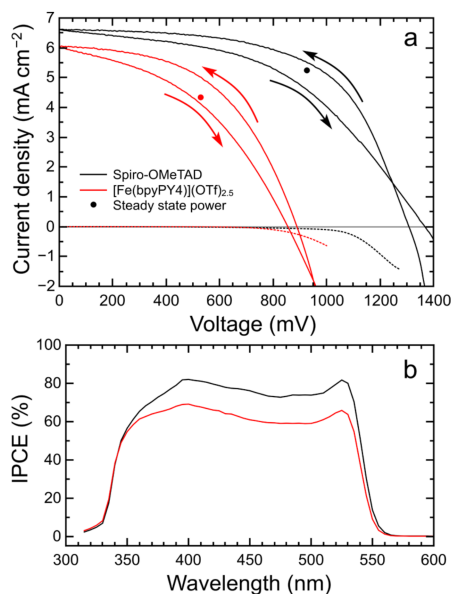


Figure 4. (a) J - V curves (scan rate = 10 mV s⁻¹) and (b) IPCE spectra measured for the best-performing FAPbBr₃ PSCs based on the [Fe(bpyPY4)](OTf)_{2.5} (red) and Spiro-OMeTAD (black) HTMs recorded under 1 Sun (100 mW cm⁻²) AM1.5G irradiation (solid curves) and in the dark (dashed curves). Filled circles in panel (a) show quasi-steady-state performance after 600 s of operation at the maximum power point potential (PCE-time transients are shown in Figure S14). Devices were masked with an aperture of 0.16 cm² to define the active area.

spiro-OMeTAD HTM. These observations were considered when selecting the performance data shown in Table 1.

The best-performing device fabricated with [Fe(bpyPY4)](OTf)_{2.5} featured an open-circuit voltage, V_{OC} , of 855 mV, a short-circuit current density, J_{SC} , of 6.0 mA cm⁻², a fill factor, FF, of 42%, and a PCE of 2.2%. This can be compared to the performance of the best Spiro-OMeTAD-based PSC that achieved V_{OC} = 1310 mV, J_{SC} = 6.6 mA cm⁻², FF = 60%, with a resulting PCE of 5.2%. Remarkably, the Spiro-OMeTAD-based devices performed best without the use of the common additives to HTM, namely, 4-*tert*-butylpyridine and lithium bis(trifluoromethanesulfonyl)imide. Due to its high conductivity, [Fe(bpyPY4)](OTf)_{2.5} did not require the use of the aforementioned additives either. Despite the lower absolute initial efficiency, stability measurements under continuous irradiation over several days suggest that the use of the [Fe(bpyPY4)](OTf)_{2.5} hole-transporting layer provides some improvements in the stability of the FAPbBr₃ solar cells (55% efficiency loss after 120 h) as compared to the Spiro-OMeTAD benchmark HTM (80% efficiency loss after 120 h) (Figure S17).

Inspection of the data in Table 1 and Figure 4 indicates that low FF and V_{OC} contribute to lower efficiencies of the PSCs based on the iron complex HTM. The perfectly rectifying behavior of the FTO/c-TiO₂/[Fe(bpyPY4)](OTf)_{2.5}/Au diodes that demonstrate a cut-in voltage of 600 mV and negligible photocurrent (Figure S16) suggests that the HTM layer itself does not produce additional shunt resistance and does not contribute significantly to the lower FF. The underlying reasons for lower than expected V_{OC} achieved with the [Fe(bpyPY4)]-

(OTf)_{2.5} HTM integrated with the FAPbBr₃ perovskite are also yet to be established. Indeed, data in Figure 3a suggest that the open-circuit voltage provided by the Fe-based material should be higher than that available with Spiro-OMeTAD, which contrasts with our experimental observations. In principle, this can be rationalized in terms of insufficient driving force for the charge transfer between [Fe(bpyPY4)](OTf)_{2.5} and FAPbBr₃ as defined by small differences between their HOMO and E_{VB} (Table S1), which facilitates recombination losses at the perovskite/HTM interface. This hypothesis is supported by a more than 3-fold higher recombination resistance derived from electrochemical impedance spectra recorded for the Spiro-OMeTAD-based solar cell (1250 Ω) as compared to that obtained for the device with [Fe(bpyPY4)](OTf)_{2.5} as a HTM (400 Ω) (Figure S18). However, further scrutiny is needed to unambiguously establish the reasons for the comparatively low V_{OC} and FF achieved here with the new HTM.

In conclusion, an iron complex featuring a polypyridyl hexadentate ligand was synthesized and applied as a HTM in planar FAPbBr₃ PSCs. The [Fe(bpyPY4)](OTf)_{2+x} blends with $x \geq 0.1$ exhibit higher conductivity and a more negative HOMO as compared to the benchmark 10% oxidized Spiro-OMeTAD films. However, the open-circuit voltage of the PSCs employing the Fe-based HTM was lower than expected and inferior to the V_{OC} of the devices with a conventional organic HTM. While lower recombination resistance in the [Fe(bpyPY4)](OTf)_{2.5}-based devices as compared to that in PSC with the Spiro-OMeTAD hole-transporting layer suggested charge recombination as a plausible explanation, extended studies on the origins of this phenomenon are identified as future work. Most importantly, the present report provides the first demonstration of the capacity of a transition metal complex to sustain efficient hole transport in all-solid-state PSCs via the redox activity of the metal center. We anticipate that this finding might open up new possibilities for design of efficient and versatile charge-transporting materials for solar cells and other solution-processed electronic devices.

■ ASSOCIATED CONTENT

Supporting Information

The Supporting Information is available free of charge on the ACS Publications website at DOI: 10.1021/acseenergylett.7b00522.

Experimental methods; XRD data; UV-vis and Mössbauer spectra; conductivity data; cyclic voltammetry; PESA and UPS data; summary of energy levels; PL quenching data; SEM images; quasi-steady-state power measurements; complete J - V data; long-term stability data; and electrochemical impedance spectroscopy (PDF)

■ AUTHOR INFORMATION

Corresponding Authors

*E-mail: alexandr.simonov@monash.edu. URL: <http://www.spicciagroup.net> (A.N.S.).

*E-mail: udo.bach@monash.edu. URL: <http://www.udobach.com> (U.B.).

ORCID

Alexandr N. Simonov: 0000-0003-3063-6539

Udo Bach: 0000-0003-2922-4959

Author Contributions

†M.K.K. and I.B. contributed equally.

Notes

The authors declare no competing financial interest.

ACKNOWLEDGMENTS

The authors acknowledge the Australian Research Council (CE170100026, DP160104575, CE140100012), the Australian Renewable Energy Agency (ARENA), and the Australian Centre for Advanced Photovoltaics (ACAP) for financial support, Monash Centre for Electron Microscopy for providing microscopy facilities, Dr. E. Della Gaspera (CSIRO) for help with the PESA measurements, Dr. T. Gengenbach (CSIRO) for undertaking the UPS measurements, and Mr. L. Jiang (Monash University) for assistance with setting up the environmental chamber. The synthesis of the bpyPY4 ligand was supported by NSF Grant CHE-1464841 to J. R. Long. S.M. acknowledges the Alexander von Humboldt Foundation for a Feodor Lynen Fellowship. D.Z.Z. thanks the National Science Foundation for a Graduate Research Fellowship.

REFERENCES

- (1) Kojima, A.; Teshima, K.; Shirai, Y.; Miyasaka, T. Organometal Halide Perovskites as Visible-Light Sensitizers for Photovoltaic Cells. *J. Am. Chem. Soc.* **2009**, *131* (17), 6050–6051.
- (2) Kim, H.-S.; Lee, C.-R.; Im, J.-H.; Lee, K.-B.; Moehl, T.; Marchioro, A.; Moon, S.-J.; Humphry-Baker, R.; Yum, J.-H.; Moser, J. E.; et al. Lead Iodide Perovskite Sensitized All-Solid-State Submicron Thin Film Mesoscopic Solar Cell with Efficiency Exceeding 9%. *Sci. Rep.* **2012**, *2*, 591.
- (3) Lee, M. M.; Teuscher, J.; Miyasaka, T.; Murakami, T. N.; Snaith, H. J. Efficient Hybrid Solar Cells Based on Meso-Superstructured Organometal Halide Perovskites. *Science* **2012**, *338* (6107), 643–647.
- (4) Caliò, L.; Kazim, S.; Grätzel, M.; Ahmad, S. Hole-Transport Materials for Perovskite Solar Cells. *Angew. Chem., Int. Ed.* **2016**, *55* (47), 14522–14545.
- (5) Teh, C. H.; Daik, R.; Lim, E. L.; Yap, C. C.; Ibrahim, M. A.; Ludin, N. A.; Sopian, K.; Mat Teridi, M. A. A review of organic small molecule-based hole-transporting materials for meso-structured organic–inorganic perovskite solar cells. *J. Mater. Chem. A* **2016**, *4* (41), 15788–15822.
- (6) Wang, Y.-K.; Jiang, Z.-Q.; Liao, L.-S. New advances in small molecule hole-transporting materials for perovskite solar cells. *Chin. Chem. Lett.* **2016**, *27* (8), 1293–1303.
- (7) Yan, W.; Ye, S.; Li, Y.; Sun, W.; Rao, H.; Liu, Z.; Bian, Z.; Huang, C. Hole-Transporting Materials in Inverted Planar Perovskite Solar Cells. *Adv. Energy Mater.* **2016**, *6* (17), 1600474.
- (8) Kumar, C. V.; Sfyr, G.; Raptis, D.; Stathatos, E.; Lianos, P. Perovskite solar cell with low cost Cu-phthalocyanine as hole transporting material. *RSC Adv.* **2015**, *5* (5), 3786–3791.
- (9) Cho, K. T.; Trukhina, O.; Roldán-Carmona, C.; Ince, M.; Gratia, P.; Grancini, G.; Gao, P.; Marszalek, T.; Pisula, W.; Reddy, P. Y.; et al. Molecularly Engineered Phthalocyanines as Hole-Transporting Materials in Perovskite Solar Cells Reaching Power Conversion Efficiency of 17.5%. *Adv. Energy Mater.* **2017**, *7* (7), 1601733.
- (10) Wang, Y.; Liu, X.; Shan, H.; Chen, Q.; Liu, T.; Sun, X.; Ma, D.; Zhang, Z.; Xu, J.; Xu, Z.-X. Tetra-alkyl-substituted copper (II) phthalocyanines as dopant-free hole-transport layers for planar perovskite solar cells with enhanced open circuit voltage and stability. *Dyes Pigm.* **2017**, *139*, 619–626.
- (11) Yang, G.; Wang, Y.-L.; Xu, J.-J.; Lei, H.-W.; Chen, C.; Shan, H.-Q.; Liu, X.-Y.; Xu, Z.-X.; Fang, G.-J. A facile molecularly engineered copper (II) phthalocyanine as hole transport material for planar perovskite solar cells with enhanced performance and stability. *Nano Energy* **2017**, *31*, 322–330.
- (12) Hua, Y.; Xu, B.; Liu, P.; Chen, H.; Tian, H.; Cheng, M.; Kloo, L.; Sun, L. High conductivity Ag-based metal organic complexes as dopant-free hole-transport materials for perovskite solar cells with high fill factors. *Chem. Sci.* **2016**, *7*, 2633–2638.
- (13) Chou, H.-H.; Chiang, Y.-H.; Li, M.-H.; Shen, P.-S.; Wei, H.-J.; Mai, C.-L.; Chen, P.; Yeh, C.-Y. Zinc Porphyrin–Ethinylaniline Conjugates as Novel Hole-Transporting Materials for Perovskite Solar Cells with Power Conversion Efficiency of 16.6%. *ACS Energy Lett.* **2016**, *1* (5), 956–962.
- (14) Dao, Q.-D.; Fujii, A.; Tsuji, R.; Takeoka, Y.; Ozaki, M. Efficiency enhancement in perovskite solar cell utilizing solution-processable phthalocyanine hole transport layer with thermal annealing. *Org. Electron.* **2017**, *43*, 156–161.
- (15) Ren, X.; Alleyne, B. D.; Djurovich, P. I.; Adachi, C.; Tsyba, I.; Bau, R.; Thompson, M. E. Organometallic Complexes as Hole-Transporting Materials in Organic Light-Emitting Diodes. *Inorg. Chem.* **2004**, *43* (5), 1697–1707.
- (16) Freitag, M.; Daniel, Q.; Pazoki, M.; Sveinbjörnsson, K.; Zhang, J.; Sun, L.; Hagfeldt, A.; Boschloo, G. High-efficiency dye-sensitized solar cells with molecular copper phenanthroline as solid hole conductor. *Energy Environ. Sci.* **2015**, *8* (9), 2634–2637.
- (17) Kashif, M. K.; Milhaisen, R. A.; Nippe, M.; Hellerstedt, J.; Zee, D. Z.; Duffy, N. W.; Halstead, B.; De Angelis, F.; Fantacci, S.; Fuhrer, M. S.; et al. Cobalt Polypyridyl Complexes as Transparent Solution-Processable Solid-State Charge Transport Materials. *Adv. Energy Mater.* **2016**, *6* (24), 1600874.
- (18) Hanusch, F. C.; Wiesenmayer, E.; Mankel, E.; Binek, A.; Angloher, P.; Fraunhofer, C.; Giesbrecht, N.; Feckl, J. M.; Jaegermann, W.; Johrendt, D.; et al. Efficient Planar Heterojunction Perovskite Solar Cells Based on Formamidinium Lead Bromide. *J. Phys. Chem. Lett.* **2014**, *5* (16), 2791–2795.
- (19) Arora, N.; Orlandi, S.; Dar, M. I.; Aghazada, S.; Jacopin, G.; Cavazzini, M.; Mosconi, E.; Gratia, P.; De Angelis, F.; Pozzi, G.; et al. High Open-Circuit Voltage: Fabrication of Formamidinium Lead Bromide Perovskite Solar Cells Using Fluorene–Dithiophene Derivatives as Hole-Transporting Materials. *ACS Energy Lett.* **2016**, *1* (1), 107–112.
- (20) White, T. P.; Lal, N. N.; Catchpole, K. R. Tandem Solar Cells Based on High-Efficiency c-Si Bottom Cells: Top Cell Requirements for > 30% Efficiency. *IEEE J. Photovolt.* **2014**, *4* (1), 208–214.
- (21) Kashif, M. K.; Nippe, M.; Duffy, N. W.; Forsyth, C. M.; Chang, C. J.; Long, J. R.; Spiccia, L.; Bach, U. Stable Dye-Sensitized Solar Cell Electrolytes Based on Cobalt(II)/(III) Complexes of a Hexadentate Pyridyl Ligand. *Angew. Chem., Int. Ed.* **2013**, *52* (21), 5527–5531.
- (22) Dualeh, A.; Moehl, T.; Nazeeruddin, M. K.; Grätzel, M. Temperature Dependence of Transport Properties of Spiro-MeOTAD as a Hole Transport Material in Solid-State Dye-Sensitized Solar Cells. *ACS Nano* **2013**, *7* (3), 2292–2301.
- (23) Hawash, Z.; Ono, L. K.; Raga, S. R.; Lee, M. V.; Qi, Y. Air-Exposure Induced Dopant Redistribution and Energy Level Shifts in Spin-Coated Spiro-MeOTAD Films. *Chem. Mater.* **2015**, *27* (2), 562–569.

Supporting Information

Polypyridyl Iron Complex as a Hole-Transporting Material for Formamidinium Lead Bromide Perovskite Solar Cells

Muhammad K. Kashif,^{†,+} Iacopo Benesperi,^{‡,+} Rebecca A. Milhuisen,^{†,§} Steffen Meyer,[‡] Jack Hellerstedt,^{||,⊥,#} David Zee,^{∇,○} Noel W. Duffy,[◆] Barry Halstead,[◆] Michael S. Fuhrer,^{||,⊥,#} John Cashion,^{||} Yi-Bing Cheng,[†] Leone Spiccia,^{‡,¶} Alexandr N. Simonov,^{*,‡,¶} and Udo Bach^{*,§,◆,&,\$}

[†]Department of Materials Science and Engineering, 20 Research Way, Monash University, Victoria 3800, Australia

[‡]School of Chemistry, 17 Rainforest walk, Monash University, Victoria 3800, Australia

[§]ARC Centre of Excellence in Exciton Science, Monash University, Victoria 3800, Australia

^{||}School of Physics and Astronomy, 19 Rainforest Walk, Monash University, Victoria 3800, Australia

[⊥]Monash Centre for Atomically Thin Materials, Monash University, Victoria 3800, Australia

[#]Center for Nanophysics and Advanced Materials, University of Maryland, College Park, Maryland 20742-4111, USA

[∇]Department of Chemistry, University of California, Berkeley, 420 Latimer Hall, Berkeley, California 94720, USA

[○]Materials Sciences Division, Lawrence Berkeley National Laboratory, 1 Cyclotron Road, Berkeley, California 94720, USA

[◆]CSIRO, Research Way, Clayton, Victoria 3168, Australia

[¶]ARC Centre of Excellence for Electromaterials Science, Monash University, Victoria 3800, Australia

[&]Melbourne Centre for Nanofabrication, 151 Wellington Road, Clayton, Victoria 3168, Australia

^{\$}Department of Chemical Engineering, Monash University, Victoria 3800, Australia

ABSTRACT: An efficient hole transporting material (HTM) is indispensable for high-performing perovskite solar cells (PSC), which have recently emerged as a breakthrough photovoltaic technology. Here, we demonstrate the capacity of the transition metal complex (6,6'-bis(1,1-di(pyridin-2-yl)ethyl)-2,2'-bipyridine)-iron(II/III) trifluoromethanesulfonate ([Fe(bpyPY4)](OTf)_{2+x}) to act as an additive-free, solution-processable HTM in PSCs based on the formamidinium lead bromide absorber. State-of-the-art physical methods have been employed to characterize [Fe(bpyPY4)](OTf)_{2+x} and in particular to demonstrate its significantly higher conductivity compared to the conventional HTM spiro-OMeTAD. A maximum power conversion efficiency of 2.2% was obtained for a device employing [Fe(bpyPY4)](OTf)_{2+x}, which is the first evidence of the applicability as HTM in PSC of a solid material in which conductivity is provided by a redox transformation of a transition metal.

Table of contents

Experimental methods.....	53
Materials.....	53
Synthesis of 6,6'-bis(1,1-di(pyridin-2-yl)ethyl)-2,2'-bipyridine (bpyPY4).....	53
Synthesis of [Fe(bpyPY4)](OTf) ₂	53
Synthesis of [Fe(bpyPY4)](OTf) ₃	54
Synthesis of formamidinium bromide (FABr).....	54
Conductivity measurements.....	54
Solar cell preparation.....	55
Characterization.....	56
Results.....	59
Single crystal XRD details for [Fe(bpyPY4)](OTf) ₂ and [Fe(bpyPY4)](OTf) ₃	59
XRD patterns of [Fe(bpyPY4)](OTf) _{2.5} films.....	60
Mössbauer spectroscopy.....	61
UV-Vis absorbance.....	61
Conductivity.....	62
Cyclic voltammetry.....	63
Photoelectron spectroscopy in air.....	63
Ultraviolet photoelectron spectroscopy.....	64
Energy levels.....	64
UV-Vis spectrum and Tauc plot for FAPbBr ₃	64
Photoluminescence quenching.....	65
Cross-sectional SEM images.....	65
Surface SEM images and composition of FAPbBr ₃	66
XRD patterns for FAPbBr ₃ and PbBr ₂ films.....	66
Quasi-steady-state power measurement.....	67
Complete J-V scan data.....	67
FTO TiO ₂ [Fe(bpyPY4)](OTf) _{2.5} Au diode.....	68
Long-term stability.....	69
Electrochemical impedance spectroscopy.....	70
References.....	70
Complete single crystal XRD data refinement for [Fe(bpyPY4)](OTf) ₂	124
Complete single crystal XRD data refinement for [Fe(bpyPY4)](OTf) ₃	132

Experimental methods

Materials

Unless otherwise specified, all materials were purchased from either Alfa Aesar or Sigma-Aldrich and used as received. Spiro-OMeTAD (2,2',7,7'-tetrakis-(*N,N*-di-4-methoxyphenylamino)-9,9'-spirobifluorene) was purchased from Luminescence Technology Corp. (Lumtec). Fluorine-doped tin oxide (FTO) glass TEC8 (sheet resistance $8 \Omega \square^{-1}$) was purchased from Dyesol. Interdigitated array microelectrodes were purchased from BAS-ALS, Japan.

Synthesis of 6,6'-bis(1,1-di(pyridin-2-yl)ethyl)-2,2'-bipyridine (bpyPY4)

The ligand bpyPY4 was synthesized according to a method reported in the literature.^{S1} In a round-bottomed flask under nitrogen atmosphere, 2,2'-(ethane-1,1-diyl)dipyridine (2.28 g, 12.4 mmol, 3 eq) was added to 90 mL of dry tetrahydrofuran (THF). The solution was cooled down to $-78 \text{ }^\circ\text{C}$ (acetone/dry ice). Once the temperature was reached, *n*-butyllithium (2.5 M in hexane, 5 mL, 12.5 mmol, 3 eq) was added dropwise and the solution was stirred for 30 min. A solution of 6,6'-dibromo-2,2'-bipyridine (1.30 g, 4.14 mmol, 1 eq) in 45 mL of dry THF (prepared under nitrogen atmosphere, gentle heating may be required for full dissolution) was subsequently added, and the cooling bath removed. The solution was stirred for 1 h, then refluxed for 36 h while keeping the nitrogen atmosphere. After cooling to room temperature, the reaction was quenched with 60 mL of water. The organic and aqueous phases were separated and the aqueous phase was washed three times with dichloromethane for a total amount of 60 mL. The combined organic phases were dried with MgSO_4 and the solvent removed with rotary evaporation. The crude product was suspended in ethyl acetate and kept in an ultrasonic bath for 1.5 h. After decanting, ethyl acetate was pipetted out and replaced with a fresh portion, and the sonication was repeated. Afterwards, the slightly beige solid was filtered and used as is. Yield: 1.46 g (68%). ^1H NMR (400 MHz, CDCl_3): $\delta = 8.57$ (dq, $J = 1 \text{ Hz}$, 4.8 Hz, 4H), 8.01 (dd, $J = 0.8 \text{ Hz}$, 7.8 Hz, 2H), 7.60-7.52 (m, 6H), 7.12-7.07 (m, 10H), 2.39 (s, 6H).

Synthesis of $[\text{Fe}(\text{bpyPY4})](\text{OTf})_2$

Inside a glove-box, bpyPY4 (0.30 g, 0.576 mmol, 1 eq) was suspended in 5 mL of CH_3CN inside a vial. In a separate vial, $\text{Fe}(\text{OTf})_2$ (0.20 g, 0.565 mmol, 1 eq) was dissolved in 6 mL of CH_3CN . The $\text{Fe}(\text{OTf})_2$ solution was added dropwise to the bpyPY4 suspension while stirring at $60 \text{ }^\circ\text{C}$. After addition, the mixture was stirred for 30 min and then filtered through a $0.45 \mu\text{m}$ PTFE membrane syringe filter to remove the excess of undissolved bpyPY4. The vial containing the metal complex solution was placed in a capped Schott bottle containing diethyl ether and the metal complex was obtained through recrystallization *via* solvent diffusion over two weeks. The crystals were recovered, washed with $(\text{C}_2\text{H}_5)_2\text{O}$ and dissolved again in a minimum amount of CH_3CN . The solution was placed in a Schott bottle again for a second recrystallization in a similar fashion. The obtained crystals were blood-red in color.

Yield: 0.34 g (69%). ¹H NMR (400 MHz, DMSO-d₆): δ = 8.52 (d, *J* = 7 Hz, 2H), 8.45 (d, *J* = 8 Hz, 2H), 8.32 (d, *J* = 7.4 Hz, 2H) 8.25-8.18 (m, 4H), 7.95-7.87 (m, 4H), 7.82 (dd, *J* = 1.2 Hz, 5.1 Hz, 2H), 7.28 (ddd, *J* = 1 Hz, 7.6 Hz, 6 Hz, 2H), 7.21 (dd, *J* = 1.4 Hz, 6.8 Hz, 2H), 6.98 (ddd, *J* = 1.4 Hz, 7.1 Hz, 5.2 Hz, 2H), 2.89 (s, 6H). HR-MS (ESI): *m/z* calcd for [Fe(bpyPY4)]²⁺: 228.0857, found: 228.0849; calcd for [Fe(bpyPY4)](OTf)⁺: 725.1240, found: 725.1220; calcd for OTf⁻: 148.9526, found: 148.9529. Elem. anal. calcd for C₃₆H₂₈F₆FeN₆O₆S₂: C, 49.44; H, 3.23; Fe, 6.39; N, 9.61; S, 7.33. Found: C, 49.65; H, 3.18; Fe, 6.40; N, 9.74; S, 7.35.

Synthesis of [Fe(bpyPY4)](OTf)₃

The synthetic procedure for the Fe(III) complex is equivalent to the one for [Fe(bpyPY4)](OTf)₂. In this case, the initial quantity of Fe(OTf)₃ was 0.78 g (0.760 mmol, 1 eq) and the initial quantity of bpyPY4 was 0.40 g (0.768 mmol, 1 eq). The obtained crystals were dark red/brown in color. Yield: 0.75 g (95%). Elem. anal. calcd for C₃₇H₂₈F₉FeN₆O₉S₃: C, 43.41; H, 2.76; Fe, 5.46; N, 8.21; S, 9.40. Found: C, 44.01; H, 2.89; Fe, 5.34; N, 9.15; S, 8.73.

Synthesis of formamidinium bromide (FABr)

In a 250 mL beaker, formamidinium acetate (18.41 g, 177 mmol, 1 eq) was dissolved in a 48% w/w solution of HBr in water (40 mL, 354 mmol, 2 eq). The solution was stirred at 50 °C for 1 h and the solvent was subsequently removed at 100 °C under a nitrogen stream to facilitate evaporation. The obtained solid was washed with diethyl ether and recrystallized twice from ethanol. The purification process yielded white crystals. The obtained powder was kept at 80 °C under high vacuum overnight to ensure complete dryness and then handled under inert atmosphere. Yield: 11.54 g (52%). ¹H NMR (400 MHz, MeOD-d₄): δ = 7.86 (s, 1H).

Conductivity measurements

Interdigitated array (IDA) microelectrodes were comprised of 65 gold electrode pairs spaced 10 μm apart on a quartz substrate. Each electrode finger was 5 μm wide, 2 mm long and 90 nm thick. A non-conducting passivation layer masked most of the substrate, exposing the 2 × 2 mm area of the IDA gold electrode pairs. Prior to use, IDA electrodes were thoroughly washed with acetonitrile and dried under a stream of nitrogen.

Inside a glove-box, equimolar solutions of [Fe(bpyPY4)](OTf)₂ and [Fe(bpyPY4)](OTf)_{2.9} were prepared by dissolving [Fe(bpyPY4)](OTf)₂ (43.7 mg, 50 mM) and [Fe(bpyPY4)](OTf)_{2.9} (51.2 mg, 50 mM) in acetonitrile (1 mL). Solutions of various compositions (from Fe²⁺ to Fe³⁺) were prepared by mixing the required amounts of the aforementioned solutions. For comparison with a standard hole-conducting material, a 10% oxidized spiro-OMeTAD solution in chlorobenzene was prepared following a previously described method.^{S2} Briefly, spiro-OMeTAD dissolved in dichloromethane was oxidized by reaction with an equimolar amount of Ag(OTf) to give spiro-OMeTAD(OTf) and Ag⁰. Silver was removed by filtration and spiro-OMeTAD(OTf) was purified *via* precipitation from the solution with diethyl ether. 10 mol % of spiro-OMeTAD(OTf) was added to the spiro-OMeTAD solution used for the experiments.

Solutions were drop-cast onto the electrode so that the film was covering both the interdigitated area and the surrounding passivation layer. IDAs coated with such thin films were then allowed to dry under nitrogen atmosphere inside the glove-box.

A Bio-Logic VSP potentiostat was used to record current-voltage characteristics of the two-probe IDA electrodes. The potential was cycled between -0.5 and $+0.5$ V at a scan rate of 0.10 V s^{-1} . Room temperature conductivity measurements were undertaken inside a glove-box. Conductivity measurements over the temperature range 10-300 K were performed using a physical property measurement system that uses liquid helium. Thin films on IDA electrodes were exposed for a very short time to air upon transferring and loading into the sample chamber of the cryostat. The sample chamber was purged with helium gas and sealed at atmospheric pressure, and measurements were undertaken starting at 300 K and cooling down in 10 or 5 K intervals.

The conductivities (σ) of the thin films were calculated from the slope of the acquired current-voltage curves by applying the relationship $\sigma = S/(d((2n-1)lh))$ [$S\ m^{-1}$] (where S is the slope of the linear fit to the experimental I - V data, d is the electrode spacing, n is the number of electrode pairs, l is the electrode length and h is the film thickness). The film thickness was measured using an optical profilometer on scratches engraved along both sides of the electrode area after acquiring the current-voltage data.

Solar cell preparation

Glass covered with fluorine-doped tin(IV) oxide (FTO) was patterned using a laser engraver (Universal Laser Systems, VLS3.50) and subsequently washed in three steps with a 1 vol % solution of Hellmanex in water, pure water and 96 vol % ethanol, each time under sonication (Elma, Elmasonic S300H) at 50 °C for 20 min. After the last cleaning step, the FTO substrates were dried under an air stream. A compact TiO_2 blocking layer (c- TiO_2) was deposited onto the FTO surface by spray pyrolysis, employing 2.8 mL of a titanium diisopropoxide bis(acetylacetonate) solution in isopropanol (1:9 vol.) and a substrate temperature of 475 °C. Prior to perovskite deposition, the FTO|c- TiO_2 substrates were further cleaned by ozone plasma for 10 min (Harrick Plasma, PDC-002; plasma intensity set to “high”; air pressure inside the chamber *ca* 1100 mTorr).

All further procedures were carried out in a glove-box under a high-purity nitrogen atmosphere with less than 0.1 ppm oxygen and water. The perovskite precursor solution (30 weight %) was prepared by dissolving FABr (52.3 mg) and $PbBr_2$ (153.6 mg) in *N,N*-dimethylformamide (470 μ L). After dissolution, a 47% w/w solution of HBr in water was added (23.4 μ L). The spiro-OMeTAD solution was prepared by dissolving spiro-OMeTAD (20.6 mg) in chlorobenzene (250 μ L). The $[Fe(bpyPY4)](OTf)_{2.5}$ solution was prepared by dissolving $[Fe(bpyPY4)](OTf)_2$ (21.9 mg) and $[Fe(bpyPY4)](OTf)_{2.9}$ (25.6 mg) in nitromethane (1 mL), giving a $Fe^{II}:Fe^{III}$ ratio of approximately 1:1. In the preliminary experiments, 4-*tert*-butylpyridine and lithium bis(trifluoromethanesulfonyl)imide were introduced into the

HTM solutions. However, further studies have indicated that the best performance of the solar cells based on both spiro-OMeTAD and [Fe(bpyPY4)](OTf)_{2+x} are achieved with additive-free HTM layers.

A ~1.2 cm² perovskite layer was deposited on the FTO|c-TiO₂ substrate by spin-coating 25 μL of the perovskite solution at 4000 rpm for 30 s with an acceleration of 4000 rpm s⁻¹. Upon 3 s of the spinning, a 380 kPa nitrogen flow was applied for 10 s.⁵³ The resulting film was annealed on a hotplate at 170 °C for 10 min. After cooling, a HTM layer was deposited by spin-coating either 25 μL of the spiro-OMeTAD solution at 3000 rpm for 30 s with an acceleration of 3000 rpm s⁻¹, or 18 μL of the [Fe(bpyPY4)](OTf)_{2.5} solution at 2000 rpm for 40 s with an acceleration of 200 rpm s⁻¹. As a final step, a 80 nm layer of Au was deposited by thermal evaporation (DDong DD-GCMO3CR; deposition started when vacuum reached 3×10⁻¹ Torr; deposition speed: 0.2 Å s⁻¹ between 0-50 Å, 1 Å s⁻¹ between 50-400 Å, 2.5 Å s⁻¹ between 400-800 Å).

Device encapsulation was performed under nitrogen atmosphere (glove-box) by dispensing UV-curable epoxy resin from Lumtec (LT-U001) onto the edges of a cover glass with a recess in the middle (purchased from HanaAMT). The glass was then gently pressed on the solar cell devices before being illuminated under UV light (2.5 mW cm⁻², peak intensity at 365 nm) for 12 min.

Characterization

NMR analysis was performed on a Bruker Avance III 400 equipped with an Ultrashield 400 Plus magnet.

High resolution mass spectroscopic analysis was performed on an Agilent 6220 Accurate Mass LC-TOF system with Agilent 1200 Series HPLC. The mass spectrometer was fitted with the Agilent Multimode Source. The reference compound used for reference mass correction was a purine/HP0921 mix. The syringe pump used for injection was a KD Scientific syringe pump running at 600 μL h⁻¹. ESI conditions: 8 L min⁻¹ N₂, 325° drying gas temperature; capillary voltage: 3500 V; fragmentor voltage: 160 V.

UV-Vis spectra were recorded on a PerkinElmer Lambda 950 spectrophotometer.

Photoluminescence spectra were recorded on a Horiba Jobin-Yvon FluoroMax-4 with an excitation wavelength of 380 nm and 4.3 nm slit aperture, using internal signal, blank and baseline corrections.

Mössbauer spectra were taken on a standard Wissel spectrometer operating in constant acceleration mode with data collection into 1024 channels. The ⁵⁷Co in Rh source and the absorber were kept at room temperature. Calibration was carried out using α-iron and all isomer shifts are quoted relative to α-iron at room temperature. The samples were sealed into perspex holders at a loading of 140 mg cm⁻². The spectra were least squares fitted to

doublets using Voigtian profiles, with corresponding members having the same intensity and linewidth.

X-ray diffraction (XRD) patterns of FTO, lead bromide and perovskite films were recorded on a Philips PW1130 X-ray diffractometer with Cu K α radiation at 2° min⁻¹ with 0.02° resolution. XRD patterns of the [Fe(bpyPY4)](OTf)_{2.5} films were recorded on a Bruker D2 Phaser X-ray diffractometer with Cu K α radiation ($\lambda = 1.54184 \text{ \AA}$) with 0.02° resolution. The drop-cast and spin-coated films were analyzed at 1.2 and 0.2° min⁻¹, respectively.

Photoelectron spectroscopy in air (PESA) measurements were conducted on a Riken Keiki AC-2 photoelectron spectrometer. The error in the ionization energies determined from the PESA measurements on a given sample was $\pm 0.05 \text{ eV}$.

Ultraviolet photoelectron spectroscopy (UPS) analysis was performed using an AXIS Ultra DLD spectrometer (Kratos Analytical Inc., Manchester, UK) with a helium discharge source optimized for He I radiation (21.22 eV), a hemispherical analyzer operating in the fixed analyzer transmission mode and the standard aperture (analysis area > 1 mm²). The total pressure in the main vacuum chamber during analysis was typically between 10⁻⁹ and 10⁻⁸ mbar. Each specimen was analyzed at an emission angle of 0° as measured from the surface normal and samples were biased at -2 V. The bias serves to facilitate the observation of the secondary electron cut-off from the UPS data by separating sample analyzer cut-offs and providing a higher secondary electron yield. Valence band spectra were acquired at a pass energy of 5 eV with a step width of 0.025 eV. The error in the ionization energies determined by UPS was estimated to be $\pm 0.1 \text{ eV}$.

Scanning electron microscopy (SEM) surface profile and cross-section images were recorded using a FEI Magellan 400 FEG microscope. Images were captured using an accelerating potential of 5 kV and a beam current of 6.3 pA. Cross-section samples were prepared by fracturing the complete solar cell devices. Energy dispersive X-ray (EDX) point analyses were performed using a FEI Nova NanoSEM 450 microscope fitted with a Bruker Quantax 400 X-ray analysis system. Analyses were performed using an accelerating potential of 5 kV and a spot size 6 at 20k magnification.

Current-voltage (J-V) characterization of the solar cells was performed using a Photo Emission Tech. model SS50AAA solar simulator with the current-voltage curves measured by a Bio-Logic VSP potentiostat. The intensity of the solar simulator was set using a calibrated silicon reference cell with a KG3 glass filter (PV Measurements, Inc.). The curves were recorded at a scan rate of 0.01 V s⁻¹ with a delay of 0.1 s from forward bias to the short circuit condition. Steady state current characterization was performed using the same solar simulator employed for the current-voltage characterization. The device was connected to a BioLogic VSP potentiostat to record the current at a fixed voltage taken from the maximum power point of the J-V curve over time every 0.1 s.

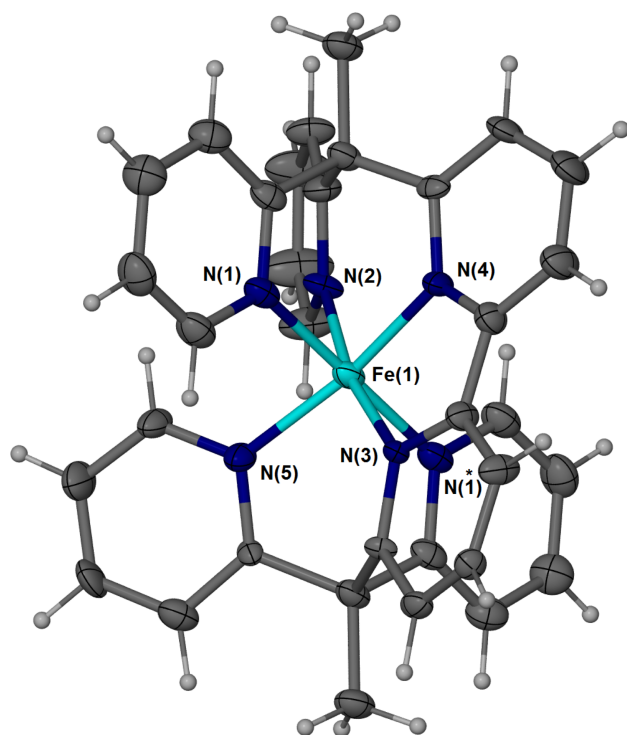
Incident photon-to-electron conversion efficiency (IPCE) spectra were measured by dispersing light from a 300 W xenon lamp through a monochromator (Oriel Cornerstone 260). The short-circuit current was recorded using a Keithley 2400 source measure unit. The system was calibrated with a calibrated photodiode (Peccell technologies).

Long-term stability measurements were conducted inside a Vötsch Atlas SC³ 340 environmental chamber equipped with a solar simulator. The chamber temperature was maintained at 25 °C (actual cell temperature was higher due to continuous irradiation) and the relative humidity inside the chamber was 20%. Solar cells were kept under constant 1 sun AM1.5G illumination for 120 h under open circuit condition. *J-V* curves for each cell were measured every 10 minutes. Light intensity fluctuations were monitored through the measurement of a reference Si solar cell and the maximum intensity variation during the experiment was within $\pm 2.5\%$ of the nominal value.

Electrochemical impedance spectroscopic measurements were performed under 27 mW cm^{-2} illumination provided by a 435 nm LED powered by a PP210 potentiostat. Spectra were recorded using a 10 mV perturbation at an applied potential of 400 and 700 mV for the [Fe(bpyPY4)](OTf)_{2.5} and spiro-OMeTAD-based devices, respectively. A Zahner Zennium electrochemical workstation ECW IM6 was used as a frequency response analyzer, and impedance measurements were performed in the 4 MHz to 1 Hz frequency range. Impedance data were analyzed using Zview equivalent circuit modeling software (Scribner).

Results

Single crystal XRD details for $[\text{Fe}(\text{bpyPY4})](\text{OTf})_2$ and $[\text{Fe}(\text{bpyPY4})](\text{OTf})_3$



Crystal data for $[\text{Fe}(\text{bpyPY4})](\text{OTf})_2$

Crystal composition: $[\text{Fe}(\text{bpyPY4})](\text{OTf})_2$

Crystal system, space group: Triclinic, P-1

Unit cell dimensions: $a = 8.3101(3) \text{ \AA}$ $\alpha = 114.636(4) \text{ deg}$

$b = 10.4017(3) \text{ \AA}$ $\beta = 95.979(3) \text{ deg}$

$c = 11.6371(5) \text{ \AA}$ $\gamma = 98.975(3) \text{ deg}$

Crystal data for $[\text{Fe}(\text{bpyPY4})](\text{OTf})_3$

Crystal composition: $[\text{Fe}(\text{bpyPY4})](\text{OTf})_3 \cdot \text{MeCN}$

Crystal system, space group: Monoclinic, $P2_1/n$

Unit cell dimensions: $a = 18.2511(10) \text{ \AA}$ $\alpha = 90 \text{ deg}$

$b = 13.9494(5) \text{ \AA}$ $\beta = 117.614(7) \text{ deg}$

$c = 19.6316(10) \text{ \AA}$ $\gamma = 90 \text{ deg}$

Figure S1. Structure of $[\text{Fe}(\text{bpyPY4})]^{2+}$ with 50% thermal ellipsoids; geometry inferred by single crystal X-ray analysis. Crystal data for $[\text{Fe}(\text{bpyPY4})](\text{OTf})_2$ and $[\text{Fe}(\text{bpyPY4})](\text{OTf})_3$. The complete data refinements for both $[\text{Fe}(\text{bpyPY4})](\text{OTf})_2$ and $[\text{Fe}(\text{bpyPY4})](\text{OTf})_3$ are given in the tables in the Appendix B.

XRD patterns of $[\text{Fe}(\text{bpyPY4})](\text{OTf})_{2.5}$ films

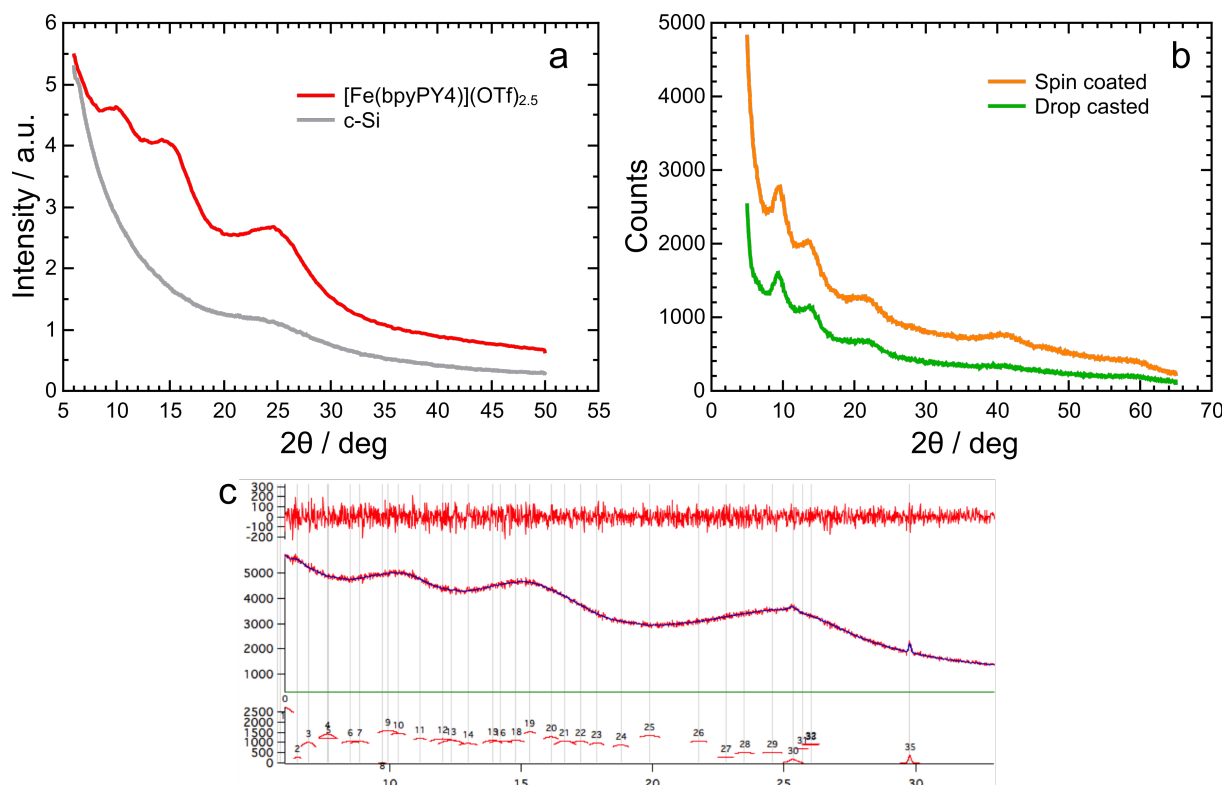
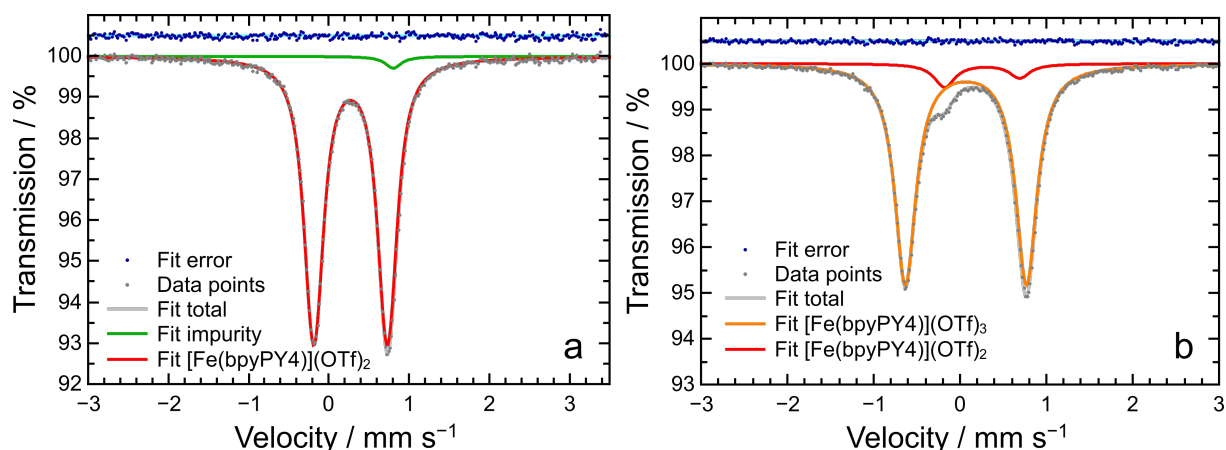


Figure S2. X-ray diffraction analysis of the thin $[\text{Fe}(\text{bpyPY4})](\text{OTf})_{2.5}$ films. (a) Grazing angle X-ray diffractogram (GAXRD) of a $0.95 \mu\text{m}$ thick film spin-coated onto a single crystalline Si substrate (red). The gray curve shows the diffractogram of an uncoated substrate. (b) XRD patterns of films deposited by drop-casting (green) and spin-coating (orange). (c) Fitting of the GAXRD pattern from panel a using the single-crystal data for $[\text{Fe}(\text{bpyPY4})](\text{OTf})_2$ with peak broadening defined by Sherrer equation and crystallite sizes ranging from 30 nm to sub-nanometer scale.

Mössbauer spectroscopy



Sample	χ^2	Ferric doublet				Ferrous doublet				
		δ [mm s ⁻¹]	Δ [mm s ⁻¹]	Γ [mm s ⁻¹]	Area [%]	δ [mm s ⁻¹]	Δ [mm s ⁻¹]	Asym. A(L)/A(R)	Γ [mm s ⁻¹]	Area [%]
Fe[bpyPY4](OTf) ₃	0.504	0.07(1)	1.40(1)	0.31(1)	92.2	0.26(1)	0.86(2)	1.67(7)	0.29(1)	7.8
Fe[bpyPY4](OTf) ₂	0.675					0.27(1)	0.92(1)		0.31(1)	98.1

Figure S4. Mössbauer spectra of (a) $[\text{Fe}(\text{bpyPY4})](\text{OTf})_2$ and (b) $[\text{Fe}(\text{bpyPY4})](\text{OTf})_3$, with voigtian fitting of two populations. For both images, the fit error is the difference between the value of the total fitting line and the data point at each velocity value, centered on a line at 100.5% transmission for easiness of plotting. The spectrum of $[\text{Fe}(\text{bpyPY4})](\text{OTf})_2$ shows a doublet corresponding to the Fe(II) complex (red) and a singlet corresponding to an impurity (1.9 atom %, green). The spectrum of $[\text{Fe}(\text{bpyPY4})](\text{OTf})_3$ shows a symmetric doublet corresponding to the Fe(III) complex (orange) and an asymmetric doublet corresponding to the Fe(II) complex (red); the asymmetry is attributed to crystal field effects. The table lists all main parameters for the Fe(II) and Fe(III) doublets in each sample. δ – isomer shift; Δ – quadrupole splitting; Γ – linewidth; Asym. – asymmetry of the doublet given as the ratio of the areas of the left and right peaks; Area – total area of the doublet.

UV-Vis absorbance

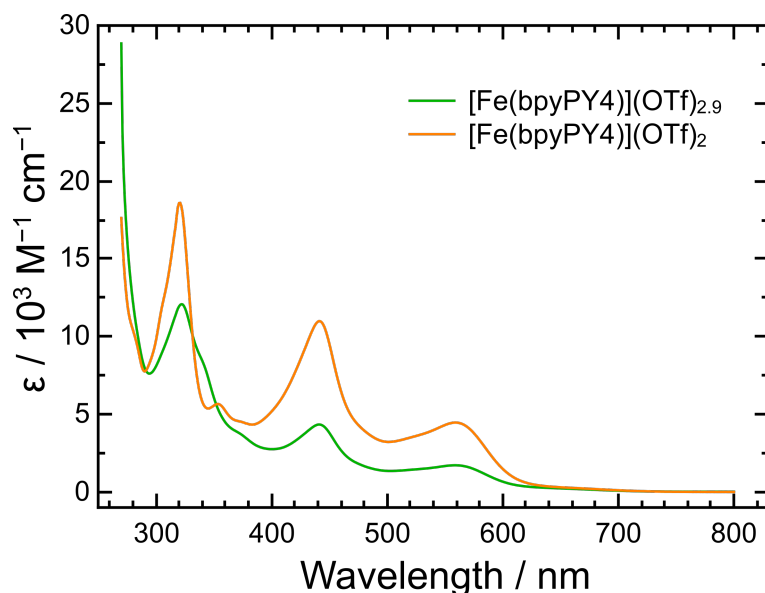


Figure S3. UV-Vis spectra of $[\text{Fe}(\text{bpyPY4})](\text{OTf})_2$ (orange) and $[\text{Fe}(\text{bpyPY4})](\text{OTf})_{2.9}$ (green) measured in acetonitrile at room temperature, indicating the molar extinction coefficient.

Conductivity

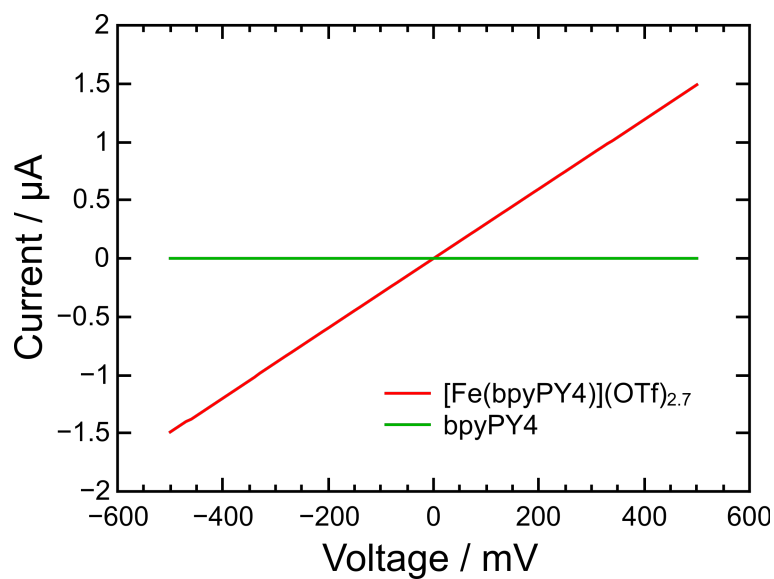


Figure S5S5. Room temperature current-voltage curve for the $[\text{Fe}(\text{bpyPY4})](\text{OTf})_{2.7}$ (red) and bpyPY4 (green) thin films drop-cast onto an IDA electrode.

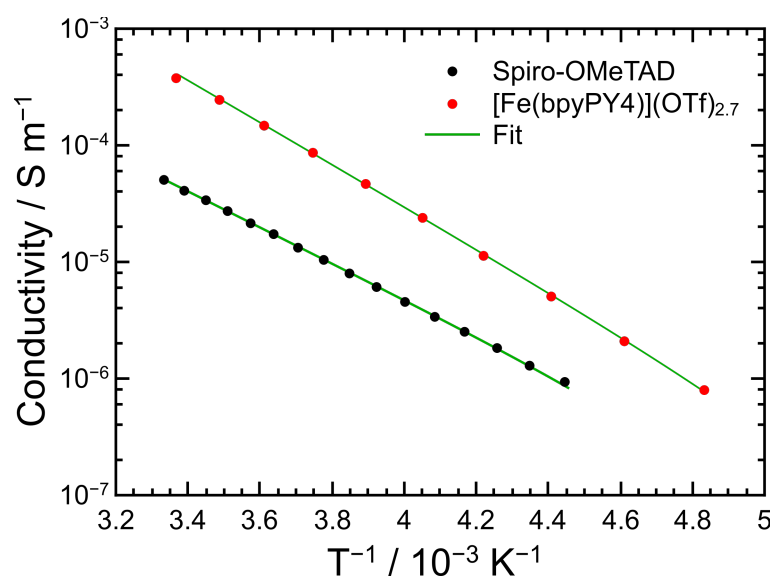


Figure S6. Arrhenius plot of the conductivity of the $[\text{Fe}(\text{bpyPY4})](\text{OTf})_{2.7}$ (red) and 10% oxidized spiro-OMeTAD (black) thin films drop-cast onto IDA electrodes.

Cyclic voltammetry

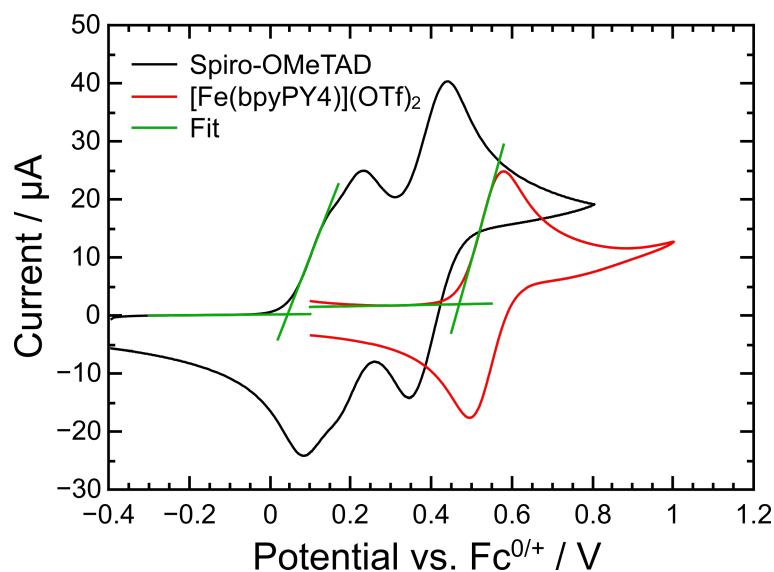


Figure S7. Cyclic voltammograms (scan rate 0.1 V s^{-1}) obtained with a gold electrode (3 mm diameter) for oxidation of 2.3 mM spiro-OMeTAD in acetonitrile:chlorobenzene 3.38:1 vol. ($0.077 \text{ M n-Bu}_4\text{NPF}_6$) (black) and 3 mM $[\text{Fe}(\text{bpyPY}4)](\text{OTf})_2$ in acetonitrile ($0.1 \text{ M n-Bu}_4\text{NPF}_6$) (red). Measurements were undertaken inside a nitrogen-filled glove-box. Green lines show the estimated oxidation onsets.

Photoelectron spectroscopy in air

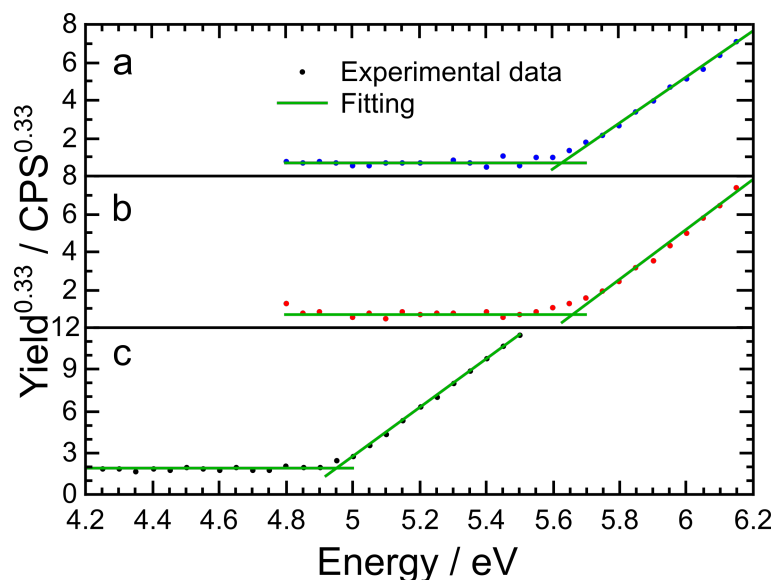


Figure S8. PESA measurements for the (a) FAPbBr₃, (b) $[\text{Fe}(\text{bpyPY}4)](\text{OTf})_{2.5}$ and (c) spiro-OMeTAD spin-coated films. FAPbBr₃ was deposited on FTO/c-TiO₂, while $[\text{Fe}(\text{bpyPY}4)](\text{OTf})_{2.5}$ and spiro-OMeTAD were deposited on FTO/c-TiO₂/FAPbBr₃. Green lines show linear fits used to derive $E_{\text{VB}}/\text{HOMO}$.

Ultraviolet photoelectron spectroscopy

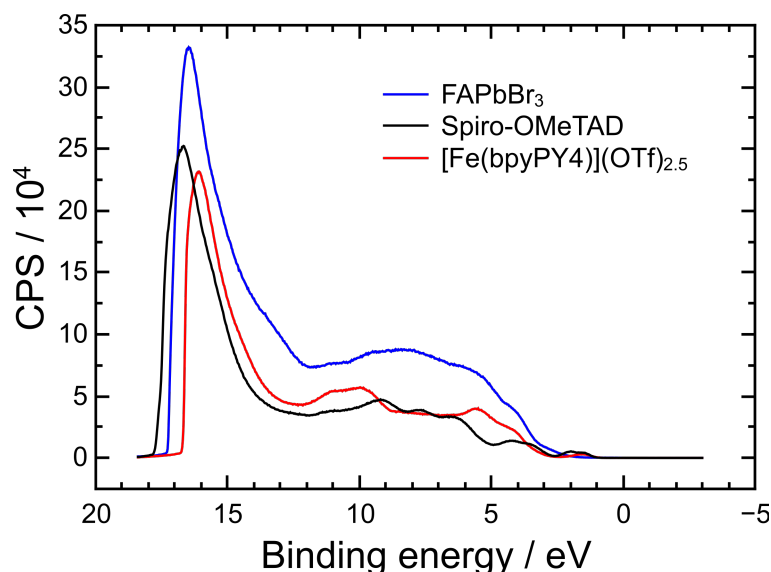


Figure S9. UPS data for the spin-coated FAPbBr₃ (blue), spiro-OMeTAD (black) and [Fe(bpyPY4)](OTf)_{2.5} (red) films. As a support, a compact TiO₂ layer on FTO was used for FAPbBr₃, while HTMs were deposited on FTO|c-TiO₂|FAPbBr₃.

Energy levels

Table S1. Highest occupied molecular orbital (HOMO) positions for [Fe(bpyPY4)](OTf)_{2.5} and spiro-OMeTAD and valence band edge (E_{VB}) energy level and band gap for FAPbBr₃. All values are referred to vacuum.

Material	HOMO (eV)	HOMO/ E_{VB} (eV)		E_g (eV)
	(Voltammetry) ^a	(UPS) ^b	(PESA) ^b	(Tauc) ^c
FAPbBr ₃		-5.83	-5.62	2.28
[Fe(bpyPY4)](OTf) _{2.5}	-5.57	-5.46	-5.67	
spiro-OMeTAD	-5.14	-4.69	-4.95	

(a) Calculated using the onset of the first oxidation peak (shown in Figure S7) assuming that the formal potential of the Fc^{0/+} redox couple is 5.1 eV.^{S4} (b) Derived from the data shown in Figures S8 and S9. (c) Derived from the Tauc plot exemplified in Figure S10.

UV-Vis spectrum and Tauc plot for FAPbBr₃

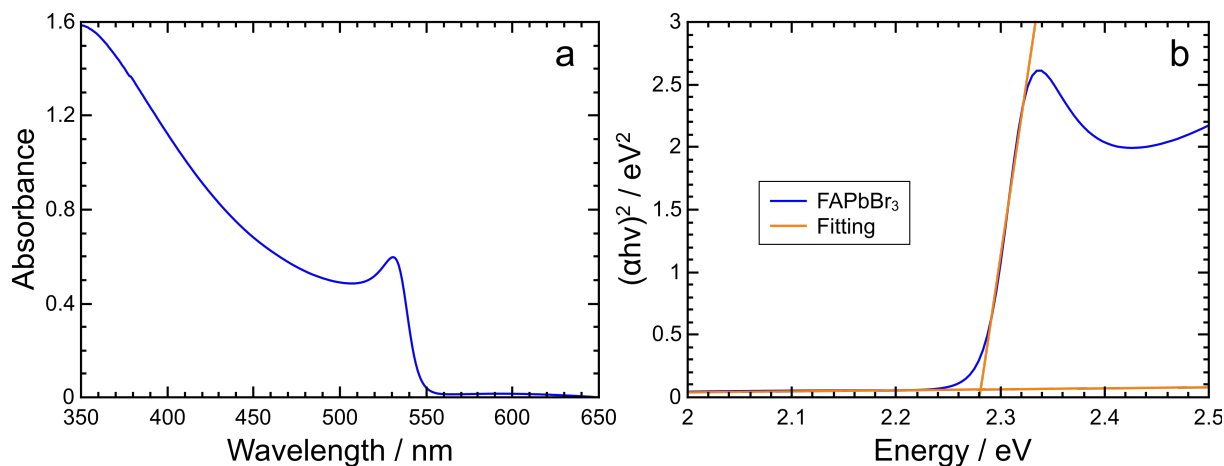


Figure S10. (a) UV-Vis absorption spectrum of the FAPbBr₃ perovskite film spin-coated on glass. (b) Tauc plot constructed using the data in panel a (blue) and linear fit used to derive E_g (orange).

Photoluminescence quenching

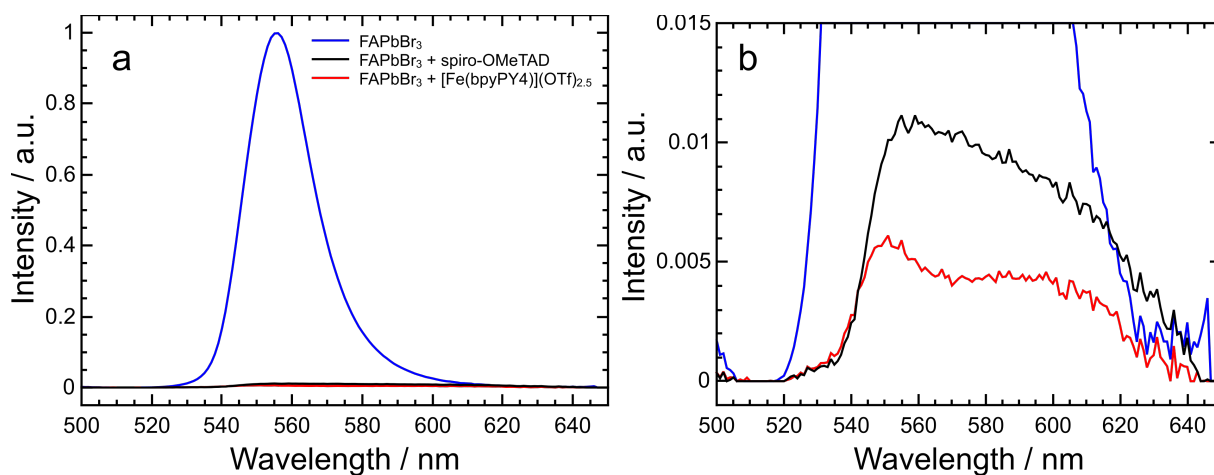


Figure S11. Photoluminescence spectra of the FAPbBr₃ film spin-coated on a glass substrate without (blue) and with the spiro-OMeTAD (black) or [Fe(bpyPY4)](OTf)_{2.5} (red) films deposited on top. Illumination was from the glass side. Data are normalized to the peak value for the unmodified FAPbBr₃ film. Panels **a** and **b** show full and low intensity ranges of the ordinate axis, respectively.

Cross-sectional SEM images

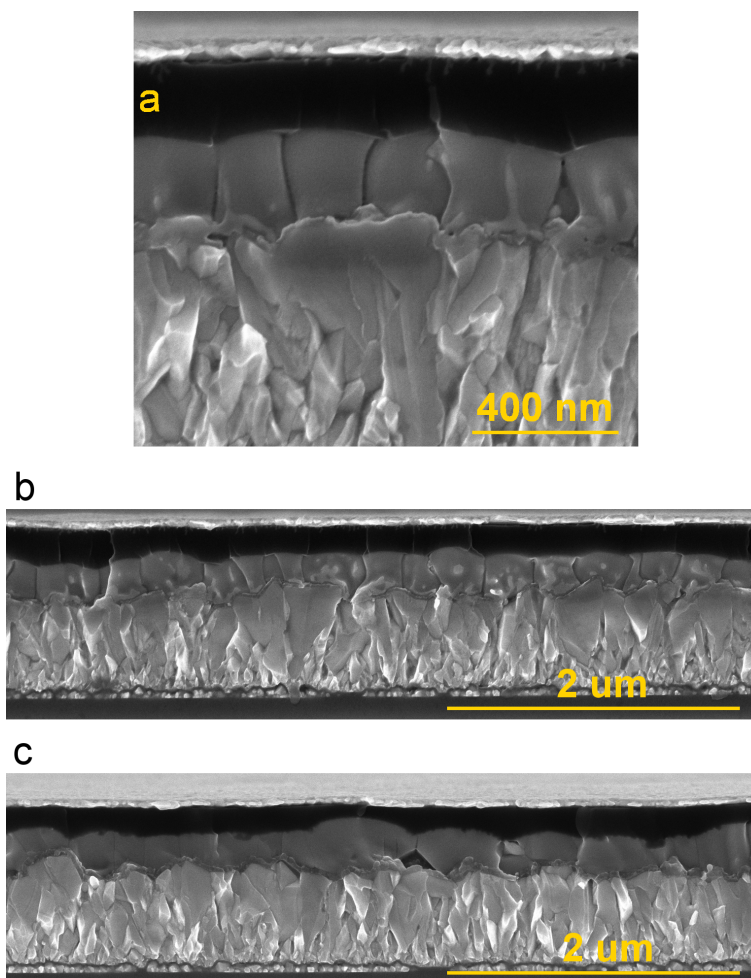


Figure S12. Cross-sectional SEM images of the FTO/c-TiO₂/FAPbBr₃/HTM/Au devices based on the (a, b) spiro-OMeTAD and (c) [Fe(bpyPY4)](OTf)_{2.5} HTM.

Surface SEM images and composition of FAPbBr₃

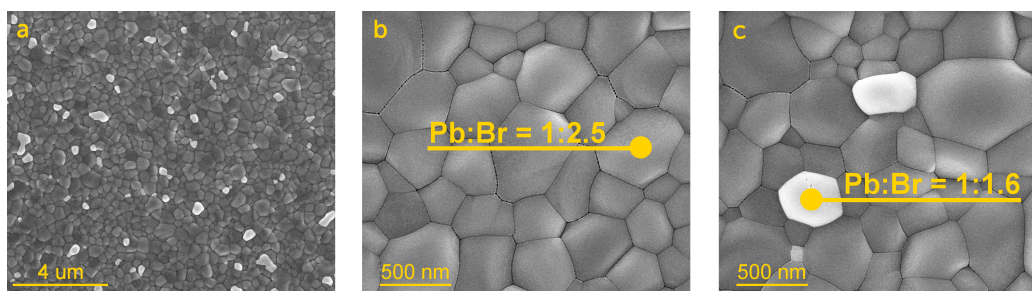


Figure S13. (a) Lower (20k \times) and (b, c) higher (120k \times) magnification SEM images of the FAPbBr₃ perovskite surface. The lighter-colored grains are comprised of PbBr₂. In panels **b** and **c**, the atomic Pb:Br ratios were derived from the energy dispersive X-ray analysis (EDX) centered on the areas marked with circles. Note that EDX is not a fully quantitative analytic method. Furthermore, the size of the PbBr₂ grains is notably smaller than the depth and breadth of the point EDX analysis under employed conditions, which results in a lower than expected Pb:Br ratio. The slight inconsistency of the EDX results obtained for the FAPbBr₃ grains with the expected stoichiometry is due to damage of the perovskite by the electron beam.

XRD patterns for FAPbBr₃ and PbBr₂ films

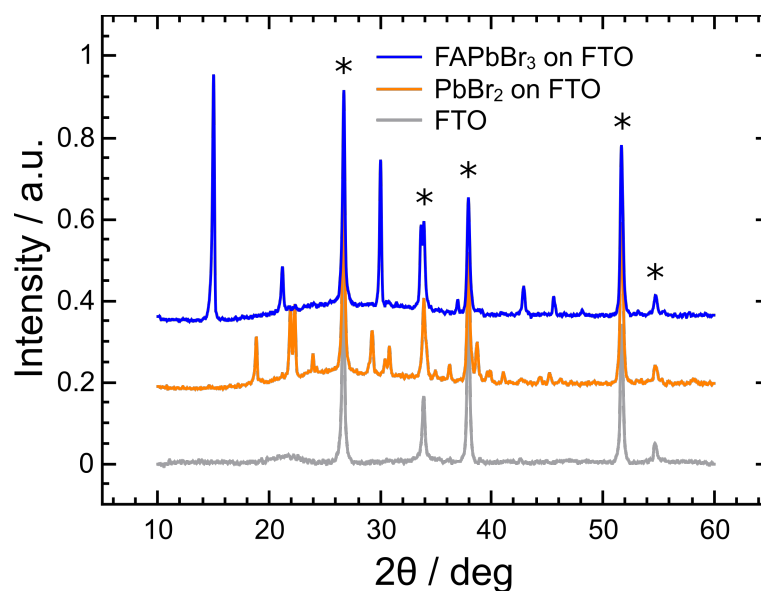


Figure S14. XRD patterns of bare FTO (gray), and FTO modified with FAPbBr₃ (blue) or PbBr₂ (orange) films. No PbBr₂ peaks are detected for the perovskite film. The * symbols show peaks corresponding to the FTO substrate.

Quasi-steady-state power measurement

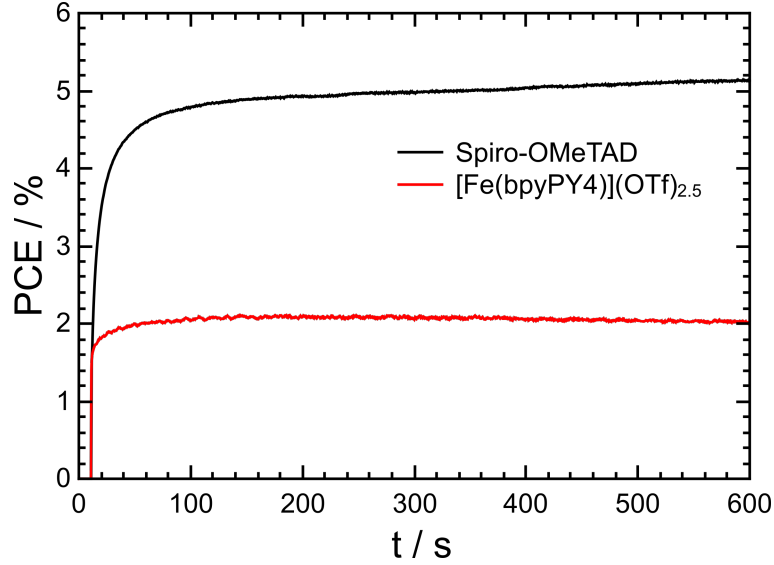


Figure S15. Maximum-power-point PCE transients measured under 1 sun AM1.5G irradiation for the best-performing spiro-OMeTAD-based (applied voltage 926 mV) and [Fe(bpyPY4)](OTf)_{2.5}-based (applied voltage 529 mV) solar cells.

Complete J - V scan data

Table S2. Complete list of photovoltaic parameters^a for FAPbBr₃ perovskite solar cells with different HTMs under 1 sun AM1.5G irradiation.

Hole transporting material	V_{OC} (mV)	J_{SC} (mA cm ⁻²)	FF (%)	PCE (%)
Spiro-OMeTAD (best, SC → FB)	1368	6.6	48	4.3
Spiro-OMeTAD (best, FB → SC)	1308	6.6	60	5.2
Spiro-OMeTAD (average, SC → FB)	1310 ± 50	6.4 ± 0.3	50 ± 4	4.2 ± 0.3
Spiro-OMeTAD (average, FB → SC)	1290 ± 40	6.3 ± 0.4	61 ± 6	4.9 ± 0.4
[Fe(bpyPY4)](OTf) _{2.5} (best, SC → FB)	855	6.0	42	2.2
[Fe(bpyPY4)](OTf) _{2.5} (best, FB → SC)	889	6.0	50	2.7
[Fe(bpyPY4)](OTf) _{2.5} (average, SC → FB)	760 ± 60	6.1 ± 0.3	42 ± 2	2.0 ± 0.3
[Fe(bpyPY4)](OTf) _{2.5} (average, FB → SC)	820 ± 60	6.1 ± 0.2	47 ± 2	2.4 ± 0.3

(a) Derived from the J - V curves (scan rate = 10 mV s⁻¹) for seven spiro-OMeTAD-based and 15 [Fe(bpyPY4)](OTf)_{2.5}-based devices. V_{OC} , open-circuit voltage; J_{SC} , short-circuit current density; FF , fill factor; SC, short circuit; FB, forward bias.

FTO|TiO₂|[Fe(bpyPY4)](OTf)_{2.5}|Au diode

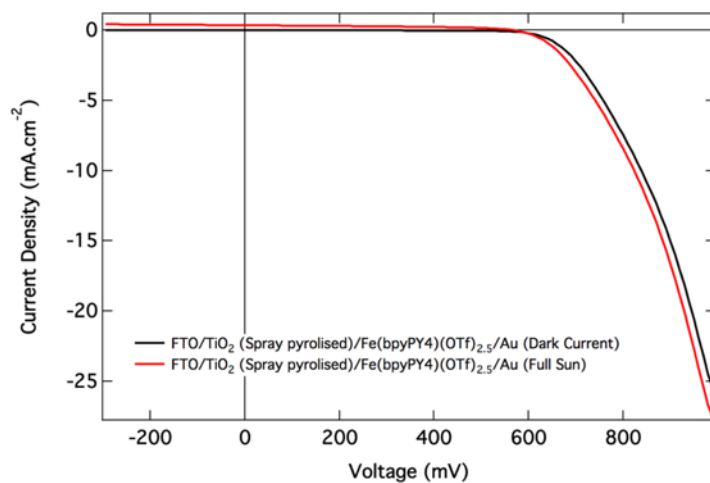


Figure S16. J-V characterization of the FTO|c-TiO₂|[Fe(bpyPY4)](OTf)_{2.5}|Au diode, showing good rectifying properties of Fe(bpyPY4)](OTf)_{2.5} and no electron injection under 1 sun irradiation. The small photocurrent (ca 300 μA cm⁻² at -0.3 V) is generated by titania as confirmed in control experiments undertaken with no Fe(bpyPY4)](OTf)_{2.5} present.

Long-term stability

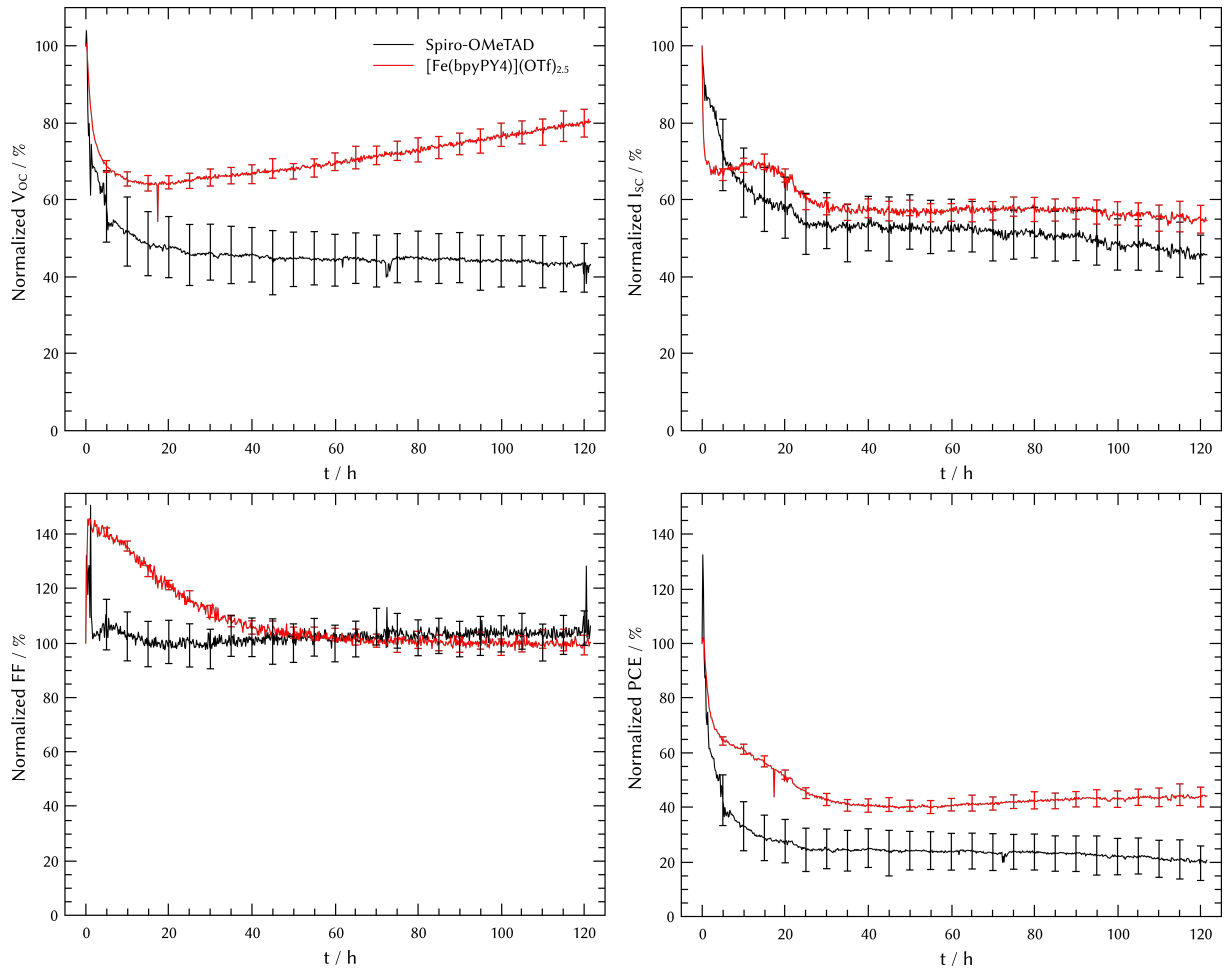


Figure S17. Evolution of the photovoltaic parameters of encapsulated FAPbBr₃-based planar solar cells fabricated with Spiro-OMeTAD (black) or [Fe(bpyPY4)](OTf)_{2.5} (red) as a HTM under continuous 1 sun irradiation at 25 °C (actual cell temperature was higher due to continuous irradiation) and 20% relative humidity. Curves represent average values for five devices; standard deviation error bars are shown every 30 experimental points for clarity. All parameters are normalized to the corresponding initial values at $t = 0$.

Electrochemical impedance spectroscopy

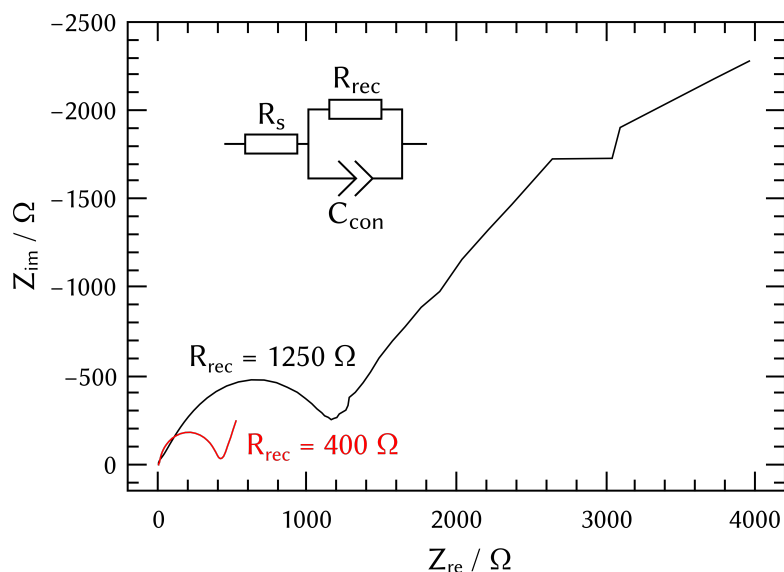


Figure S18. Nyquist impedance spectra for FTO|c-TiO₂|FAPbBr₃|HTM|Au devices with spiro-OMeTAD (black) or [Fe(bpyPY₄)](OTf)_{2.5} (red) as an HTM. Measurements were performed under illumination (27 mW cm⁻²) with an applied potential of 700 mV for the device with spiro-OMeTAD and of 400 mV for the device with [Fe(bpyPY₄)](OTf)_{2.5}, in the frequency range 1 Hz – 4 MHz. The recombination resistance (R_{rec}) was calculated by fitting the semicircle in the middle frequency range ($50 < Z_{\text{re}} < 1200 \Omega$ for spiro-OMeTAD and $15 < Z_{\text{re}} < 400 \Omega$ for [Fe(bpyPY₄)](OTf)_{2.5}) to the simplified version of the equivalent circuit introduced by Pascoe et al.^{S5} (R_s - series resistance; C_{con} - constant phase shift element used to simulate capacitive behavior at the interface). R_{rec} does not contribute to the low frequency range, which facilitates analysis of the data based on the equivalent circuit shown in the figure.

References

- (S1) Kashif, M. K.; Nippe, M.; Duffy, N. W.; Forsyth, C. M.; Chang, C. J.; Long, J. R.; Spiccia, L.; Bach, U. Stable Dye-Sensitized Solar Cell Electrolytes Based on Cobalt(II)/(III) Complexes of a Hexadentate Pyridyl Ligand. *Angew. Chem. Int. Ed.* **2013**, *52* (21), 5527–5531.
- (S2) Cappel, U. B.; Daeneke, T.; Bach, U. Oxygen-Induced Doping of Spiro-MeOTAD in Solid-State Dye-Sensitized Solar Cells and Its Impact on Device Performance. *Nano Lett.* **2012**, *12* (9), 4925–4931.
- (S3) Huang, F.; Dkhissi, Y.; Huang, W.; Xiao, M.; Benesperi, I.; Rubanov, S.; Zhu, Y.; Lin, X.; Jiang, L.; Zhou, Y.; et al. Gas-assisted preparation of lead iodide perovskite films consisting of a monolayer of single crystalline grains for high efficiency planar solar cells. *Nano Energy* **2014**, *10*, 10–18.
- (S4) Cardona, C. M.; Li, W.; Kaifer, A. E.; Stockdale, D.; Bazan, G. C. Electrochemical Considerations for Determining Absolute Frontier Orbital Energy Levels of Conjugated Polymers for Solar Cell Applications. *Adv. Mater.* **2011**, *23* (20), 2367–2371.
- (S5) Pascoe, A. R.; Duffy, N. W.; Scully, A. D.; Huang, F.; Cheng, Y.-B. Insights into Planar CH₃NH₃PbI₃ Perovskite Solar Cells Using Impedance Spectroscopy. *J. Phys. Chem. C* **2015**, *119* (9), 4444–4453.

3. Influence of the counter-ion on the hole transporting properties of metal complexes

3.1. The long journey there

I have attempted several synthetic pathways to obtain the ligand 2,5-di(pyridin-2-yl)pyrrole (py₂pz, Figure 19) for the preparation of the neutral cobalt(II) complex designed as a new HTM. Initially, following the work of Bakkali *et al.*,^[216] electrosynthesis was performed to reduce pyridazine to pyrrole. This process is very interesting as its first step involves a Diels-Alder cycloaddition of a tetrazine with an alkene. Thereby, depending on the alkene used for the reaction, different functionalities can be easily attached to the final central pyrrole of the ligand. The yield for the electrosynthesis reported in the paper was very high (82%) but, due to differences in the electrochemical cell and setup available to us and those used in Ref. [216], together with the bigger scale of my synthesis, I could only achieve a 7% conversion. In the same paper, the authors report a second method for the reduction of pyridazine, based on chemical redox reaction with zinc powder. Although the final conditions optimised by me to improve the yield (room temperature, 2.5 eq Zn, 2 h) were quite different compared to those reported in the paper, the final conversion yield – 22% – was similar. Due to the expensiveness of the initial tetrazine, a 22% conversion yield in the second step was considered too low to be affordable. The synthetic pathway chosen for the ligand synthesis – described in the coming chapter – is less flexible in terms of modifications possible on the central pyrrole functionality and requires one additional reaction step compared to that reported in Ref. [216]. However, it can yield large quantities of the product starting from inexpensive reagents.

Having already investigated a metal complex with a hexadentate ligand and an iron metal centre (see chapter 2), I aimed to further study complexes based on different metal ions to broaden the range of examined hole transporting materials. A suitable metal centre should have relatively stable 2+ and 3+ oxidation forms and only few transition metals comply with this requirement. Cobalt was initially not considered, since its complexes decompose the MAPbI₃ perovskite, as concluded in the previous chapter. A complex with the hexadentate ligand and a nickel metal centre was synthesised but its reversible potential was too positive to be successfully employed in perovskite solar cells. An attempt to synthesise a complex with the hexadentate ligand and a manganese metal centre was also made. However, while manganese easily complexates with bipyridyl and trispyridyl ligands, virtually no complexation occurred with the hexadentate ligand. Finally, iron did not complexate with the py₂pz ligand designed to form the neutral complex. Thus, as a last attempt to find a suitable metal complex/perovskite combination, the deposition of the cobalt hexadentate complex was tested on the mixed cation perovskite ((Rb_{0.05}Cs_{0.05}FA_{0.75}MA_{0.15})Pb(I_{0.85}Br_{0.15})₃). Unlike MAPbI₃, this new perovskite material was not degraded by the complex. Therefore, complexes featuring a cobalt metal centre were used for the present study.

3.2. Introduction

Charge transport properties are fundamental for materials used in energy applications. In the case of solid-state redox-active metal complexes, charges move through the layer by hopping from complex to complex – *i.e.* from cation to cation. In order to balance the charges, a metal complex can have several counter-ions. As an example, the HTM layer of the iron complex studied in chapter 2 presented 2.5 triflate anions per complex ion. The triflate ion does not contribute to the transport of holes from the perovskite layer to the counter electrode and has the side-effect of distantiating the cations, potentially hindering the charge transport process. For this reason, a metal complex that is neutral in its reduced form and only possesses one counter-ion in its oxidised form might provide advantageous hole transporting properties as compared to a complex with the hexadentate ligand and two counter-ions in its reduced form employed in our previous study.^[217] Complex neutrality can be achieved by employing a negatively charged ligand, which counter-balances the positive charge of the metal centre. In order to balance a doubly-charged metal ion, two negatively charged ligands are required, suggesting the need for tridentate ones. The smallest modification that can be made to a tridentate pyridyl ligand in order to make it negatively charged is to replace the middle pyridine with a pyrrole. The pyrrole moiety can be easily deprotonated by removing the slightly acidic proton attached to the central nitrogen atom. On the basis of the above, the ligand chosen for this study was 2,5-di(pyridin-2-yl)pyrrole (py_2pz), which is depicted in Figure 19 together with the hexadentate ligand bpyPY4 , already employed in chapter 2, to which the former is compared.

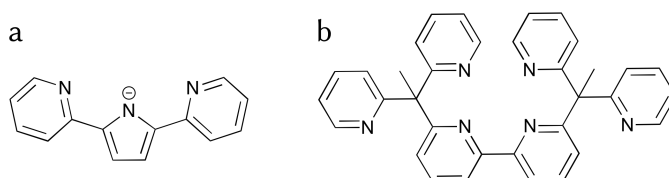


Figure 19. Structures of (a) the deprotonated 2,5-di(pyridin-2-yl)pyrrole (py_2pz) ligand and (b) the 6,6'-bis(1,1-di(pyridin-2-yl)ethyl)-2,2'-bipyridine (bpyPY4) ligand.

For the new complex, assuming a 1:1 ratio of reduced to oxidised species in the final film, only 0.5 counter-ions will be present per redox couple, as opposed to the 2.5 for the complex based on bpyPY4 . The metal centre chosen for the study is cobalt. This metal possesses relatively stable 2+ and 3+ oxidation forms and is known to complexate with both bpyPY4 ^[213] and py_2pz ^[218] ligands. Although the same HOMO level should not be expected for the two complexes, differences in V_{OC} in the final PSCs can be compared to the differences in the relevant energy levels, while the conductivity can be directly compared between the two.

The perovskite chosen for this study is one with a high degree of ion mixing, namely $(\text{Rb}_{0.05}\text{Cs}_{0.05}\text{FA}_{0.75}\text{MA}_{0.15})\text{Pb}(\text{I}_{0.85}\text{Br}_{0.15})_3$ (MixCP). This perovskite is impervious to the contact with the $[\text{Co}(\text{bpyPY4})](\text{OTf})_2$ complex – unlike MAPbI_3 – which was the major reason for

employing it in the present study. The MixCP is a recently developed perovskite composition, which was presented for the first time by Saliba *et al.* in late 2016.^[219] This highly mixed cation material was proven to be very stable in the long-term even at high temperatures and devices based thereon reached PCEs in excess of 21%. Herein, the perovskite layer for the PSCs was kindly deposited by Dr. Jinbao Zhang (Monash University), to whom go my gratitude and all the credit.

3.3. Results and discussion

3.3.1. Ligands and complexes synthesis and characterisation

The synthesis of the bpyPY4 ligand has been discussed in detail in chapter 2 and the synthesis of $[\text{Co}(\text{bpyPY4})](\text{OTf})_2$ is also equivalent to that of $[\text{Fe}(\text{bpyPY4})](\text{OTf})_2$, with a conversion yield of 77%. The synthesis of py_2pz and of the related cobalt complex $[\text{Co}(\text{py}_2\text{pz})_2]$ is based on a paper by Cizek *et al.*^[218] and is outlined in Figure 20. Comprehensive description of the procedures used is provided in section 6.2, while key aspects of the synthesis are briefly summarised as follow. The synthesis of the ligand involved three steps and only the second one required harsher reaction conditions, such as the use of a superbases to lithiate 2-bromopyridine. Furthermore, the product obtained at the first step of synthesis was purified with a simple distillation – without the need for a chromatographic column – making the complete procedure even more facile. All three steps involved inexpensive precursors only.

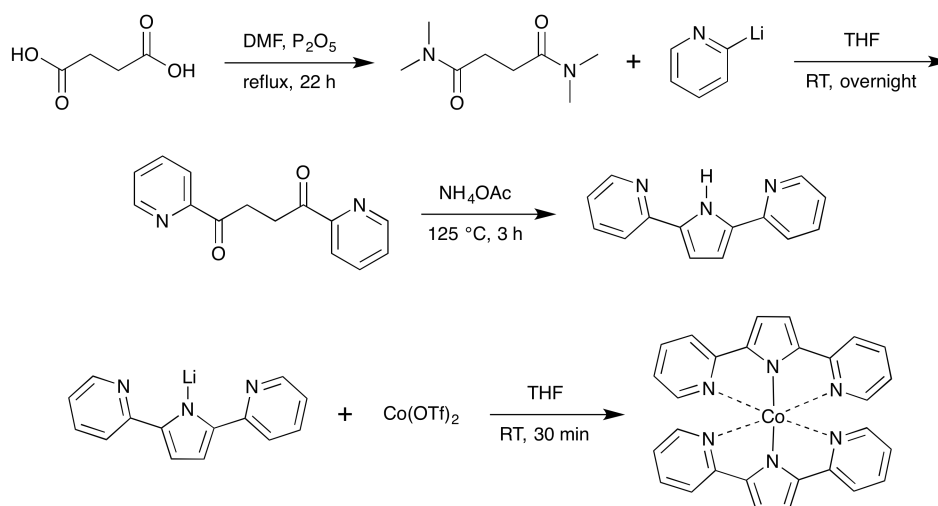


Figure 20. Reaction schemes for the syntheses of the py_2pz ligand and the $[\text{Co}(\text{py}_2\text{pz})_2]$ complex.

The synthesis of the final cobalt(II) complex again required the use of a superbases (*n*-butyllithium) in order to deprotonate the pyrrole, whose proton is only very slightly acidic. Upon addition of the cobalt(II) salt, the complexation was almost instantaneous, denoted by a colour change in the solution from yellow to red. A high conversion yield of 81% after purification of the product confirmed that the complexation is energetically favoured. The synthesis of $[\text{Co}(\text{bpyPY4})](\text{OTf})_3$ and $[\text{Co}(\text{py}_2\text{pz})_2](\text{OTf})$ was conducted

following the same procedure, namely *via* one-electron oxidation of the Co(II) species of the relevant metal complex with Ag(OTf). The conversion yields for [Co(bpyPY4)](OTf)₃ and [Co(py₂pz)₂](OTf) were 90% and 94%, respectively. Single crystal XRD (sc-XRD) data for [Co(bpyPY4)](OTf)₂ and [Co(bpyPY4)](OTf)₃ have already been published by Kashif *et al.*^[213] Sc-XRD analysis of [Co(py₂pz)₂] suggests that the compound crystallises with an orthorhombic lattice and a *P2₁2₁2₁* space group. In this configuration, two complex cations occupy slightly different positions in the crystal lattice. [Co(py₂pz)₂](OTf) crystallised with a tetragonal lattice and a *P4₁* space group, with ½MeCN (inferred by NMR spectroscopy) as crystallisation solvent. Despite repeated measurements, it was not possible to correctly model the anion and the solvent molecule based on the results of the XRD analysis, while the cation was well resolved. Molecular structures of the two different [Co(py₂pz)₂] cations and of [Co(py₂pz)₂](OTf) are depicted in Figure 21, while full sc-XRD refinements for both are reported in Appendix B.

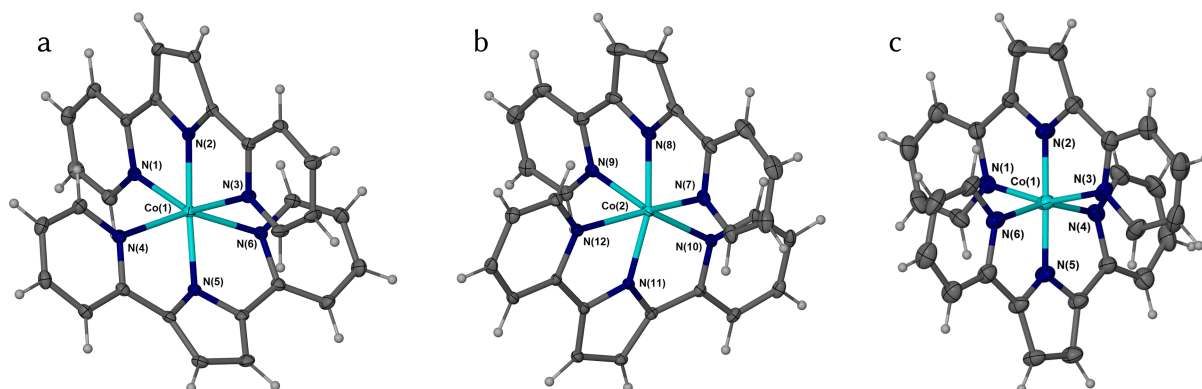


Figure 21. Molecular structures of (a, b) [Co(py₂pz)₂] and (c) [Co(py₂pz)₂](OTf) with 50% thermal ellipsoids as inferred by sc-XRD analysis.

Normalised UV-Vis spectra for all the complexes involved in the study, namely [Co(py₂pz)₂], [Co(py₂pz)₂](OTf), [Co(bpyPY4)](OTf)₂ and [Co(bpyPY4)](OTf)₃ are compared in Figure 22. Solutions of both Co(II) species were red, while those of Co(III) species were yellow.

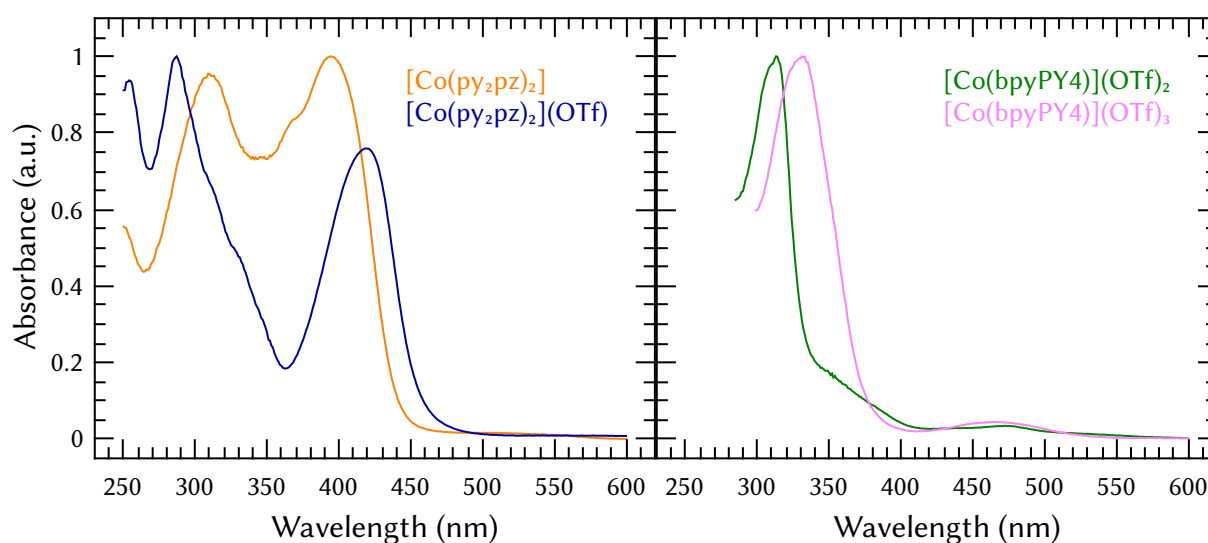


Figure 22. Normalised UV-Vis spectra of the solutions of [Co(py₂pz)₂] (orange) in chloroform and of [Co(py₂pz)₂](OTf) (blue), [Co(bpyPY4)](OTf)₂ (green) and [Co(bpyPY4)](OTf)₃ (magenta) in acetonitrile.

Molar extinction coefficients (ϵ) were estimated on the basis of the UV-Vis absorption data presented in Figure 22. For $[\text{Co}(\text{py}_2\text{pz})_2]$, ϵ is estimated to be $34\,000\text{ M}^{-1}\text{ cm}^{-1}$ for the peak at 394 nm and $32\,500\text{ M}^{-1}\text{ cm}^{-1}$ for the peak at 309 nm; for $[\text{Co}(\text{py}_2\text{pz})_2](\text{OTf})$, ϵ is *ca.* $24\,500\text{ M}^{-1}\text{ cm}^{-1}$ for the peak at 419 nm and *ca.* $32\,500\text{ M}^{-1}\text{ cm}^{-1}$ for the peak at 287 nm; for $[\text{Co}(\text{bpyPY4})](\text{OTf})_2$, ϵ is *ca.* $500\text{ M}^{-1}\text{ cm}^{-1}$ for the peak at 472 nm and *ca.* $12\,000\text{ M}^{-1}\text{ cm}^{-1}$ for the peak at 313 nm; for $[\text{Co}(\text{bpyPY4})](\text{OTf})_3$, ϵ is *ca.* $500\text{ M}^{-1}\text{ cm}^{-1}$ for the peak at 465 nm and *ca.* $7\,000\text{ M}^{-1}\text{ cm}^{-1}$ for the peak at 331 nm.

3.3.2. Electronic properties and conductivity

In order to determine the HOMO level of the complexes, cyclic voltammetric (CV) analysis was carried out under inert, dry atmosphere inside a glove-box on 1 mM solutions of the relevant complex in acetonitrile. The supporting electrolyte $n\text{-Bu}_4\text{NPF}_6$ was added to the solution with a concentration of 0.1 M. The voltammograms for oxidation of $[\text{Co}(\text{py}_2\text{pz})_2]$ and $[\text{Co}(\text{bpyPY4})](\text{OTf})_2$ are shown in Figure 23.

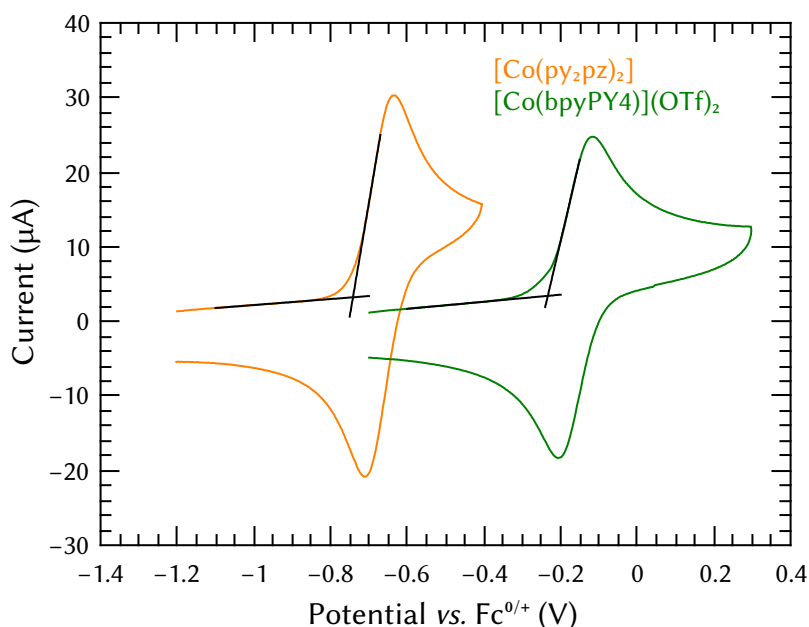


Figure 23. Cyclic voltammograms for oxidation of 1 mM $[\text{Co}(\text{py}_2\text{pz})_2]$ (orange) and 1 mM $[\text{Co}(\text{bpyPY4})](\text{OTf})_2$ (green) in acetonitrile (0.1 M $n\text{-Bu}_4\text{NPF}_6$) obtained at a scan rate of 0.100 V s^{-1} with a glassy carbon electrode (3 mm diameter). Measurements were undertaken inside a N_2 -filled glove-box. Black lines show the estimated oxidation onsets.

The mid-point potential ($E_{1/2}$, average of the oxidative and reductive peak potentials) measured for $[\text{Co}(\text{bpyPY4})](\text{OTf})_2$ ($-161\text{ mV vs. Fc}^{0/+}$, corresponding to $479\text{ mV vs. NHE}^{[220]}$) was in good agreement with the value measured by Kashif *et al.*^[213] for the same compound (465 mV vs. NHE). The previously reported reversible potential for $[\text{Co}(\text{py}_2\text{pz})_2]$ ^[218] ($-300\text{ mV vs. Ag/AgNO}_3$) was measured in a different solvent system and with a different supporting electrolyte and it is not directly comparable with the $E_{1/2}$ value of $-674\text{ mV vs. Fc}^{0/+}$ obtained herein. The HOMO level was calculated from the potential of the onset of the oxidation peak (as shown in Figure 23) assuming an absolute standard reversible potential for ferrocene (approximated to be equal to $E_{1/2}$) on the vacuum scale of -5.1 eV .^[220] The HOMO level

calculated for $[\text{Co}(\text{bpyPY4})](\text{OTf})_2$ was -4.87 eV, while that calculated for $[\text{Co}(\text{py}_2\text{pz})_2]$ was -4.36 eV.

The HOMO levels of the examined compounds were additionally probed by photoelectron spectroscopy in air (PESA). This technique measures the absolute energy of the photon required to pull a single electron from the surface of a solid, thus providing its ionisation energy. This is intrinsically expressed as an absolute potential and can be used as an approximation for the HOMO level of the examined compound, which is analysed in the form of a solid homogeneous film. PESA measurements were performed on solid-state films of $[\text{Co}(\text{bpyPY4})](\text{OTf})_{2.66}$ and $[\text{Co}(\text{py}_2\text{pz})_2](\text{OTf})_{0.66}$ (the Co(III):Co(II) ratio of 2:1 was found to provide the highest efficiency of PSCs; *vide infra*) and the measured HOMO levels were more than 1 eV deeper compared to those derived from the voltammetric data. Differences of a few hundred meVs are not uncommon for the HOMO values measured in solution and in the solid-state due to inter-molecular interactions in the latter case. However, such significant discrepancies between the two techniques as those found here have not been reported in the available literature. Furthermore, the values derived from PESA measurements appear unrealistic and would result in an unfavourable energy alignment with the E_{VB} of the MixCP perovskite, leading to non-working devices (which is not the case, *vide infra*). Interestingly, measurements undertaken on other compounds – e.g. MAPbI₃, MixCP, spiro-OMeTAD and bithi-MeOMeTPA – using the same PESA instrument and on the same day, produced HOMO energy values in accordance with those reported in the literature or similar to those measured by voltammetry. In particular, the E_{VB} for MixCP measured by PESA was -5.65 eV. The experimental data of the measurement are depicted in Figure 24. Thus, the data obtained by PESA for the films of the $[\text{Co}(\text{bpyPY4})](\text{OTf})_{2.66}$ and $[\text{Co}(\text{py}_2\text{pz})_2](\text{OTf})_{0.66}$ complexes were considered as unreliable, with the underlying reasons not understood at this stage.

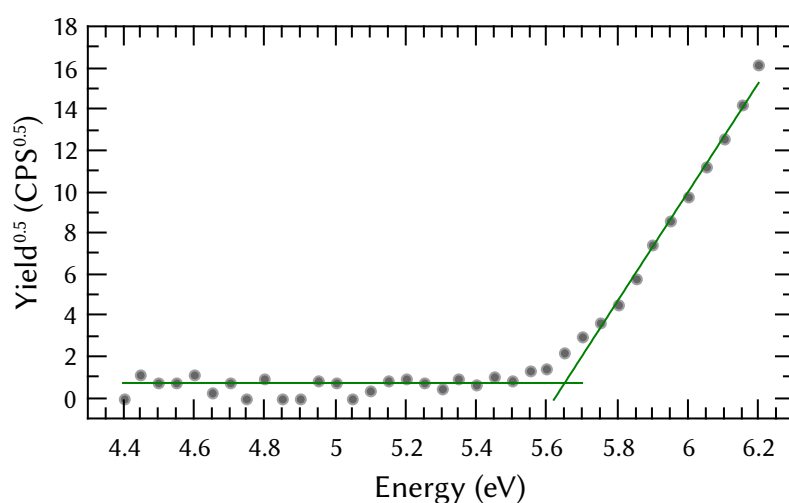


Figure 24. PESA measurement of the MixCP film deposited of FTO|c-TiO₂. Green lines show linear fits used to derive E_{VB} .

Two-probe conductivity measurements were performed for the $[\text{Co}(\text{bpyPY4})](\text{OTf})_{2.66}$ and $[\text{Co}(\text{py}_2\text{pz})_2](\text{OTf})_{0.66}$ films deposited onto interdigitated array electrodes (IDAs, comprised of

gold fingers deposited on glass) both in their pristine form and with the additives LiTFSI and tBP introduced. Films were prepared *via* drop-casting appropriate solutions onto IDAs but it was not possible to measure any appreciable conductivity with said approach. In their paper, Kashif *et al.*^[211] report a conductivity value of $1.1 \times 10^{-8} \text{ S m}^{-1}$ for a film of $[\text{Co}(\text{bpyPY4})](\text{OTf})_2$ and a very high conductivity value of 3.0 S m^{-1} for $[\text{Co}(\text{bpyPY4})](\text{OTf})_{2.33}$. These results, that were also obtained with IDA electrodes similar to those used in the present work, are in stark contrast with the very low conductivity found here for $[\text{Co}(\text{bpyPY4})](\text{OTf})_{2.66}$, which also features a mixture of the Co(II) and Co(III) species. A private consultation with the authors of Ref. [211] revealed that normal drop-casting yielded no conductivity during their measurements as well. The deposition method used by Kashif to obtain conductive films on the IDA electrodes involved continuous CV experiments – sweeping the applied potential between -1 and 1 V – after depositing the drop of solution onto the electrode and while the solvent evaporated. After complete dryness of the film, they were able to measure the linear *I-V* profile of the compound and calculate a conductivity value. This method was deemed too dissimilar from the actual deposition technique employed for PSC fabrication and was therefore not employed.

Spiro-OMeTAD is known to form a good blocking contact with titania and gold in a diode configuration, blocking the current flow until the built-in potential is reached (*e.g.* see Figure 39 in section 4.3.3). In order to verify the rectifying properties of the examined cobalt complexes, diodes with the structure FTO|c-TiO₂|HTM|Au were fabricated for the Co(II) and Co(III) species of each compound and for $[\text{Co}(\text{bpyPY4})](\text{OTf})_{2.66}$ and $[\text{Co}(\text{py}_2\text{pz})_2](\text{OTf})_{0.66}$, both in their pristine form and mixed with the additives (LiTFSI and tBP). Figure 25 shows the dark *I-V* curves for each HTM composition. Data obtained under 1 sun illumination were essentially the same and are therefore not shown.

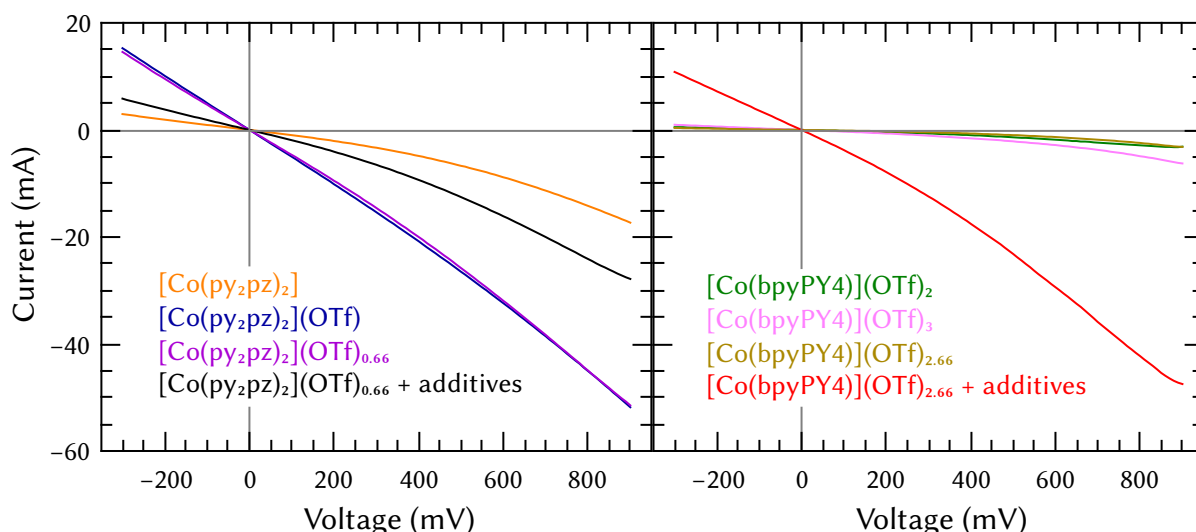


Figure 25. *I-V* characterisation (scan rate 0.100 V s^{-1}) of FTO|c-TiO₂|HTM|Au diodes for $[\text{Co}(\text{py}_2\text{pz})_2]$ (orange), $[\text{Co}(\text{py}_2\text{pz})_2](\text{OTf})$ (blue), pristine $[\text{Co}(\text{py}_2\text{pz})_2](\text{OTf})_{0.66}$ (purple), $[\text{Co}(\text{py}_2\text{pz})_2](\text{OTf})_{0.66}$ plus additives (black), $[\text{Co}(\text{bpyPY4})](\text{OTf})_2$ (green), $[\text{Co}(\text{bpyPY4})](\text{OTf})_3$ (magenta), pristine $[\text{Co}(\text{bpyPY4})](\text{OTf})_{2.66}$ (ochre) and $[\text{Co}(\text{bpyPY4})](\text{OTf})_{2.66}$ plus additives (red) HTMs.

All diodes display a very poor rectifying behaviour, with a low shunt resistance clearly identifiable. This could be an indication of either poor material properties or poor film formation, with a high density of pinholes leading to short-circuit paths in the diodes. The poor performances of cobalt complexes with both ligands in the diodes are expected to influence the performance of PSCs as well, lowering the shunt resistance and therefore the efficiency of the devices.

3.3.3. Solar cell characterisation

A set of solar cells was fabricated employing the MixCP perovskite and either $[\text{Co}(\text{bpyPY4})](\text{OTf})_{2.66}$ or $[\text{Co}(\text{py}_2\text{pz})_2](\text{OTf})_{0.66}$ as HTM. The device structure was $\text{FTO}|\text{c-TiO}_2|\text{mp-TiO}_2|\text{MixCP}|\text{HTM}|\text{Au}$. The two hole transporters were deposited using the same procedure and conditions previously introduced for the $[\text{Fe}(\text{bpyPY4})](\text{OTf})_{2.5}$ HTM in chapter 2 (see section 6.3 or Ref. [217] for details). Co-based hole conductors were deposited with and without the LiTFSI and tBP additives. Two reference solar cells were also fabricated using the state-of-the-art spiro-OMeTAD HTM modified with the same two additives. Blends of the cobalt complexes examined here were found to be stable in air and therefore encapsulation of devices was not necessary for the short-term tests.

An initial screening of PSCs prepared with different Co(II):Co(III) ratios in the HTM was performed and ratios of 1:0, 2:1, 1:1, 1:2 and 0:1 were tested. It was found that the PSCs fabricated with a ratio of 1:2 provided the highest efficiency for both types of HTM. Thus, $[\text{Co}(\text{bpyPY4})](\text{OTf})_{2.66}$ and $[\text{Co}(\text{py}_2\text{pz})_2](\text{OTf})_{0.66}$ were the two particular mixtures used for all further studies. PSCs fabricated with pristine $[\text{Co}(\text{bpyPY4})](\text{OTf})_{2.66}$ produced very low photocurrent densities of few $\mu\text{A cm}^{-2}$ and were therefore not studied further. J - V curves for the best-performing $[\text{Co}(\text{bpyPY4})](\text{OTf})_{2.66}$ and pristine $[\text{Co}(\text{py}_2\text{pz})_2](\text{OTf})_{0.66}$ -based PSCs as well as those for the best-performing devices based on the $[\text{Co}(\text{py}_2\text{pz})_2](\text{OTf})_{0.66}$ HTM with additives (with and without hysteresis) are shown in Figure 26. Table 9 lists all main photovoltaic parameters of the tested solar cells. Eight devices were fabricated for each composition of the Co-based HTMs but two based on $[\text{Co}(\text{bpyPY4})](\text{OTf})_{2.66}$ were non-functional and were not included in the calculation of the data shown in Table 9.

PSCs with both $[\text{Co}(\text{bpyPY4})](\text{OTf})_{2.66}$ and $[\text{Co}(\text{py}_2\text{pz})_2](\text{OTf})_{0.66}$ showed poor performance in terms of all major photovoltaic parameters. Lower V_{OC} values compared to the spiro-OMeTAD-based devices were expected due to the higher HOMO levels of the two complexes (in fact, V_{OC} values were even higher than expected) but short-circuit current densities and fill factors were very low due to other, not initially obvious reasons. In order to identify possible causes for the overall low performance, estimates of the shunt and series resistances were derived from linear fits to the I - V curves near short-circuit and open-circuit, respectively. Shunt resistances for the Co-based HTMs were generally very small, with values of only a few $\text{k}\Omega$ (*cf.* 71 $\text{k}\Omega$ for the spiro-OMeTAD-based PSCs), which is consistent with unsatisfactory rectifying behaviour of the corresponding diodes (Figure 25).

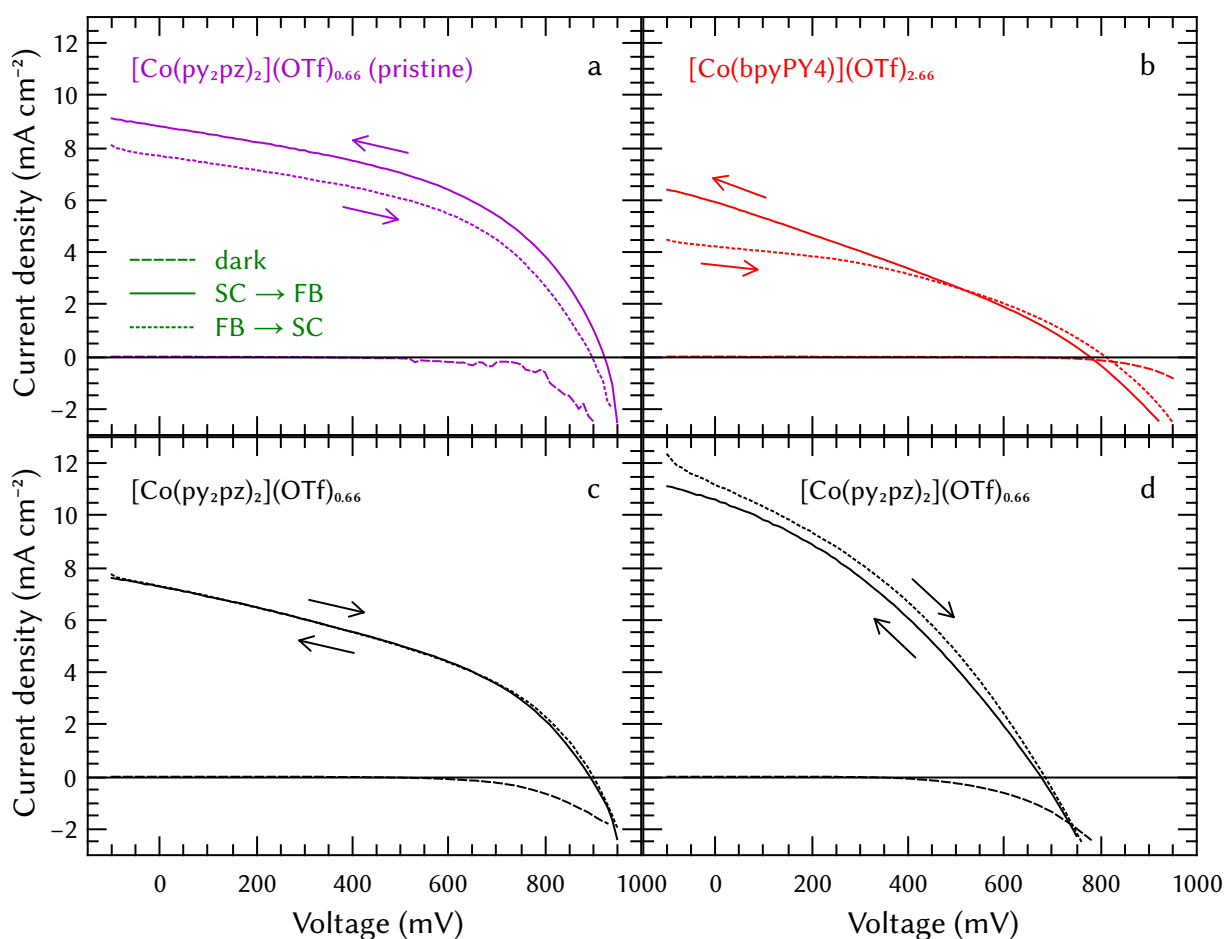


Figure 26. J-V curves (scan rate 100 mV s^{-1}) for the best-performing MixCP PSCs based on the (a) pristine $[\text{Co}(\text{py}_2\text{pz})_2](\text{OTf})_{0.66}$ (purple), (b) $[\text{Co}(\text{bpyPY4})](\text{OTf})_{2.66}$ plus additives (red) and (c, d) $[\text{Co}(\text{py}_2\text{pz})_2](\text{OTf})_{0.66}$ plus additives (black) HTMs recorded under 1 sun AM1.5G irradiation. Devices were masked with an aperture of 0.16 cm^2 to define the active area. Panels (c) and (d) show data for the $[\text{Co}(\text{py}_2\text{pz})_2](\text{OTf})_{0.66}$ -based PSCs without and with hysteresis, respectively.

Moreover, the poor conductivity of both complexes gave rise to very high series resistances of hundreds of ohms, which can be compared to only 29Ω for the reference devices. Thus, both low R_{sh} and high R_s account for the poor FF of all devices with Co complex-based HTMs. Most likely, the poor conductivity of these HTMs also contributes to the very low short-circuit current densities.

The use of the additives with the $[\text{Co}(\text{py}_2\text{pz})_2](\text{OTf})_{0.66}$ HTM does not improve average PCEs of PSCs derived from the J - V data but it significantly suppresses variability of the results, as concluded from much lower standard deviations of all photovoltaic parameters (Table 9). Modification of this Co complex with the additives also provides a *ca.* 50% increase in J_{sc} – most likely due to an increase in conductivity of the HTM layer – but at the same time lowers the V_{oc} and FF parameters. Moreover, devices with $[\text{Co}(\text{py}_2\text{pz})_2](\text{OTf})_{0.66}$ mixed with LiTFSI and tBP as an HTM layer exhibit a very rare behaviour: the efficiency measured in the $\text{FB} \rightarrow \text{SC}$ scan direction is higher than that measured in the opposite direction. Although the average PCE is similar in both cases, six out of eight devices consistently show a higher PCE in the former case. The remaining two devices, interestingly, show

essentially no hysteresis (hysteresis index^[59] 0.005). One of the latter two devices was also the best-performing of the group with its parameters provided in Table 9.

Table 9. Complete list of photovoltaic parameters^a for the MixCP perovskite solar cells with different HTMs under 1 sun AM1.5G irradiation.

Hole transporting material	V_{OC} (mV)	J_{SC} (mA cm ⁻²)	FF (%)	PCE (%)	ss-PCE ^b (%)	R_{sh} (k Ω)	R_s (Ω)
[Co(bpyPY4)](OTf) _{2.66} (best, SC \rightarrow FB)	811	4.2	39	1.3	0.9	3.3	48
[Co(bpyPY4)](OTf) _{2.66} (best, FB \rightarrow SC)	778	5.9	30	1.4	0.9	1.2	48
[Co(bpyPY4)](OTf) _{2.66} (average, SC \rightarrow FB)	800 \pm 40	3 \pm 1	32 \pm 6	0.8 \pm 0.4	NM ^c	3 \pm 1	1000 \pm 500
[Co(bpyPY4)](OTf) _{2.66} (average, FB \rightarrow SC)	790 \pm 70	4 \pm 1	28 \pm 3	0.9 \pm 0.4	NM	1.6 \pm 0.4	800 \pm 300
[Co(py ₂ pz) ₂](OTf) _{0.66} (best, SC \rightarrow FB)	900	7.3	40	2.6	4.0	1.6	200
[Co(py ₂ pz) ₂](OTf) _{0.66} (best, FB \rightarrow SC)	893	7.3	41	2.6	4.0	1.8	220
[Co(py ₂ pz) ₂](OTf) _{0.66} (average, SC \rightarrow FB)	820 \pm 70	9 \pm 1	36 \pm 3	2.5 \pm 0.1	NM	1.2 \pm 0.3	240 \pm 20
[Co(py ₂ pz) ₂](OTf) _{0.66} (average, FB \rightarrow SC)	780 \pm 70	9 \pm 1	35 \pm 3	2.4 \pm 0.2	NM	1.5 \pm 0.5	250 \pm 30
[Co(py ₂ pz) ₂](OTf) _{0.66} , pristine (best, SC \rightarrow FB)	897	7.7	48	3.3	2.7	2.6	190
[Co(py ₂ pz) ₂](OTf) _{0.66} , pristine (best, FB \rightarrow SC)	923	8.8	48	3.9	2.3	2.0	130
[Co(py ₂ pz) ₂](OTf) _{0.66} , pristine (average, SC \rightarrow FB)	840 \pm 40	5 \pm 1	41 \pm 4	1.8 \pm 0.7	NM	1.8 \pm 0.5	300 \pm 100
[Co(py ₂ pz) ₂](OTf) _{0.66} , pristine (average, FB \rightarrow SC)	900 \pm 20	6 \pm 1	43 \pm 5	2.3 \pm 0.8	NM	2.3 \pm 0.4	250 \pm 90
Spiro-OMeTAD (best, SC \rightarrow FB)	989	20.27	66	13.3	NM	6.9	39
Spiro-OMeTAD (best, FB \rightarrow SC)	1022	20.28	72	15.0	NM	74	27
Spiro-OMeTAD (average, SC \rightarrow FB)	992 \pm 4	20.21 \pm 0.08	66 \pm 1	13.2 \pm 0.2	NM	7.0 \pm 0.2	40 \pm 1
Spiro-OMeTAD (average, FB \rightarrow SC)	1020 \pm 3	20.26 \pm 0.03	72 \pm 1	14.9 \pm 0.2	NM	71 \pm 4	29 \pm 3

(a) Derived from the J - V curves (scan rate 100 mV s⁻¹) of eight [Co(py₂pz)₂](OTf)_{0.66}-based, six [Co(bpyPY4)](OTf)_{2.66}-based and two spiro-OMeTAD-based devices. V_{OC} – open circuit voltage; J_{SC} – short-circuit current density; FF – fill factor; ss-PCE – quasi-steady-state PCE after 5 min of testing; R_{sh} – shunt resistance; R_s – series resistance; SC – short circuit; FB – forward bias. (b) the quasi-steady-state PCE for the best-performing cells was recorded by first applying the V_{p_m} derived from the SC \rightarrow FB direction, then the V_{p_m} corresponding to the FB \rightarrow SC direction. (c) NM: not measured.

The lack of hysteresis was not the only peculiarity of the $[\text{Co}(\text{py}_2\text{pz})_2](\text{OTf})_{0.66}$ solar cells with additives. When performing quasi-steady-state measurements for 5 min, the PCE value at the end of the measurement was lower than that derived from the J - V curve for both $[\text{Co}(\text{bpyPY4})](\text{OTf})_{2.66}$ and $[\text{Co}(\text{py}_2\text{pz})_2](\text{OTf})_{0.66}$, while it was *ca.* 50% higher in the case of $[\text{Co}(\text{py}_2\text{pz})_2](\text{OTf})_{0.66}$ plus additives. This trend is confirmed by a similar measurement conducted on a second device for each case, not reported in Table 9. The device fabricated with $[\text{Co}(\text{bpyPY4})](\text{OTf})_{2.66}$ showed a relatively constant PCE-time behaviour for 5 minutes, while that with $[\text{Co}(\text{py}_2\text{pz})_2](\text{OTf})_{0.66}$ underwent a constant decay in efficiency. The PCE of the PSC fabricated with $[\text{Co}(\text{py}_2\text{pz})_2](\text{OTf})_{0.66}$ plus additives, on the other hand, was still slightly raising at the end of the measurement period and the final stabilised efficiency might be even higher than the recorded 4%. Figure 27 shows representative current-time measurements for each HTM.

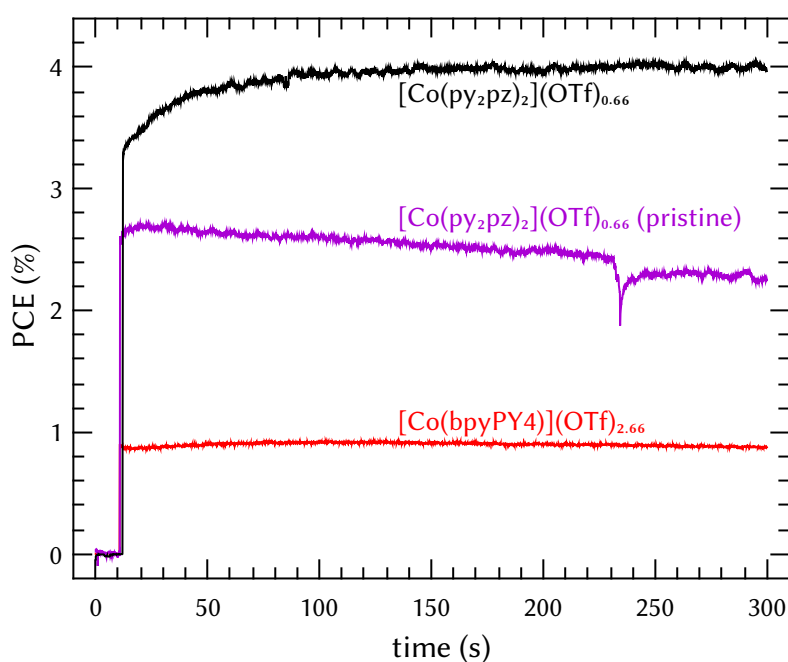


Figure 27. Maximum power point PCE transients measured under 1 sun AM1.5G irradiation for the best-performing PSC with $[\text{Co}(\text{bpyPY4})](\text{OTf})_{2.66}$ plus additives (red, 440 mV applied voltage), pristine $[\text{Co}(\text{py}_2\text{pz})_2](\text{OTf})_{0.66}$ (purple, 640 mV applied voltage) and $[\text{Co}(\text{py}_2\text{pz})_2](\text{OTf})_{0.66}$ plus additives (black, 620 mV applied voltage) HTMs.

3.3.4. Influence of the counter-ion

Notwithstanding their low performances, a direct comparison between the properties of the complexes based on both ligands is still possible, in order to verify the initial hypothesis on the influence of the counter-ion on the HTM performance. While a direct comparison of their conductivities was found problematic, the comparison of the parameters of PSCs fabricated with the examined Co-based hole transporting materials provides useful insights. Overall, the results obtained clearly demonstrate that $[\text{Co}(\text{py}_2\text{pz})_2](\text{OTf})_{0.66}$ is more efficient than $[\text{Co}(\text{bpyPY4})](\text{OTf})_{2.66}$ as a hole conductor in PSCs. Indeed, devices fabricated with the former are twice as efficient as those fabricated with the latter when considering the J - V

curve measurements and four times as efficient when considering the quasi-steady-state measurements. Moreover, the devices featuring pristine $[\text{Co}(\text{bpyPY4})](\text{OTf})_{2.66}$ were non-functional, due to a very low photocurrent density, while those with pristine $[\text{Co}(\text{py}_2\text{pz})_2](\text{OTf})_{0.66}$ showed a photocurrent density three orders of magnitude higher. This observation clearly indicates significant differences in conductivity between the two materials. This is further supported by the extrapolated value of the series resistance, which is much higher for the devices with $[\text{Co}(\text{bpyPY4})](\text{OTf})_{2.66}$ compared to the $[\text{Co}(\text{py}_2\text{pz})_2](\text{OTf})_{0.66}$ -based PSCs. The series resistance typically reflects the quality of the contacts between the various layers in a solar cell. In this case however, considering that the absolute values are very high for both HTMs, significantly different R_s can also be interpreted in terms of superior conductivity of $[\text{Co}(\text{py}_2\text{pz})_2](\text{OTf})_{0.66}$ over $[\text{Co}(\text{bpyPY4})](\text{OTf})_{2.66}$. Thus, the aggregate of the obtained data supports the initial hypothesis that the metal complexes featuring a lower number of counter-ions might exhibit better charge transfer properties.

3.4. Conclusions

Two cobalt complexes, $[\text{Co}(\text{bpyPY4})](\text{OTf})_{2.66}$ and $[\text{Co}(\text{py}_2\text{pz})_2](\text{OTf})_{0.66}$, the former previously used as a hole transporting material in ssDSSCs with a different Co(II):Co(III) ratio and the latter newly synthesised, were characterised and employed as HTMs in $(\text{Rb}_{0.05}\text{Cs}_{0.05}\text{FA}_{0.75}\text{MA}_{0.15})\text{Pb}(\text{I}_{0.85}\text{Br}_{0.15})_3$ perovskite solar cells. Both materials exhibited low conductivity and unsatisfactory rectifying behaviour. PSCs fabricated with hole transporting layers based on $[\text{Co}(\text{bpyPY4})](\text{OTf})_{2.66}$ or $[\text{Co}(\text{py}_2\text{pz})_2](\text{OTf})_{0.66}$ showed PCEs of only few percent, that were significantly lower than the reference devices fabricated with spiro-OMeTAD (approximately 14%). Nevertheless and most importantly, it was possible to draw conclusions on the influence of counter-ions on the hole transporting properties of the investigated materials, which was the aim of the present study.

The combination of all the obtained results clearly shows that the absence of the counter-ions is beneficial for both the conductivity and the overall performance of solid-state films of the redox-active cobalt complexes employed as HTMs in PSCs. Further studies are needed to confirm that the initial hypothesis is correct for redox-active metal complexes in general, regardless of the nature of the metal centre. As a last consideration, noteworthy is the fact that – as opposed to its application in PSCs – $[\text{Co}(\text{bpyPY4})](\text{OTf})_{2.33}$ performs relatively well as a solid-state HTM in ssDSSCs as demonstrated by Kashif *et al.*,^[211] although the deposition technique employed in that study was quite different compared to the present one. This difference in performance leads to the conclusion that a particular HTM may not be efficient *per se*, but that its performance can greatly vary depending on the light absorber to which it is applied.

4. Bithiophene core-based organic hole transporter

4.1. The long journey there

The bithiophene core-based HTM subject of this chapter (bithi-MeOMeTPA, see Figure 28) is the first molecule on which I worked during my thesis. At the time there was only a small number of reported hole conductors for PSCs. The idea behind the work was to design a molecule similar to spiro-OMeTAD in terms of geometry and side groups but with different electronic properties. Rather than giving the molecule its three-dimensional structure through an sp^3 carbon, the crossed shape was achieved through twisting due to steric hindrance of a bithiophene core given by two methyl groups attached to it. While the sp^3 carbon in spiro-OMeTAD acts as an insulator between the two π -systems, thereby impeding electronic coupling between the two branches of the molecule, the bithiophene core was supposed to allow electronic coupling, spreading the HOMO throughout the molecule.

When I was ready to begin the synthesis, after completing the theoretical calculations and waiting about seven weeks for the ordered chemicals to reach Melbourne, the paper reporting on KTM3 was published by Krishnamoorthy *et al.*^[112] The molecule was very similar to mine, with four triphenylamine branches and a 3,3'-bithiophene core, as opposed to the 2,2'-bithiophene of bithi-MeOMeTPA (Figure 28). Despite the similarities I decided to continue the work on the HTM I designed, partly because the two molecules presented enough differences, partly because it would have been interesting to compare the performances of the two different cores. Shortly after I completed the synthesis of bithi-MeOMeTPA, however, Li *et al.* published their work on H112.^[113] This second molecule was almost identical to mine, with the only difference given by the absence of the two methyl groups responsible for the twisting of the core.

After the publication of the work on H112 I decided to change the aim of the work on bithi-MeOMeTPA and – rather than just characterising a new hole conductor – to perform a comparative study between my HTM and H112, to verify the correlation between molecular geometry and charge transport performance. Further theoretical calculations, in fact, showed how the absence of the two methyl groups makes H112 relatively flat, compared to bithi-MeOMeTPA. I contacted the research group at Nanyang University and proposed a collaboration on this project. After an initial positive response, however, they were not able to provide me with their compound and the only commercial source available was too expensive. Since there was no time to synthesise another compound, I decided to carry on the study “at a distance”, by comparing my work to the published data. The solar cell architecture is different in the two cases (planar in my work, mesoporous in the published study) but the reference spiro-OMeTAD hole transporter was deposited using the same recipe and procedure, which enables an indirect comparison between the two HTMs using the same reference. The recipe and procedure for the deposition of bithi-MeOMeTPA was also the same as that of H112 to facilitate comparisons.

4.2. Introduction

Analysis of the latest advances in the development of the charge transporting materials for photovoltaic applications (see section 1.5.2 and references therein) suggests that differences in molecular geometry affect several key properties of such materials, which open additional possibilities to design better performing hole transporters for perovskite and other solar cells. In particular, molecules with a more defined 3D structure are more likely to form amorphous and glassy films that present fewer pinholes and defects compared to molecules with a more planar structure. On the other hand, the structure of the latter facilitates π -stacking and thereby improves charge transport properties of films. Indeed, several efficient molecules that belong to both categories have already been reported (see *e.g.* Tables 2 and 4 in section 1.5.2). Due to their very different compositions, however, it is hard to make an unambiguous conclusion on which of the various parameters of an HTM are more important to achieve good performances: those improving the film quality or those providing more efficient charge transport. Studies by Zhang *et al.*^[134,221] provide some important insights into the interrelation between the geometrical structure and the hole transporting efficiency for a few organic HTMs. However these molecules, while structurally similar, significantly differ in terms of electronic configuration – either due to the introduction of double bonds or to the extension of aromatic conjugation – which obscures the underlying structure-function relationships.

Krishnamoorthy *et al.*^[112] and Li *et al.*^[113] have reported on two hole conductors, KTM3 and H112, respectively (Figure 28), that have very similar molecular structures but which belong to the two different categories of molecular geometries stated above, as demonstrated by computational studies undertaken herein (*vide infra*). Although similar, these two molecules are still not perfectly comparable since KTM3 features a 3,3'-bithiophene core, while H112 is based on a 2,2'-bithiophene centre. In this study, a third molecule has been synthesised – bithi-MeOMeTPA – that bridges the gap between the two (Figure 28). Bithi-MeOMeTPA features a 2,2'-bithiophene core similarly to H112 but belongs to the molecular geometry category of KTM3 as provided by steric twisting induced by two methyl groups. It is important to highlight that these methyl groups change the geometrical structure but do not alter the electronic configuration of the molecule itself other than the effects ensuing from the geometry change (*vide infra*).

In the present study, bithi-MeOMeTPA is compared to both KTM3 and H112 in terms of properties relevant to their application as hole transporting materials for perovskite solar cells. Comprehensive characterisation of bithi-MeOMeTPA has been undertaken using state-of-the-art techniques including UV-Vis, CV, PESA and differential scanning calorimetry (DSC). Since a direct comparison of the three hole conductors in the same laboratory was not possible, the differences in solar cell parameters are analysed relative to the same state-of-the-art reference HTM – spiro-OMeTAD.

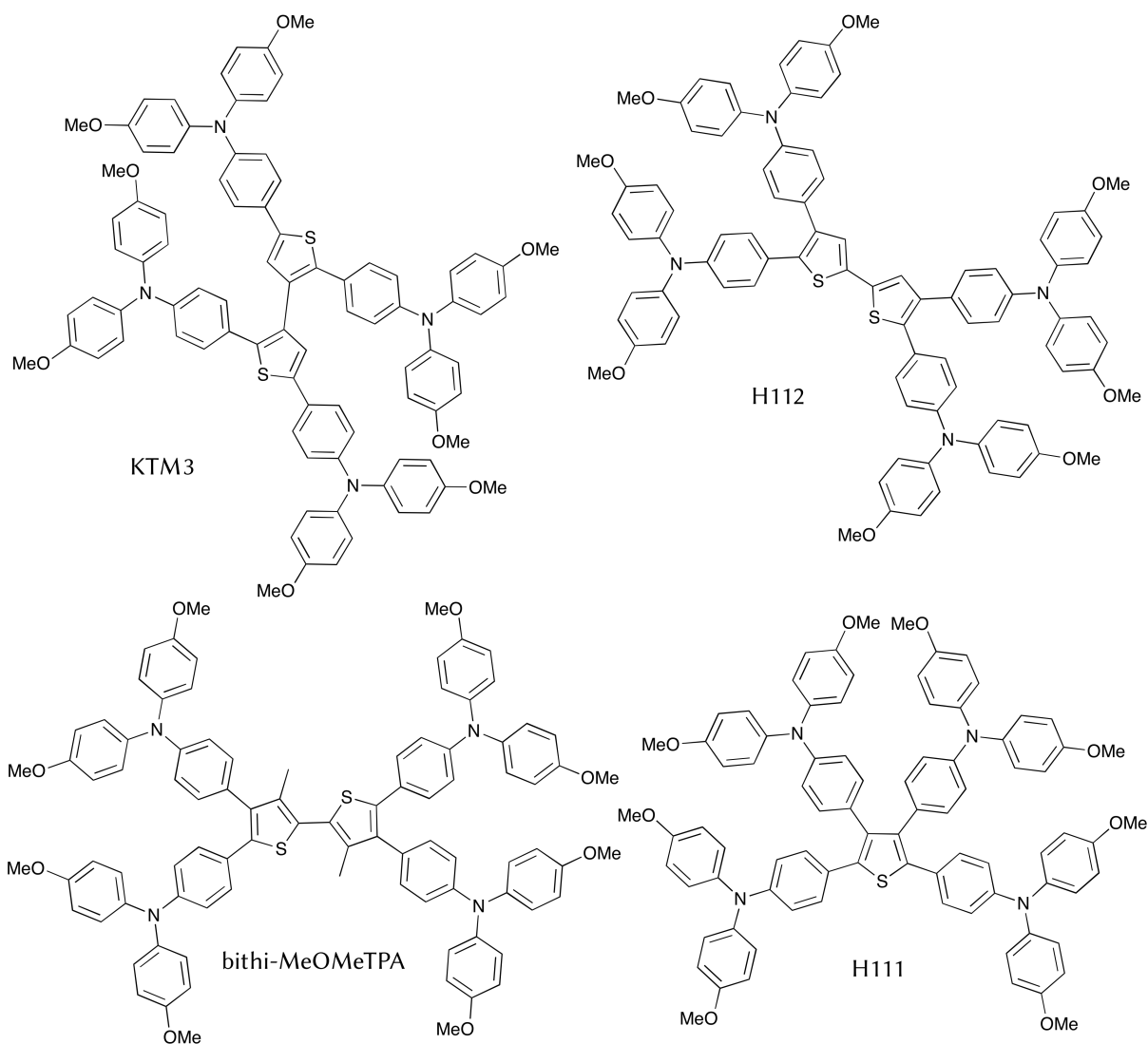


Figure 28. Molecular structures of KTM3, H112, H111 and bithi-MeOMeTPA.

4.3. Results and discussion

4.3.1. Computational analysis

Computational studies to determine molecular geometry, HOMO levels and orbital shapes were executed for the three organic hole conductors examined. Molecular geometries for KTM3 and bithi-MeOMeTPA were calculated using the MOPAC2012 software package,^[222] while MOPAC2016^[223] was used for H112. In all cases, calculations were performed using the PM7 semi-empirical method.^[224] Density functional theory (DFT) single point energy calculations to determine orbital energies and shapes were conducted using the Gaussian 09 software package^[225] under the B3LYP level of theory^[225] with a 6-31+G* basis set and simulating a chlorobenzene (CBZ) solution environment. The semi-empirical PM7 method was chosen to determine the molecular geometry because it produced calculated energy values closer to the experimental ones and at a fraction of the computational cost compared to the DFT method.

Computational analysis is very useful for studies on hole transporting materials and other molecules for solar cell applications as it provides information on their key parameters, some of which cannot be acquired empirically. In the case of HTMs, of the utmost importance are the HOMO energy level and orbital shapes. The HOMO energy level calculation is useful in the molecule design stage as it can give an indication of whether the designed molecule will exhibit favourable properties for the intended application and allows a relative comparison with other designs. Furthermore, it is important to compare the calculated HOMO level with that measured experimentally, as it gives an indication of the experiment-theory agreement and therefore of the reliability of the calculations. In general, the further away the theoretical value is from the experimental one, the less likely it is that the calculated molecular geometry and orbital shapes are a representation of reality. The latter property is currently inaccessible from experiment, but is important to consider as it plays a key role in the charge transport process. In the case of hole conductors, the HOMO and HOMO-1 are the orbitals that play a role in charge transport. For the process to be efficient, it is important for the electron density of both to be widely spread across the molecule and to be especially present in the more external side groups, which are those in contact with the light absorber. The more delocalised the orbitals are, the less important a correct molecular orientation becomes when stacking in the solid state, thus increasing charge transport efficiency.

Comparisons of the optimised molecular geometries show that bithi-MeOMeTPA has a very well defined 3D structure, while KTM3 and H112 are more planar. This is clearly represented in Figure 29, which shows the three compounds seen along the longer molecular axis. In bithi-MeOMeTPA the two triphenylamine branches on each thiophene form three visible “arms” that radiate out of the central axis.

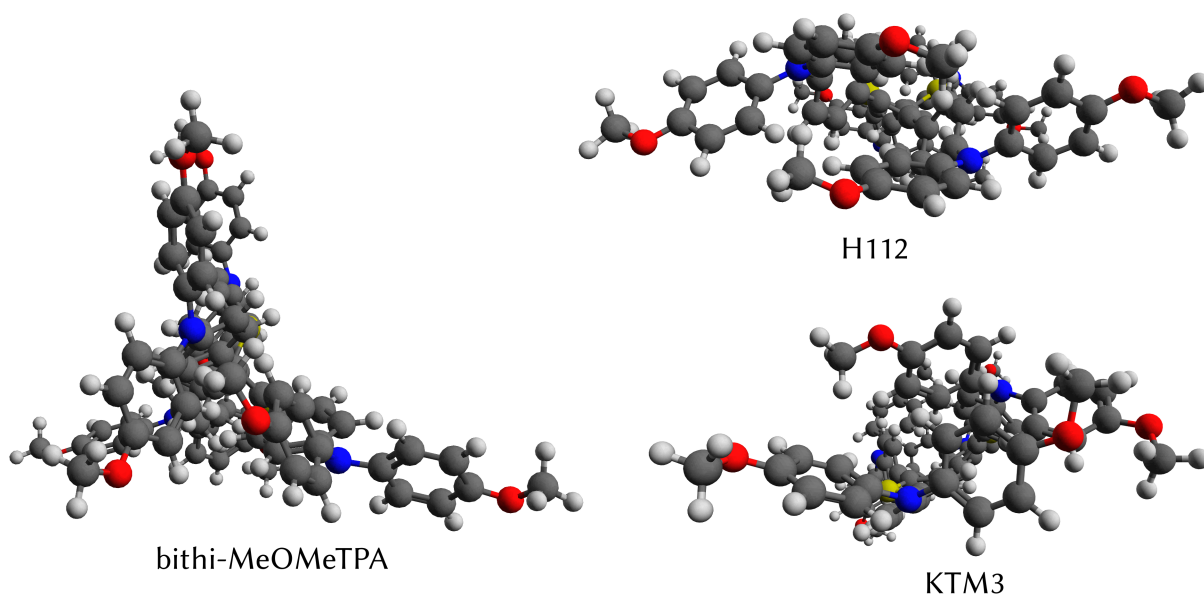


Figure 29. View along the longer molecular axis of the optimised geometries for bithi-MeOMeTPA, KTM3 and H112.

H112, on the contrary, is much more flat, with only two “arms” radiating from the central axis in opposite directions (Figure 29) and with the aromatic rings (except those attached to the thiophene groups) lying mostly parallel to the main molecule plane, allowing for good intermolecular π -stacking (Figure 30). The KTM3 molecule is also relatively flat when viewed along the longer axis, though not as wide as H112 and with the aromatic rings being not as stacked (Figure 29). This is best seen in Figure 31, from which it is clear that most of the aromatic rings lie orthogonal to the main molecular plane (*i.e.* that of the bithiophene), making π -stacking difficult.

The dihedral angles between the planes of the two thiophenes and of each thiophene with the two benzene rings attached to them are listed in Table 10. These angles, despite not giving a full picture of the molecular geometry (the position of the triphenylamine branches is also important in this case), are useful to understand the relative position of the rings close to the central core and help in understanding the shape of the molecular orbitals, which will be discussed below.

Table 10. Dihedral angles^a between the planes of the two thiophene rings and between the planes of each thiophene ring and the two benzene rings attached to them.

HTM	t-t' (deg)	t-5 (deg)	t-4(2) (deg)	t'-5' (deg)	t'-4'(2') (deg)
H112	62.3	79.4	78.1	87.6	84.8
KTM3	47.0	25.3	85.4	28.4	86.6
Bithi-MeOMeTPA	74.7	62.6	73.4	60.2	76.7

(a) Derived from molecular geometry optimisation calculations. t is the thiophene drawn on top in Figures 30, 31 and 32, while t' is the thiophene drawn on bottom. The numbers indicate the benzene rings based on their position relative to the thiophene ring to which they are attached – the number in parenthesis is related to KTM3, which has a different position for two of the rings.

The HOMO of bithi-MeOMeTPA is delocalised across all four triphenylamine branches but there is little electron density in the central core, showing that the twisting breaks aromatic conjugation (Figure 32). The HOMO-1 also spans across all four branches and has little electron density in the central core. However, while in the HOMO most of the electron density is located on the two bottom branches (as seen in Figure 32), in the HOMO-1 the two upper branches are those with more electron density. The LUMO of bithi-MeOMeTPA is located mostly on the bithiophene core, reaching up to the aromatic ring of each triphenylamine branch closest to the core.

The HOMO of KTM3, unlike that of bithi-MeOMeTPA, spans across the bithiophene core as well, as the two rings are much more in plane (Figure 31 and Table 10). However, electron density is not present in all the four triphenylamine branches: the orbital is located in only one of the two branches attached to each thiophene. This is due to the fact that only the 5 and 5' benzene rings are mostly in plane with each thiophene, while the other two are mostly orthogonal to them.

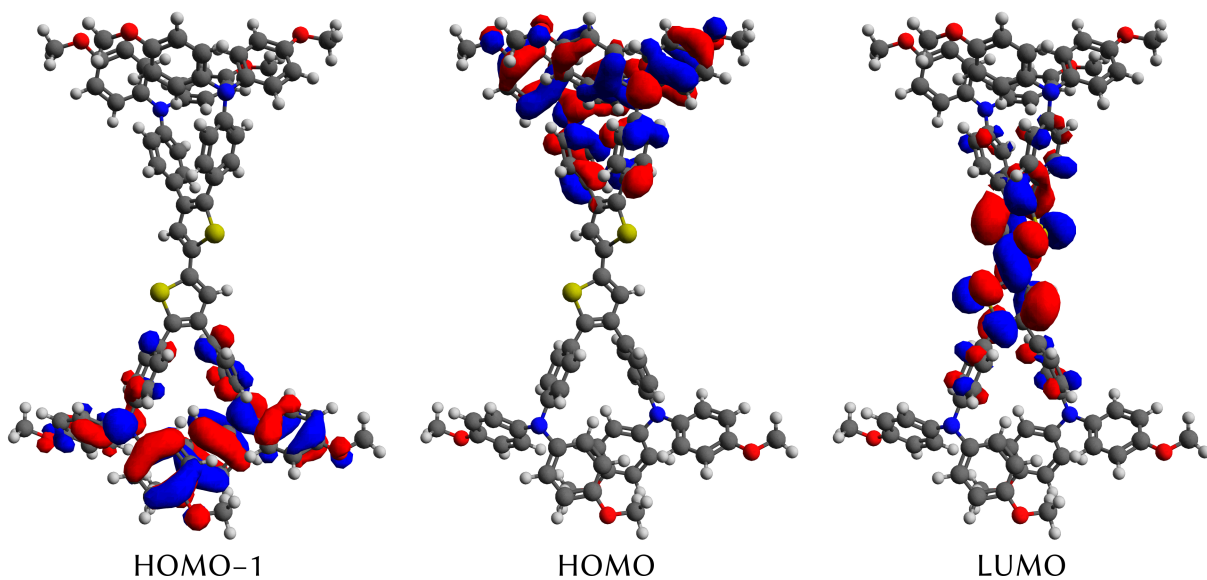


Figure 30. Main orbitals of H112.

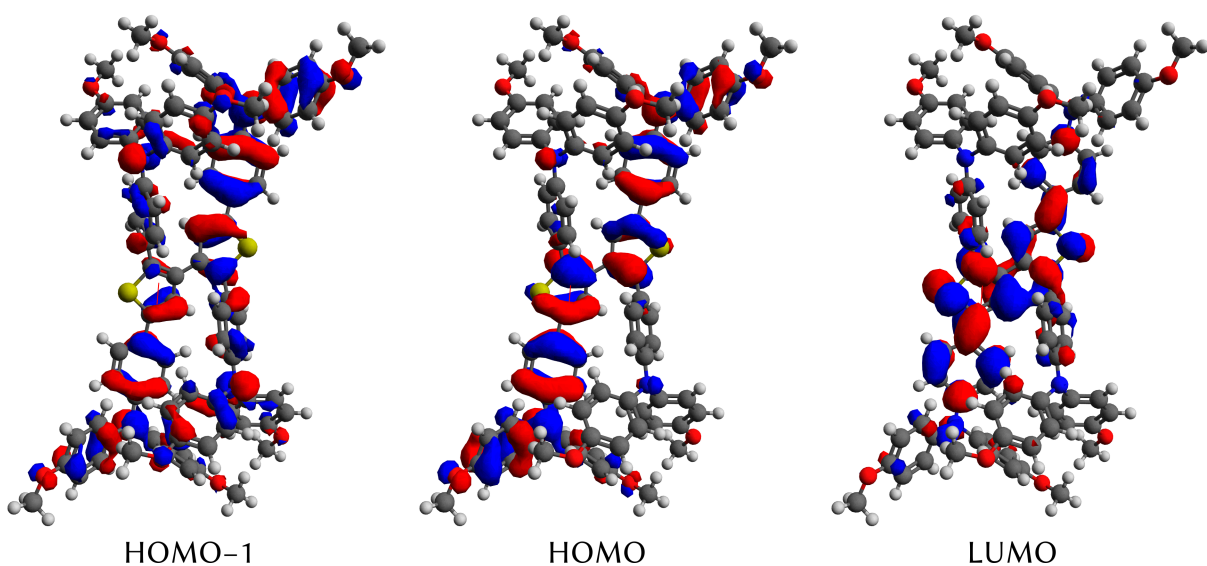


Figure 31. Main orbitals of KTM3.

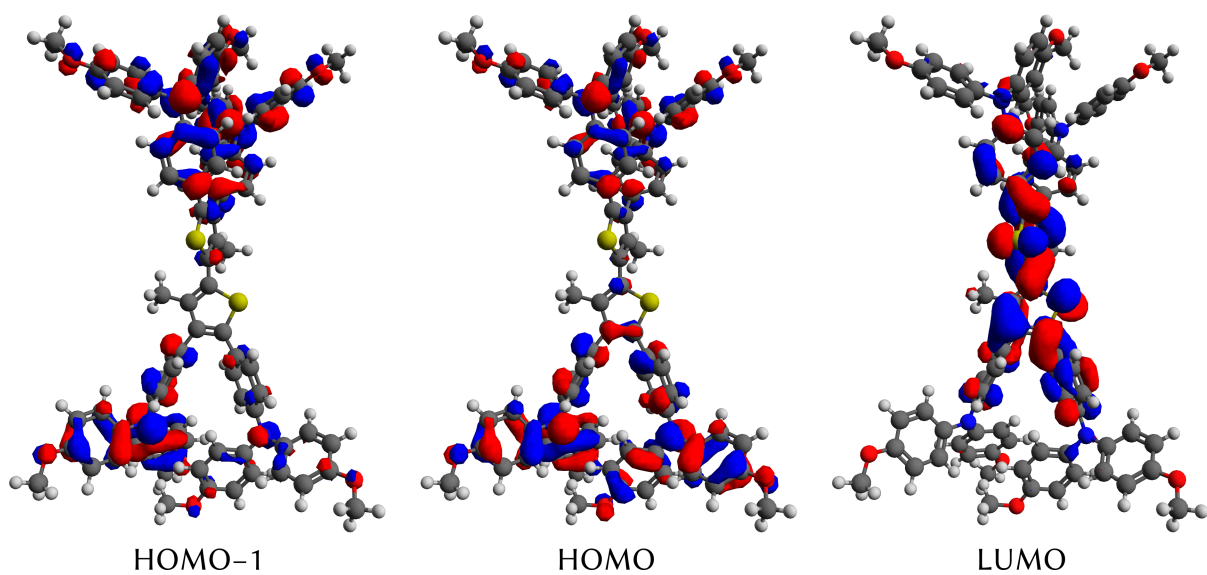


Figure 32. Main orbitals of bithi-MeOMeTPA.

The HOMO-1 on the other hand is localised across all the molecule, although there is still a higher electron density in the two branches where the HOMO is localised. The LUMO is localised on the bithiophene core and the four aromatic rings attached to it, similarly to bithi-MeOMeTPA.

In H112, despite the fact that the molecule is generally more flat than the other two considered, the four benzene rings are almost orthogonally attached to the bithiophene core (Figure 30 and Table 10). For this reason, the HOMO orbital does not span across the whole length of the molecule – as found for KTM3 – but is only localised in the two branches attached to the same thiophene. In a similar way, the HOMO-1 is only localised in the two branches attached to the other thiophene. The angles between the two thiophene rings and the four benzene rings attached to them were also found to affect the LUMO, which is localised only in the central core and with little electron density reaching the four rings attached to it – unlike for bithi-MeOMeTPA and KTM3.

The calculated HOMO energy levels were found to have only small variations for bithi-MeOMeTPA, KTM3 and H112 molecules (HOMO = -4.90, -4.96 and -4.98 eV, respectively). This suggests that the molecules' energy levels are largely independent in respect to the geometrical differences or the different bond position in the bithiophene core.

Previously, Chi *et al.*^[226] have done an extensive simulation work on both KTM3 and H112, calculating crystal structure, hole mobilities and hole hopping pathways for the two HTMs, in addition to the molecular orbital analysis. They conducted their study with the Gaussian 09 software package by performing DFT calculations under the B3LYP level of theory with the 6-31G(d,p) basis set for geometry optimisation and energy calculations. The HOMO levels calculated for the two HTMs are almost 0.5 eV higher than those calculated in the present study and also significantly deviate from the experimental results.^[112,113] Thus, the semi-empirical PM7 method used here for the calculation of molecular geometry produces more precise results. The different geometries obtained in their study also give rise to very different orbital shapes compared to the present work.

4.3.2. Synthesis of bithi-MeOMeTPA

The synthesis of bithi-MeOMeTPA requires five reaction steps: three to prepare the triphenylamine branches, one to brominate the bithiophene core and a last one to link the two. Here, triphenylamine was synthesised *via* an Ullmann reaction, while the final linking was done *via* Suzuki coupling. A scheme of all five reaction steps is depicted in Figure 33, while the experimental details are given in section 6.2. Despite several purification steps, the CNHS elemental analysis of the compound yielded a percentage value for carbon deviating from the theoretical value by more than 1% (the two measurements gave values of 75.32% and 75.88%, while the theoretical value is 76.79%); the compound was therefore deemed non perfectly pure. The values for all other elements, however, were within the measurement error range ($\leq 0.30\%$). Furthermore, a MALDI-TOF mass spectrum of the compound between

0 and 2000 m/z revealed peaks corresponding to the main product and its fragments only. The ^1H NMR spectrum only shows the peaks related to the main compound as well. Therefore, the impurity is not detectable with MALDI-TOF and in a percentage low enough to not be detected by NMR. Moreover, it also only affects the percentage of carbon in the elemental analysis, while by chance all the other elements fall within the experimental error of the theoretical value.

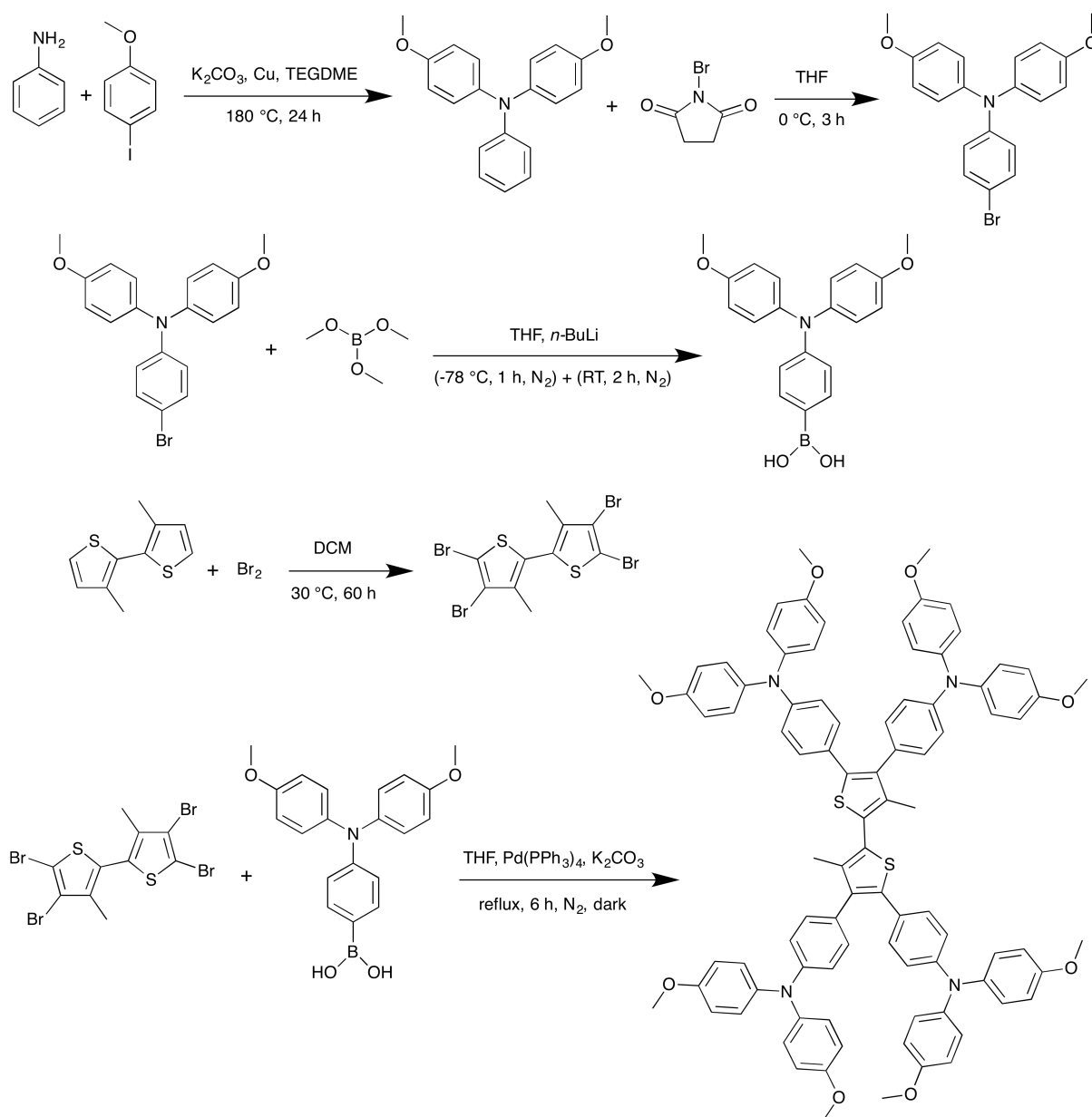


Figure 33. Reaction scheme for the synthesis of bithi-MeOMeTPA. TEGDME = tetraethylene glycol dimethyl ether.

4.3.3. Comparison of the properties of bithi-MeOMeTPA, KTM3 and H112

UV-Vis spectroscopy is a powerful technique to analyse the differences in the electronic properties of materials, in particular those induced by differences in the chemical nature of the core as applies to the bithi-MeOMeTPA, KTM3 and H112 set of compounds. Indeed, the four triphenylamine branches are the same in all three molecules, so any difference in the spectra can be confidently attributed to the effects from the central core. The UV-Vis spectra

for the three HTMs examined here are compared in Figure 34 along with the data for the H111 material taken from Ref. [113] (see Figure 28). The absorption peak at 300-310 nm found for all compounds is attributed to the triphenylamine groups and is not discussed further. The molar extinction coefficient estimated from the UV-Vis spectroscopic data for bithi-MeOMeTPA at 309 nm is $65\,000\text{ M}^{-1}\text{ cm}^{-1}$.

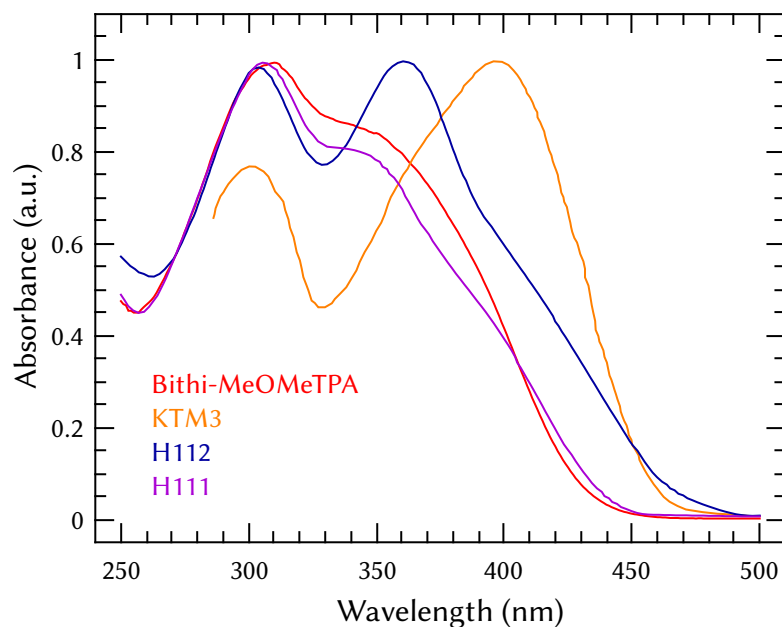


Figure 34. Normalised UV-Vis spectra of the solutions of bithi-MeOMeTPA (red) in chloroform, KTM3 (orange) in chlorobenzene, H112 (blue) and H111 (purple). Spectrum of KTM3 is adapted from Ref. [112] with the permission from RSC. Spectra of H111 and H112 are adapted from Ref. [113] with the permission from Wiley.

KTM3 has a spectrum very different from the other compounds in Figure 34, with a prominent peak at 397 nm as a main distinctive feature, which may be due to the different position of the bond that links the two thiophenes (3,3' instead of 2,2', Figure 28). Of greater interest is the comparison between the bithi-MeOMeTPA, H111 and H112 hole conductors. As discussed in section 1.5.2, the main structural difference between the latter two is the number of thiophene units in the central core: one for H111 and two for H112. In the UV-Vis spectra, this variation in aromatic conjugation is most probably reflected by very significant differences in the relative absorption for peaks in the 350-360 range, where only a shoulder is found for H111 in contrast to a very well defined peak for H112. The UV-Vis spectrum of bithi-MeOMeTPA is resembling that of H111 rather than that of H112, despite the presence of two bithiophene units in the core. This observation supports the outcomes of the computational analysis, *i.e.* the disruption of the aromatic conjugation between the two core units and corresponding suppression of absorption at higher wavelengths due to the twisting of the bithiophene core. Following this interpretation, the peak at 397 nm found for KTM3 can be hypothesised to be similar in nature to that at 360 nm for H112 and therefore be indicative of insignificant core twisting in the former. The difference in peak wavelength might result from the different bond position between the thiophenes in KTM3 and H112.

A differential scanning calorimetry (DSC) experiment was conducted on a powder sample of bithi-MeOMeTPA to determine phase transition temperatures for the compound. Figure 35 shows the DSC curves of the 1st and 2nd heating and cooling cycles.

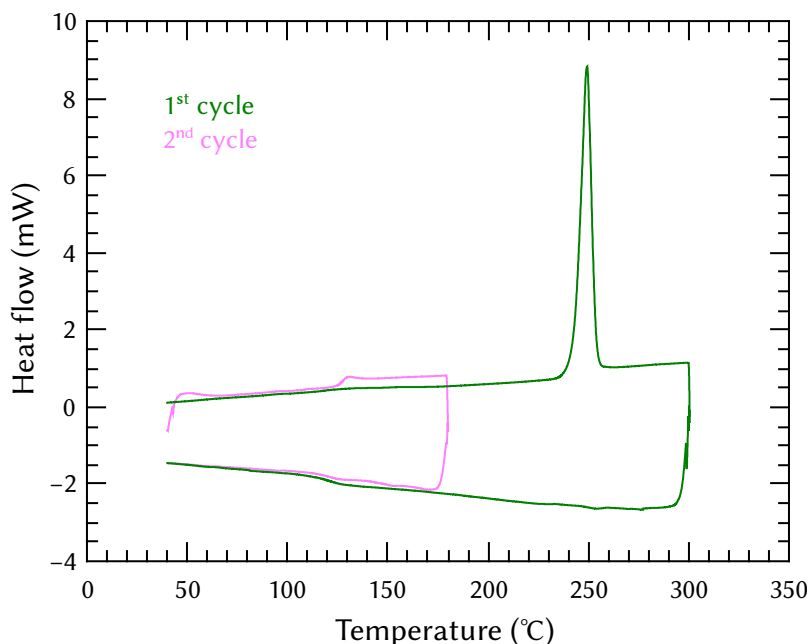


Figure 35. DSC curves ($10\text{ }^{\circ}\text{C min}^{-1}$ ramp) of bithi-MeOMeTPA. The first cycle (green) shows the peak related to the melting temperature, the second cycle (magenta) shows the second order transition related to the glass transition temperature.

During the first DSC cycle, the melting temperature of the crystalline powder was determined as $249.4\text{ }^{\circ}\text{C}$. During the subsequent cooling ramp, the liquid solidified as an amorphous film as no crystallisation peaks were detected, though a small second order transition at approximately $120\text{ }^{\circ}\text{C}$ was observed. After the glassy film was formed, it was possible to detect the second order transition attributed to the glass transition of the compound in the second cycle. Given a long-standing debate on the measurement of T_g by DSC,^[227] the two values for bithi-MeOMeTPA are provided here: 124.5 and $127.5\text{ }^{\circ}\text{C}$, as derived from the transition onset and midpoint, respectively. In both cases, the T_g is higher than that measured for H112 ($120\text{ }^{\circ}\text{C}$),^[113] which suggest a slightly improved stability for the bithi-MeOMeTPA film. It should be noted that no experimental detail was given by Li *et al.* on the heating rate used in their measurement of H112, which is well known to influence the phase transition temperatures.^[228] The glass transition temperature of KTM3 is surprisingly low at $65\text{ }^{\circ}\text{C}$,^[112] which is not only lower than that of H111 ($100\text{ }^{\circ}\text{C}$)^[113] but is even lower than that of a much smaller molecule, H101^[111] ($73\text{ }^{\circ}\text{C}$, see Figure 14 in section 1.5.2). No explanation for the very low T_g of KTM3 is given in the paper by Krishnamoorthy *et al.*

HOMO energies were measured here for bithi-MeOMeTPA and spiro-OMeTAD both in the solid state with PESA and in solution by voltammetry (1 mM solutions in chloroform with 0.1 M *n*-Bu₄NPF₆ as a supporting electrolyte). The voltammograms for the two HTMs are shown in Figure 36a, while the PESA data for the two hole conductors and the MAPbI₃

perovskite employed in the current work are depicted in Figure 37. For convenience, voltammograms for oxidation of KTM3^[112] and H112^[113] are shown in Figure 36b and c, although it should be noted that the solvent, concentration, reference electrode and supporting electrolyte used by Krishnamoorthy *et al.* and Li *et al.* were different from those employed here. Under voltammetric conditions, bithi-MeOMeTPA undergoes one chemically reversible oxidation with a mid-point potential of *ca.* 243 mV vs. Fc^{0/+}. This contrasts with the more complicated behaviours reported for KTM3 and H112, where two consecutive processes with close but obviously different reversible potentials can be easily distinguished (Figure 36). Qualitatively similar voltammetry with two resolved processes was reported for H111 as well, although the latter contains only one thiophene central unit.^[113] This difference in electro-oxidation of bithi-MeOMeTPA as compared to the other HTMs discussed here might then be also associated with the twisting of the central core in the former.

The HOMO of spiro-OMeTAD derived from voltammetric data in the present work (-5.20 eV) and reported in the study on H112^[113] (-5.21 eV) are in perfect agreement, while the value measured by Krishnamoorthy *et al.*^[112] is significantly more positive (-5.04 eV).

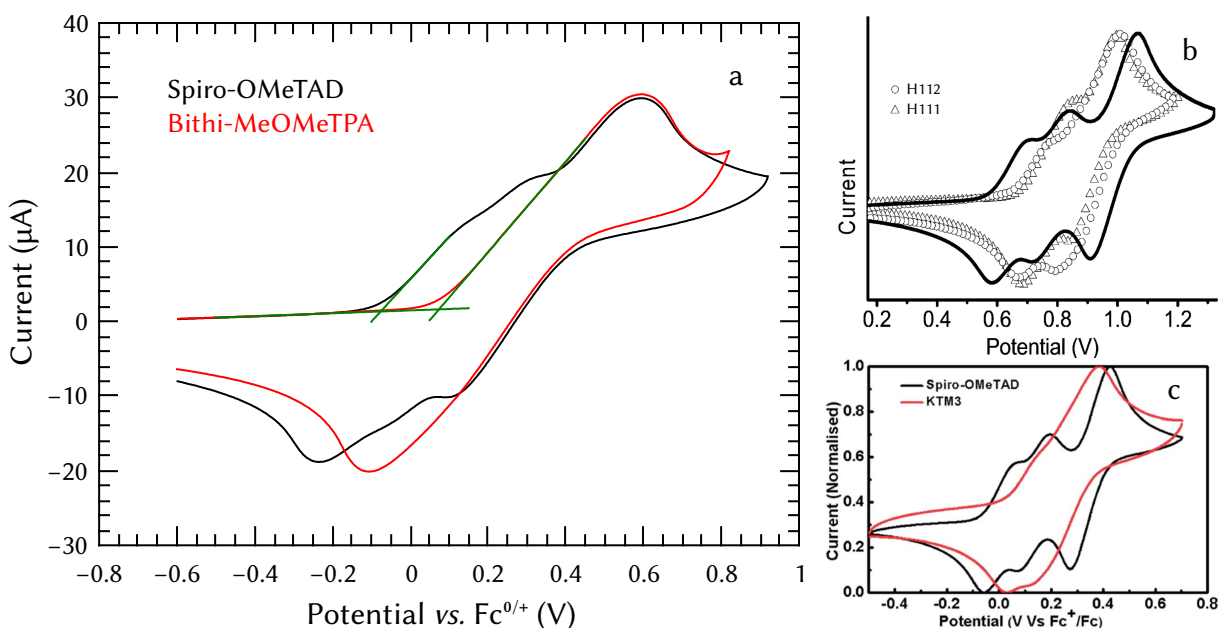


Figure 36. (a) Cyclic voltammograms (scan rate 0.1 V s^{-1}) for oxidation of 1 mM solutions of bithi-MeOMeTPA (red) and spiro-OMeTAD (black) in chloroform ($0.1 \text{ M n-Bu}_4\text{NPF}_6$) obtained with a glassy carbon electrode (3 mm diameter). Measurements were undertaken inside a N_2 -filled glove-box. Green lines show the estimated oxidation onsets. (b) Cyclic voltammograms (0.1 V s^{-1}) for oxidation of solutions of H112 (circles) and H111 (triangles) in dichloromethane ($0.1 \text{ M n-Bu}_4\text{NPF}_6$), reproduced from Ref. [113] with the permission from Wiley. (c) Cyclic voltammogram for oxidation of KTM3 (red), reproduced from Ref. [112] with the permission from RSC.

The voltammetric measurement on bithi-MeOMeTPA provided a HOMO level of -5.35 eV, which can be compared to -5.29 eV for H112 and -5.13 eV for KTM3 derived using the same technique. Given the differences in the measured HOMO of spiro-OMeTAD, it is useful to compare the relative differences between the reference HTM and the other three, which are -0.14, -0.09 and -0.09 eV for bithi-MeOMeTPA, H112 and KTM3, respectively. On this basis,

it can be concluded that H112 and KTM3 have similar HOMO energy, while that of bithi-MeOMeTPA is *ca.* 0.05 eV more negative.

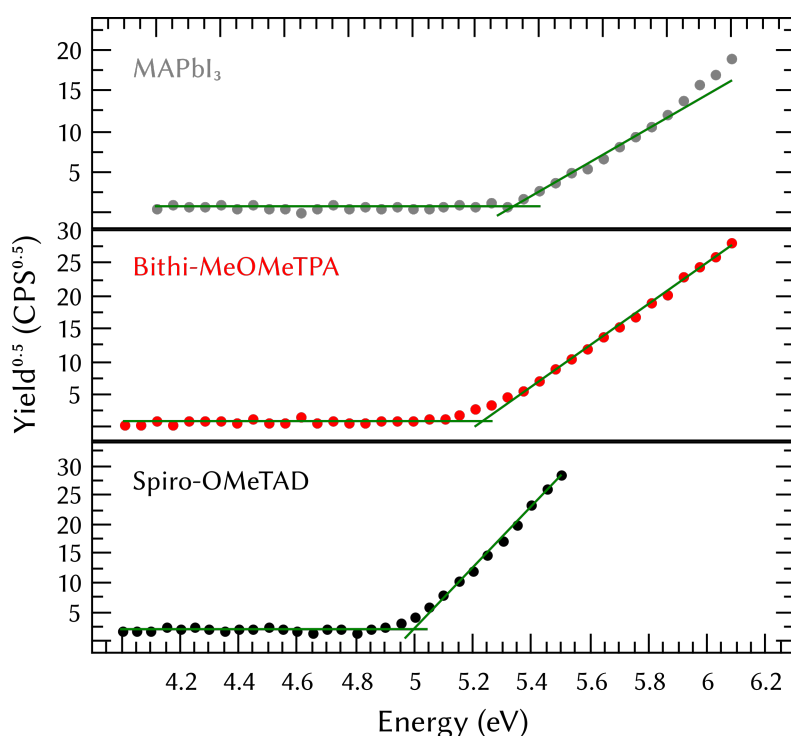


Figure 37. PESA measurements of the MAPbI₃ (grey) film deposited on FTO/c-TiO₂ and of the bithi-MeOMeTPA (red) and spiro-OMeTAD (black) films deposited on FTO/c-TiO₂/MAPbI₃. Green lines show linear fits used to derive E_{VB}/HOMO.

The HOMO level measured here for the solid-state bithi-MeOMeTPA by PESA was -5.32 eV, while that for spiro-OMeTAD was -5.00 eV. The solid-state HOMO level for bithi-MeOMeTPA is equivalent to that measured in solution, within the experimental error, while that of spiro-OMeTAD is 200 meV higher. Using the same technique, Krishnamoorthy *et al.*^[112] derived a HOMO energy of -5.29 eV for KTM3 and of -5.22 eV for spiro-OMeTAD. The latter value is unusually low and closer to the value obtained with CV. Unusual is also the fact that the value recorded in the solid state is lower than that measured in solution in the same work. Notwithstanding the uncertainties briefly summarised above, it can be concluded from both PESA and voltammetric studies that the HOMO energies of the thiophene-based HTMs KTM3, H112 and bithi-MeOMeTPA are lower than that of spiro-OMeTAD, which should theoretically produce higher V_{OC} in PSCs. Measurements of HOMO energies in vacuum with ultraviolet photoelectron spectroscopy (UPS), in order to verify the effect of photo-oxidation in air on the position of the HOMO level for bithi-MeOMeTPA, have not been performed. Photo-oxidation in air is a well known phenomenon for organic hole conductors. However, a study from Hawash *et al.*^[229] showed how the values for the HOMO level of spiro-OMeTAD measured with PESA and UPS – initially significantly different – become comparable after the HTM film was left in air to allow for photo-oxidation to occur. PESA was therefore regarded as the best method to measure the HOMO level in the solid state for the investigated materials, since all compounds were pre-oxidised

before cell fabrication (*vide infra*). Furthermore, neither Krishnamoorthy *et al.*^[112] nor Li *et al.*^[113] have undertaken UPS analysis in their studies, therefore this particular measurement would not provide further data for the comparison of the three hole conductors.

The E_{VB} for the MAPbI₃ perovskite film was measured by PESA to lie between -5.49 and -5.52 eV, which is slightly lower than the value of -5.43 eV commonly reported in the literature.^[19] This discrepancy is attributed to different fabrication methods of the perovskite layer, giving raise to films with slightly different electronic properties.

Conductivity measurements were performed for bithi-MeOMeTPA and spiro-OMeTAD both in their pristine form and with the conventional HTM additives LiTFSI, tBP and *p*-dopant Co complex which were also employed for solar cell fabrication. Layers of the two HTMs were deposited onto interdigitated IDA electrodes and conductivities were extracted from the two-probe *I-V* scan measurements according to the following equation:

$$\sigma = S \cdot \frac{d}{(2p-1)lh}, \quad (3)$$

Where σ is the conductivity, S is the slope of the linear approximation to the *I-V* data, d is the spacing between the two fingers of an electrode pair, p is the number of electrode pairs, l is the electrode overlap length and h is the thickness of the deposited film.^[230] The *I-V* scans measured for the two hole conductors are provided in Figure 38.

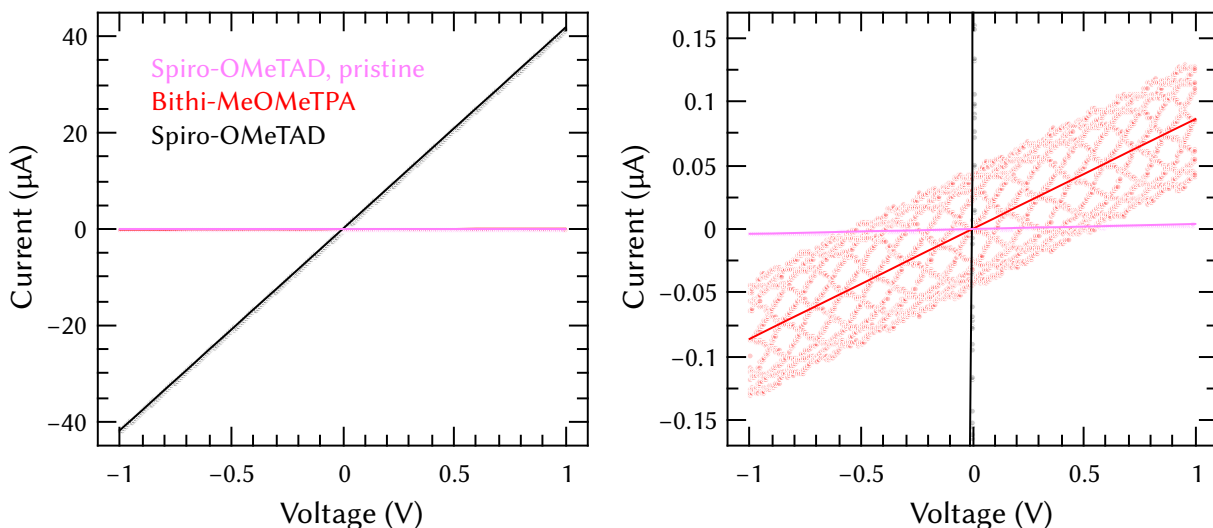


Figure 38. Representative *I-V* scans (scan rate 0.1 V s^{-1}) of spiro-OMeTAD (pristine, magenta and with additives, black) and bithi-MeOMeTPA (with additives, red) films spin-coated on IDA electrodes. The light dots of each colour represent the experimental data for each compound. The solid lines represent the linear fits of the experimental data. Panels (a) and (b) show full and low current ranges of the ordinate axis, respectively. Pristine bithi-MeOMeTPA was not conductive and resulted in a horizontal scatter centred at zero current (data not shown).

The conductivity measured for pristine spiro-OMeTAD was $4.9 \pm 0.9 \times 10^{-8} \text{ mS cm}^{-1}$, while *p*-doping and modification with with LiTFSI and tBP enabled significant improvements to $4 \pm 1 \times 10^{-4} \text{ mS cm}^{-1}$, in keeping with previous reports.^[231] Unfortunately, the conductivity of bithi-MeOMeTPA was almost three orders of magnitude lower than that of spiro-OMeTAD

and too low to be measured for pristine, non-modified films. Introduction of additives produced a bithi-MeOMeTPA layer with a conductivity of $7.2 \pm 0.9 \times 10^{-7} \text{ mS cm}^{-1}$.

Rectifying behaviours of spiro-OMeTAD and bithi-MeOMeTPA – both in their pristine form and mixed with the additives employed in PSCs fabrication – were probed by measuring I - V curves of diodes with a FTO|c-TiO₂|HTM|Au configuration in the dark. Measurements of the diodes under 1 sun irradiation were also performed (data not shown), with results similar to those obtained in the dark. Pristine layers of both HTMs showed very low forward currents and unsatisfactory rectifying behaviour, which was more pronounced for the bithi-MeOMeTPA film as best seen in the enhanced plot in Figure 39b. Modification with additives significantly improved the quality of the diodes, which exhibited negligible shunt and much higher forward currents, which were an order of magnitude higher for spiro-OMeTAD as compared to bithi-MeOMeTPA due to significant differences in conductivities (Figure 38). The measured cut-in voltages were 843 mV and 972 mV for the diodes based on spiro-OMeTAD (plus additives) and bithi-MeOMeTPA (plus additives), respectively.

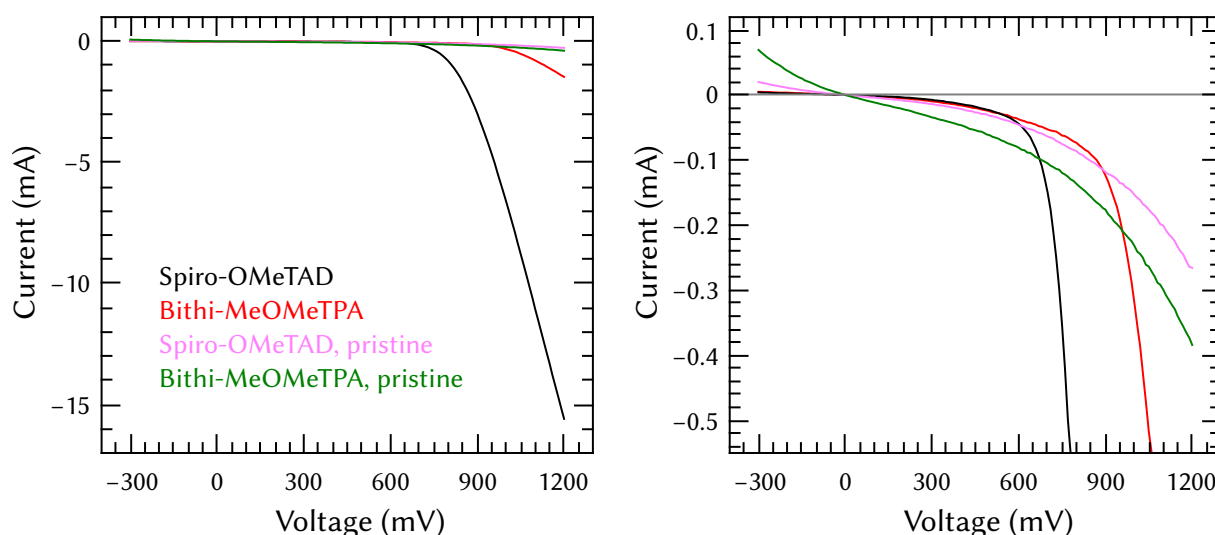


Figure 39. I - V characterisation (scan rate 0.1 V s^{-1}) of FTO|c-TiO₂|HTM|Au diodes for spiro-OMeTAD (pristine – magenta and with additives – black) and bithi-MeOMeTPA (pristine – green and with additives – red) HTMs. Left and right plots show the same data but with a different range on the ordinate scale.

4.3.4. Comparison of bithi-MeOMeTPA-, KTM3- and H112-based solar cells

Perovskite solar cells with the MAPbI₃ absorber and configuration FTO|c-TiO₂|MAPbI₃|HTM|Au were fabricated using either bithi-MeOMeTPA or spiro-OMeTAD as a hole transporter. The planar architecture was chosen for the devices to allow the use of the gas-assisted method – well established in our laboratory – for their fabrication.^[30] Spiro-OMeTAD-based PSCs produced with this method have efficiencies close to those reported by Krishnamoorthy *et al.*^[112] and Li *et al.*^[113] for their spiro-OMeTAD-based devices, facilitating the comparison. Solar cells fabricated to study KTM3^[112] and H112^[113] were based on a mesoporous TiO₂ layer, which is the only major difference with the PSCs constructed herein. The recipe used for the preparation of both bithi-MeOMeTPA and spiro-OMeTAD

solutions is described in section 6.3 and was adopted from the report on H112 with insignificant modifications to facilitate the comparison of the results.

J - V curves for the best-performing devices based on all examined HTMs are shown in Figure 40, where the data for KTM3 were kindly provided by the authors of Ref. [112] and those for H112 extracted from the relevant figure in Ref. [113]. Table 11 shows major photovoltaic parameters extracted from the J - V measurements for the tested solar cells (six for spiro-OMeTAD and seven for bithi-MeOMeTPA) with the data taken from literature for the KTM3-, H112- and corresponding reference spiro-OMeTAD-based devices. The scan direction is not reported for H112 and KTM3, although a FB \rightarrow SC direction is assumed as it provides better results except very rare cases (*e.g.* see Figure 26 in section 3.3.3).

As stated above, a direct comparison of the bithi-MeOMeTPA HTM introduced in the present study and those reported in Refs. [112,113] cannot be made, due to the fact that they have been fabricated and characterised in different environments. Therefore, discussions below are based on the relative differences between the solar cell parameters obtained with thiophene-based HTMs and the respective data for spiro-OMeTAD.

Table 11. Complete list of photovoltaic parameters^a for the MAPbI₃ perovskite solar cells with different HTMs under 1 sun AM1.5G irradiation.

Hole transporting material	V_{oc} (mV)	J_{sc} (mA cm ⁻²)	FF (%)	PCE (%)
Bithi-MeOMeTPA (best, FB \rightarrow SC)	892	18.1	59	9.5
Bithi-MeOMeTPA (best, SC \rightarrow FB)	837	17.8	50	7.5
Bithi-MeOMeTPA (average, FB \rightarrow SC)	860 \pm 20	17 \pm 3	55 \pm 3	8 \pm 1
Bithi-MeOMeTPA (average, SC \rightarrow FB)	800 \pm 30	16 \pm 3	50 \pm 1	7 \pm 1
Spiro-OMeTAD (best, FB \rightarrow SC)	984	18.7	72	13.3
Spiro-OMeTAD (best, SC \rightarrow FB)	951	18.4	36	6.3
Spiro-OMeTAD (average, FB \rightarrow SC)	980 \pm 10	17 \pm 1	72 \pm 1	12.2 \pm 0.9
Spiro-OMeTAD (average, SC \rightarrow FB)	940 \pm 10	17 \pm 2	39 \pm 2	6.1 \pm 0.7
H112 (best) ^[113]	1070	20.0	71	15.2
H112 (average) ^[113]	1070 \pm 20	19.7 \pm 0.3	70 \pm 2	14.7 \pm 0.4
Spiro-OMeTAD (reference for H112) (best) ^[113]	1050	19.9	69	14.4
Spiro-OMeTAD (reference for H112) (average) ^[113]	1050 \pm 10	19.5 \pm 0.9	69 \pm 2	14.0 \pm 0.4
KTM3 ^[112]	1080	13.0	78	11.0
Spiro-OMeTAD (reference for KTM3) ^[112]	1060	17.2	62	11.4

(a) Derived from the J - V curves (scan rate 100 mV s⁻¹ for bithi-MeOMeTPA- and spiro-OMeTAD-based devices fabricated here; unknown for the others). V_{oc} – open circuit voltage; J_{sc} – short-circuit current density; FF – fill factor; SC – short circuit; FB – forward bias. (b) Data provided for seven bithi-MeOMeTPA-based and six spiro-OMeTAD-based devices (this work); five H112-based and spiro-OMeTAD-based devices (Ref. [113]); unknown number KTM3-based and spiro-OMeTAD-based devices (Ref. [112]).

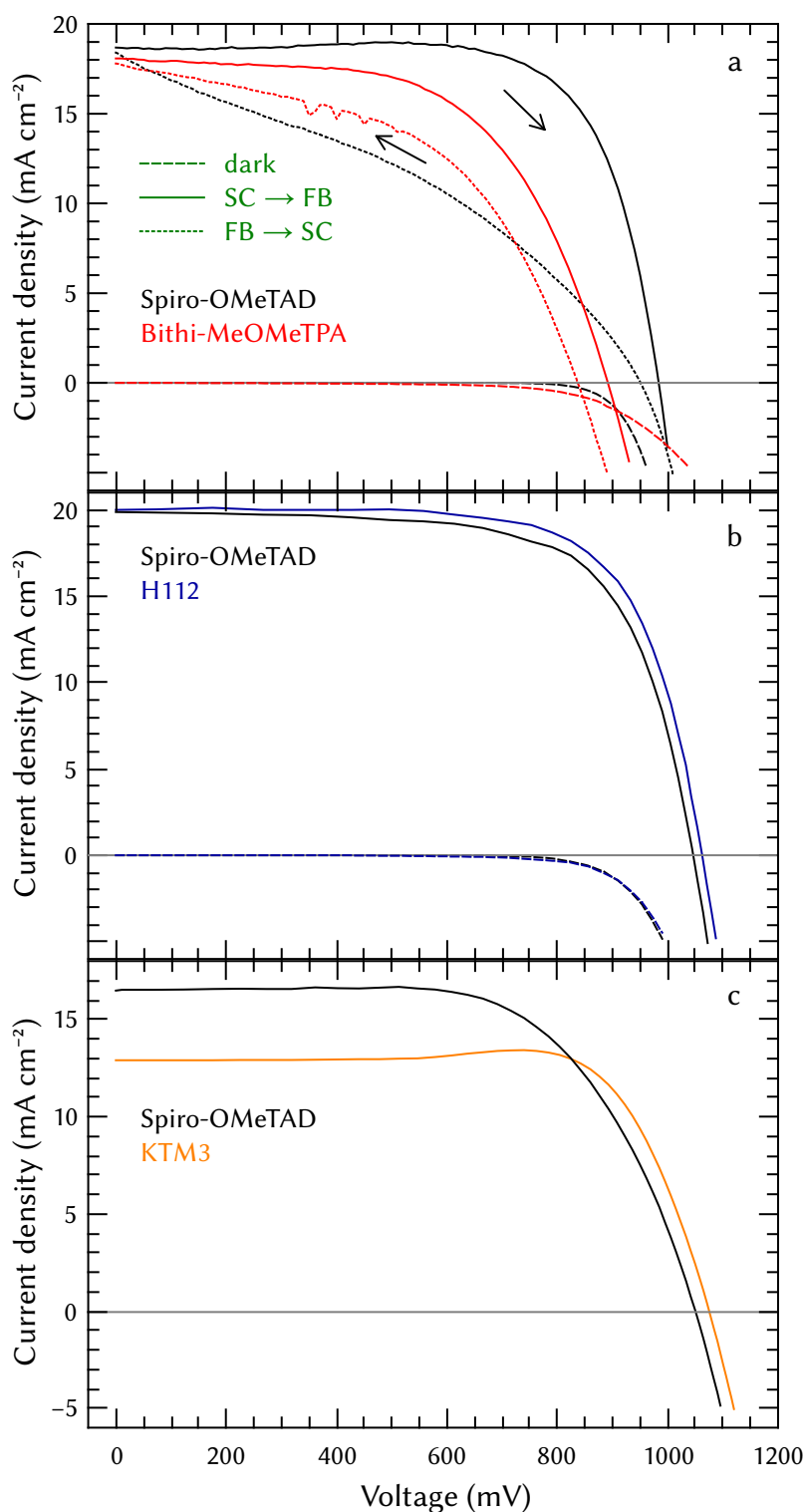


Figure 40. J-V curves (scan rate 100 mV s^{-1} ; 1 sun AM1.5G irradiation) for the best-performing MAPbI₃ PSCs based on different HTMs (all with LiTFSI, tBP and p-doping Co complex additives): (a) bithi-MeOMeTPA (red) and spiro-OMeTAD (black); (b) H112 (blue) and spiro-OMeTAD reported in Ref. [112] and (c) KTM3 (orange) and spiro-OMeTAD reported in Ref. [113]. Devices in panel (a) were masked with an aperture of 0.16 cm^2 to define the active area. Solid curves show sweeps measured in the SC \rightarrow FB direction; dotted curves show data obtained in the FB \rightarrow SC direction; dashed curves show data obtained in the dark.

The very first fact to consider is the enormous hysteresis of the PSCs based on spiro-OMeTAD (hysteresis index of 0.6), while for those based on bithi-MeOMeTPA the hysteresis

is mitigated (hysteresis index of 0.2). The large hysteresis makes it impossible to understand which hole conductor is higher performing – spiro-OMeTAD or bithi-MeOMeTPA. Unfortunately, the hysteretic behaviours of H112, KTM3 and spiro-OMeTAD have not been investigated by either Li *et al.*^[113] or Krishnamoorthy *et al.*,^[112] so it is not possible to say if the large hysteresis reported in the present study is due to sub-optimal device fabrication, to the use of planar structure for the devices, to the particular HTM recipe used for this study or a combination thereof. Nevertheless, a comparison of the various HTMs based on the FB \rightarrow SC sweep J - V curves can be considered valid, as they have all been measured under similar conditions. Furthermore, a quasi-steady-state measurement shows that bithi-MeOMeTPA's PCE is mostly stable over a 15 min measurement period (PCE = 6.6% at 630 mV).

The most noteworthy difference between the three bithiophene-based HTMs is the lower V_{OC} and FF of bithi-MeOMeTPA as compared to KTM3 and H112 (Table 11). Indeed, for the latter two materials these parameters are slightly higher than for the reference HTM, while the solar cells based on the hole transporter introduced here are excelled by spiro-OMeTAD devices despite the deeper HOMO level. There is no clear evidence about the reasons for this behaviour. However, this difference might be attributed to a small amount of photoshunting and a higher series resistance, as suggested by the slopes of the J - V curve for bithi-MeOMeTPA-based PSCs close to short-circuit and open-circuit, respectively (Figure 40a). It was hypothesised above that a more 3D-structured molecule should produce more amorphous and glassy films with fewer pinholes compared to a flatter molecule with higher π -stacking capabilities (which should more easily form crystalline domains) leading, in principle, to reduced shunt pathways. The experimental results, however, suggest that this does not apply in the bithi-MeOMeTPA case. This observation can be interpreted as an insufficient quality of the films due to a lack of optimisation of the deposition procedures. As mentioned above, the same recipe for the HTM solution as in Ref. [113] was employed here to deposit bithi-MeOMeTPA, which was based on the assumption of very similar solubilities of this HTM and H112. However, it is noted that in the experimental section of the paper by Li *et al.*^[113] the recipe for the preparation of the spiro-OMeTAD solution was the only one reported and I assumed that the same recipe was applied to H112 as well. During the preparation of the HTM solutions, however, it became evident that the solubility of these bithiophene-based compounds in chlorobenzene is poorer than that of spiro-OMeTAD, which might result in a solution that is too concentrated for optimal deposition, leading to non-uniform film formation.

Another notable distinction between the three bithiophene-based HTMs is the low J_{SC} for the KTM3-based devices (Table 11), which was not discussed in the related paper. A possible insight about this evidence may come from the IPCE spectrum of the KTM3-based device,^[112] which shows an unusually low profile in the wavelength range between 500 and 800 nm, where the molar extinction coefficient of MAPbI₃ is lower as compared to shorter wavelengths. The IPCE for the spiro-OMeTAD-based device is not reported in the

publication but given the higher reported J_{SC} , it is expected that the difference is caused by an increased photon-to-electron conversion exactly in that range of wavelengths. H112 did not demonstrate similar behaviour and the J_{SC} of the devices based thereon were very close to the short-circuit current densities for the corresponding spiro-OMeTAD reference solar cells.^[113]

In summary, the data presented above allows for the suggestion of a plausible geometry-performance trend for the three examined bithiophene-based hole conductors. H112 has the most planar structure of the three and is the only HTM to outperform spiro-OMeTAD. KTM3 is intermediate in terms of bithiophene core twisting and provides PCEs that are only slightly inferior to those achieved with spiro-OMeTAD. Bithi-MeOMeTPA is the HTM with the higher degree of twisting of the core and that with the best defined 3D structure and the PSCs based on this compound are those with the lower efficiency compared to those fabricated with spiro-OMeTAD. A direct comparison between the three compounds in the same environment would be required to make strong conclusions about a geometry-performance relationship. With the present indirect comparison it can be hypothesised that higher π -stacking capabilities typical of flatter molecules – leading to higher conductivities – are more important than better film-forming properties typical of more 3D-structured materials to obtain efficient HTMs in PSCs.

The outcome of the present study is also in agreement with the works of Zhang *et al.*,^[134,221] although their analyses are based on molecules having significantly different electronic properties. In the work in Ref. [134] in particular, spiro-OMeTAD is compared to another hole conductor, H11. This new compound, while being relatively close in electronic properties and chemical composition to the former, is slightly more planar (the twisting angle between the two halves of the molecule is 81° as compared to 90° for spiro-OMeTAD) and outperforms the former. The third HTM investigated in Zhang's work, H12, while being even more planar than the other two possesses completely different electronic properties due to the double bond connecting the two halves of the molecule. Its performance, therefore, cannot be compared to those of the other two compounds. Furthermore, no direct comparison of spiro-OMeTAD and bithiophene-based HTMs and their performance in PSCs should be made based solely on structural geometry considerations. Molecular geometry is only one of the many parameters that determine the overall behaviour of a hole conductor and other factors, of which the molecule's chemical composition is the most prominent, can be equally or even more important.

4.4. Conclusions

A new organic small molecular hole conductor based on a sterically twisted bithiophene core and four triphenylamine branches, bithi-MeOMeTPA, was synthesised and its physico-chemical properties were assessed. Some of its properties, namely UV-Vis absorption, HOMO energy level and glass transition temperature were compared to the corresponding

parameters reported for two similar HTMs reported in the literature, H112^[113] and KTM3.^[112] Others, namely conductivity and rectifying behaviour in a diode, were compared with respect to the reference, state-of-the-art HTM spiro-OMeTAD. Finally, the performance of the newly synthesised molecule as a hole transporting material in PSC was compared to those of H112 and KTM3, to derive a relation between molecular geometry and device efficiency. Although a proper comparison between the three bithiophene-based hole transporters would require simultaneous testing in the same environment, it is possible to make an indirect comparison between the three on the basis of their relative performances with respect to the reference HTM spiro-OMeTAD.

The molecular geometries of the three examined bithiophene-based hole conductors were derived from computational chemistry methods and compared. The results showed that H112 is a relatively flat molecule, which should be capable of efficient π -stacking of its triphenylamine branches. Due to the almost orthogonal configuration between the thiophenes and the benzene rings attached to them, however, its HOMO was located on only half of the molecule, with the HOMO-1 located in the other half. KTM3 showed some degree of twisting and a less flat molecular configuration compared to H112. However, due to more favourable thiophene-benzene alignment, its HOMO runs across all the molecule, involving the central core and two opposite triphenylamine branches. Bithi-MeOMeTPA, with its twisted core, possesses a very well defined 3D molecular structure and its HOMO spans across all four triphenylamine branches, leaving the central core void of electron density. These differences in molecular configuration are also reflected in the experimentally obtained UV-Vis spectra.

For what concerns solar cell performances, the papers describing H112 and KTM3 are lacking some key measurements to enable proper comparisons, mainly because they were published before these supplementary but very important experiments (*e.g.* J - V scans in both directions and quasi-steady-state measurements) became common and mandatory practice. Based on the results of forward bias to short-circuit sweeps of the J - V curves, H112 is the best-performing HTM of the three, followed by KTM3 and bithi-MeOMeTPA. This trend in device performance follows the one in molecular geometries, going from the flatter H112 to the more 3D-structured bithi-MeOMeTPA. This comparison, despite not being conclusive as the three compounds were not tested in the same environment, suggests that, at least for what concerns organic small molecular hole transporters with the same functional groups, compounds that have a more planar structure perform better as HTMs.

5. Conclusions and perspective

The transition of human energy production from fossil fuels to renewable energy sources is becoming ever more urgent, if we are to avoid the effects of climate change becoming irreparable. Together with wind energy, the large-scale production of solar energy will play a key role in this transition thanks to the abundance of energy provided by the Sun. Existing solar panel technologies have already reached good energy conversion efficiencies and have recently become market viable, rivalling – and even beating – fossil fuels in cost efficiency. However, in order to supply a sufficiently high portion of our society's energy needs from solar sources, a combination of higher panel efficiencies and lower panel prices will need to be achieved, as well as the development of more flexible technologies to support solar installations in more, diverse environments.

Solar cells based on organometal halide perovskite light absorbers – a recently developed category of materials – have demonstrated a great potential in addressing all of the issues above. Their optoelectronic properties make these materials an ideal partner of silicon in multi-junction solar cells, allowing a significant increase in panel efficiency. Perovskites are fabricated using a solution-based process requiring low energy input and utilising Earth-abundant materials, allowing for a reduction of the panel and, thus, final energy prices. Furthermore, they work efficiently in diffused light and – in laboratory-scale devices – have already reached a remarkable 22% solar energy conversion efficiency, allowing the installation of solar energy collectors in environments where silicon panels are inefficient and unfeasible.

Perovskite solar cells belong to the family of *p-i-n* junction devices, where the light absorbing material (*i*) is brought in contact with an electron (*n*) and a hole (*p*) selective transporting layer on either side. To date, the state-of-the-art hole transporting material is spiro-OMeTAD, an organic small molecule. While efficient, the excruciating synthesis and purification steps required to obtain a solar-grade material make spiro-OMeTAD very expensive. For this reason, together with long-term stability issues, a new and superior hole conductor will need to be found before this kind of solar cells can reach the market stage. In the past four years extensive research efforts have produced a plethora of new HTMs, each belonging to one of the four categories of organic small molecules, polymers, inorganic metal salts and oxides or transition metal complexes. A few of the studied compounds outperform spiro-OMeTAD in PSCs but none has managed to establish itself as the new leading material in the field. Therefore, the quest remains to find a new, efficient material that will help the commercialisation of the perovskite solar cell technology.

This thesis focused both on the development of new hole transporting materials for PSCs and on the study of some of their fundamental properties, to provide useful insights for further research. State-of-the-art techniques have been used to provide a complete characterisation of each material. For example, energy levels have been probed with several methods both in solution (cyclic voltammetry) and in the solid state (ultraviolet

photoelectron spectroscopy and photoelectron spectroscopy in air) to identify possible differences in the energy levels either due to the different physical states of the molecule or associated with the different methods used. The electric properties of the materials have been studied both with conductivity measurements and by fabricating diodes to verify their rectifying behaviour. The optimisation of the deposition of the various components of a solar cell has been very thorough, with several key parameters taken into account (e.g. precursor solution composition and concentration, spin-coating speed and deposition method), which lead to the fabrication of over one thousand devices during the candidature. Solar cells underwent complete characterisation as well, with techniques such as current-voltage and quasi-steady-state analysis, incident photon-to-electron conversion efficiency and scanning electron microscopy. Both the synthesis and the characterisation of these new materials have not always been free of trouble. Some of the syntheses performed have not given the results reported or expected and the optimal deposition of the bromide-based perovskite has required numerous efforts.

In the present work, a new category of materials, namely redox-active transition metal complexes, has been introduced to act as a solid-state hole conductor in PSCs. In chapter 2, the first compound of this category – a Fe(II/III) metal complex based on the hexadentate polypyridyl bpyPY4 ligand and the OTf⁻ counter-ion – is presented and integrated into photovoltaic devices based on the FAPbBr₃ light absorber. The studied Fe complex shows a conductivity five times higher and a deeper HOMO level compared to those of spiro-OMeTAD (conductivity for the latter was measured in the 10% oxidised state, since conductivity of the pristine compound is very low). Despite the favourable electronic properties, devices fabricated with the Fe complex are less efficient than those fabricated with spiro-OMeTAD and in particular the V_{oc} is significantly lower, notwithstanding the deeper HOMO of the Fe complex. While preliminary results show that recombination losses at the HTM/perovskite interface may be the cause of the poor performance, further in-depth studies are required to fully understand the reasons behind it.

After having introduced this new category of HTM materials to the field, a plausible approach to improve their charge transporting properties was identified. Given that transition metal complexes are typically cationic materials, it was postulated that the counter-ions required to balance the charge in the solid-state film would spatially separate the complexes, hindering the charge transport process. Chapter 3 aims to verify this hypothesis *via* comparisons of the characteristics of HTMs based on two Co(II/III) complexes differing in the number of counter-ions, which were applied to a mixed cation perovskite light absorber. One complex features the same neutral bpyPY4 ligand of the Fe complex mentioned above, while the other examined Co-based HTM is comprised of two negatively charged py₂pz ligands. The negatively charged ligands balance the charge of Co(II) making the complex neutral without additional counter-ions, while the Co(III) state of the complex is balanced by a single counter-ion, greatly reducing the concentration of the latter in the solid-state film. Despite the overall low performances of both materials in PSCs,

the results obtained suggest that the HTM film with fewer counter-ions exhibits superior charge transporting properties. This conclusion was based on two facts: first, solar cell efficiencies achieved with the py₂pz-based complex were at least two-fold higher than those obtained with the bpyPY4-based cobalt HTM. Second, functioning devices could only be produced with the pristine form (that is, without the inclusion of any additives) of the py₂pz-based complex as an HTM, while solar cells fabricated with the pristine form of the complex based on the bpyPY4 ligand were non-functional due to very low current densities.

The application of the three studied metal complexes to perovskite solar cells did not produce outstanding results, which is attributed to sub-optimal contacts at the HTM|perovskite interface. The design of the Fe complex applied for the first time to PSCs was based on a similar Co complex (later employed in the second study herein) that has produced promising results in ssDSSCs, which motivated further exploration. The study reported in chapter 3 was mainly focused on establishing the differences between two different materials rather than pursuing record efficiencies. For these reasons, redox-active metal complexes should not be discarded as HTMs for PSCs and other solution processed electronic devices. Rather, future studies should focus on the synthesis of ligands with functional groups that allow better interaction with the perovskite layer, building on the knowledge acquired in the present work. Ideally, the ligand will be negatively charged and will feature functional groups that allow good electric contact with the perovskite light absorber. The complex should also be of a suitable redox potential to energetically match the perovskite absorber. The nature of the metal centre is also extremely important and iron is likely a good choice as it has stable 2+ and 3+ oxidation states only, is non-toxic and Earth-abundant. Other potential choices are manganese and copper.

Finally, chapter 4 reports on the study of organic small molecule hole conductors, both experimentally and through DFT calculations. A newly synthesised molecule featuring a twisted bithiophene core and four triphenylamine branches was compared to two similar molecules previously reported in the literature, to establish an interrelation between the geometrical structure of these HTMs and their performance in PSCs. The three compounds examined, in fact, are all based on the same type of core and side branches and their structural differences are associated with variations in core twisting or thiophene-thiophene bond position. Notwithstanding different molecular geometries, the electronic properties of these HTMs were very similar, which was critical for a reliable analysis of the structure-function relationships. The study suggests that a flatter molecule provides better results as a hole transporter in a perovskite solar cell.

To date, the available literature includes more than a hundred published papers reporting on organic hole transporting materials for perovskite solar cells – some of them with very good results and a thorough characterisation. However, very few of these publications focus on fundamental aspects of the materials and aim to further our understanding on which particular configuration of a parameter that is common to all (or many) organic hole

conductors (*e.g.* molecular geometry) works best, in order to guide future research in the right direction. The present study aims to broaden the fundamental knowledge on hole conductors. The fact that the three examined molecules were not tested in the same environment, however, limits the conclusions which may be drawn, to some extent. In the future, it would be useful to test these compounds together in the same laboratory – to verify the outcomes of this study – and to perform a similar comparison with different materials, to confirm that a certain molecular geometry is truly beneficial for the hole transport. Not limited to molecular geometry, similar comparative studies would be also highly useful for other characteristics as well.

As a closing remark, I would like to say that during my PhD candidature I have seen or heard of several good scientific studies, very thorough in their analysis and with interesting conclusions, rejected from higher ranked journals because “the cell efficiency is too low”. I agree that higher efficiencies bring the technology closer to market and that if a device performs too poorly it is hard to differentiate whether the result stems from an actual behaviour or merely poor construction. However, we should agree that an iodide perovskite-based device with 14% or more PCE is adequate to give meaningful and trustworthy results. Not all studies should be focused on reaching top efficiency and not all research groups will have sufficient resources to achieve it. This should not be a reason to reject a paper, where the work is soundly done and useful to the research community. Indeed, the knowledge that a good study will have a chance to be published in more renowned journals may well give the impetus to pursue more fundamental and comparative studies, which in the medium term will allow us to reach higher device efficiency, improved stability and lower price in a shorter time.

6. Experimental section

6.1. Materials

Unless otherwise specified, all materials were purchased from either Alfa Aesar or Sigma-Aldrich and used as received. Spiro-OMeTAD (2,2',7,7'-tetrakis-(*N,N*-di-*p*-methoxyphenylamino)-9,9'-spirobifluorene) was purchased from Luminescence Technology Corp. (Lumtec). 3,3'-dimethyl-2,2'-bithiophene was purchased from Fluorochem. Recrystallised formamidinium iodide, recrystallised methylammonium bromide and fluorine-doped tin oxide (FTO) glass TEC8 (sheet resistance $8 \Omega \square^{-1}$) were purchased from Dyesol. Interdigitated array microelectrodes were purchased from BAS-ALS, Japan.

6.2. Syntheses

Synthesis of *N,N,N',N'*-tetramethylsuccinamide (1)

DMF (460 mL, excess), succinic acid (21.3 g, 180 mmol, 1.00 eq) and phosphorus pentoxide (54.8 g, 386 mmol, 2.14 eq) were poured in a 1 L flask and stirred at reflux for 21.5 h. The solvent was removed with rotary evaporation. The crude product was purified by vacuum distillation. Distillation was started at 160 °C and 1 mbar and ended at 190 °C and 0.3 mbar. After distillation, the product was recrystallised from ethanol as a white solid. Yield: 22.4 g (72%). MS (ESI): *m/z* calcd. for [M+Na⁺]: 195.1, found: 195.1. ¹H NMR (400 MHz, CDCl₃): δ 2.61 (s, 4H, CH₂), 2.95 (d, *J* = 46.5 Hz, 12H, CH₃).

Synthesis of 1,4-di-(2-pyridyl)-butan-1,4-dione (2)

2-bromopyridine (1.8 mL, 18.9 mmol, 2.05 eq) was poured in a 50 mL flask, degassed and kept under nitrogen atmosphere, then diluted in 15 mL of anhydrous THF. The flask was immersed in an acetone/dry ice bath and, once the temperature was stabilised, *n*-butyllithium 2.5 M in hexanes (7.5 mL, 18.9 mmol, 2.05 eq) was added dropwise to the solution under vigorous stirring, which turned from colourless to yellow-red. The mixture was stirred for 2.5 h. Vacuum pre-dried (50 °C, 1 mbar, 2 h) compound **1** (1.58 g, 9.2 mmol, 1.00 eq) was added as a solid to the mixture, the bath was removed and the reaction proceeded under stirring at room temperature (RT) overnight. The flask was opened and Na₂SO₄·10H₂O (12.6 g, excess) was added to the mixture. The solution turned rust-red and a precipitate formed. The solution was filtered and the filtrate was dispersed in water. The dispersion was acidified with HCl to pH 6.5 and then filtered. The filtrate was recrystallised from EtOAc to yield the pure product (586.4 mg). The water liquor was extracted three times with DCM, the organic phase was dried with MgSO₄ and the solvent removed with rotary evaporation. The crude product was purified with a silica chromatographic column using a 2:1 petroleum benzine (PB)-EtOAc solvent mixture as eluent. The column yielded 176.0 mg of off-white product. Yield: 762.4 (35%). MS (ESI): *m/z* calcd. for [M+Na⁺]: 263.1, found: 263.0.

¹H NMR (400 MHz, DMSO-d₆): δ 3.57 (s, 4H, CH₂), 7.68 (ddd, *J* = 7.4 Hz, 4.8 Hz, 1.4 Hz, 2H, aromatics), 7.93-8.04 (m, 4H, aromatics), 8.76 (ddd, *J* = 4.8 Hz, 1.7 Hz, 0.9 Hz, 2H, aromatics).

Synthesis of 2,5-dipyridin-2-yl-pyrrole (3)

Compound 2 (4.520 g, 18.8 mmol, 1.00 eq) and ammonium acetate (17.34 g, excess) were poured into a 100 mL flask, degassed and kept under nitrogen atmosphere. The mixture was heated to 125 °C and then kept stirring at this temperature for 3 h. After cooling, water was added and the resulting aqueous solution was extracted three times with DCM. The organic phase was dried with MgSO₄ and the solvent removed with rotary evaporation. The crude product was purified with a silica chromatographic column using a 9:1 DCM-EtOAc solvent mixture as eluent at the beginning, to remove an impurity with a high R_f, and 2:1 afterwards. Yield: 4.040 g (97%). MS (ESI): *m/z* calcd. for [M+H⁺]: 222.1, found: 222.1. ¹H NMR (400 MHz, CDCl₃): δ 6.77 (d, *J* = 2.6 Hz, 2H, aromatics), 7.06 (ddd, *J* = 7.3 Hz, 4.9 Hz, 1.3 Hz, 2H, aromatics) 7.55-7.65 (m, 4H, aromatics), 8.53 (ddd, *J* = 4.9 Hz, 1.8 Hz, 1.0 Hz, 2H, aromatics), 10.60 (s broad, 1H, NH).

Synthesis of bis-(2,5-dipyridin-2-yl-pyrrole)-cobalt(II) [Co(py₂pz)₂] (4)

Compound 3 (601.0 mg, 2.72 mmol, 2.00 eq) was poured into a 100 mL flask, degassed and kept under nitrogen atmosphere. Anhydrous THF (40 mL) was added and the flask was immersed in an acetone/dry ice bath and, once the temperature was stabilised, *n*-butyllithium 2.5 M in hexanes (1.1 mL, 2.72 mmol, 2.05 eq) was added dropwise to the solution under vigorous stirring, which turned from a very pale to an intense yellow. The mixture was allowed to react for 30 min. Co(OTf)₂·½MeCN (511.7 mg, 1.36 mmol, 1.00 eq) was added to the solution and the bath was removed. Upon addition of the cobalt salt the solution turned red. The solution was stirred for 2 h at RT, then it was poured into water. The aqueous solution was extracted three times with DCM, the organic phase was dried with MgSO₄ and the solvent removed with rotary evaporation. The crude product was transferred inside a glove-box to be recrystallised twice via slow diffusion of Et₂O inside a chloroform solution of the complex. The final compound was obtained as purple needles. Yield: 550.3 mg (81%). HR-MS (ESI): *m/z* calcd. for [Co(py₂pz)₂]⁺: 499.1076, found: 499.1068. Elem. anal. calcd. for C₂₈H₂₀CoN₆: C, 67.34; H, 4.04; Co, 11.80; N, 16.83. Found: C, 67.36; H, 4.30; Co, 10.75; N, 16.99.

Synthesis of bis-(2,5-dipyridin-2-yl-pyrrole)-cobalt(III) trifluoromethanesulfonate [Co(py₂pz)₂](OTf) (5)

Inside a glove-box, compound 4 (250.1 mg, 0.56 mmol, 1.00 eq) was dissolved in DCM (3 mL) inside a vial. In a separate vial, Ag(OTf) (143.9 mg, 0.56 mmol, 1.00 eq) was dissolved in MeCN (3 mL) and added dropwise to the former solution under stirring. The solution turns from red to black (yellow when highly diluted) upon addition of the silver salt. After stirring for 15 min, the mixture was taken out of the glovebox to remove Ag⁰ by filtration and remove the solvent by rotary evaporation. The crude product was taken again inside the

glove-box to recrystallise via slow diffusion of Et₂O inside a MeCN solution of the complex. The final crystals are black in colour, with ½ MeCN crystallisation solvent inside. Yield: 312.8 mg (93%). HR-MS (ESI): *m/z* calcd. for [Co(py₂pz)₂]⁺: 499.1076, found: 499.1068; calcd. for OTf⁻: 148.9526, found: 148.9529. Elem. anal. calcd. for C₆₀H₄₃Co₂F₆N₁₃O₆S₂: C, 53.86; H, 3.24; Co, 8.81; N, 13.61; S, 4.79. Found: C, 53.58; H, 3.30; Co, 8.40; N, 13.58; S, 4.70. ¹H NMR (400 MHz, MeOD-d₄): δ 2.03 (s, 1.5H, MeCN), 6.68-6.70 (m, 4H, aromatics), 6.81 (ddd, *J* = 6.4 Hz, 5.8 Hz, 2.4 Hz, 4H, aromatics) 7.44 (s, 4H, aromatics), 7.69-7.75 (m, 8H, aromatics). ¹³C NMR (101 MHz, MeOD-d₄): δ 115.57, 120.31, 123.88, 141.79, 143.92, 152.24, 160.14.

Synthesis of 4,4'-dimethoxytriphenylamine (6)

Aniline (4.108 mL, 45.0 mmol, 1.00 eq), 4-iodoanisole (21.06 g, 90.0 mmol, 2.00 eq), potassium carbonate (12.43 g, 89.9 mmol, 2.00 eq), Cu powder (6.50 g, excess) and tetraethylene glycol dimethyl ether (TEGDME, 30 mL) were poured in a 100 mL flask, degassed and kept under nitrogen atmosphere. The mixture was heated to 180 °C and stirred at this temperature for 24 h. The reaction mixture was hot filtered and poured in 500 mL of water. The precipitated product was filtered again and recrystallised from EtOAc. After filtration, a light beige solid was obtained. Yield: 3.81 g (28%). ¹H NMR (400 MHz, CDCl₃): δ 3.77 (s, 6H, OMe), 6.77-6.93 (m, 7H, aromatics), 7.01-7.04 (m, 4H, aromatics), 7.12-7.17 (m, 2H, aromatics).

Synthesis of 4,4'-dimethoxy-4''-bromo-triphenylamine (7)

Compound 6 (3.50 g, 11.5 mmol, 1.00 eq) and THF (68 mL) were poured in an Erlenmeyer flask and cooled down to 0 °C with an ice bath. *N*-bromosuccinimide (2.04 g, 11.5 mmol, 1.00 eq) was then added and the solution was stirred for 5 h at 0 °C. The reaction was quenched with water and extracted with DCM. The organic fraction was dried with magnesium sulphate and the crude product was purified with a chromatographic column using an 8:1 petroleum benzene (PB)-DCM solvent mixture as eluent. After evaporating the solvent, a yellow viscous liquid was obtained. Yield: 4.45 g (101%). ¹H NMR (400 MHz, CDCl₃): δ 1.26-1.30 (m, impurity), 2.07 (s, impurity), 3.81 (s, 6H, OMe), 4.12 (q, impurity), 6.80-6.86 (m, 6H, aromatics), 7.04-7.06 (m, 4H, aromatics), 7.24-7.27 (m, 2H, aromatics).

Both the yield value and the NMR show that the product is not pure – most probably due to some residual succinimide – but it was used as is for the preparation of 8.

Synthesis of (4-(bis(4-methoxyphenyl)amino)phenyl)boronic acid (8)

Compound 7 (4.20 g, 10.9 mmol, 1 eq) was dissolved in dry THF (10 mL) under nitrogen purge in a dry ice-acetone bath at -78 °C. When the temperature was reached, *n*-butyllithium 1.6 M in hexanes (8.13 mL, 13.0 mmol, 1.19 eq) was added dropwise under vigorous stirring. After 90 min, trimethyl borate (1.45 mL, 13.0 mmol, 1.19 eq) was added dropwise and the bath was removed. The solution was stirred at room temperature for 3 h. Water was further added to the solution followed by 6 M HCl_{aq} until pH < 7 was achieved. The reaction mixture was poured in water and extracted with three 30 mL portions of DCM.

The organic fraction was dried with magnesium sulphate and the crude product was purified with a chromatographic column using a PB-EtOAc solvent mixture as eluent with a gradient that started with a 4:1 ratio and ended with a 1:1 ratio. After evaporating the solvent, a yellow-brown solid was obtained. Yield: 2.35 g (62% yield). ¹H NMR (400 MHz, CDCl₃): δ 3.80 (s, 6H, OMe), 5.28 (s, 0.4H, boronic acid), 6.83-6.88 (m, 4H, aromatics), 6.91-6.94 (m, 2H, aromatics), 7.08-7.14 (m, 4H, aromatics), 7.93-7.96 (m, 2H, aromatics).

Synthesis of 3,3'-dimethyl-4,4',5,5'-tetrabromo-2,2'-bithiophene (9)

3,3'-dimethyl-2,2'-bithiophene (0.43 mL, 2.58 mmol, 1.00 eq) was dissolved in 15 mL of DCM in a 250 mL flask. Br₂ (0.73 mL, 14.2 mmol, 5.52 eq) was dissolved in DCM (total solution volume of 50 mL) and was added dropwise to the solution of 3,3'-dimethyl-2,2'-bithiophene. Once the addition was completed, the mixture was heated to 35 °C and stirred for 24 h. During this stirring period, two more portions of Br₂ (0.1 mL, 1.95 mmol, 0.76 eq) were added to the solution when it lost its red colour. After the reaction was finished, 100 mL of a saturated solution of sodium bisulphite in water were added to remove the excess of Br₂. The organic fraction was separated and washed again with a saturated solution of sodium chloride and sodium bicarbonate, separated again and dried with magnesium sulphate. After the solvent was evaporated, the crude product was recrystallised from a 1:1 chloroform-ethanol solvent mixture. After filtration, a yellow-pink solid was obtained. Yield: 1.00 g (76%). ¹H NMR (400 MHz, CDCl₃): δ 2.14 (s, 6H, Me).

Synthesis of 3,3'-dimethyl-4,4',5,5'-tetrakis-(*p*-(*N,N*-di-*p*-methoxyphenylamino)phenyl)-2,2'-bithiophene (bithi-MeOMeTPA) (10)

Compound **9** (0.69 g, 1.35 mmol, 1 eq), compound **8** (2.00 g, 5.73 mmol, 4.24 eq) and tetrakis(triphenylphosphine)palladium(0) (0.15 g, 0.13 mmol, 0.10 eq) were poured in a 3-neck flask and purged with nitrogen. In separate flasks, THF (20 mL) and a 2M potassium carbonate solution in water (3 mL) were also degassed and then poured into the main flask. The flask was covered with aluminium foil to keep it in the dark, the solution was heated to reflux and it was stirred under these conditions for 24 h. After cooling, the reaction mixture was poured into water and extracted with DCM. The organic fraction was again washed with water and then dried with magnesium sulphate. After evaporating the solvent, the crude product was purified with a chromatographic column with a PB-EtOAc mixture that started with a 4:1 ratio and increased the amount of EtOAc as the purification proceeded. After evaporating the solvent, the product fractions were recrystallised twice by dissolving the product at reflux in EtOAc and adding PB to the solution while heating until a precipitate was formed, then quickly cooling the solution in a freezer. After filtration – to ensure the complete removal of all palladium traces – the product was dissolved in 7 mL of dichloromethane and 312 mg of Quadrapure BZA® were added to the solution, which was then stirred at reflux for 48 h. To remove the Quadrapure beads, a small chromatographic column was prepared using DCM as eluent to filtrate the content of the flask. The beads were retained on top of the column while the product dropped in a stirred Erlenmeyer flask

containing 75 mL of methanol, precipitating. The flask was kept heated at 45 °C to remove the dropping DCM in order to promote the precipitation of the product. After elution was complete, the flask was stored in a freezer to complete precipitation. After filtration, a pale yellow solid was obtained. Yield: 0.32 g (17% yield). HR-MS (ESI): m/z calcd. for M^+ : 1406.5256, found: 1406.5284. Elem. anal. calcd. for $C_{90}H_{78}O_8N_4S_2$: C, 76.79; H, 5.59; N, 3.98; S, 4.55. Found: C, 75.32; H, 5.79; N, 3.86; S, 4.38. 1H NMR (400 MHz, $CDCl_3$): δ 1.24 (s, 3H, thiophene CH_3), 1.53 (s, 3H, thiophene CH_3), 3.78 (s, 24H, OMe), 6.79-7.07 (m, 48H, aromatics). ^{13}C NMR (101 MHz, $CDCl_3$): δ 1.23, 15.47, 29.92, 55.70, 114.88, 119.77, 120.42, 126.80, 127.04, 129.46, 129.66, 131.09, 137.38, 138.69, 141.19, 147.65, 156.00, 156.18.

Synthesis of methylammonium iodide (11)

100 mL of ultra-pure water (Milli-Q Millipore; 18 M Ω cm) were poured in a 500 mL round-bottomed flask and degassed by streaming nitrogen through the liquid for 10 min. The nitrogen environment was maintained throughout the synthesis. 100 mL of a freshly opened 40% w/w solution of methylamine in water (1.56 mol, 2 eq) were added to the flask and the latter was cooled to 0 °C with an ice bath. Once temperature was stabilised, 50 mL of a freshly opened 57% w/w solution of HI in water (0.66 mol, 1 eq) were added dropwise under vigorous stirring. Once the addition was completed, the ice bath was removed and the solution was stirred for 1 h. Upon reaction completion, the solvent was removed by rotary evaporation. The obtained white powder was ground with a pestle, transferred in a flask and kept under high vacuum (Schlenk) at 60 °C for 24 h to ensure dryness. After drying, the compound was handled in inert atmosphere (glove-box). 1H NMR (400 MHz, MeOD): δ 2.56 (s, 3H, CH_3), 4.81 (s, 3H, NH_3).

6.3. Fabrication of devices

General procedure for substrate preparation for diodes and solar cells

Glass covered with fluorine-doped tin(IV) oxide (FTO) was patterned using a laser engraver (Universal Laser Systems, VLS3.50) and subsequently washed in three steps with a 1 vol.% solution of Hellmanex in water, pure water and 96 vol.% ethanol, each time under sonication (Elma, Elmasonic S300H) at 50 °C for 20 min. After the last cleaning step, the FTO substrates were dried under an air stream. A compact TiO_2 blocking layer (c- TiO_2) was deposited onto the FTO surface by spray pyrolysis. For the deposition, 20 mL of a 1:19 solution of titanium diisopropoxide bis(acetylacetonate) in isopropanol were prepared to be sprayed on a substrate heated at 500 °C (solution is only partly used for the deposition). The solution was pumped at 0.5 mL min^{-1} through a Sono-Tek AccuMist ultrasonic spray nozzle mounted on a custom-made xyz stage with a New Era Pump Systems syringe pump model NE-1000X. The nozzle was kept at 13.5 cm from the glass and it was programmed to scan the width of two glasses positioned side by side on the hotplate with 1.5 cm intervals in height between each scan, for a total of 10 scans along the height, then to scan the height of the two glasses with 1.5 cm intervals in width between each scan, for a total of 17 scans along the width; the

scanning procedure was repeated eight times. Prior to perovskite or HTM deposition, the FTO|c-TiO₂ substrates were further cleaned by ozone plasma for 10 min (Harrick Plasma, PDC-002; plasma intensity set to “high”; air pressure inside the chamber *ca* 1100 mTorr). When a mesoporous titania layer was required, after plasma cleaning a 1:6 wt.% solution of TiO₂ nanoparticles paste (Dyesol 30 NR-D) in ethanol was spin-coated on the substrate at 4 000 rpm for 30 s with an acceleration of 2 000 rpm s⁻¹. After deposition, the mesoporous layer was first dried at 150 °C for 5 min and then sintered at 500 °C for 30 min in air.

Preparation of the MAPbI₃-based devices

All procedures were carried out in a glove-box under a high-purity nitrogen atmosphere with less than 0.1 ppm oxygen and water. The solution of MAPbI₃ was prepared by dissolving 289 mg of PbI₂ and 100 mg of compound **11** in 500 μL of DMF. The solution was shaken for 20 min then centrifuged for 5 min at 10 000 rpm. The ~1.2 cm² perovskite layer was deposited on the FTO|c-TiO₂ substrate by spin-coating 25 μL of the perovskite solution at 6 500 rpm for 30 s with an acceleration of 6 500 rpm s⁻¹. After approximately 2.5 s of the spinning, a 380 kPa nitrogen flow was applied for 10 s. The resulting film was annealed on a hotplate at 100 °C for 10 min, then allowed to reach room temperature.

For the HTM deposition, 100 mg mL⁻¹ solutions were prepared by dissolving 17.5 mg of spiro-OMeTAD and 22.5 mg of bithi-MeOMeTPA in 175 and 225 μL of CBZ, respectively. 9.29 μL of tBP, 5.65 μL of a 520 mg mL⁻¹ solution of LiTFSI in MeCN and 7.9 μL of a 500 mg mL⁻¹ solution of FK269 in MeCN were further added to the spiro-OMeTAD solution. 11.9 μL of tBP, 7.26 μL of a 520 mg mL⁻¹ solution of LiTFSI in MeCN and 8.8 μL of a 500 mg mL⁻¹ solution of FK269 in MeCN were further added to the bithi-MeOMeTPA solution. Afterwards, the bithi-MeOMeTPA solution was kept on a hotplate at 80 °C for 30 min under stirring to ensure complete dissolution. Both materials were deposited on the perovskite layer by spin-coating 25 μL of each solution at 4 000 rpm for 30 s with an acceleration of 4 000 rpm s⁻¹.

As a final step, an 80 nm layer of Au was deposited by thermal evaporation (DDong DD-GCMO3CR; deposition started when vacuum reached 3 × 10⁻¹ Torr; deposition speed: 0.2 Å s⁻¹ between 0-50 Å, 1 Å s⁻¹ between 50-400 Å, 2 Å s⁻¹ between 400-800 Å).

Preparation of MixCP-based devices

All procedures were carried out in a glove-box under a high-purity nitrogen atmosphere with less than 0.1 ppm oxygen and water. The solution of (Rb_{0.05}Cs_{0.05}FA_{0.75}MA_{0.15})Pb(I_{0.85}Br_{0.15})₃ was prepared by dissolving 461.0 mg of PbI₂, 16.8 mg of MABr, 13.0 mg of CsI, 10. mg of RbI, 37.5 mg of FABr and 77.4 mg of FAI in 750 μL of a 1:4 vol.% solution of DMSO in DMF. The ~1.2 cm² perovskite layer was deposited on the FTO|c-TiO₂|mp-TiO₂ substrate by spin-coating 25 μL of the perovskite solution with a two-step program of 1 000 rpm for 10 s at 1 000 rpm s⁻¹ acceleration and 4 000 rpm for 30 s at 4 000 rpm s⁻¹ acceleration. Upon 15 s of the spinning, 110 μL of CBZ were pipetted on the

substrate. The resulting film was annealed on a hotplate at 100 °C for 40 min, then allowed to reach room temperature.

For the HTM deposition, 25 mM solutions of the Co complexes were prepared by dissolving 12.5 mg of $[\text{Co}(\text{py}_2\text{pz})_2]$ in 1 mL of CBZ and 16.7 mg of $[\text{Co}(\text{py}_2\text{pz})_2](\text{OTf})$, 24.0 mg of $[\text{Co}(\text{bpyPY4})](\text{OTf})_2$ and 26.7 mg of $[\text{Co}(\text{bpyPY4})](\text{OTf})_3$ each in 1 mL of nitromethane. The final HTM solutions were prepared by mixing 160 μL of the Co(III) species solution and 80 μL of the Co(II) species solution for the complexes with each ligand (pristine HTMs) or by adding 1.49 μL of a 520 mg mL^{-1} solution of LiTFSI in MeCN and 3.36 μL of tBP to the same mixture prepared for the pristine HTMs (HTMs with additives). The spiro-OMeTAD solution was prepared by dissolving 13.2 mg of spiro-OMeTAD, 5.40 μL of tBP and 2.40 μL of a 520 mg mL^{-1} solution of LiTFSI in MeCN in 160 μL of CBZ. The Co complex HTMs were deposited on the perovskite layer by spin-coating 25 μL of each solution at 2 000 rpm for 40 s with an acceleration of 200 rpm s^{-1} , while the spiro-OMeTAD was deposited by spin-coating 25 μL of the solution at 3 000 rpm for 30 s with an acceleration of 3 000 rpm s^{-1} .

As a final step, a 110 nm layer of Au was deposited by thermal evaporation (DDong DD-GCMO3CR; deposition started when vacuum reached 3×10^{-1} Torr; deposition speed: 0.2 \AA s^{-1} between 0-50 \AA , 1 \AA s^{-1} between 50-500 \AA , 2 \AA s^{-1} between 500-1,100 \AA).

Preparation of diodes

Each HTM composition was deposited on the FTO|c-TiO₂ substrate using the same solution and spin-coating procedure described for the solar cell fabrication. As a final step, a 110 nm layer of Au was deposited by thermal evaporation (DDong DD-GCMO3CR; deposition started when vacuum reached 3×10^{-1} Torr; deposition speed: 0.2 \AA s^{-1} between 0-50 \AA , 1 \AA s^{-1} between 50-500 \AA , 2 \AA s^{-1} between 500-1,100 \AA).

Preparation of IDAs for conductivity measurements

IDA electrodes were fabricated using photolithography. A thin photoresist layer was spin-coated onto a clean glass substrate and exposed to UV light through a chrome photomask of the desired pattern. The UV-exposed parts of the photoresist were subsequently removed by immersion into a developer solution and rinsed with deionised water. 10 nm chromium and 80 nm gold layers were evaporated on top using an e-beam evaporator. Substrates were sonicated in acetone for lift-off and rinsed with isopropanol, leaving behind chromium and gold layers in the desired pattern. As a result, six IDAs were deposited in line on a single glass substrate. IDA geometry: 75 finger couples, 90 nm electrode thickness, 9.5 μm electrode spacing, 2.03 mm overlap length.

Spiro-OMeTAD and bithi-MeOMeTPA were deposited on the electrodes using the same solution and spin-coating procedures described for the solar cell fabrication of MAPbI₃-based devices. The pristine solutions were prepared with similar concentrations but without mixing the various additives. Pristine bithi-MeOMeTPA and all the Co complex HTMs (100

mM concentration solutions) were doctor-bladed on the IDAs to obtain thicker films but conductivity could not be measured for thicknesses <500 nm, for which equation 3 (section 4.3.3) is considered valid.

6.4. Characterisation

NMR analysis was performed on a Bruker Avance III 400 equipped with an Ultrashield 400 Plus magnet.

Low resolution mass spectroscopic analyses were performed on an Agilent Technologies 1260 Infinity series system fitted with a Binary Pump VL, HiP degasser, ALS autosampler and 6120 Quadrupole LC/MS detector. ESI conditions: capillary voltage 3 kV; fragmentor voltage 60 V; drying N₂ flow 11 L min⁻¹ at 250 °C; methanol mobile phase pumped at 0.25 mL min⁻¹. Software: OpenLAB CDS Chemstation edition, version A.01.05 with Agilent MassHunter Easy Access walk up software interface.

High resolution mass spectroscopic analysis for the Co complexes was performed on an Agilent 6220 Accurate Mass LC-TOF system with Agilent 1200 Series HPLC. The mass spectrometer was fitted with the Agilent Multimode Source. The reference compound used for reference mass correction was a purine/HP0921 mix. The syringe pump used for injection was a KD Scientific syringe pump running at 600 µL h⁻¹. ESI conditions: 8 L min⁻¹ N₂, 325° drying gas temperature; capillary voltage: 3 500 V; fragmentor voltage: 160 V.

High resolution mass spectroscopic analysis for bithi-MeOMeTPA was performed on a ThermoFisher Q-Exactive Orbitrap in electrospray positive ion mode, with the compound diluted in chloroform and direct infusion injection at 5 µL min⁻¹. ESI conditions: capillary temperature 280 °C; spray voltage 5 kV; sheath gas flow 2 (arbitrary units).

UV-Vis spectra were recorded on a Varian Cary 300 Bio spectrophotometer.

Crystals for single-crystal XRD analysis were mounted under oil on a nylon cryoloop and quenched to 123 K. Data were collected using an OXFORD Gemini Ultra diffractometer and processed, including an empirical absorption correction, using proprietary software CrysAlisPro.^[232] All structures were solved and refined using conventional methods with the SHELX-2014 software suite.^[233] Non-hydrogen atoms were modelled with anisotropic displacement parameters and hydrogen atoms attached to carbon were placed in calculated positions.

Differential scanning calorimetry measurements were conducted on a TA Instruments DSC Q100 V9.9 Build 303 calorimeter with a heating rate of 10 °C min⁻¹ and a nitrogen gas flow of 50 mL min⁻¹. 5.0 mg of sample were placed in a hermetically sealed aluminium pan. The first heating cycle was run from 40 °C to 300 °C, followed by a 2 min isothermal and a cooling cycle to 40 °C. The second heating cycle was run from 40 °C to 180 °C, followed by a 2 min isothermal and a cooling cycle to 40 °C.

Photoelectron spectroscopy in air (PESA) measurements were conducted on a Riken Keiki AC-2 photoelectron spectrometer. The error in the ionization energies determined from the PESA measurements on a given sample was ± 0.05 eV.

Current-voltage (J - V) characterization of the diodes and of the solar cells was performed using an Oriel 91191-1000 solar simulator fitted with an OPS-A1000 power supply. Current-voltage curves were measured by a Keithley 2400 source meter. The intensity of the solar simulator was set using a calibrated silicon reference cell with a KG3 glass filter (Pecell technologies). The curves were recorded with 10 mV steps at 100 mV s^{-1} . Quasi-steady-state current characterisation was performed using the same solar simulator employed for the current-voltage characterisation. The device was connected to a Bio-Logic VSP potentiostat to record the current at a fixed voltage taken from the maximum power point of the J - V curve over time every 0.1 s.

Cyclic voltammograms were recorded with a Bio-Logic VSP potentiostat on 1 mM solutions of each compound inside a nitrogen-filled glove-box. The working electrode was a glassy carbon electrode with 3 mm diameter; the reference electrode was a silver wire immersed in a 0.1 M solution of AgNO_3 in acetonitrile; the counter-electrode was a platinum grid. After measurement, each solution was spiked with ferrocene, its cyclic voltammogram recorded and corresponding $E_{1/2}$ for the $\text{Fc}^{0/+}$ process was used to calibrate the potential scale.

Conductivity measurements were performed by recording the current-voltage curves for three electrodes on the same substrate, namely the two lateral ones and one in the middle, for each HTM (electrode preparation detailed in section 6.3). J - V curves were recorded with a Bio-Logic VSP potentiostat inside a nitrogen-filled glove-box by performing cyclic voltammetry with applied potentials between -1 and 1 V, with a scan rate of 100 mV s^{-1} . The curve obtained for each electrode was fitted linearly. Equation 3 (section 4.3.3) was used to calculate the conductivity from each curve, with the HTM film thickness measured with a Veeco Dektak 150 profilometer.

Appendix A – Solar cell measurement techniques

J-V curve measurement

Measurements of cell efficiencies are standardised and regulated by international procedures. The procedure for measuring cell efficiencies is defined by ASTM International with code ASTM E927-10.^[234] The procedure for long-term measurements of cell efficiencies is defined by the International Electrotechnical Commission with code IEC 61215.^[235]

The efficiency of a solar cell is a ratio between the power generated by the cell and the power irradiated and is computed with the following equation:

$$\text{PCE} = \frac{P_m}{E A_c}, \quad (4)$$

where PCE is the power conversion efficiency, P_m the maximum power generated by the cell in W, E the power of light incident on the cell in W m^{-2} and A_c the area of the cell in m^2 . Standard test conditions require a value for E of 1000 W m^{-2} generated by an AM1.5G (the solar radiation spectrum on the Earth's surface) lamp with the cell at a constant temperature of $25 \text{ }^\circ\text{C}$.

The value of P_m in equation 4 is experimentally measured with a so-called *I-V* scan measurement. In principle, a variable load (between zero – short circuit – and infinite – open circuit) is applied to the solar cell while shining light on it and its current and voltage response is measured at each applied load. The result of the measurement is a curve similar to that in Figure 41. P_m is defined as the point where the product of the measured current and voltage is maximum and the two values take the name of current (I_{P_m}) and voltage (V_{P_m}) at the maximum power point, respectively. From the *I-V* curve it is possible to derive several useful parameters: the short circuit current, I_{SC} , which is the current that the cell is able to provide when no load is applied to it; the open circuit voltage, V_{OC} , which is the voltage that the cell is able to provide when an infinite load (*i.e.* when its circuit is open) is applied to it. From the two aforementioned parameters a third can be derived, called fill factor (*FF*) or ideality factor. The *FF* is derived from equation 5:

$$\text{FF} = \frac{P_m}{V_{OC} I_{SC}}, \quad (5)$$

it can have a value between 0 and 1 and it gives an indication of the “squareness” of the *I-V* curve. From a visual point of view, it is the ratio between the areas of the blue and green squares in Figure 41. In practical terms, it defines the ratio between the actual power generated by the cell and the power that the same cell could have generated if its *I-V* curve was a perfect square.

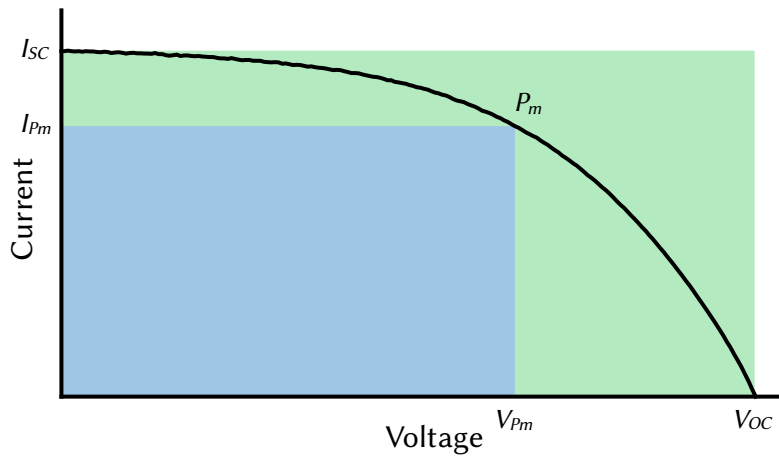


Figure 41. Example of an I-V curve for a solar cell with the indication of the key parameters that can be extracted from it.

In practice, automating the variation of the load during the measurement is not easy and – depending on the shape of the curve for a certain cell – there is the risk of missing relevant measuring points especially in the proximity of P_m . For this reason, in normal laboratory practice, an external voltage bias is applied to the cell in place of the load and its current response is measured for each potential. This method allows the measurement of the I - V curve in a short amount of time and it also gives the possibility to measure the cell response both beyond the V_{oc} and I_{sc} points as well as the cell's current response in the dark. Measuring the cell's behaviour past its V_{oc} point is particularly useful to extrapolate another parameter – the series resistance (R_s) – which will be described at the end of this section.

As explained in section 1.4.6, perovskite solar cells suffer from a hysteretic behaviour when measuring I - V curves to determine their efficiency. Due to the physico-chemical peculiarities of PSCs, their current-voltage response varies if the applied potential during measurement sweeps from the short circuit (SC) condition towards forward bias (FB) or *vice versa*. Moreover, the hysteresis is more or less pronounced depending on the potential sweep rate ($V\ s^{-1}$) at which the measurement is conducted. For this reason, when reporting the I - V curve of a PSC, it is important to always provide the data obtained in both scan directions and the scan rate at which the measurements have been taken. Steady-state current measurements, which will be described in the next section, should be provided as well for a complete and more reliable device characterisation. Methods for proper PSC characterisation are still being discussed among the scientific community. Dunbar *et al.*^[236] provided some suggestions on this regard.

The measured current is not an intrinsic property of a solar cell: two solar cells with the same efficiency will generate different currents if they have different active areas. For this reason, the measured current should be normalised to the cell's area, to obtain the value of the current density (J), measured in $A\ m^{-2}$. This is done in order to standardise the results provided in scientific reports and to allow for facile comparisons of different solar cells. Contrary to the current, in fact, the current density is an intrinsic property of the device.

When the current density is provided in place of the current, the measured curve takes the name of J - V curve.

From an electronic point of view, a solar cell is a photodiode. While an ideal solar cell behaves exactly like a diode, a real device has other circuit components associated to it, that derive from fabrication imperfections. These non-ideal components are equivalent to resistors and are called series resistance (R_s) and shunt resistance (R_{sh}). The series resistance is placed in series to the diode, while the shunt resistance is in parallel: Figure 42 demonstrates their positions in the equivalent circuit of the solar cell. The series resistance reflects the quality of the contacts between the various layers of the solar cell and of the actual contacts between the solar cell and the external

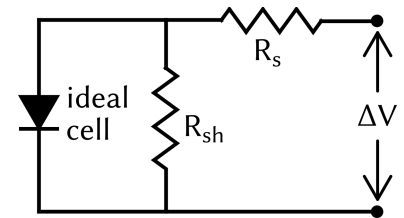


Figure 42: Equivalent circuit of a real solar cell.

Since this resistance is in series to the circuit, it is important for its value to be as low as possible, to minimise the potential drop within the device. The shunt resistance arises from current leakages within the device, due to pinholes or short circuits in general. In electronics, a diode is commonly used to block the current flow of a circuit in a certain direction. The current block will work if the potential applied to the circuit is lower than a threshold, called built-in potential, which is characteristic of the diode. After that threshold, a current will start flowing through the diode. However, if there are short circuit paths within the diode, there will be a current flow even at applied potentials lower than the built-in one. The shunt resistance is visualised as a resistance in parallel to the main circuit: for this reason, it is important for its value to be very high.

Both series and shunt resistances can be calculated from an I - V curve as shown in Figure 43, where the I - V curves for a solar cell with low R_s and $R_{sh} = \infty$ (high-performing) and a device with unsatisfactory series and shunt resistances (low-performing) are depicted. The series

resistance is calculated from the slope of the linear fit of the curve near the open circuit voltage (in green in the figure). The higher the series resistance, the less vertical the curve will be close to that point. The shunt resistance is calculated at the other end of the curve, from the slope of the linear fit close to the short circuit current (in black in the figure). The lower the shunt resistance, the less horizontal the initial part of the curve will be. As it can be seen from the figure, both the shunt and the series resistances have a big impact on the FF of the solar cell and, hence, on the final efficiency of the device.

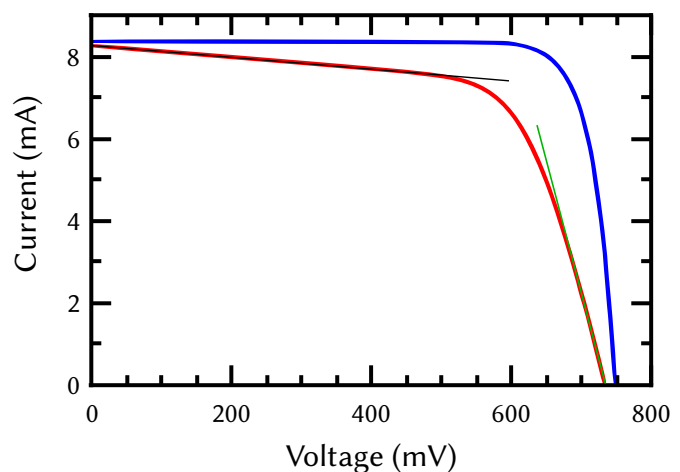


Figure 43: I - V curves of a high-performing (blue) and of a low-performing (red) solar cell. Linear fits of the curve for shunt (black) and series (green) resistances are shown.

Steady-state measurement

The measurement of the J - V curve of a cell will give an indication of the efficiency of the cell at that precise moment, but it will not give any information about the cell's behaviour over time. A solar cell may be unstable under illumination and lose efficiency after only one minute or – on the opposite – it may require some time under illumination to reach its full efficiency. Both situations are often encountered in perovskite solar cells. For this reason, to provide a complete set of data about a solar cell, it is useful to run a steady-state measurement for a PSC device. There are two different methods to measure the steady-state efficiency of a solar cell and both involve measuring the device's current over time, while keeping it under a certain applied voltage and under illumination. The first method consists in applying a fixed voltage to the cell – usually corresponding to the V_{p_m} of the J - V curve – while measuring the current. It is the simplest method and it does not require any particular hardware or software. The second method is called maximum power point tracking and in this case the applied voltage is not fixed but small perturbations are constantly applied to seek the maximum current output. After applying a perturbation in one direction, if the measured current is higher than that of the previous point the next perturbation will be applied in the same direction, otherwise it will be applied in the opposite one. This method requires a particular hardware or software that is able to apply the voltage perturbation and analyse the current response from the device. A steady-state measurement is usually run for a predefined amount of time, usually varying from few minutes to several hours. With this technique it is possible to prove that a certain solar cell is able to reach and maintain a certain maximum power point during the time of measurement, or to analyse its decay/growth behaviour over time.

Incident photon-to-electron conversion efficiency measurement

The incident photon-to-electron conversion efficiency (IPCE) measurement is used to verify the solar cell's current response at different light wavelengths. It measures the percentage of photons shined on the device that are converted into “useful” electrons, *i.e.* electrons that are able to flow through the external circuit, based on the following equation:

$$\text{IPCE} = \frac{\#_{e^-}}{\#_{ph}} = \frac{h\nu}{e} \cdot \frac{I_{SC}}{E A_C}, \quad (6)$$

where $\#_{e^-}$ is the number of incident photons, $\#_{ph}$ is the number of generated electrons, $h\nu$ is the energy of the photon and e the elementary charge. IPCE also takes the name of external quantum efficiency (EQE) and it can be seen as the electronic version of a UV-Vis spectrum. There are mainly three reasons that can lower the IPCE to below 100%. The first reason is photon absorption by components of the cell other than the light absorber (*e.g.* glass support and charge transport materials). The second reason is that there is not enough material to absorb all the incoming light, either due to insufficient material thickness, low

extinction coefficient or lack of absorption of the material at that particular wavelength. The third reason is charge recombination inside the solar cell. IPCE spectra are usually measured at low light intensities (10% sun or less) and at the short circuit condition. Ideally, after correcting for the lower light intensity, the integrated current of the IPCE spectrum should be equal to the J_{sc} of the J - V curve.

Appendix B – Detailed crystallographic information

Complete single crystal XRD data refinement for [Fe(bpyPY4)](OTf)₂

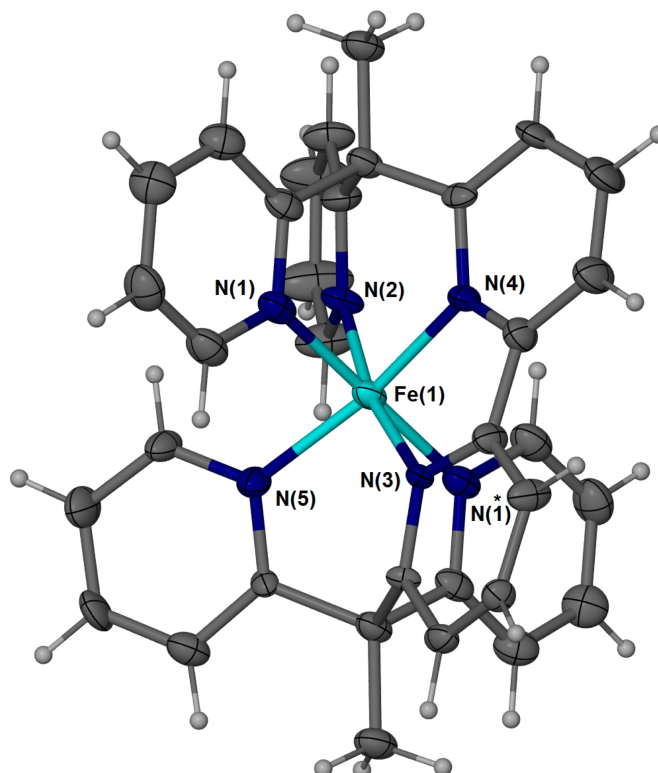


Figure 44. Molecular diagram of the complex cation in [Fe(bpyPY4)](OTf)₂ with non-hydrogen atoms represented by 50% thermal ellipsoids and hydrogen atoms as spheres of arbitrary size. The two triflate counter ions have been omitted for clarity. Note: The complex cation was modelled as disordered over two positions related by the crystallographic inversion centre located at the Fe site. The unique triflate anion was similarly modelled as disordered.

Table 1. Crystal data and structure refinement for [Fe(bpyPY4)](OTf)₂.

Identification code	mx05_15	
Empirical formula	C ₃₆ H ₂₈ F ₆ Fe N ₆ O ₆ S ₂	
Formula weight	874.61	
Temperature	123.01(10) K	
Wavelength	0.71073 Å	
Crystal system, space group	Triclinic, P-1	
Unit cell dimensions	a = 8.3101(3) Å b = 10.4017(3) Å c = 11.6371(5) Å	alpha = 114.636(4) deg. beta = 95.979(3) deg. gamma = 98.975(3) deg.
Volume	886.96(6) Å ³	
Z, Calculated density	1, 1.637 Mg/m ³	

Absorption coefficient	0.632 mm ⁻¹
F(000)	446
Crystal size	0.20 x 0.17 x 0.09 mm
Theta range for data collection	1.960 to 30.467 deg.
Limiting indices	-11<=h<=11, -14<=k<=14, -15<=l<=16
Reflections collected / unique	13623 / 4881 [R(int) = 0.0292]
Completeness to theta = 25.242	100.0 %
Absorption correction	Semi-empirical from equivalents
Max. and min. transmission	1.00000 and 0.86358
Refinement method	Full-matrix least-squares on F ²
Data / restraints / parameters	4881 / 30 / 413
Goodness-of-fit on F ²	1.059
Final R indices [I>2sigma(I)]	R1 = 0.0421, wR2 = 0.0960
R indices (all data)	R1 = 0.0597, wR2 = 0.1069
Extinction coefficient	n/a
Largest diff. peak and hole	0.380 and -0.456 e.A ⁻³

Table 2. Atomic coordinates (x 10⁴) and equivalent isotropic displacement parameters (A² x 10³) for [Fe(bpyPY4)](OTf)₂. U(eq) is defined as one third of the trace of the orthogonalized Uij tensor.

	x	y	z	U(eq)
Fe(1)	0	10000	5000	21(1)
S(1)	3430(1)	5842(1)	8173(1)	34(1)
F(1)	3629(9)	8705(7)	9459(4)	59(1)
F(1')	3318(9)	8451(7)	8834(6)	73(2)
F(2)	1407(10)	7613(7)	8046(9)	62(2)
F(2')	1095(12)	6948(7)	7696(11)	89(3)
F(3)	3721(4)	8107(4)	7479(3)	47(1)
F(3')	3179(6)	7145(5)	6826(4)	69(1)
O(1)	2674(2)	5801(2)	9213(2)	48(1)
O(2)	5213(2)	6244(2)	8450(2)	35(1)
O(3)	2725(6)	4979(5)	6797(4)	53(1)
O(3')	2757(6)	4436(4)	7091(4)	44(1)
N(1)	941(2)	10633(2)	3781(2)	24(1)
N(2)	-2022(19)	9055(9)	3657(14)	22(2)
N(3)	2010(20)	10568(9)	6231(13)	16(2)
N(4)	1146(6)	8450(6)	4079(5)	21(1)
N(5)	-636(6)	11847(6)	5789(5)	22(1)
C(1)	3007(12)	7651(10)	8254(10)	34(2)

C(1')	2718(17)	7117(10)	7886(12)	49(2)
C(2)	1859(3)	11987(2)	4173(2)	31(1)
C(3)	2573(3)	12433(2)	3351(2)	35(1)
C(4)	2337(3)	11468(3)	2067(2)	35(1)
C(5)	1364(3)	10096(2)	1649(2)	30(1)
C(6)	682(2)	9689(2)	2516(2)	23(1)
C(7)	-380(2)	8155(2)	2108(2)	23(1)
C(8)	-593(3)	7218(2)	657(2)	29(1)
C(9)	-2020(20)	8270(20)	2381(17)	29(4)
C(10)	-3506(14)	7558(8)	1525(10)	31(2)
C(11)	-4966(6)	7634(7)	1899(5)	52(2)
C(12)	-4996(6)	8451(7)	3183(5)	57(2)
C(13)	-3498(6)	9167(6)	4024(4)	42(1)
C(14)	2098(14)	11567(17)	7453(16)	14(2)
C(15)	3554(15)	11970(7)	8363(10)	22(1)
C(16)	4876(4)	11320(4)	8027(4)	20(1)
C(17)	4631(5)	10130(5)	6848(4)	27(1)
C(18)	3164(5)	9762(4)	5980(4)	22(1)
C(19)	2619(5)	8470(4)	4738(4)	25(1)
C(20)	3483(6)	7386(5)	4214(4)	34(1)
C(21)	2856(7)	6323(5)	2969(4)	38(1)
C(22)	1524(8)	6460(7)	2245(7)	27(1)
C(23)	747(10)	7607(10)	2785(8)	20(1)
C(24)	-1406(5)	12416(5)	5103(4)	28(1)
C(25)	-1957(6)	13684(5)	5650(4)	35(1)
C(26)	-1753(6)	14381(5)	6967(4)	34(1)
C(27)	-939(7)	13823(8)	7687(8)	29(1)
C(28)	-401(9)	12567(9)	7071(8)	16(1)

Table 3. Bond lengths [Å] and angles [deg] for [Fe(bpyPY4)](OTf)₂.

Fe(1)-N(1)#1	1.9764(17)
Fe(1)-N(1)	1.9764(17)
Fe(1)-N(2)	1.972(15)
Fe(1)-N(3)	1.920(16)
Fe(1)-N(4)	1.977(6)
Fe(1)-N(5)	1.939(6)
S(1)-O(1)	1.4338(18)
S(1)-O(2)	1.4382(16)
S(1)-O(3)	1.468(4)
S(1)-O(3')	1.449(4)
S(1)-C(1)	1.933(10)
S(1)-C(1')	1.670(13)
F(1)-C(1)	1.352(9)
F(1')-C(1')	1.336(9)
F(2)-C(1)	1.317(13)
F(2')-C(1')	1.316(17)
F(3)-C(1)	1.331(12)
F(3')-C(1')	1.340(14)
N(1)-C(2)	1.353(3)
N(1)-C(6)	1.357(2)
N(2)-C(9)	1.36(2)
N(2)-C(13)	1.347(16)
N(3)-C(14)	1.35(2)
N(3)-C(18)	1.344(13)
N(4)-C(19)	1.368(6)

N(4)-C(23)	1.360(10)
N(5)-C(24)	1.342(7)
N(5)-C(28)	1.337(10)
C(2)-C(3)	1.373(3)
C(3)-C(4)	1.381(3)
C(4)-C(5)	1.381(3)
C(5)-C(6)	1.385(3)
C(6)-C(7)	1.547(3)
C(7)-C(8)	1.531(3)
C(7)-C(9)	1.446(18)
C(7)-C(14)#1	1.593(15)
C(7)-C(23)	1.486(10)
C(7)-C(28)#1	1.587(9)
C(9)-C(10)	1.38(2)
C(10)-C(11)	1.334(13)
C(11)-C(12)	1.382(7)
C(12)-C(13)	1.383(7)
C(14)-C(15)	1.402(18)
C(15)-C(16)	1.385(11)
C(16)-C(17)	1.380(5)
C(17)-C(18)	1.389(5)
C(18)-C(19)	1.468(5)
C(19)-C(20)	1.388(5)
C(20)-C(21)	1.386(6)
C(21)-C(22)	1.383(9)
C(22)-C(23)	1.391(13)
C(24)-C(25)	1.380(6)
C(25)-C(26)	1.372(6)
C(26)-C(27)	1.381(9)
C(27)-C(28)	1.374(12)
N(1)-Fe(1)-N(1)#1	180.00(8)
N(1)-Fe(1)-N(4)	77.13(14)
N(1)#1-Fe(1)-N(4)	102.87(14)
N(2)-Fe(1)-N(1)#1	94.1(5)
N(2)-Fe(1)-N(1)	85.9(5)
N(2)-Fe(1)-N(4)	92.0(4)
N(3)-Fe(1)-N(1)#1	82.6(4)
N(3)-Fe(1)-N(1)	97.5(4)
N(3)-Fe(1)-N(2)	169.6(5)
N(3)-Fe(1)-N(4)	79.2(4)
N(3)-Fe(1)-N(5)	95.3(3)
N(5)-Fe(1)-N(1)	88.48(14)
N(5)-Fe(1)-N(1)#1	91.52(14)
N(5)-Fe(1)-N(2)	94.7(3)
N(5)-Fe(1)-N(4)	163.67(13)
O(1)-S(1)-O(2)	115.18(11)
O(1)-S(1)-O(3)	125.8(2)
O(1)-S(1)-O(3')	105.44(19)
O(1)-S(1)-C(1)	99.6(3)
O(1)-S(1)-C(1')	104.1(5)
O(2)-S(1)-O(3)	113.7(2)
O(2)-S(1)-O(3')	113.8(2)
O(2)-S(1)-C(1)	98.1(3)
O(2)-S(1)-C(1')	108.1(5)
O(3)-S(1)-C(1)	95.6(4)
O(3')-S(1)-C(1')	109.6(4)
C(2)-N(1)-Fe(1)	121.82(14)
C(2)-N(1)-C(6)	118.49(18)
C(6)-N(1)-Fe(1)	119.68(13)
C(9)-N(2)-Fe(1)	124.2(12)

C(13)-N(2)-Fe(1)	118.0(9)
C(13)-N(2)-C(9)	117.8(13)
C(14)-N(3)-Fe(1)	119.1(11)
C(18)-N(3)-Fe(1)	120.2(7)
C(18)-N(3)-C(14)	118.9(13)
C(19)-N(4)-Fe(1)	116.4(4)
C(23)-N(4)-Fe(1)	123.1(6)
C(23)-N(4)-C(19)	118.9(6)
C(24)-N(5)-Fe(1)	122.9(4)
C(28)-N(5)-Fe(1)	119.9(5)
C(28)-N(5)-C(24)	117.1(6)
F(1)-C(1)-S(1)	108.5(7)
F(2)-C(1)-S(1)	112.0(7)
F(2)-C(1)-F(1)	106.3(8)
F(2)-C(1)-F(3)	108.8(8)
F(3)-C(1)-S(1)	115.3(6)
F(3)-C(1)-F(1)	105.5(7)
F(1')-C(1')-S(1)	113.0(10)
F(1')-C(1')-F(3')	106.0(10)
F(2')-C(1')-S(1)	115.3(9)
F(2')-C(1')-F(1')	105.9(10)
F(2')-C(1')-F(3')	106.0(11)
F(3')-C(1')-S(1)	110.1(8)
N(1)-C(2)-C(3)	122.75(19)
C(2)-C(3)-C(4)	118.9(2)
C(3)-C(4)-C(5)	118.8(2)
C(4)-C(5)-C(6)	120.2(2)
N(1)-C(6)-C(5)	120.75(18)
N(1)-C(6)-C(7)	116.79(17)
C(5)-C(6)-C(7)	122.45(17)
C(6)-C(7)-C(14)#1	104.4(6)
C(6)-C(7)-C(28)#1	109.9(3)
C(8)-C(7)-C(6)	111.13(17)
C(8)-C(7)-C(14)#1	112.4(5)
C(8)-C(7)-C(28)#1	112.4(3)
C(9)-C(7)-C(6)	109.2(7)
C(9)-C(7)-C(8)	106.7(7)
C(9)-C(7)-C(14)#1	6.1(11)
C(9)-C(7)-C(23)	121.4(9)
C(9)-C(7)-C(28)#1	107.2(9)
C(23)-C(7)-C(6)	99.9(3)
C(23)-C(7)-C(8)	108.3(4)
C(23)-C(7)-C(14)#1	119.8(7)
C(23)-C(7)-C(28)#1	14.6(4)
C(28)#1-C(7)-C(14)#1	106.1(7)
N(2)-C(9)-C(7)	113.0(13)
N(2)-C(9)-C(10)	120.0(15)
C(10)-C(9)-C(7)	126.6(14)
C(11)-C(10)-C(9)	122.0(11)
C(10)-C(11)-C(12)	119.0(6)
C(11)-C(12)-C(13)	118.1(4)
N(2)-C(13)-C(12)	122.9(7)
N(3)-C(14)-C(7)#1	116.7(10)
N(3)-C(14)-C(15)	119.4(14)
C(9)#1-C(14)-N(3)	159(8)
C(9)#1-C(14)-C(7)#1	45(7)
C(9)#1-C(14)-C(15)	81(8)
C(15)-C(14)-C(7)#1	121.0(12)
C(16)-C(15)-C(14)	120.4(10)
C(17)-C(16)-C(15)	118.1(5)
C(16)-C(17)-C(18)	118.8(3)

N(3)-C(18)-C(17)	122.0(7)
N(3)-C(18)-C(19)	111.4(6)
C(17)-C(18)-C(19)	126.6(3)
N(4)-C(19)-C(18)	112.5(4)
N(4)-C(19)-C(20)	121.3(4)
C(20)-C(19)-C(18)	126.1(4)
C(21)-C(20)-C(19)	118.0(4)
C(22)-C(21)-C(20)	119.6(5)
C(21)-C(22)-C(23)	120.4(7)
N(4)-C(23)-C(7)	113.1(7)
N(4)-C(23)-C(22)	118.6(8)
C(22)-C(23)-C(7)	128.0(7)
N(5)-C(24)-C(25)	123.6(4)
C(26)-C(25)-C(24)	118.3(4)
C(25)-C(26)-C(27)	118.8(5)
C(28)-C(27)-C(26)	119.4(7)
N(5)-C(28)-C(7)#1	117.7(7)
N(5)-C(28)-C(27)	122.7(8)
C(23)#1-C(28)-N(5)	112(3)
C(23)#1-C(28)-C(7)#1	68(2)
C(23)#1-C(28)-C(27)	85(3)
C(27)-C(28)-C(7)#1	119.4(6)

Symmetry transformations used to generate equivalent atoms:
#1 -x, -y+2, -z+1

Table 4. Anisotropic displacement parameters ($\text{Å}^2 \times 10^3$) for $[\text{Fe}(\text{bpyPY4})](\text{OTf})_2$.

The anisotropic displacement factor exponent takes the form:
 $-2 \pi^2 [h^2 a^2 U_{11} + \dots + 2 h k a^* b^* U_{12}]$

	U11	U22	U33	U23	U13	U12
Fe(1)	22(1)	19(1)	17(1)	3(1)	-1(1)	7(1)
S(1)	31(1)	30(1)	27(1)	0(1)	2(1)	5(1)
F(1)	76(3)	35(2)	47(3)	0(2)	11(3)	18(2)
F(1')	113(5)	32(3)	84(5)	26(4)	29(5)	34(4)
F(2)	45(3)	84(4)	81(4)	49(4)	20(3)	37(3)
F(2')	56(4)	112(6)	141(8)	89(6)	19(4)	44(5)
F(3)	49(2)	53(2)	55(2)	38(2)	11(2)	16(2)
F(3')	97(3)	76(3)	63(2)	55(2)	20(2)	23(2)
O(1)	43(1)	50(1)	61(1)	34(1)	20(1)	10(1)
O(2)	32(1)	34(1)	38(1)	15(1)	8(1)	8(1)
O(3)	63(3)	34(2)	34(2)	-6(2)	-7(2)	5(2)
O(3')	63(3)	24(2)	28(2)	1(2)	4(2)	-1(2)
N(1)	22(1)	20(1)	22(1)	3(1)	2(1)	5(1)
N(2)	15(2)	21(5)	17(3)	-1(4)	4(2)	2(4)
N(3)	23(2)	12(4)	13(3)	4(3)	3(2)	5(3)
N(4)	26(3)	20(2)	14(2)	4(2)	4(2)	10(2)
N(5)	25(3)	26(3)	18(2)	10(2)	8(2)	10(2)
C(1)	35(4)	34(5)	39(6)	18(4)	10(4)	18(4)
C(1')	60(6)	45(6)	57(7)	31(5)	21(5)	19(5)

C(2)	31(1)	23(1)	29(1)	4(1)	-1(1)	4(1)
C(3)	34(1)	25(1)	42(1)	13(1)	2(1)	1(1)
C(4)	31(1)	37(1)	37(1)	15(1)	9(1)	5(1)
C(5)	26(1)	32(1)	27(1)	7(1)	7(1)	7(1)
C(6)	19(1)	22(1)	24(1)	4(1)	4(1)	7(1)
C(7)	24(1)	19(1)	20(1)	3(1)	1(1)	6(1)
C(8)	32(1)	26(1)	20(1)	2(1)	1(1)	6(1)
C(9)	38(5)	29(5)	16(4)	7(4)	6(3)	7(3)
C(10)	24(2)	37(5)	18(3)	3(4)	0(2)	-2(4)
C(11)	25(2)	74(4)	32(3)	1(3)	-2(2)	8(2)
C(12)	25(2)	92(5)	34(3)	8(3)	9(2)	10(3)
C(13)	28(2)	66(4)	23(2)	9(2)	5(2)	12(2)
C(14)	9(2)	15(3)	12(4)	1(3)	2(2)	-1(2)
C(15)	28(3)	16(3)	16(3)	4(3)	1(2)	-1(3)
C(16)	17(2)	22(2)	20(2)	8(2)	0(1)	4(1)
C(17)	22(2)	39(2)	20(2)	9(2)	4(2)	15(2)
C(18)	22(2)	26(2)	19(2)	8(2)	5(1)	12(2)
C(19)	29(2)	24(2)	23(2)	9(2)	4(2)	11(2)
C(20)	38(2)	33(2)	27(2)	8(2)	4(2)	19(2)
C(21)	54(3)	29(2)	29(2)	4(2)	7(2)	25(2)
C(22)	36(4)	20(3)	19(2)	0(2)	7(3)	12(3)
C(23)	24(3)	19(3)	13(2)	6(2)	7(2)	-1(2)
C(24)	36(2)	36(2)	18(2)	12(2)	10(2)	22(2)
C(25)	44(2)	38(2)	33(2)	18(2)	10(2)	26(2)
C(26)	43(3)	21(2)	35(2)	7(2)	5(2)	19(2)
C(27)	28(3)	26(3)	24(2)	3(2)	3(3)	6(3)
C(28)	19(3)	16(2)	16(2)	8(2)	9(2)	6(2)

Table 5. Hydrogen coordinates ($\times 10^4$) and isotropic displacement parameters ($\text{Å}^2 \times 10^3$) for $[\text{Fe}(\text{bpyPY4})](\text{OTf})_2$.

	x	y	z	U(eq)
H(2)	2017	12658	5055	37
H(3)	3219	13390	3660	42
H(4)	2835	11743	1481	43
H(5)	1162	9428	764	36
H(8A)	-1256	6250	427	44
H(8B)	499	7137	424	44
H(8C)	-1159	7668	192	44
H(10)	-3486	6997	643	37
H(11)	-5971	7133	1291	63
H(12)	-6017	8520	3478	68
H(13)	-3511	9764	4901	51
H(15)	3634	12693	9215	27
H(16)	5922	11683	8593	24
H(17)	5452	9572	6633	33
H(20)	4473	7374	4694	40
H(21)	3340	5506	2616	46
H(22)	1136	5766	1373	33
H(24)	-1581	11918	4191	34
H(25)	-2465	14064	5128	42
H(26)	-2163	15232	7375	40

H(27)

-753

14303

8601

35

Complete single crystal XRD data refinement for [Fe(bpyPY4)](OTf)₃

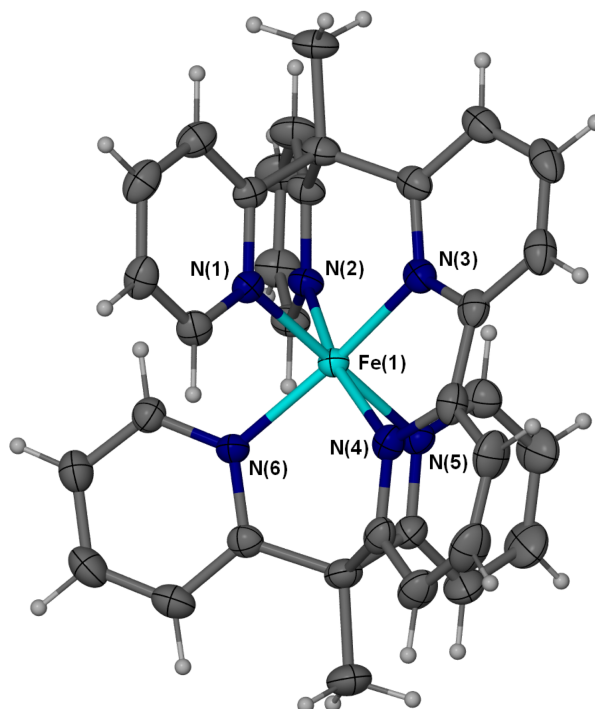


Figure 45. Molecular diagram of the complex cation in [Fe(bpyPY4)](OTf)₃·MeCN with non-hydrogen atoms represented by 50% Thermal ellipsoids and hydrogen atoms as spheres of arbitrary size. The three triflate counter ions and lattice MeCN solvent molecule have been omitted for clarity.

Table 1. Crystal data and structure refinement for [Fe(bpyPY4)](OTf)₃·MeCN.

Identification code	shelx	
Empirical formula	C ₃₉ H ₃₁ F ₉ Fe N ₇ O ₉ S ₃	
Formula weight	1064.74	
Temperature	123(2) K	
Wavelength	0.71073 Å	
Crystal system, space group	Monoclinic, P2(1)/n	
Unit cell dimensions	a = 18.2511(10) Å	alpha = 90 deg.
	b = 13.9494(5) Å	beta = 117.614(7) deg.
	c = 19.6316(10) Å	gamma = 90 deg.
Volume	4428.7(4) Å ³	
Z, Calculated density	4, 1.597 Mg/m ³	
Absorption coefficient	0.582 mm ⁻¹	
F(000)	2164	
Crystal size	0.25 x 0.08 x 0.05 mm	

Theta range for data collection 3.399 to 25.999 deg.

Limiting indices -22<=h<=22, -17<=k<=13, -23<=l<=24

Reflections collected / unique 36252 / 8695 [R(int) = 0.0345]

Completeness to theta = 25.242 99.8 %

Absorption correction Semi-empirical from equivalents

Max. and min. transmission 1.00000 and 0.98482

Refinement method Full-matrix least-squares on F²

Data / restraints / parameters 8695 / 0 / 678

Goodness-of-fit on F² 1.023

Final R indices [I>2sigma(I)] R1 = 0.0596, wR2 = 0.1586

R indices (all data) R1 = 0.0782, wR2 = 0.1739

Extinction coefficient n/a

Largest diff. peak and hole 2.795 and -0.739 e.A⁻³

Table 2. Atomic coordinates (x 10⁴) and equivalent isotropic displacement parameters (A² x 10³) for [Fe(bpyPY4)](OTf)₃·MeCN. U(eq) is defined as one third of the trace of the orthogonalized Uij tensor.

	x	y	z	U(eq)
Fe(1)	8583(1)	814(1)	1343(1)	20(1)
S(1)	8949(1)	1289(1)	5970(1)	45(1)
S(2)	6248(1)	-974(1)	1985(1)	31(1)
S(3)	8727(1)	4232(1)	-1655(1)	44(1)
F(1)	8627(3)	-243(3)	5106(2)	83(1)
F(2)	7613(2)	723(2)	4755(2)	73(1)
F(3)	7938(3)	-154(3)	5742(2)	97(1)
F(4)	5233(3)	29(3)	2277(2)	89(1)
F(5)	6164(5)	847(2)	2190(3)	152(3)
F(6)	6457(2)	25(3)	3184(2)	73(1)
F(7)	9113(6)	3549(7)	-2667(5)	64(2)
F(7')	10285(4)	3935(6)	-1448(5)	88(2)
F(8)	7825(4)	3482(4)	-3041(3)	60(2)
F(8')	9381(8)	3108(10)	-2313(9)	126(5)
F(9)	8644(5)	2489(4)	-2180(4)	65(2)
F(9')	9741(6)	2768(6)	-1141(7)	123(4)
O(1)	9211(2)	1743(3)	5474(2)	60(1)
O(2)	9551(2)	751(3)	6597(2)	66(1)
O(3)	8406(3)	1888(4)	6141(2)	81(1)
O(4)	5715(3)	-868(3)	1192(2)	70(1)
O(5)	7111(3)	-860(4)	2203(3)	90(2)
O(6)	6103(2)	-1760(2)	2360(2)	52(1)
O(7)	8026(5)	3915(6)	-1487(4)	38(2)

O(7')	8121(5)	3642(7)	-1780(5)	60(2)
O(8)	9491(4)	4069(6)	-1075(4)	48(2)
O(8')	9216(5)	4592(6)	-840(4)	62(2)
O(9)	8678(16)	4959(17)	-2199(12)	64(5)
O(9')	8535(12)	5138(13)	-2043(10)	50(3)
N(1)	7450(2)	1206(2)	1113(2)	22(1)
N(2)	8268(2)	-523(2)	1366(2)	24(1)
N(3)	8054(2)	891(2)	229(2)	25(1)
N(4)	9039(2)	2013(2)	1218(2)	26(1)
N(5)	9715(2)	414(2)	1583(2)	26(1)
N(6)	8962(2)	981(2)	2447(2)	23(1)
N(7)	10531(5)	1613(5)	456(4)	102(2)
C(1)	7333(2)	2025(2)	1418(2)	27(1)
C(2)	6555(2)	2381(3)	1209(2)	31(1)
C(3)	5876(2)	1876(3)	683(2)	33(1)
C(4)	6000(2)	1032(3)	379(2)	31(1)
C(5)	6792(2)	708(2)	593(2)	23(1)
C(6)	6982(2)	-163(3)	206(2)	27(1)
C(7)	6179(2)	-654(3)	-368(2)	35(1)
C(8)	7554(2)	-872(3)	810(2)	27(1)
C(9)	7366(3)	-1836(3)	791(2)	37(1)
C(10)	7916(3)	-2433(3)	1358(3)	42(1)
C(11)	8632(3)	-2068(3)	1939(2)	36(1)
C(12)	8792(2)	-1109(3)	1928(2)	28(1)
C(13)	7409(2)	328(3)	-219(2)	28(1)
C(14)	7085(2)	366(3)	-1014(2)	33(1)
C(15)	7369(2)	1065(3)	-1335(2)	36(1)
C(16)	7912(2)	1757(3)	-879(2)	35(1)
C(17)	8239(2)	1663(3)	-83(2)	28(1)
C(18)	8771(2)	2343(3)	487(2)	30(1)
C(19)	9033(3)	3215(3)	349(3)	40(1)
C(20)	9610(3)	3718(3)	963(3)	43(1)
C(21)	9978(3)	3302(3)	1686(3)	36(1)
C(22)	9698(2)	2423(3)	1800(2)	29(1)
C(23)	10177(2)	1769(3)	2495(2)	29(1)
C(24)	10974(3)	2266(3)	3065(3)	41(1)
C(25)	10370(2)	873(3)	2145(2)	28(1)
C(26)	11165(2)	565(3)	2357(2)	39(1)
C(27)	11294(3)	-195(4)	1987(3)	49(1)
C(28)	10633(3)	-622(3)	1385(3)	45(1)
C(29)	9845(3)	-306(3)	1198(2)	34(1)
C(30)	9672(2)	1442(3)	2893(2)	26(1)
C(31)	9928(3)	1573(3)	3670(2)	37(1)
C(32)	9457(3)	1223(3)	3992(2)	39(1)
C(33)	8727(3)	744(3)	3529(2)	36(1)
C(34)	8500(2)	640(3)	2765(2)	28(1)
C(35)	8249(3)	368(4)	5374(3)	54(1)
C(36)	6024(4)	37(3)	2435(3)	51(1)
C(37)	8561(6)	3390(7)	-2439(5)	44(2)
C(37')	9587(7)	3479(8)	-1627(8)	68(3)
C(38)	10912(6)	2282(6)	474(5)	98(2)
C(39)	11323(6)	3206(7)	508(7)	133(4)

Table 3. Bond lengths [Å] and angles [deg] for [Fe(bpyPY4)](OTf)₃·MeCN.

Fe(1)-N(4)	1.933(3)
Fe(1)-N(3)	1.942(3)

Fe(1)-N(2)	1.958(3)
Fe(1)-N(6)	1.960(3)
Fe(1)-N(5)	1.975(3)
Fe(1)-N(1)	1.976(3)
S(1)-O(1)	1.418(4)
S(1)-O(2)	1.425(3)
S(1)-O(3)	1.450(4)
S(1)-C(35)	1.807(5)
S(2)-O(4)	1.411(3)
S(2)-O(6)	1.413(3)
S(2)-O(5)	1.436(4)
S(2)-C(36)	1.808(5)
S(3)-O(7')	1.308(8)
S(3)-O(8)	1.349(6)
S(3)-O(9')	1.43(2)
S(3)-O(9)	1.45(2)
S(3)-O(8')	1.512(7)
S(3)-O(7)	1.527(8)
S(3)-C(37)	1.846(10)
S(3)-C(37')	1.868(12)
F(1)-C(35)	1.347(7)
F(2)-C(35)	1.327(5)
F(3)-C(35)	1.325(6)
F(4)-C(36)	1.328(7)
F(5)-C(36)	1.298(6)
F(6)-C(36)	1.309(6)
F(7)-C(37)	1.297(14)
F(7')-C(37')	1.317(12)
F(8)-C(37)	1.322(11)
F(8')-C(37')	1.325(17)
F(9)-C(37)	1.338(10)
F(9')-C(37')	1.313(14)
N(1)-C(1)	1.352(5)
N(1)-C(5)	1.353(4)
N(2)-C(8)	1.345(5)
N(2)-C(12)	1.350(5)
N(3)-C(13)	1.348(5)
N(3)-C(17)	1.358(5)
N(4)-C(22)	1.343(5)
N(4)-C(18)	1.364(5)
N(5)-C(29)	1.344(5)
N(5)-C(25)	1.353(5)
N(6)-C(30)	1.344(5)
N(6)-C(34)	1.348(5)
N(7)-C(38)	1.154(9)
C(1)-C(2)	1.375(5)
C(2)-C(3)	1.382(6)
C(3)-C(4)	1.385(6)
C(4)-C(5)	1.381(5)
C(5)-C(6)	1.555(5)
C(6)-C(8)	1.526(5)
C(6)-C(7)	1.535(5)
C(6)-C(13)	1.541(5)
C(8)-C(9)	1.384(5)
C(9)-C(10)	1.379(6)
C(10)-C(11)	1.372(6)
C(11)-C(12)	1.372(5)
C(13)-C(14)	1.390(5)
C(14)-C(15)	1.385(6)
C(15)-C(16)	1.376(6)
C(16)-C(17)	1.396(5)

C(17)-C(18)	1.445(5)
C(18)-C(19)	1.379(6)
C(19)-C(20)	1.370(6)
C(20)-C(21)	1.386(6)
C(21)-C(22)	1.386(5)
C(22)-C(23)	1.534(5)
C(23)-C(30)	1.527(5)
C(23)-C(24)	1.531(5)
C(23)-C(25)	1.543(5)
C(25)-C(26)	1.381(5)
C(26)-C(27)	1.366(6)
C(27)-C(28)	1.372(7)
C(28)-C(29)	1.381(6)
C(30)-C(31)	1.385(5)
C(31)-C(32)	1.371(6)
C(32)-C(33)	1.388(6)
C(33)-C(34)	1.365(5)
C(38)-C(39)	1.477(11)
N(4)-Fe(1)-N(3)	80.11(13)
N(4)-Fe(1)-N(2)	167.06(12)
N(3)-Fe(1)-N(2)	94.58(12)
N(4)-Fe(1)-N(6)	94.89(12)
N(3)-Fe(1)-N(6)	167.37(12)
N(2)-Fe(1)-N(6)	92.59(12)
N(4)-Fe(1)-N(5)	79.05(12)
N(3)-Fe(1)-N(5)	101.72(12)
N(2)-Fe(1)-N(5)	90.61(12)
N(6)-Fe(1)-N(5)	88.57(12)
N(4)-Fe(1)-N(1)	101.44(12)
N(3)-Fe(1)-N(1)	78.84(12)
N(2)-Fe(1)-N(1)	88.96(12)
N(6)-Fe(1)-N(1)	90.93(12)
N(5)-Fe(1)-N(1)	179.32(13)
O(1)-S(1)-O(2)	117.3(2)
O(1)-S(1)-O(3)	112.7(3)
O(2)-S(1)-O(3)	116.0(3)
O(1)-S(1)-C(35)	103.6(2)
O(2)-S(1)-C(35)	102.4(2)
O(3)-S(1)-C(35)	101.9(3)
O(4)-S(2)-O(6)	117.1(2)
O(4)-S(2)-O(5)	114.7(3)
O(6)-S(2)-O(5)	112.1(3)
O(4)-S(2)-C(36)	105.1(2)
O(6)-S(2)-C(36)	102.2(2)
O(5)-S(2)-C(36)	103.5(3)
O(8)-S(3)-O(9')	120.0(8)
O(7')-S(3)-O(9)	123.1(11)
O(7')-S(3)-O(8')	116.2(5)
O(9)-S(3)-O(8')	110.6(9)
O(8)-S(3)-O(7)	114.2(4)
O(9')-S(3)-O(7)	110.3(7)
O(8)-S(3)-C(37)	107.6(5)
O(9')-S(3)-C(37)	102.3(6)
O(7)-S(3)-C(37)	99.6(4)
O(7')-S(3)-C(37')	106.2(6)
O(9)-S(3)-C(37')	100.3(9)
O(8')-S(3)-C(37')	94.6(6)
C(1)-N(1)-C(5)	120.0(3)
C(1)-N(1)-Fe(1)	119.7(2)
C(5)-N(1)-Fe(1)	120.0(2)

C(8)-N(2)-C(12)	119.8(3)
C(8)-N(2)-Fe(1)	120.7(2)
C(12)-N(2)-Fe(1)	119.4(2)
C(13)-N(3)-C(17)	119.6(3)
C(13)-N(3)-Fe(1)	122.0(2)
C(17)-N(3)-Fe(1)	117.0(2)
C(22)-N(4)-C(18)	119.5(3)
C(22)-N(4)-Fe(1)	122.0(2)
C(18)-N(4)-Fe(1)	117.4(2)
C(29)-N(5)-C(25)	119.5(3)
C(29)-N(5)-Fe(1)	121.0(3)
C(25)-N(5)-Fe(1)	119.5(2)
C(30)-N(6)-C(34)	119.3(3)
C(30)-N(6)-Fe(1)	121.1(2)
C(34)-N(6)-Fe(1)	119.6(2)
N(1)-C(1)-C(2)	121.8(3)
C(1)-C(2)-C(3)	118.9(4)
C(2)-C(3)-C(4)	119.1(4)
C(5)-C(4)-C(3)	120.3(4)
N(1)-C(5)-C(4)	120.0(3)
N(1)-C(5)-C(6)	116.6(3)
C(4)-C(5)-C(6)	123.1(3)
C(8)-C(6)-C(7)	110.9(3)
C(8)-C(6)-C(13)	111.9(3)
C(7)-C(6)-C(13)	110.5(3)
C(8)-C(6)-C(5)	110.8(3)
C(7)-C(6)-C(5)	110.8(3)
C(13)-C(6)-C(5)	101.6(3)
N(2)-C(8)-C(9)	120.6(3)
N(2)-C(8)-C(6)	116.9(3)
C(9)-C(8)-C(6)	122.5(3)
C(10)-C(9)-C(8)	119.0(4)
C(11)-C(10)-C(9)	120.2(4)
C(10)-C(11)-C(12)	118.4(4)
N(2)-C(12)-C(11)	121.9(3)
N(3)-C(13)-C(14)	119.8(4)
N(3)-C(13)-C(6)	114.4(3)
C(14)-C(13)-C(6)	124.6(3)
C(15)-C(14)-C(13)	119.0(4)
C(16)-C(15)-C(14)	120.4(4)
C(15)-C(16)-C(17)	117.9(4)
N(3)-C(17)-C(16)	120.8(4)
N(3)-C(17)-C(18)	113.0(3)
C(16)-C(17)-C(18)	126.2(4)
N(4)-C(18)-C(19)	121.1(4)
N(4)-C(18)-C(17)	112.2(3)
C(19)-C(18)-C(17)	126.6(4)
C(20)-C(19)-C(18)	118.3(4)
C(19)-C(20)-C(21)	119.8(4)
C(20)-C(21)-C(22)	119.7(4)
N(4)-C(22)-C(21)	119.5(4)
N(4)-C(22)-C(23)	114.8(3)
C(21)-C(22)-C(23)	124.6(4)
C(30)-C(23)-C(24)	110.9(3)
C(30)-C(23)-C(22)	113.7(3)
C(24)-C(23)-C(22)	109.7(3)
C(30)-C(23)-C(25)	107.6(3)
C(24)-C(23)-C(25)	110.9(3)
C(22)-C(23)-C(25)	103.8(3)
N(5)-C(25)-C(26)	120.4(4)
N(5)-C(25)-C(23)	116.6(3)

C(26)-C(25)-C(23)	122.9(3)
C(27)-C(26)-C(25)	119.9(4)
C(26)-C(27)-C(28)	119.7(4)
C(27)-C(28)-C(29)	118.8(4)
N(5)-C(29)-C(28)	121.5(4)
N(6)-C(30)-C(31)	120.7(3)
N(6)-C(30)-C(23)	116.0(3)
C(31)-C(30)-C(23)	123.3(3)
C(32)-C(31)-C(30)	119.8(4)
C(31)-C(32)-C(33)	119.1(4)
C(34)-C(33)-C(32)	118.8(4)
N(6)-C(34)-C(33)	122.3(4)
F(3)-C(35)-F(2)	106.9(5)
F(3)-C(35)-F(1)	106.9(5)
F(2)-C(35)-F(1)	105.5(4)
F(3)-C(35)-S(1)	113.0(4)
F(2)-C(35)-S(1)	112.6(4)
F(1)-C(35)-S(1)	111.5(4)
F(5)-C(36)-F(6)	107.9(5)
F(5)-C(36)-F(4)	107.5(5)
F(6)-C(36)-F(4)	106.6(4)
F(5)-C(36)-S(2)	111.8(4)
F(6)-C(36)-S(2)	112.5(4)
F(4)-C(36)-S(2)	110.3(4)
F(7)-C(37)-F(8)	107.8(8)
F(7)-C(37)-F(9)	108.8(9)
F(8)-C(37)-F(9)	108.6(8)
F(7)-C(37)-S(3)	109.0(8)
F(8)-C(37)-S(3)	112.9(7)
F(9)-C(37)-S(3)	109.6(6)
F(9')-C(37')-F(7')	108.5(11)
F(9')-C(37')-F(8')	108.0(12)
F(7')-C(37')-F(8')	104.1(11)
F(9')-C(37')-S(3)	109.8(9)
F(7')-C(37')-S(3)	115.6(8)
F(8')-C(37')-S(3)	110.6(10)
N(7)-C(38)-C(39)	173.1(10)

Symmetry transformations used to generate equivalent atoms:

Table 4. Anisotropic displacement parameters ($\text{Å}^2 \times 10^3$) for $[\text{Fe}(\text{bpyPY4})](\text{OTf})_3 \cdot \text{MeCN}$.

The anisotropic displacement factor exponent takes the form:

$$-2 \pi^2 [h^2 a^{*2} U_{11} + \dots + 2 h k a^* b^* U_{12}]$$

	U11	U22	U33	U23	U13	U12
Fe(1)	19(1)	19(1)	21(1)	0(1)	8(1)	0(1)
S(1)	46(1)	50(1)	28(1)	2(1)	8(1)	2(1)
S(2)	38(1)	27(1)	26(1)	-1(1)	12(1)	-11(1)
S(3)	53(1)	42(1)	38(1)	9(1)	22(1)	-2(1)
F(1)	101(3)	59(2)	64(2)	-10(2)	17(2)	10(2)
F(2)	64(2)	78(2)	41(2)	8(2)	-6(1)	-3(2)
F(3)	96(3)	118(3)	56(2)	17(2)	17(2)	-51(2)
F(4)	96(3)	92(3)	64(2)	-1(2)	24(2)	59(2)

F(5)	384(9)	20(2)	133(4)	-15(2)	188(5)	-29(3)
F(6)	93(2)	83(2)	40(2)	-28(2)	27(2)	-19(2)
F(7)	75(6)	69(6)	69(5)	4(4)	50(5)	-2(4)
F(7')	72(5)	88(5)	125(6)	10(4)	63(5)	-8(4)
F(8)	70(4)	59(4)	35(3)	-4(3)	11(3)	-22(3)
F(8')	108(9)	133(11)	174(14)	-80(9)	97(10)	-36(8)
F(9)	113(6)	29(3)	63(4)	6(3)	51(4)	2(3)
F(9')	112(7)	63(5)	214(11)	52(6)	93(7)	20(4)
O(1)	64(2)	59(2)	55(2)	8(2)	26(2)	-4(2)
O(2)	51(2)	73(3)	42(2)	14(2)	-6(2)	-1(2)
O(3)	70(3)	101(3)	65(2)	-30(2)	26(2)	10(2)
O(4)	103(3)	55(2)	25(2)	2(2)	6(2)	33(2)
O(5)	65(3)	122(4)	106(3)	-63(3)	60(3)	-57(3)
O(6)	75(2)	32(2)	66(2)	15(2)	46(2)	9(2)
O(7)	28(3)	50(5)	32(4)	12(3)	12(3)	2(3)
O(7')	50(5)	67(6)	62(6)	7(4)	24(4)	-16(4)
O(8)	31(3)	58(5)	45(4)	8(4)	9(3)	-6(3)
O(8')	81(5)	66(5)	44(4)	-2(3)	34(4)	-25(4)
O(9)	78(10)	67(11)	42(8)	12(7)	24(5)	-14(8)
O(9')	61(7)	37(5)	38(7)	3(4)	11(5)	-16(5)
N(1)	22(1)	21(1)	24(1)	3(1)	11(1)	1(1)
N(2)	23(2)	21(1)	23(2)	-2(1)	7(1)	1(1)
N(3)	23(2)	27(2)	25(2)	1(1)	10(1)	6(1)
N(4)	27(2)	22(2)	31(2)	0(1)	16(1)	2(1)
N(5)	22(2)	25(2)	29(2)	-1(1)	11(1)	2(1)
N(6)	21(1)	21(2)	23(1)	-2(1)	9(1)	-2(1)
N(7)	112(5)	86(4)	92(4)	-9(4)	33(4)	-16(4)
C(1)	32(2)	20(2)	31(2)	0(1)	16(2)	-2(1)
C(2)	36(2)	23(2)	42(2)	4(2)	25(2)	5(2)
C(3)	29(2)	29(2)	46(2)	11(2)	21(2)	7(2)
C(4)	24(2)	31(2)	35(2)	5(2)	11(2)	1(2)
C(5)	23(2)	21(2)	24(2)	4(1)	10(1)	-1(1)
C(6)	23(2)	27(2)	24(2)	-3(1)	5(2)	0(1)
C(7)	26(2)	35(2)	31(2)	-6(2)	2(2)	-4(2)
C(8)	27(2)	22(2)	27(2)	-5(1)	9(2)	0(1)
C(9)	35(2)	24(2)	40(2)	-6(2)	9(2)	-5(2)
C(10)	45(2)	20(2)	52(3)	-3(2)	15(2)	-4(2)
C(11)	36(2)	26(2)	38(2)	4(2)	10(2)	5(2)
C(12)	25(2)	25(2)	27(2)	-2(2)	7(2)	2(1)
C(13)	25(2)	28(2)	27(2)	-4(2)	10(2)	7(1)
C(14)	28(2)	38(2)	26(2)	-4(2)	8(2)	9(2)
C(15)	34(2)	50(2)	23(2)	4(2)	12(2)	17(2)
C(16)	35(2)	42(2)	32(2)	9(2)	20(2)	12(2)
C(17)	25(2)	32(2)	31(2)	3(2)	16(2)	7(2)
C(18)	31(2)	30(2)	34(2)	6(2)	21(2)	6(2)
C(19)	48(3)	35(2)	47(2)	10(2)	31(2)	0(2)
C(20)	51(3)	27(2)	64(3)	3(2)	38(2)	-5(2)
C(21)	37(2)	28(2)	50(2)	-5(2)	25(2)	-7(2)
C(22)	31(2)	25(2)	39(2)	-6(2)	23(2)	-3(2)
C(23)	24(2)	30(2)	32(2)	-5(2)	10(2)	-6(2)
C(24)	30(2)	46(3)	42(2)	-12(2)	12(2)	-14(2)
C(25)	23(2)	31(2)	30(2)	0(2)	13(2)	-1(2)
C(26)	23(2)	54(3)	36(2)	-3(2)	10(2)	1(2)
C(27)	29(2)	64(3)	54(3)	-1(2)	20(2)	14(2)
C(28)	38(2)	49(3)	51(3)	-7(2)	22(2)	13(2)
C(29)	34(2)	30(2)	37(2)	-4(2)	15(2)	4(2)
C(30)	26(2)	22(2)	29(2)	-3(1)	12(2)	0(1)
C(31)	36(2)	36(2)	31(2)	-8(2)	10(2)	-5(2)
C(32)	45(2)	44(2)	27(2)	-5(2)	15(2)	1(2)
C(33)	40(2)	41(2)	32(2)	0(2)	21(2)	0(2)
C(34)	26(2)	30(2)	29(2)	1(2)	14(2)	0(2)

C(35)	56(3)	58(3)	34(2)	8(2)	8(2)	-1(2)
C(36)	83(4)	31(2)	42(3)	-1(2)	31(3)	2(2)
C(37)	50(6)	39(5)	42(5)	10(4)	21(5)	-6(4)
C(37')	60(7)	54(7)	96(9)	-8(6)	41(7)	-15(5)
C(38)	119(7)	81(5)	108(6)	-29(4)	63(5)	-32(5)
C(39)	120(7)	104(7)	218(12)	-17(7)	115(8)	-26(6)

Table 5. Hydrogen coordinates ($\times 10^4$) and isotropic displacement parameters ($\text{\AA}^2 \times 10^3$) for $[\text{Fe}(\text{bpyPY4})](\text{OTf})_3 \cdot \text{MeCN}$.

	x	y	z	U(eq)
H(1)	7801	2363	1786	32
H(2)	6485	2963	1423	37
H(3)	5332	2105	532	40
H(4)	5538	675	22	37
H(7A)	5822	-186	-749	52
H(7B)	6310	-1175	-628	52
H(7C)	5892	-916	-93	52
H(9)	6865	-2084	394	44
H(10)	7799	-3098	1347	50
H(11)	9007	-2471	2339	43
H(12)	9286	-850	2327	33
H(14)	6676	-80	-1332	39
H(15)	7188	1067	-1873	43
H(16)	8059	2282	-1098	42
H(19)	8819	3461	-158	47
H(20)	9757	4350	893	51
H(21)	10421	3617	2103	44
H(24A)	11288	2470	2798	62
H(24B)	10837	2828	3283	62
H(24C)	11309	1820	3479	62
H(26)	11622	880	2760	47
H(27)	11838	-428	2145	59
H(28)	10716	-1125	1102	54
H(29)	9385	-605	787	41
H(31)	10429	1904	3979	44
H(32)	9629	1307	4525	47
H(33)	8392	493	3739	43
H(34)	7998	315	2447	34
H(39A)	10906	3686	206	199
H(39B)	11711	3126	296	199
H(39C)	11624	3419	1043	199

Complete single crystal XRD data refinement for [Co(py₂pz)₂]

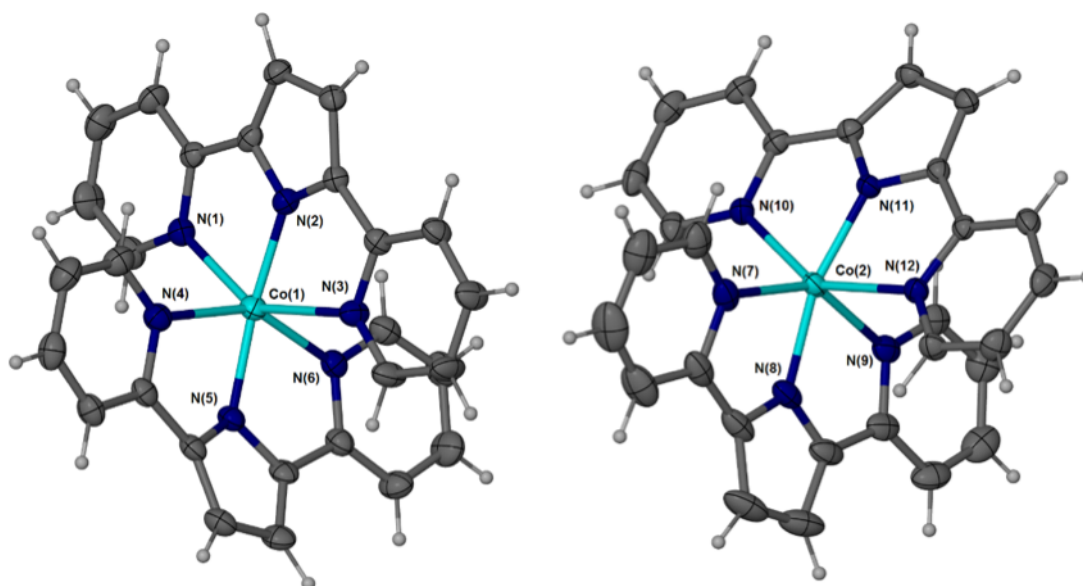


Figure 46. Molecular diagram of the two independent, but closely similar, molecules of [Co(py₂pz)₂] with non-hydrogen atoms represented by 50% displacement ellipsoids and hydrogen atoms as spheres of arbitrary size.

Table 1. Crystal data and structure refinement for [Co(py₂pz)₂].

Identification code	shelx	
Empirical formula	C ₂₈ H ₂₀ Co N ₆	
Formula weight	499.43	
Temperature	123(2) K	
Wavelength	0.71073 Å	
Crystal system, space group	Orthorhombic, P2(1)2(1)2(1)	
Unit cell dimensions	a = 8.7311(4) Å	alpha = 90 deg.
	b = 15.3564(7) Å	beta = 90 deg.
	c = 34.5783(17) Å	gamma = 90 deg.
Volume	4636.2(4) Å ³	
Z, Calculated density	8, 1.431 Mg/m ³	
Absorption coefficient	0.770 mm ⁻¹	
F(000)	2056	
Crystal size	0.25 x 0.10 x 0.05 mm	
Theta range for data collection	3.316 to 30.800 deg.	
Limiting indices	-8<=h<=11, -21<=k<=19, -48<=l<=44	
Reflections collected / unique	34633 / 12605 [R(int) = 0.0468]	

Completeness to theta = 25.242	99.6 %
Absorption correction	Semi-empirical from equivalents
Max. and min. transmission	1.00000 and 0.90970
Refinement method	Full-matrix least-squares on F ²
Data / restraints / parameters	12605 / 0 / 631
Goodness-of-fit on F ²	1.017
Final R indices [I>2sigma(I)]	R1 = 0.0425, wR2 = 0.0839
R indices (all data)	R1 = 0.0561, wR2 = 0.0915
Absolute structure parameter	-0.011(8)
Extinction coefficient	n/a
Largest diff. peak and hole	1.067 and -0.654 e.A ⁻³

Table 2. Atomic coordinates (x 10⁴) and equivalent isotropic displacement parameters (A² x 10³) for [Co(py₂pz)₂]. U(eq) is defined as one third of the trace of the orthogonalized Uij tensor.

	x	y	z	U(eq)
Co(1)	9606(1)	3714(1)	8585(1)	24(1)
Co(2)	4974(1)	8963(1)	8849(1)	22(1)
N(1)	11901(3)	3874(2)	8883(1)	25(1)
N(2)	9550(3)	2947(2)	9035(1)	22(1)
N(3)	7240(3)	2969(2)	8572(1)	26(1)
N(4)	8603(3)	4934(2)	8861(1)	26(1)
N(5)	9021(3)	4472(2)	8154(1)	24(1)
N(6)	10204(3)	2967(2)	8062(1)	25(1)
N(7)	5872(3)	9385(2)	8260(1)	29(1)
N(8)	4646(3)	7964(2)	8508(1)	28(1)
N(9)	3834(3)	7851(2)	9220(1)	27(1)
N(10)	7256(3)	8982(2)	9170(1)	24(1)
N(11)	4794(3)	9856(2)	9248(1)	20(1)
N(12)	2678(3)	9590(2)	8761(1)	21(1)
C(1)	13114(4)	4346(2)	8772(1)	32(1)
C(2)	14457(4)	4404(2)	8985(1)	38(1)
C(3)	14548(4)	3953(2)	9328(1)	36(1)
C(4)	13317(4)	3459(2)	9448(1)	30(1)
C(5)	12005(4)	3432(2)	9222(1)	22(1)
C(6)	10628(4)	2938(2)	9314(1)	22(1)
C(7)	10089(4)	2453(2)	9630(1)	25(1)
C(8)	8615(4)	2164(2)	9529(1)	24(1)
C(9)	8330(4)	2487(2)	9157(1)	22(1)
C(10)	7048(4)	2460(2)	8888(1)	22(1)
C(11)	5729(4)	1966(2)	8942(1)	28(1)
C(12)	4594(4)	1998(2)	8667(1)	33(1)
C(13)	4785(4)	2520(2)	8345(1)	36(1)

C(14)	6125(4)	2991(2)	8310(1)	33(1)
C(15)	8516(4)	5149(2)	9235(1)	31(1)
C(16)	7773(4)	5885(3)	9367(1)	36(1)
C(17)	7091(4)	6427(2)	9097(1)	32(1)
C(18)	7171(4)	6226(2)	8710(1)	29(1)
C(19)	7931(4)	5467(2)	8596(1)	25(1)
C(20)	8031(4)	5144(2)	8202(1)	24(1)
C(21)	7173(4)	5259(2)	7865(1)	30(1)
C(22)	7669(4)	4616(2)	7604(1)	31(1)
C(23)	8799(4)	4139(2)	7796(1)	25(1)
C(24)	9569(4)	3304(2)	7733(1)	27(1)
C(25)	9626(5)	2849(2)	7386(1)	34(1)
C(26)	10320(5)	2045(2)	7373(1)	41(1)
C(27)	10944(5)	1707(2)	7709(1)	39(1)
C(28)	10862(4)	2186(2)	8040(1)	31(1)
C(29)	6488(4)	10142(3)	8153(1)	37(1)
C(30)	7071(5)	10305(3)	7790(1)	47(1)
C(31)	7024(6)	9639(4)	7520(1)	53(1)
C(32)	6366(5)	8851(3)	7621(1)	48(1)
C(33)	5760(4)	8739(3)	7989(1)	34(1)
C(34)	4969(5)	7970(2)	8124(1)	34(1)
C(35)	4262(6)	7245(3)	7955(1)	46(1)
C(36)	3499(5)	6802(3)	8246(1)	44(1)
C(37)	3757(4)	7273(2)	8589(1)	32(1)
C(38)	3285(4)	7203(2)	8994(1)	30(1)
C(39)	2349(5)	6547(2)	9147(1)	38(1)
C(40)	2021(5)	6552(3)	9535(1)	42(1)
C(41)	2605(5)	7207(2)	9769(1)	38(1)
C(42)	3501(4)	7842(2)	9595(1)	31(1)
C(43)	8537(4)	8534(2)	9095(1)	27(1)
C(44)	9843(4)	8594(2)	9317(1)	32(1)
C(45)	9843(4)	9151(2)	9630(1)	32(1)
C(46)	8551(4)	9627(2)	9714(1)	26(1)
C(47)	7253(4)	9534(2)	9480(1)	22(1)
C(48)	5818(4)	9995(2)	9532(1)	22(1)
C(49)	5183(4)	10564(2)	9804(1)	24(1)
C(50)	3698(4)	10764(2)	9672(1)	24(1)
C(51)	3504(4)	10306(2)	9324(1)	21(1)
C(52)	2325(4)	10202(2)	9033(1)	20(1)
C(53)	953(4)	10664(2)	9008(1)	25(1)
C(54)	-47(4)	10499(2)	8710(1)	30(1)
C(55)	316(4)	9870(2)	8436(1)	31(1)
C(56)	1685(4)	9439(2)	8474(1)	26(1)

Table 3. Bond lengths [Å] and angles [deg] for [Co(py₂pz)₂].

Co(1)-N(2)	1.953(3)
Co(1)-N(5)	1.957(3)
Co(1)-N(6)	2.204(3)
Co(1)-N(1)	2.267(3)
Co(1)-N(4)	2.279(3)
Co(1)-N(3)	2.361(3)
Co(2)-N(11)	1.952(2)
Co(2)-N(8)	1.956(3)
Co(2)-N(12)	2.245(3)
Co(2)-N(7)	2.278(3)
Co(2)-N(10)	2.281(3)

Co(2)-N(9)	2.357(3)
N(1)-C(1)	1.339(4)
N(1)-C(5)	1.359(4)
N(2)-C(9)	1.346(4)
N(2)-C(6)	1.349(4)
N(3)-C(14)	1.332(5)
N(3)-C(10)	1.353(4)
N(4)-C(15)	1.336(5)
N(4)-C(19)	1.363(4)
N(5)-C(23)	1.356(4)
N(5)-C(20)	1.357(4)
N(6)-C(28)	1.332(4)
N(6)-C(24)	1.367(4)
N(7)-C(29)	1.333(5)
N(7)-C(33)	1.368(5)
N(8)-C(37)	1.344(5)
N(8)-C(34)	1.360(4)
N(9)-C(42)	1.327(5)
N(9)-C(38)	1.354(5)
N(10)-C(43)	1.338(4)
N(10)-C(47)	1.367(4)
N(11)-C(48)	1.344(4)
N(11)-C(51)	1.347(4)
N(12)-C(56)	1.336(4)
N(12)-C(52)	1.365(4)
C(1)-C(2)	1.386(5)
C(2)-C(3)	1.376(5)
C(3)-C(4)	1.379(5)
C(4)-C(5)	1.386(5)
C(5)-C(6)	1.457(5)
C(6)-C(7)	1.404(5)
C(7)-C(8)	1.406(5)
C(8)-C(9)	1.400(5)
C(9)-C(10)	1.457(5)
C(10)-C(11)	1.392(5)
C(11)-C(12)	1.374(5)
C(12)-C(13)	1.383(5)
C(13)-C(14)	1.381(5)
C(15)-C(16)	1.380(5)
C(16)-C(17)	1.385(6)
C(17)-C(18)	1.374(5)
C(18)-C(19)	1.399(5)
C(19)-C(20)	1.450(5)
C(20)-C(21)	1.399(5)
C(21)-C(22)	1.405(5)
C(22)-C(23)	1.396(5)
C(23)-C(24)	1.464(5)
C(24)-C(25)	1.388(5)
C(25)-C(26)	1.377(5)
C(26)-C(27)	1.386(6)
C(27)-C(28)	1.362(5)
C(29)-C(30)	1.378(6)
C(30)-C(31)	1.385(7)
C(31)-C(32)	1.384(7)
C(32)-C(33)	1.391(6)
C(33)-C(34)	1.444(6)
C(34)-C(35)	1.400(6)
C(35)-C(36)	1.386(7)
C(36)-C(37)	1.406(5)
C(37)-C(38)	1.462(6)
C(38)-C(39)	1.401(6)

C(39)-C(40)	1.374(6)
C(40)-C(41)	1.387(6)
C(41)-C(42)	1.388(5)
C(43)-C(44)	1.379(5)
C(44)-C(45)	1.380(5)
C(45)-C(46)	1.375(5)
C(46)-C(47)	1.398(5)
C(47)-C(48)	1.450(5)
C(48)-C(49)	1.400(4)
C(49)-C(50)	1.408(5)
C(50)-C(51)	1.404(5)
C(51)-C(52)	1.449(5)
C(52)-C(53)	1.395(5)
C(53)-C(54)	1.375(5)
C(54)-C(55)	1.389(5)
C(55)-C(56)	1.373(5)
N(2)-Co(1)-N(5)	163.43(12)
N(2)-Co(1)-N(6)	110.27(10)
N(5)-Co(1)-N(6)	75.35(11)
N(2)-Co(1)-N(1)	74.04(11)
N(5)-Co(1)-N(1)	120.78(11)
N(6)-Co(1)-N(1)	102.71(11)
N(2)-Co(1)-N(4)	98.72(11)
N(5)-Co(1)-N(4)	74.34(11)
N(6)-Co(1)-N(4)	149.68(11)
N(1)-Co(1)-N(4)	93.41(10)
N(2)-Co(1)-N(3)	72.58(11)
N(5)-Co(1)-N(3)	92.64(11)
N(6)-Co(1)-N(3)	86.61(11)
N(1)-Co(1)-N(3)	146.52(10)
N(4)-Co(1)-N(3)	93.99(10)
N(11)-Co(2)-N(8)	164.88(12)
N(11)-Co(2)-N(12)	73.93(10)
N(8)-Co(2)-N(12)	97.07(11)
N(11)-Co(2)-N(7)	117.39(11)
N(8)-Co(2)-N(7)	74.61(12)
N(12)-Co(2)-N(7)	93.62(10)
N(11)-Co(2)-N(10)	73.61(11)
N(8)-Co(2)-N(10)	115.54(11)
N(12)-Co(2)-N(10)	147.27(10)
N(7)-Co(2)-N(10)	97.54(10)
N(11)-Co(2)-N(9)	95.19(11)
N(8)-Co(2)-N(9)	72.39(12)
N(12)-Co(2)-N(9)	90.44(10)
N(7)-Co(2)-N(9)	147.01(11)
N(10)-Co(2)-N(9)	96.51(10)
C(1)-N(1)-C(5)	117.6(3)
C(1)-N(1)-Co(1)	129.0(3)
C(5)-N(1)-Co(1)	113.4(2)
C(9)-N(2)-C(6)	108.8(3)
C(9)-N(2)-Co(1)	125.9(2)
C(6)-N(2)-Co(1)	124.0(2)
C(14)-N(3)-C(10)	118.3(3)
C(14)-N(3)-Co(1)	129.7(2)
C(10)-N(3)-Co(1)	111.9(2)
C(15)-N(4)-C(19)	118.6(3)
C(15)-N(4)-Co(1)	129.1(2)
C(19)-N(4)-Co(1)	112.1(2)
C(23)-N(5)-C(20)	108.0(3)
C(23)-N(5)-Co(1)	120.6(2)

C(20)-N(5)-Co(1)	121.7(2)
C(28)-N(6)-C(24)	118.0(3)
C(28)-N(6)-Co(1)	128.1(2)
C(24)-N(6)-Co(1)	112.9(2)
C(29)-N(7)-C(33)	118.2(3)
C(29)-N(7)-Co(2)	129.5(3)
C(33)-N(7)-Co(2)	112.4(3)
C(37)-N(8)-C(34)	109.2(3)
C(37)-N(8)-Co(2)	125.4(3)
C(34)-N(8)-Co(2)	123.6(2)
C(42)-N(9)-C(38)	118.7(3)
C(42)-N(9)-Co(2)	129.1(2)
C(38)-N(9)-Co(2)	111.5(3)
C(43)-N(10)-C(47)	118.2(3)
C(43)-N(10)-Co(2)	129.0(2)
C(47)-N(10)-Co(2)	112.8(2)
C(48)-N(11)-C(51)	109.5(3)
C(48)-N(11)-Co(2)	125.0(2)
C(51)-N(11)-Co(2)	124.4(2)
C(56)-N(12)-C(52)	118.9(3)
C(56)-N(12)-Co(2)	127.3(2)
C(52)-N(12)-Co(2)	113.7(2)
N(1)-C(1)-C(2)	123.5(4)
C(3)-C(2)-C(1)	118.3(4)
C(2)-C(3)-C(4)	119.4(3)
C(3)-C(4)-C(5)	119.4(4)
N(1)-C(5)-C(4)	121.8(3)
N(1)-C(5)-C(6)	113.2(3)
C(4)-C(5)-C(6)	125.0(3)
N(2)-C(6)-C(7)	109.2(3)
N(2)-C(6)-C(5)	114.5(3)
C(7)-C(6)-C(5)	136.3(3)
C(6)-C(7)-C(8)	106.3(3)
C(9)-C(8)-C(7)	106.2(3)
N(2)-C(9)-C(8)	109.5(3)
N(2)-C(9)-C(10)	114.9(3)
C(8)-C(9)-C(10)	135.5(3)
N(3)-C(10)-C(11)	121.7(3)
N(3)-C(10)-C(9)	113.8(3)
C(11)-C(10)-C(9)	124.5(3)
C(12)-C(11)-C(10)	119.0(3)
C(11)-C(12)-C(13)	119.4(3)
C(14)-C(13)-C(12)	118.4(3)
N(3)-C(14)-C(13)	123.1(3)
N(4)-C(15)-C(16)	123.3(4)
C(15)-C(16)-C(17)	118.2(4)
C(18)-C(17)-C(16)	119.9(3)
C(17)-C(18)-C(19)	119.2(3)
N(4)-C(19)-C(18)	120.9(3)
N(4)-C(19)-C(20)	113.6(3)
C(18)-C(19)-C(20)	125.5(3)
N(5)-C(20)-C(21)	109.5(3)
N(5)-C(20)-C(19)	114.5(3)
C(21)-C(20)-C(19)	135.0(3)
C(20)-C(21)-C(22)	106.4(3)
C(23)-C(22)-C(21)	106.4(3)
N(5)-C(23)-C(22)	109.7(3)
N(5)-C(23)-C(24)	113.6(3)
C(22)-C(23)-C(24)	135.6(3)
N(6)-C(24)-C(25)	120.9(3)
N(6)-C(24)-C(23)	113.2(3)

C(25)-C(24)-C(23)	125.8(3)
C(26)-C(25)-C(24)	119.7(3)
C(25)-C(26)-C(27)	118.8(4)
C(28)-C(27)-C(26)	118.8(3)
N(6)-C(28)-C(27)	123.8(4)
N(7)-C(29)-C(30)	124.1(4)
C(29)-C(30)-C(31)	118.0(5)
C(32)-C(31)-C(30)	119.2(4)
C(31)-C(32)-C(33)	119.8(4)
N(7)-C(33)-C(32)	120.7(4)
N(7)-C(33)-C(34)	114.0(3)
C(32)-C(33)-C(34)	125.3(4)
N(8)-C(34)-C(35)	108.1(4)
N(8)-C(34)-C(33)	114.8(3)
C(35)-C(34)-C(33)	136.6(4)
C(36)-C(35)-C(34)	107.4(4)
C(35)-C(36)-C(37)	106.5(4)
N(8)-C(37)-C(36)	108.9(4)
N(8)-C(37)-C(38)	114.8(3)
C(36)-C(37)-C(38)	136.3(4)
N(9)-C(38)-C(39)	121.0(4)
N(9)-C(38)-C(37)	113.6(3)
C(39)-C(38)-C(37)	125.4(4)
C(40)-C(39)-C(38)	119.2(4)
C(39)-C(40)-C(41)	119.9(4)
C(40)-C(41)-C(42)	117.5(4)
N(9)-C(42)-C(41)	123.7(4)
N(10)-C(43)-C(44)	123.2(3)
C(43)-C(44)-C(45)	118.6(3)
C(46)-C(45)-C(44)	119.6(3)
C(45)-C(46)-C(47)	119.4(3)
N(10)-C(47)-C(46)	120.9(3)
N(10)-C(47)-C(48)	113.6(3)
C(46)-C(47)-C(48)	125.4(3)
N(11)-C(48)-C(49)	109.0(3)
N(11)-C(48)-C(47)	114.1(3)
C(49)-C(48)-C(47)	136.9(3)
C(48)-C(49)-C(50)	106.4(3)
C(51)-C(50)-C(49)	106.3(3)
N(11)-C(51)-C(50)	108.8(3)
N(11)-C(51)-C(52)	113.7(3)
C(50)-C(51)-C(52)	137.5(3)
N(12)-C(52)-C(53)	120.1(3)
N(12)-C(52)-C(51)	113.3(3)
C(53)-C(52)-C(51)	126.6(3)
C(54)-C(53)-C(52)	119.8(3)
C(53)-C(54)-C(55)	119.7(3)
C(56)-C(55)-C(54)	117.8(3)
N(12)-C(56)-C(55)	123.6(3)

Symmetry transformations used to generate equivalent atoms:

Table 4. Anisotropic displacement parameters ($\text{Å}^2 \times 10^3$) for $[\text{Co}(\text{py}_2\text{pz})_2]$.
The anisotropic displacement factor exponent takes the form:
 $-2 \pi^2 [h^2 a^{*2} U_{11} + \dots + 2 h k a^* b^* U_{12}]$

	U11	U22	U33	U23	U13	U12
Co(1)	26(1)	23(1)	22(1)	3(1)	1(1)	-2(1)
Co(2)	20(1)	26(1)	21(1)	-6(1)	-1(1)	3(1)
N(1)	24(1)	25(1)	26(2)	-1(1)	2(1)	0(1)
N(2)	20(1)	25(1)	22(2)	-1(1)	0(1)	0(1)
N(3)	22(1)	31(2)	25(2)	5(1)	0(1)	-3(1)
N(4)	26(1)	26(1)	26(2)	1(1)	2(1)	0(1)
N(5)	28(1)	21(1)	22(2)	3(1)	3(1)	1(1)
N(6)	25(2)	23(1)	27(2)	2(1)	1(1)	-2(1)
N(7)	22(1)	43(2)	23(2)	-4(1)	-3(1)	6(1)
N(8)	29(2)	31(1)	26(2)	-8(1)	-5(1)	10(1)
N(9)	23(1)	26(1)	33(2)	-5(1)	-4(1)	7(1)
N(10)	21(1)	26(1)	24(2)	-2(1)	2(1)	1(1)
N(11)	20(1)	21(1)	20(1)	-3(1)	0(1)	1(1)
N(12)	22(1)	25(1)	17(2)	-1(1)	0(1)	0(1)
C(1)	30(2)	31(2)	36(2)	1(2)	4(2)	-2(2)
C(2)	25(2)	39(2)	49(3)	-1(2)	5(2)	-10(2)
C(3)	24(2)	43(2)	40(2)	-10(2)	-4(2)	-1(2)
C(4)	24(2)	37(2)	28(2)	-2(2)	-5(2)	-1(2)
C(5)	25(2)	21(2)	20(2)	-4(1)	0(1)	4(1)
C(6)	21(2)	23(2)	23(2)	-6(1)	-2(1)	4(1)
C(7)	28(2)	27(2)	20(2)	-2(1)	-2(2)	1(2)
C(8)	26(2)	25(2)	20(2)	0(1)	4(1)	-1(1)
C(9)	20(2)	22(2)	23(2)	-1(1)	2(1)	1(1)
C(10)	20(1)	22(2)	25(2)	1(1)	2(1)	3(1)
C(11)	27(2)	27(2)	29(2)	7(1)	1(2)	-3(1)
C(12)	25(2)	38(2)	37(2)	11(2)	-3(2)	-10(2)
C(13)	30(2)	47(2)	32(2)	14(2)	-13(2)	-11(2)
C(14)	28(2)	38(2)	31(2)	13(2)	-4(2)	-5(2)
C(15)	28(2)	37(2)	28(2)	-1(2)	-2(2)	-1(2)
C(16)	33(2)	45(2)	29(2)	-11(2)	2(2)	-3(2)
C(17)	27(2)	31(2)	39(2)	-11(2)	6(2)	-2(2)
C(18)	28(2)	22(2)	37(2)	0(2)	3(2)	2(1)
C(19)	23(2)	21(2)	30(2)	3(1)	4(2)	-2(1)
C(20)	28(2)	19(2)	26(2)	4(1)	4(2)	0(1)
C(21)	32(2)	26(2)	31(2)	7(2)	4(2)	5(2)
C(22)	37(2)	34(2)	21(2)	7(2)	4(2)	2(2)
C(23)	32(2)	25(2)	18(2)	5(1)	6(1)	0(1)
C(24)	31(2)	24(2)	25(2)	2(1)	4(2)	1(1)
C(25)	43(2)	36(2)	23(2)	-1(2)	1(2)	6(2)
C(26)	52(3)	36(2)	35(2)	-10(2)	3(2)	8(2)
C(27)	43(2)	28(2)	46(3)	-2(2)	1(2)	7(2)
C(28)	30(2)	30(2)	34(2)	5(2)	0(2)	1(2)
C(29)	24(2)	52(2)	35(2)	0(2)	-4(2)	5(2)
C(30)	33(2)	68(3)	41(3)	15(2)	-4(2)	5(2)
C(31)	51(3)	81(4)	26(2)	11(2)	2(2)	14(3)
C(32)	55(3)	63(3)	25(2)	-5(2)	-3(2)	19(2)
C(33)	28(2)	48(2)	25(2)	-7(2)	-6(2)	15(2)
C(34)	38(2)	40(2)	24(2)	-10(2)	-7(2)	18(2)
C(35)	64(3)	41(2)	33(2)	-16(2)	-16(2)	15(2)
C(36)	56(3)	31(2)	46(3)	-13(2)	-24(2)	8(2)
C(37)	31(2)	27(2)	37(2)	-10(2)	-12(2)	9(1)
C(38)	27(2)	24(2)	40(2)	-4(2)	-11(2)	9(1)

C(39)	41(2)	23(2)	52(3)	-1(2)	-12(2)	0(2)
C(40)	40(2)	32(2)	53(3)	14(2)	-7(2)	-1(2)
C(41)	37(2)	39(2)	37(2)	10(2)	-5(2)	6(2)
C(42)	25(2)	30(2)	37(2)	0(2)	-6(2)	6(2)
C(43)	24(2)	23(2)	33(2)	4(1)	5(2)	2(1)
C(44)	21(2)	30(2)	47(2)	11(2)	3(2)	3(1)
C(45)	23(2)	36(2)	39(2)	14(2)	-8(2)	-2(2)
C(46)	25(2)	28(2)	26(2)	5(2)	-5(2)	-6(1)
C(47)	22(2)	23(2)	20(2)	4(1)	-1(1)	-4(1)
C(48)	24(2)	22(2)	20(2)	1(1)	-1(1)	-2(1)
C(49)	29(2)	25(2)	18(2)	-3(1)	1(2)	-4(1)
C(50)	26(2)	23(2)	23(2)	-3(1)	6(1)	-2(1)
C(51)	21(2)	19(2)	22(2)	1(1)	4(1)	0(1)
C(52)	19(1)	20(2)	21(2)	2(1)	3(1)	-2(1)
C(53)	25(2)	20(2)	29(2)	-2(1)	7(2)	1(1)
C(54)	22(2)	27(2)	41(2)	6(1)	-2(2)	5(2)
C(55)	27(2)	38(2)	28(2)	2(2)	-7(2)	0(2)
C(56)	27(2)	30(2)	20(2)	-4(1)	-3(1)	1(1)

Table 5. Hydrogen coordinates ($\times 10^4$) and isotropic displacement parameters ($\text{Å}^2 \times 10^3$) for $[\text{Co}(\text{py}_2\text{pz})_2]$.

	x	y	z	U(eq)
H(1)	13051	4659	8536	39
H(2)	15292	4746	8896	45
H(3)	15451	3981	9481	43
H(4)	13367	3140	9683	36
H(7)	10616	2341	9865	30
H(8)	7946	1819	9682	28
H(11)	5615	1612	9165	33
H(12)	3686	1664	8698	40
H(13)	4011	2555	8152	44
H(14)	6258	3347	8088	39
H(15)	8991	4778	9419	37
H(16)	7730	6015	9635	43
H(17)	6569	6937	9179	39
H(18)	6715	6598	8524	35
H(21)	6407	5687	7820	36
H(22)	7306	4524	7348	37
H(25)	9187	3092	7159	41
H(26)	10371	1727	7137	49
H(27)	11421	1151	7709	47
H(28)	11299	1950	8269	38
H(29)	6529	10597	8339	44
H(30)	7492	10857	7726	57
H(31)	7438	9722	7268	63
H(32)	6330	8388	7439	57
H(35)	4299	7086	7690	55
H(36)	2917	6283	8220	53
H(39)	1947	6105	8984	46
H(40)	1395	6109	9643	50
H(41)	2400	7220	10039	45
H(42)	3898	8296	9752	37
H(43)	8546	8156	8877	32

H(44)	10725	8258	9256	39
H(45)	10731	9206	9787	39
H(46)	8540	10016	9927	32
H(49)	5658	10774	10033	29
H(50)	2973	11135	9794	29
H(53)	710	11092	9197	30
H(54)	-981	10813	8691	36
H(55)	-361	9742	8228	37
H(56)	1941	9010	8287	31

Complete single crystal XRD data refinement for [Co(py₂pz)₂](OTf)

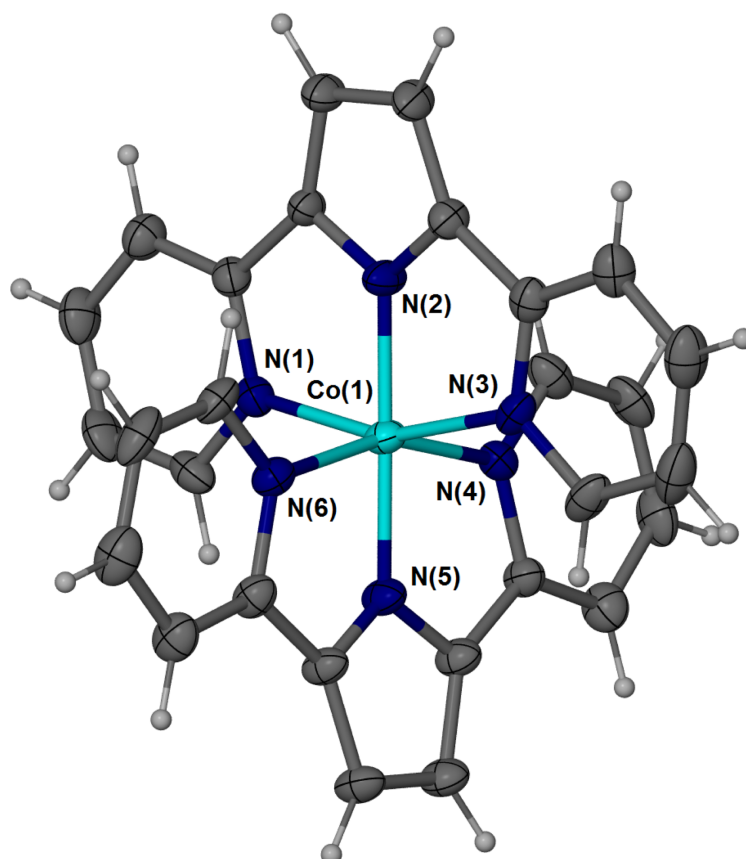


Figure 47. Molecular diagram of the complex cation in [Co(py₂pz)₂](OTf)·½MeCN with non-hydrogen atoms represented by 50% displacement ellipsoids and hydrogen atoms as spheres of arbitrary size. The triflate anion has been omitted for clarity.

Note: The triflate anion was modelled as disordered over two positions with occupancies fixed at 0.5:0.5 after trial refinement. The geometry and anisotropic refinement of all the components of the disordered anions were restrained using DFIX and ISOR. Residual disordered solvent (assumed to be MeCN), which occupied voids located between the disordered anions was accounted for using PLATON SQUEEZE. Overall the modelling of the anion/solvent regions was not satisfactory. However, the cation was well resolved and the geometry was consistent with Co(III).

Table 1. Crystal data and structure refinement for [Co(py₂pz)₂](OTf)·½MeCN.

Identification code	shelx	
Empirical formula	C ₂₉ H ₂₀ Co F ₃ N ₆ O ₃ S	
Formula weight	648.50	
Temperature	123(2) K	
Wavelength	0.71073 Å	
Crystal system, space group	Tetragonal, P4(1)	
Unit cell dimensions	a = 8.8768(3) Å	alpha = 90 deg.
	b = 8.8768(3) Å	beta = 90 deg.
	c = 36.126(2) Å	gamma = 90 deg.

Volume	2846.7(3) Å ³
Z, Calculated density	4, 1.513 Mg/m ³
Absorption coefficient	0.739 mm ⁻¹
F(000)	1320
Crystal size	0.20 x 0.15 x 0.10 mm
Theta range for data collection	3.436 to 30.591 deg.
Limiting indices	-12<=h<=12, -12<=k<=10, -50<=l<=44
Reflections collected / unique	18883 / 7030 [R(int) = 0.0318]
Completeness to theta = 25.242	99.6 %
Absorption correction	Semi-empirical from equivalents
Max. and min. transmission	1.00000 and 0.66590
Refinement method	Full-matrix least-squares on F ²
Data / restraints / parameters	7030 / 117 / 461
Goodness-of-fit on F ²	1.050
Final R indices [I>2sigma(I)]	R1 = 0.0575, wR2 = 0.1581
R indices (all data)	R1 = 0.0622, wR2 = 0.1640
Absolute structure parameter	0.33(2)
Extinction coefficient	n/a
Largest diff. peak and hole	0.876 and -0.769 e.Å ⁻³

Table 2. Atomic coordinates (x 10⁴) and equivalent isotropic displacement parameters (Å² x 10³) for [Co(py₂pz)₂](OTf)·½MeCN. U(eq) is defined as one third of the trace of the orthogonalized Uij tensor.

	x	y	z	U(eq)
Co(1)	7163(1)	7991(1)	2444(1)	22(1)
S(1)	10043(11)	12613(6)	3756(2)	82(2)
S(2)	9001(12)	12434(7)	3701(2)	93(2)
F(1)	7150(20)	12329(19)	4008(4)	150(7)
F(2)	7120(20)	13174(19)	3456(5)	170(8)
F(3)	7770(20)	10882(15)	3564(5)	159(7)
F(4)	11760(50)	12280(30)	3412(5)	370(30)
F(5)	11720(30)	11350(20)	3961(6)	165(8)
F(6)	11750(30)	13744(19)	3883(6)	196(10)
O(1)	9877(19)	14125(10)	3879(3)	87(4)

O(2)	10462(19)	11569(11)	4046(3)	74(3)
O(3)	10570(30)	12320(20)	3404(3)	123(6)
O(4)	8720(20)	12729(16)	4071(3)	98(5)
O(5)	8787(19)	13557(12)	3436(3)	80(4)
O(6)	8938(19)	10911(9)	3576(3)	70(3)
N(1)	5144(5)	8860(4)	2553(1)	22(1)
N(2)	7147(4)	7846(5)	2943(2)	25(1)
N(3)	9174(5)	7082(5)	2537(1)	24(1)
N(4)	8069(5)	9996(5)	2367(1)	23(1)
N(5)	7173(5)	8075(5)	1942(2)	26(1)
N(6)	6296(5)	5984(5)	2320(1)	24(1)
C(1)	4175(6)	9386(6)	2305(2)	28(1)
C(2)	2781(6)	9995(6)	2411(2)	34(1)
C(3)	2411(6)	10061(6)	2781(2)	33(1)
C(4)	3424(6)	9487(6)	3039(2)	29(1)
C(5)	4786(5)	8893(5)	2926(1)	23(1)
C(6)	5963(5)	8248(5)	3155(1)	22(1)
C(7)	6292(5)	7782(6)	3518(1)	27(1)
C(8)	7708(5)	7075(6)	3508(2)	26(1)
C(9)	8205(5)	7126(5)	3139(1)	23(1)
C(10)	9434(5)	6693(5)	2896(1)	25(1)
C(11)	10771(6)	5980(6)	3000(2)	30(1)
C(12)	11845(6)	5697(7)	2738(2)	38(1)
C(13)	11605(6)	6155(7)	2371(2)	39(1)
C(14)	10244(6)	6819(6)	2280(2)	32(1)
C(15)	8438(6)	10996(6)	2633(2)	28(1)
C(16)	9100(7)	12368(6)	2549(2)	34(1)
C(17)	9386(6)	12722(6)	2188(2)	34(1)
C(18)	9023(6)	11716(6)	1906(2)	31(1)
C(19)	8345(6)	10356(5)	2001(1)	23(1)
C(20)	7843(6)	9189(5)	1751(1)	26(1)
C(21)	7827(6)	8755(6)	1377(1)	28(1)
C(22)	7130(6)	7344(5)	1356(1)	27(1)
C(23)	6752(6)	6944(5)	1726(1)	25(1)
C(24)	6164(6)	5712(5)	1947(1)	26(1)
C(25)	5537(6)	4359(5)	1820(2)	30(1)
C(26)	5078(6)	3283(6)	2077(2)	35(1)
C(27)	5225(6)	3572(6)	2450(2)	34(1)
C(28)	5840(5)	4934(6)	2561(2)	28(1)
C(29)	8030(12)	12395(14)	3682(3)	39(3)
C(30)	11035(13)	12435(12)	3750(3)	32(2)

Table 3. Bond lengths [Å] and angles [deg] for $[\text{Co}(\text{py}_2\text{pz})_2](\text{OTf}) \cdot \frac{1}{2}\text{MeCN}$.

Co(1)-N(2)	1.809(5)
Co(1)-N(5)	1.814(6)
Co(1)-N(4)	1.973(4)
Co(1)-N(3)	1.988(4)
Co(1)-N(6)	1.991(4)
Co(1)-N(1)	1.991(4)
S(1)-O(3)	1.381(9)
S(1)-O(1)	1.421(9)
S(1)-O(2)	1.447(9)
S(1)-C(29)	1.817(10)
S(2)-O(4)	1.385(9)
S(2)-O(5)	1.394(9)
S(2)-O(6)	1.426(9)

S(2)-C(30)	1.815(11)
F(1)-C(29)	1.416(12)
F(2)-C(29)	1.338(11)
F(3)-C(29)	1.427(11)
F(4)-C(30)	1.389(13)
F(5)-C(30)	1.370(11)
F(6)-C(30)	1.408(12)
N(1)-C(1)	1.327(6)
N(1)-C(5)	1.383(6)
N(2)-C(9)	1.338(6)
N(2)-C(6)	1.349(6)
N(3)-C(14)	1.348(6)
N(3)-C(10)	1.360(6)
N(4)-C(15)	1.348(6)
N(4)-C(19)	1.382(6)
N(5)-C(23)	1.326(7)
N(5)-C(20)	1.344(6)
N(6)-C(28)	1.338(6)
N(6)-C(24)	1.377(6)
C(1)-C(2)	1.404(8)
C(2)-C(3)	1.376(9)
C(3)-C(4)	1.392(7)
C(4)-C(5)	1.381(7)
C(5)-C(6)	1.451(6)
C(6)-C(7)	1.406(6)
C(7)-C(8)	1.406(7)
C(8)-C(9)	1.403(7)
C(9)-C(10)	1.453(7)
C(10)-C(11)	1.397(7)
C(11)-C(12)	1.366(8)
C(12)-C(13)	1.405(10)
C(13)-C(14)	1.383(9)
C(15)-C(16)	1.386(8)
C(16)-C(17)	1.367(9)
C(17)-C(18)	1.392(8)
C(18)-C(19)	1.392(7)
C(19)-C(20)	1.445(7)
C(20)-C(21)	1.407(7)
C(21)-C(22)	1.399(7)
C(22)-C(23)	1.425(6)
C(23)-C(24)	1.450(6)
C(24)-C(25)	1.401(7)
C(25)-C(26)	1.393(7)
C(26)-C(27)	1.379(10)
C(27)-C(28)	1.386(8)
N(2)-Co(1)-N(5)	178.3(2)
N(2)-Co(1)-N(4)	101.92(18)
N(5)-Co(1)-N(4)	79.71(17)
N(2)-Co(1)-N(3)	78.97(17)
N(5)-Co(1)-N(3)	100.52(18)
N(4)-Co(1)-N(3)	91.39(18)
N(2)-Co(1)-N(6)	98.99(19)
N(5)-Co(1)-N(6)	79.37(18)
N(4)-Co(1)-N(6)	159.05(18)
N(3)-Co(1)-N(6)	91.27(18)
N(2)-Co(1)-N(1)	79.74(17)
N(5)-Co(1)-N(1)	100.78(18)
N(4)-Co(1)-N(1)	92.58(18)
N(3)-Co(1)-N(1)	158.70(18)
N(6)-Co(1)-N(1)	92.45(18)

O(3)-S(1)-O(1)	120.1(8)
O(3)-S(1)-O(2)	117.4(9)
O(1)-S(1)-O(2)	113.9(7)
O(3)-S(1)-C(29)	100.0(12)
O(1)-S(1)-C(29)	92.6(9)
O(2)-S(1)-C(29)	107.0(9)
O(4)-S(2)-O(5)	120.2(9)
O(4)-S(2)-O(6)	118.5(8)
O(5)-S(2)-O(6)	117.1(7)
O(4)-S(2)-C(30)	94.7(10)
O(5)-S(2)-C(30)	101.7(9)
O(6)-S(2)-C(30)	94.0(9)
C(1)-N(1)-C(5)	120.0(4)
C(1)-N(1)-Co(1)	125.9(4)
C(5)-N(1)-Co(1)	114.1(3)
C(9)-N(2)-C(6)	111.9(5)
C(9)-N(2)-Co(1)	123.8(4)
C(6)-N(2)-Co(1)	123.6(3)
C(14)-N(3)-C(10)	119.5(5)
C(14)-N(3)-Co(1)	125.9(4)
C(10)-N(3)-Co(1)	114.7(3)
C(15)-N(4)-C(19)	119.1(4)
C(15)-N(4)-Co(1)	126.4(4)
C(19)-N(4)-Co(1)	114.5(3)
C(23)-N(5)-C(20)	112.4(5)
C(23)-N(5)-Co(1)	123.7(4)
C(20)-N(5)-Co(1)	123.0(4)
C(28)-N(6)-C(24)	119.3(5)
C(28)-N(6)-Co(1)	126.5(4)
C(24)-N(6)-Co(1)	114.1(3)
N(1)-C(1)-C(2)	121.5(5)
C(3)-C(2)-C(1)	119.4(5)
C(2)-C(3)-C(4)	118.7(5)
C(5)-C(4)-C(3)	120.4(5)
C(4)-C(5)-N(1)	119.9(4)
C(4)-C(5)-C(6)	127.7(5)
N(1)-C(5)-C(6)	112.4(4)
N(2)-C(6)-C(7)	106.9(4)
N(2)-C(6)-C(5)	110.0(4)
C(7)-C(6)-C(5)	143.0(4)
C(8)-C(7)-C(6)	106.9(4)
C(9)-C(8)-C(7)	107.0(4)
N(2)-C(9)-C(8)	107.3(4)
N(2)-C(9)-C(10)	109.5(4)
C(8)-C(9)-C(10)	143.3(5)
N(3)-C(10)-C(11)	121.1(5)
N(3)-C(10)-C(9)	112.4(4)
C(11)-C(10)-C(9)	126.5(5)
C(12)-C(11)-C(10)	119.3(6)
C(11)-C(12)-C(13)	119.7(5)
C(14)-C(13)-C(12)	118.6(5)
N(3)-C(14)-C(13)	121.8(6)
N(4)-C(15)-C(16)	121.8(5)
C(17)-C(16)-C(15)	119.3(5)
C(16)-C(17)-C(18)	120.5(5)
C(19)-C(18)-C(17)	118.4(5)
N(4)-C(19)-C(18)	120.9(4)
N(4)-C(19)-C(20)	112.2(4)
C(18)-C(19)-C(20)	126.9(5)
N(5)-C(20)-C(21)	106.7(4)
N(5)-C(20)-C(19)	110.1(4)

C(21)-C(20)-C(19)	143.2(5)
C(22)-C(21)-C(20)	107.6(4)
C(21)-C(22)-C(23)	106.0(4)
N(5)-C(23)-C(22)	107.3(4)
N(5)-C(23)-C(24)	110.4(4)
C(22)-C(23)-C(24)	142.1(5)
N(6)-C(24)-C(25)	120.3(5)
N(6)-C(24)-C(23)	112.1(4)
C(25)-C(24)-C(23)	127.5(5)
C(26)-C(25)-C(24)	119.1(5)
C(27)-C(26)-C(25)	119.8(5)
C(26)-C(27)-C(28)	118.9(5)
N(6)-C(28)-C(27)	122.6(5)
F(2)-C(29)-F(1)	101.3(10)
F(2)-C(29)-F(3)	102.1(10)
F(1)-C(29)-F(3)	97.0(10)
F(2)-C(29)-S(1)	128.8(13)
F(1)-C(29)-S(1)	115.2(12)
F(3)-C(29)-S(1)	107.5(11)
F(5)-C(30)-F(4)	102.3(12)
F(5)-C(30)-F(6)	101.0(10)
F(4)-C(30)-F(6)	99.9(11)
F(5)-C(30)-S(2)	119.7(13)
F(4)-C(30)-S(2)	112.1(19)
F(6)-C(30)-S(2)	118.9(13)

Symmetry transformations used to generate equivalent atoms:

Table 4. Anisotropic displacement parameters ($\text{Å}^2 \times 10^3$) for $[\text{Co}(\text{py}_2\text{pz})_2](\text{OTf}) \cdot \frac{1}{2}\text{MeCN}$.

The anisotropic displacement factor exponent takes the form:

$$-2 \pi^2 [h^2 a^{*2} U_{11} + \dots + 2 h k a^* b^* U_{12}]$$

	U11	U22	U33	U23	U13	U12
Co(1)	26(1)	22(1)	17(1)	1(1)	3(1)	-1(1)
S(1)	143(5)	49(2)	54(3)	12(2)	8(3)	-6(3)
S(2)	154(5)	70(3)	57(3)	8(2)	21(4)	-13(4)
F(1)	184(13)	130(10)	135(12)	-9(9)	32(10)	34(10)
F(2)	204(14)	168(12)	137(12)	-19(10)	-35(10)	-8(11)
F(3)	183(13)	139(11)	154(12)	-51(9)	-12(10)	-46(10)
F(4)	380(30)	370(30)	360(30)	3(13)	15(13)	23(14)
F(5)	188(13)	162(12)	146(12)	26(10)	-80(10)	15(11)

F(6)	221(14)	188(13)	181(14)	-36(11)	11(11)	-49(12)
O(1)	136(10)	49(6)	75(7)	18(5)	-30(7)	-9(7)
O(2)	121(9)	52(6)	48(6)	4(5)	16(6)	-4(6)
O(3)	150(12)	143(12)	76(9)	-22(8)	21(9)	10(10)
O(4)	115(10)	123(10)	55(7)	-16(7)	24(7)	-29(8)
O(5)	103(8)	56(6)	81(8)	27(6)	-2(7)	4(6)
O(6)	108(9)	41(5)	59(6)	8(5)	-21(6)	15(6)
N(1)	23(2)	20(2)	24(2)	2(1)	-2(1)	-1(2)
N(2)	23(2)	33(2)	18(2)	3(2)	1(1)	7(2)
N(3)	24(2)	21(2)	27(2)	-2(1)	8(2)	-2(2)
N(4)	23(2)	24(2)	22(2)	-1(1)	-2(1)	-1(2)
N(5)	33(2)	24(2)	20(3)	2(1)	3(1)	-8(2)
N(6)	26(2)	23(2)	23(2)	3(1)	4(2)	0(2)
C(1)	33(2)	25(2)	25(2)	3(2)	-9(2)	-5(2)
C(2)	25(2)	34(2)	41(3)	8(2)	-13(2)	0(2)
C(3)	22(2)	31(3)	46(3)	6(2)	-3(2)	3(2)
C(4)	26(2)	30(2)	31(2)	2(2)	4(2)	2(2)
C(5)	22(2)	23(2)	23(2)	4(2)	-1(2)	-1(2)
C(6)	19(2)	28(2)	20(2)	0(2)	2(2)	2(2)
C(7)	25(2)	36(3)	21(2)	5(2)	0(2)	3(2)
C(8)	22(2)	32(2)	24(2)	6(2)	-2(2)	5(2)
C(9)	22(2)	23(2)	24(2)	3(2)	0(2)	3(2)
C(10)	24(2)	21(2)	30(2)	-4(2)	2(2)	-2(2)
C(11)	25(2)	24(2)	41(3)	-6(2)	0(2)	1(2)
C(12)	25(2)	32(3)	57(4)	-11(3)	5(2)	2(2)
C(13)	26(2)	36(3)	56(4)	-16(3)	13(2)	-6(2)
C(14)	33(3)	28(2)	34(3)	-11(2)	15(2)	-7(2)
C(15)	28(2)	27(2)	30(2)	-7(2)	-6(2)	3(2)
C(16)	35(3)	29(2)	38(3)	-11(2)	-12(2)	-4(2)
C(17)	31(3)	24(2)	48(3)	1(2)	-8(2)	-9(2)
C(18)	34(3)	24(2)	35(3)	4(2)	-2(2)	-4(2)
C(19)	27(2)	21(2)	22(2)	-1(2)	2(2)	-4(2)
C(20)	34(2)	22(2)	21(2)	2(2)	4(2)	-5(2)
C(21)	37(3)	25(2)	21(2)	3(2)	4(2)	-4(2)
C(22)	39(3)	23(2)	20(2)	-2(2)	6(2)	-3(2)
C(23)	34(2)	19(2)	20(2)	-1(2)	5(2)	-5(2)

C(24)	29(2)	21(2)	27(2)	0(2)	6(2)	-2(2)
C(25)	34(3)	22(2)	35(3)	-1(2)	4(2)	-5(2)
C(26)	35(3)	21(2)	50(3)	0(2)	10(2)	-2(2)
C(27)	28(2)	26(2)	50(3)	13(2)	15(2)	3(2)
C(28)	26(2)	27(2)	31(2)	7(2)	10(2)	2(2)
C(29)	45(7)	49(7)	23(5)	-18(5)	-5(5)	15(6)
C(30)	48(5)	31(4)	17(4)	-4(3)	-3(4)	5(4)

Table 5. Hydrogen coordinates ($\times 10^4$) and isotropic displacement parameters ($\text{\AA}^2 \times 10^3$) for $[\text{Co}(\text{py}_2\text{pz})_2](\text{OTf}) \cdot \frac{1}{2}\text{MeCN}$.

	x	y	z	U(eq)
H(1)	4430	9350	2050	33
H(2)	2098	10359	2230	40
H(3)	1483	10489	2858	40
H(4)	3177	9504	3295	35
H(7)	5675	7920	3730	32
H(8)	8230	6644	3711	31
H(11)	10932	5695	3251	36
H(12)	12750	5192	2804	46
H(13)	12362	6013	2188	47
H(14)	10058	7097	2031	38
H(15)	8240	10753	2884	34
H(16)	9351	13056	2741	41
H(17)	9835	13663	2129	41
H(18)	9234	11951	1655	37
H(21)	8219	9317	1175	33
H(22)	6947	6769	1138	33
H(25)	5426	4178	1562	36
H(26)	4666	2353	1995	42

H(27)	4909	2851	2628	41
H(28)	5943	5129	2819	33

Bibliography

- [1] H. Rodhe, "A Comparison of the Contribution of Various Gases to the Greenhouse Effect", *Science*, vol. 248, no. 4960, pp. 1217–1219, 1990. DOI: <https://doi.org/10.1126/science.248.4960.1217>
- [2] R. W. Howarth, A. Ingraffea, and T. Engelder, "Natural gas: Should fracking stop?", *Nature*, vol. 477, no. 7364, pp. 271–275, 2011. DOI: <https://doi.org/10.1038/477271a>
- [3] B. Walsh *et al.*, "Pathways for balancing CO₂ emissions and sinks", *Nat. Commun.*, vol. 8, p. 14856, 2017. DOI: <https://doi.org/10.1038/ncomms14856>
- [4] "Renewables 2017 Global Status Report", *REN21*, 2017. URL: https://web.archive.org/web/20170621021102/http://www.ren21.net/wp-content/uploads/2017/06/170620_GSR_2017_Full_Report_FINAL.pdf
- [5] A. Vaughan, "Almost 90% of new power in Europe from renewable sources in 2016", *The Guardian*, 09-Feb-2017. URL: <https://web.archive.org/web/20170620132642/https://www.theguardian.com/environment/2017/feb/09/new-energy-europe-renewable-sources-2016>
- [6] M. Perez and R. Perez, "A Fundamental Look At Supply Side Energy Reserves For The Planet", *The International Energy Agency SHC Programme Solar Update*, vol. 62, pp. 4–6, 2015. URL: <https://web.archive.org/web/20170525011955/http://www.iea-shc.org/data/sites/1/publications/2015-11-Solar-Update-Newsletter.pdf>
- [7] R. Fu, D. Chung, T. Lowder, D. Feldman, K. Ardani, and R. Margolis, "U.S. Solar Photovoltaic System Cost Benchmark: Q1 2016", *National Renewable Energy Laboratory*, 2016. URL: <https://web.archive.org/web/20170506050746/http://www.nrel.gov/docs/fy16osti/66532.pdf>
- [8] P. R. Epstein *et al.*, "Full cost accounting for the life cycle of coal", *Ann. N. Y. Acad. Sci.*, vol. 1219, no. 1, pp. 73–98, 2011. DOI: <https://doi.org/10.1111/j.1749-6632.2010.05890.x>
- [9] "Lazard's Levelized Cost of Energy Analysis – Version 10.0", *Lazard investment bank*, 2016. URL: <https://web.archive.org/web/20170504000205/https://www.lazard.com/media/438038/levelized-cost-of-energy-v100.pdf>
- [10] G. Conibeer, "Third-generation photovoltaics", *Mater. Today*, vol. 10, no. 11, pp. 42–50, 2007. DOI: [https://doi.org/10.1016/S1369-7021\(07\)70278-X](https://doi.org/10.1016/S1369-7021(07)70278-X)
- [11] W. Shockley and H. J. Queisser, "Detailed Balance Limit of Efficiency of p-n Junction Solar Cells", *J. Appl. Phys.*, vol. 32, no. 3, pp. 510–519, 1961. DOI: <https://doi.org/10.1063/1.1736034>
- [12] S. Sharma, K. K. Jain, and A. Sharma, "Solar Cells: In Research and Applications—A Review", *Mater. Sci. Appl.*, vol. 6, pp. 1145–1155, 2015. DOI: <https://doi.org/10.4236/msa.2015.612113>
- [13] S. Rao, A. Morankar, H. Verma, and P. Goswami, "Emerging Photovoltaics: Organic, Copper Zinc Tin Sulphide, and Perovskite-Based Solar Cells", *J. Appl. Chem.*, vol. 2016, p. e3971579, 2016. DOI: <https://doi.org/10.1155/2016/3971579>
- [14] B. A. Gregg, "Excitonic Solar Cells", *J. Phys. Chem. B*, vol. 107, no. 20, pp. 4688–4698, 2003. DOI: <https://doi.org/10.1021/jp022507x>
- [15] "Best Research-Cell Efficiencies", *National Renewable Energy Laboratory*. [Online]. Available: <https://web.archive.org/web/20171109023158/https://www.nrel.gov/pv/assets/images/efficiency-chart.png>. [Accessed: 09-Nov-2017]
- [16] C. Eames, J. M. Frost, P. R. F. Barnes, B. C. O'Regan, A. Walsh, and M. S. Islam, "Ionic transport in hybrid lead iodide perovskite solar cells", *Nat. Commun.*, vol. 6, p. 7497, 2015. DOI: <https://doi.org/10.1038/ncomms8497>
- [17] A. Kojima, K. Teshima, Y. Shirai, and T. Miyasaka, "Organometal Halide Perovskites as Visible-Light Sensitizers for Photovoltaic Cells", *J. Am. Chem. Soc.*, vol. 131, no. 17, pp. 6050–6051, 2009. DOI: <https://doi.org/10.1021/ja809598r>
- [18] M. M. Lee, J. Teuscher, T. Miyasaka, T. N. Murakami, and H. J. Snaith, "Efficient Hybrid Solar Cells Based on Meso-Superstructured Organometal Halide Perovskites", *Science*, vol. 338, no. 6107, pp. 643–647, 2012. DOI: <https://doi.org/10.1126/science.1228604>
- [19] H.-S. Kim *et al.*, "Lead Iodide Perovskite Sensitized All-Solid-State Submicron Thin Film Mesoscopic Solar Cell with Efficiency Exceeding 9%", *Sci. Rep.*, vol. 2, p. 591, 2012. DOI: <https://doi.org/10.1038/srep00591>
- [20] M. Liu, M. B. Johnston, and H. J. Snaith, "Efficient planar heterojunction perovskite solar cells by vapour deposition", *Nature*, vol. 501, no. 7467, pp. 395–398, 2013. DOI: <https://doi.org/10.1038/nature12509>
- [21] G. Xing *et al.*, "Long-Range Balanced Electron- and Hole-Transport Lengths in Organic-Inorganic CH₃NH₃PbI₃", *Science*, vol. 342, no. 6156, pp. 344–347, 2013. DOI: <https://doi.org/10.1126/science.1243167>

- [22] S. D. Stranks *et al.*, “Electron-Hole Diffusion Lengths Exceeding 1 Micrometer in an Organometal Trihalide Perovskite Absorber”, *Science*, vol. 342, no. 6156, pp. 341–344, 2013. DOI: <https://doi.org/10.1126/science.1243982>
- [23] Q. Dong *et al.*, “Electron-hole diffusion lengths > 175 μm in solution-grown $\text{CH}_3\text{NH}_3\text{PbI}_3$ single crystals”, *Science*, vol. 347, no. 6225, pp. 967–970, 2015. DOI: <https://doi.org/10.1126/science.aaa5760>
- [24] D. Shi *et al.*, “Low trap-state density and long carrier diffusion in organolead trihalide perovskite single crystals”, *Science*, vol. 347, no. 6221, pp. 519–522, 2015. DOI: <https://doi.org/10.1126/science.aaa2725>
- [25] W.-J. Yin, T. Shi, and Y. Yan, “Unique Properties of Halide Perovskites as Possible Origins of the Superior Solar Cell Performance”, *Adv. Mater.*, vol. 26, no. 27, pp. 4653–4658, 2014. DOI: <https://doi.org/10.1002/adma.201306281>
- [26] J. Kim, S.-H. Lee, J. H. Lee, and K.-H. Hong, “The Role of Intrinsic Defects in Methylammonium Lead Iodide Perovskite”, *J. Phys. Chem. Lett.*, vol. 5, no. 8, pp. 1312–1317, 2014. DOI: <https://doi.org/10.1021/jz500370k>
- [27] J. Burschka *et al.*, “Sequential deposition as a route to high-performance perovskite-sensitized solar cells”, *Nature*, vol. 499, no. 7458, pp. 316–319, 2013. DOI: <https://doi.org/10.1038/nature12340>
- [28] N. J. Jeon, J. H. Noh, Y. C. Kim, W. S. Yang, S. Ryu, and S. I. Seok, “Solvent engineering for high-performance inorganic–organic hybrid perovskite solar cells”, *Nat. Mater.*, vol. 13, no. 9, pp. 897–903, 2014. DOI: <https://doi.org/10.1038/nmat4014>
- [29] M. Xiao *et al.*, “A Fast Deposition-Crystallization Procedure for Highly Efficient Lead Iodide Perovskite Thin-Film Solar Cells”, *Angew. Chem. Int. Ed.*, vol. 53, no. 37, pp. 9898–9903, 2014. DOI: <https://doi.org/10.1002/anie.201405334>
- [30] F. Huang *et al.*, “Gas-assisted preparation of lead iodide perovskite films consisting of a monolayer of single crystalline grains for high efficiency planar solar cells”, *Nano Energy*, vol. 10, pp. 10–18, 2014. DOI: <https://doi.org/10.1016/j.nanoen.2014.08.015>
- [31] V. M. Goldschmidt, “Die Gesetze der Krystallochemie”, *Naturwissenschaften*, vol. 14, no. 21, pp. 477–485, 1926. DOI: <https://doi.org/10.1007/BF01507527>
- [32] Z. Fan, K. Sun, and J. Wang, “Perovskites for photovoltaics: a combined review of organic–inorganic halide perovskites and ferroelectric oxide perovskites”, *J. Mater. Chem. A*, vol. 3, no. 37, pp. 18809–18828, 2015. DOI: <https://doi.org/10.1039/C5TA04235F>
- [33] J. H. Noh, S. H. Im, J. H. Heo, T. N. Mandal, and S. I. Seok, “Chemical Management for Colorful, Efficient, and Stable Inorganic–Organic Hybrid Nanostructured Solar Cells”, *Nano Lett.*, vol. 13, no. 4, pp. 1764–1769, 2013. DOI: <https://doi.org/10.1021/nl400349b>
- [34] G. E. Eperon, S. D. Stranks, C. Menelaou, M. B. Johnston, L. M. Herz, and H. J. Snaith, “Formamidinium lead trihalide: a broadly tunable perovskite for efficient planar heterojunction solar cells”, *Energy Environ. Sci.*, vol. 7, no. 3, pp. 982–988, 2014. DOI: <https://doi.org/10.1039/C3EE43822H>
- [35] M. R. Filip, G. E. Eperon, H. J. Snaith, and F. Giustino, “Steric engineering of metal-halide perovskites with tunable optical band gaps”, *Nat. Commun.*, vol. 5, p. 5757, 2014. DOI: <https://doi.org/10.1038/ncomms6757>
- [36] T. Baikie *et al.*, “Synthesis and crystal chemistry of the hybrid perovskite $(\text{CH}_3\text{NH}_3)\text{PbI}_3$ for solid-state sensitised solar cell applications”, *J. Mater. Chem. A*, vol. 1, no. 18, pp. 5628–5641, 2013. DOI: <https://doi.org/10.1039/C3TA10518K>
- [37] C. C. Stoumpos, C. D. Malliakas, and M. G. Kanatzidis, “Semiconducting Tin and Lead Iodide Perovskites with Organic Cations: Phase Transitions, High Mobilities, and Near-Infrared Photoluminescent Properties”, *Inorg. Chem.*, vol. 52, no. 15, pp. 9019–9038, 2013. DOI: <https://doi.org/10.1021/ic401215x>
- [38] J.-W. Lee, D.-J. Seol, A.-N. Cho, and N.-G. Park, “High-Efficiency Perovskite Solar Cells Based on the Black Polymorph of $\text{HC}(\text{NH}_2)_2\text{PbI}_3$ ”, *Adv. Mater.*, vol. 26, no. 29, pp. 4991–4998, 2014. DOI: <https://doi.org/10.1002/adma.201401137>
- [39] M. Saliba *et al.*, “Cesium-containing triple cation perovskite solar cells: improved stability, reproducibility and high efficiency”, *Energy Environ. Sci.*, vol. 9, no. 6, pp. 1989–1997, 2016. DOI: <https://doi.org/10.1039/C5EE03874J>
- [40] T. Krishnamoorthy *et al.*, “Lead-free germanium iodide perovskite materials for photovoltaic applications”, *J. Mater. Chem. A*, vol. 3, no. 47, pp. 23829–23832, 2015. DOI: <https://doi.org/10.1039/C5TA05741H>
- [41] F. Hao, C. C. Stoumpos, D. H. Cao, R. P. H. Chang, and M. G. Kanatzidis, “Lead-free solid-state organic-inorganic halide perovskite solar cells”, *Nat. Photonics*, vol. 8, no. 6, pp. 489–494, 2014. DOI: <https://doi.org/10.1038/nphoton.2014.82>
- [42] J. Yang, B. D. Siempelkamp, E. Mosconi, F. De Angelis, and T. L. Kelly, “Origin of the Thermal Instability in $\text{CH}_3\text{NH}_3\text{PbI}_3$ Thin Films Deposited on ZnO ”, *Chem. Mater.*, vol. 27, no. 12, pp. 4229–4236, 2015. DOI: <https://doi.org/10.1021/acs.chemmater.5b01598>

- [43] W. Ke *et al.*, “Low-Temperature Solution-Processed Tin Oxide as an Alternative Electron Transporting Layer for Efficient Perovskite Solar Cells”, *J. Am. Chem. Soc.*, vol. 137, no. 21, pp. 6730–6733, 2015. DOI: <https://doi.org/10.1021/jacs.5b01994>
- [44] O. Malinkiewicz *et al.*, “Perovskite solar cells employing organic charge-transport layers”, *Nat. Photonics*, vol. 8, no. 2, pp. 128–132, 2014. DOI: <https://doi.org/10.1038/nphoton.2013.341>
- [45] Y. Kato, L. K. Ono, M. V. Lee, S. Wang, S. R. Raga, and Y. Qi, “Silver Iodide Formation in Methyl Ammonium Lead Iodide Perovskite Solar Cells with Silver Top Electrodes”, *Adv. Mater. Interfaces*, vol. 2, no. 13, p. n/a-n/a, 2015. DOI: <https://doi.org/10.1002/admi.201500195>
- [46] G. A. Sepalage *et al.*, “Copper(I) Iodide as Hole-Conductor in Planar Perovskite Solar Cells: Probing the Origin of J - V Hysteresis”, *Adv. Funct. Mater.*, vol. 25, no. 35, pp. 5650–5661, 2015. DOI: <https://doi.org/10.1002/adfm.201502541>
- [47] L. Hu *et al.*, “Sequential Deposition of $\text{CH}_3\text{NH}_3\text{PbI}_3$ on Planar NiO Film for Efficient Planar Perovskite Solar Cells”, *ACS Photonics*, vol. 1, no. 7, pp. 547–553, 2014. DOI: <https://doi.org/10.1021/ph5000067>
- [48] J. Ahn, H. Hwang, S. Jeong, and J. Moon, “Metal-Nanowire-Electrode-Based Perovskite Solar Cells: Challenging Issues and New Opportunities”, *Adv. Energy Mater.*, 2017. DOI: <https://doi.org/10.1002/aenm.201602751>
- [49] J. Hyuck Heo, H. Ji Han, M. Lee, M. Song, D. Ho Kim, and S. Hyuk Im, “Stable semi-transparent $\text{CH}_3\text{NH}_3\text{PbI}_3$ planar sandwich solar cells”, *Energy Environ. Sci.*, vol. 8, no. 10, pp. 2922–2927, 2015. DOI: <https://doi.org/10.1039/C5EE01050K>
- [50] G. Giorgi and K. Yamashita, “Organic–inorganic halide perovskites: an ambipolar class of materials with enhanced photovoltaic performances”, *J. Mater. Chem. A*, vol. 3, no. 17, pp. 8981–8991, 2015. DOI: <https://doi.org/10.1039/C4TA05046K>
- [51] W. Ke *et al.*, “Efficient hole-blocking layer-free planar halide perovskite thin-film solar cells”, *Nat. Commun.*, vol. 6, p. 6700, 2015. DOI: <https://doi.org/10.1038/ncomms7700>
- [52] Y. Li *et al.*, “Hole-conductor-free planar perovskite solar cells with 16.0% efficiency”, *J. Mater. Chem. A*, vol. 3, no. 36, pp. 18389–18394, 2015. DOI: <https://doi.org/10.1039/C5TA05989E>
- [53] H. J. Snaith *et al.*, “Anomalous Hysteresis in Perovskite Solar Cells”, *J. Phys. Chem. Lett.*, pp. 1511–1515, 2014. DOI: <https://doi.org/10.1021/jz500113x>
- [54] B. Chen, M. Yang, S. Priya, and K. Zhu, “Origin of J - V Hysteresis in Perovskite Solar Cells”, *J. Phys. Chem. Lett.*, vol. 7, no. 5, pp. 905–917, 2016. DOI: <https://doi.org/10.1021/acs.jpcclett.6b00215>
- [55] J. Beilsten-Edmands, G. E. Eperon, R. D. Johnson, H. J. Snaith, and P. G. Radaelli, “Non-ferroelectric nature of the conductance hysteresis in $\text{CH}_3\text{NH}_3\text{PbI}_3$ perovskite-based photovoltaic devices”, *Appl. Phys. Lett.*, vol. 106, no. 17, p. 173502, 2015. DOI: <https://doi.org/10.1063/1.4919109>
- [56] S. van Reenen, M. Kemerink, and H. J. Snaith, “Modeling Anomalous Hysteresis in Perovskite Solar Cells”, *J. Phys. Chem. Lett.*, vol. 6, no. 19, pp. 3808–3814, 2015. DOI: <https://doi.org/10.1021/acs.jpcclett.5b01645>
- [57] W. S. Yang *et al.*, “High-performance photovoltaic perovskite layers fabricated through intramolecular exchange”, *Science*, vol. 348, no. 6240, pp. 1234–1237, 2015. DOI: <https://doi.org/10.1126/science.aaa9272>
- [58] Y. Shao, Z. Xiao, C. Bi, Y. Yuan, and J. Huang, “Origin and elimination of photocurrent hysteresis by fullerene passivation in $\text{CH}_3\text{NH}_3\text{PbI}_3$ planar heterojunction solar cells”, *Nat. Commun.*, vol. 5, p. 5784, 2014. DOI: <https://doi.org/10.1038/ncomms6784>
- [59] H.-S. Kim and N.-G. Park, “Parameters Affecting I - V Hysteresis of $\text{CH}_3\text{NH}_3\text{PbI}_3$ Perovskite Solar Cells: Effects of Perovskite Crystal Size and Mesoporous TiO_2 Layer”, *J. Phys. Chem. Lett.*, vol. 5, no. 17, pp. 2927–2934, 2014. DOI: <https://doi.org/10.1021/jz501392m>
- [60] W. Zhang, G. E. Eperon, and H. J. Snaith, “Metal halide perovskites for energy applications”, *Nat. Energy*, vol. 1, p. 16048, 2016. DOI: <https://doi.org/10.1038/nenergy.2016.48>
- [61] M. Long *et al.*, “Ultrathin efficient perovskite solar cells employing a periodic structure of a composite hole conductor for elevated plasmonic light harvesting and hole collection”, *Nanoscale*, vol. 8, no. 12, pp. 6290–6299, 2016. DOI: <https://doi.org/10.1039/C5NR05042A>
- [62] U. Bach *et al.*, “Solid-state dye-sensitized mesoporous TiO_2 solar cells with high photon-to-electron conversion efficiencies”, *Nature*, vol. 395, no. 6702, pp. 583–585, 1998. DOI: <https://doi.org/10.1038/26936>
- [63] J. H. Noh, N. J. Jeon, Y. C. Choi, M. K. Nazeeruddin, M. Grätzel, and S. I. Seok, “Nanostructured $\text{TiO}_2/\text{CH}_3\text{NH}_3\text{PbI}_3$ heterojunction solar cells employing spiro-OMeTAD/Co-complex as hole-transporting material”, *J. Mater. Chem. A*, vol. 1, no. 38, pp. 11842–11847, 2013. DOI: <https://doi.org/10.1039/C3TA12681A>
- [64] F. Huang *et al.*, “Fatigue behavior of planar $\text{CH}_3\text{NH}_3\text{PbI}_3$ perovskite solar cells revealed by light on/off diurnal cycling”, *Nano Energy*, vol. 27, pp. 509–514, 2016. DOI: <https://doi.org/10.1016/j.nanoen.2016.07.033>

- [65] G. A. Sepalage, "Application of inorganic hole transporting materials in perovskite solar cells", Monash University, 2017
- [66] L. Caliò, S. Kazim, M. Grätzel, and S. Ahmad, "Hole-Transport Materials for Perovskite Solar Cells", *Angew. Chem. Int. Ed.*, vol. 55, no. 47, pp. 14522–14545, 2016. DOI: <https://doi.org/10.1002/anie.201601757>
- [67] C. H. Teh *et al.*, "A review of organic small molecule-based hole-transporting materials for meso-structured organic–inorganic perovskite solar cells", *J. Mater. Chem. A*, vol. 4, no. 41, pp. 15788–15822, 2016. DOI: <https://doi.org/10.1039/C6TA06987H>
- [68] Y.-K. Wang, Z.-Q. Jiang, and L.-S. Liao, "New advances in small molecule hole-transporting materials for perovskite solar cells", *Chin. Chem. Lett.*, vol. 27, no. 8, pp. 1293–1303, 2016. DOI: <https://doi.org/10.1016/j.ccllet.2016.07.004>
- [69] W. Yan *et al.*, "Hole-Transporting Materials in Inverted Planar Perovskite Solar Cells", *Adv. Energy Mater.*, vol. 6, no. 17, p. 1600474, 2016. DOI: <https://doi.org/10.1002/aenm.201600474>
- [70] P. Agarwala and D. Kabra, "A review on triphenylamine (TPA) based organic hole transport materials (HTMs) for dye sensitized solar cells (DSSCs) and perovskite solar cells (PSCs): evolution and molecular engineering", *J. Mater. Chem. A*, vol. 5, no. 4, pp. 1348–1373, 2017. DOI: <https://doi.org/10.1039/C6TA08449D>
- [71] H. Wang *et al.*, "Facile Synthesis and High Performance of a New Carbazole-Based Hole-Transporting Material for Hybrid Perovskite Solar Cells", *ACS Photonics*, vol. 2, no. 7, pp. 849–855, 2015. DOI: <https://doi.org/10.1021/acsp Photonics.5b00283>
- [72] L. Yang, Y. Yan, F. Cai, J. Li, and T. Wang, "Poly(9-vinylcarbazole) as a hole transport material for efficient and stable inverted planar heterojunction perovskite solar cells", *Sol. Energy Mater. Sol. Cells*, vol. 163, pp. 210–217, 2017. DOI: <https://doi.org/10.1016/j.solmat.2017.01.040>
- [73] Z. Zhou *et al.*, "A facile one-pot synthesis of hyper-branched carbazole-based polymer as a hole-transporting material for perovskite solar cells", *J. Mater. Chem. A*, vol. 5, no. 14, pp. 6613–6621, 2017. DOI: <https://doi.org/10.1039/C6TA11238B>
- [74] F. J. Ramos, K. Rakstys, S. Kazim, M. Grätzel, M. K. Nazeeruddin, and S. Ahmad, "Rational design of triazatruxene-based hole conductors for perovskite solar cells", *RSC Adv.*, vol. 5, no. 66, pp. 53426–53432, 2015. DOI: <https://doi.org/10.1039/C5RA06876B>
- [75] K. Rakstys *et al.*, "Triazatruxene-Based Hole Transporting Materials for Highly Efficient Perovskite Solar Cells", *J. Am. Chem. Soc.*, vol. 137, no. 51, pp. 16172–16178, 2015. DOI: <https://doi.org/10.1021/jacs.5b11076>
- [76] P. Qin *et al.*, "Low band gap *S,N*-heteroacene-based oligothiophenes as hole-transporting and light absorbing materials for efficient perovskite-based solar cells", *Energy Environ. Sci.*, vol. 7, no. 9, pp. 2981–2985, 2014. DOI: <https://doi.org/10.1039/C4EE01220H>
- [77] C. Steck, M. Franckevičius, S. M. Zakeeruddin, A. Mishra, P. Bäuerle, and M. Grätzel, "A–D–A-type *S,N*-heteropentacene-based hole transport materials for dopant-free perovskite solar cells", *J. Mater. Chem. A*, vol. 3, no. 34, pp. 17738–17746, 2015. DOI: <https://doi.org/10.1039/C5TA03865K>
- [78] Y. S. Kwon, J. Lim, H.-J. Yun, Y.-H. Kim, and T. Park, "A diketopyrrolopyrrole-containing hole transporting conjugated polymer for use in efficient stable organic–inorganic hybrid solar cells based on a perovskite", *Energy Environ. Sci.*, vol. 7, no. 4, pp. 1454–1460, 2014. DOI: <https://doi.org/10.1039/C3EE44174A>
- [79] S. Jeon *et al.*, "*N*-phenylindole-diketopyrrolopyrrole-containing narrow band-gap materials for dopant-free hole transporting layer of perovskite solar cell", *Org. Electron.*, vol. 37, pp. 134–140, 2016. DOI: <https://doi.org/10.1016/j.orgel.2016.06.019>
- [80] P. Gratia *et al.*, "A Methoxydiphenylamine-Substituted Carbazole Twin Derivative: An Efficient Hole-Transporting Material for Perovskite Solar Cells", *Angew. Chem. Int. Ed.*, vol. 54, no. 39, pp. 11409–11413, 2015. DOI: <https://doi.org/10.1002/anie.201504666>
- [81] S. Fantacci, F. De Angelis, M. K. Nazeeruddin, and M. Grätzel, "Electronic and Optical Properties of the Spiro-MeOTAD Hole Conductor in Its Neutral and Oxidized Forms: A DFT/TDDFT Investigation", *J. Phys. Chem. C*, vol. 115, no. 46, pp. 23126–23133, 2011. DOI: <https://doi.org/10.1021/jp207968b>
- [82] C. Huang *et al.*, "Dopant-Free Hole-Transporting Material with a C_{3h} Symmetrical Truxene Core for Highly Efficient Perovskite Solar Cells", *J. Am. Chem. Soc.*, vol. 138, no. 8, pp. 2528–2531, 2016. DOI: <https://doi.org/10.1021/jacs.6b00039>
- [83] S. S. Reddy *et al.*, "Highly Efficient Organic Hole Transporting Materials for Perovskite and Organic Solar Cells with Long-Term Stability", *Adv. Mater.*, vol. 28, no. 4, pp. 686–693, 2016. DOI: <https://doi.org/10.1002/adma.201503729>
- [84] T. Daenke *et al.*, "Dye Regeneration Kinetics in Dye-Sensitized Solar Cells", *J. Am. Chem. Soc.*, vol. 134, no. 41, pp. 16925–16928, 2012. DOI: <https://doi.org/10.1021/ja3054578>

- [85] L. E. Polander, P. Pahner, M. Schwarze, M. Saalfrank, C. Koerner, and K. Leo, "Hole-transport material variation in fully vacuum deposited perovskite solar cells", *APL Mater.*, vol. 2, no. 8, p. 81503, 2014. DOI: <https://doi.org/10.1063/1.4889843>
- [86] C. Wehrenfennig, G. E. Eperon, M. B. Johnston, H. J. Snaith, and L. M. Herz, "High Charge Carrier Mobilities and Lifetimes in Organolead Trihalide Perovskites", *Adv. Mater.*, vol. 26, no. 10, pp. 1584–1589, 2014. DOI: <https://doi.org/10.1002/adma.201305172>
- [87] M. Abdi-Jalebi *et al.*, "Impact of a Mesoporous Titania–Perovskite Interface on the Performance of Hybrid Organic–Inorganic Perovskite Solar Cells", *J. Phys. Chem. Lett.*, vol. 7, no. 16, pp. 3264–3269, 2016. DOI: <https://doi.org/10.1021/acs.jpcclett.6b01617>
- [88] D. Bi, B. Xu, P. Gao, L. Sun, M. Grätzel, and A. Hagfeldt, "Facile synthesized organic hole transporting material for perovskite solar cell with efficiency of 19.8%", *Nano Energy*, vol. 23, pp. 138–144, 2016. DOI: <https://doi.org/10.1016/j.nanoen.2016.03.020>
- [89] B. Xu *et al.*, "A low-cost spiro[fluorene-9,9'-xanthene]-based hole transport material for highly efficient solid-state dye-sensitized solar cells and perovskite solar cells", *Energy Environ. Sci.*, vol. 9, no. 3, pp. 873–877, 2016. DOI: <https://doi.org/10.1039/C6EE00056H>
- [90] B. Xu *et al.*, "Carbazole-Based Hole-Transport Materials for Efficient Solid-State Dye-Sensitized Solar Cells and Perovskite Solar Cells", *Adv. Mater.*, vol. 26, no. 38, pp. 6629–6634, 2014. DOI: <https://doi.org/10.1002/adma.201402415>
- [91] H. J. Snaith and M. Grätzel, "Enhanced charge mobility in a molecular hole transporter via addition of redox inactive ionic dopant: Implication to dye-sensitized solar cells", *Appl. Phys. Lett.*, vol. 89, no. 26, p. 262114, 2006. DOI: <https://doi.org/10.1063/1.2424552>
- [92] J. Burschka *et al.*, "Tris(2-(1*H*-pyrazol-1-yl)pyridine)cobalt(III) as p-Type Dopant for Organic Semiconductors and Its Application in Highly Efficient Solid-State Dye-Sensitized Solar Cells", *J. Am. Chem. Soc.*, vol. 133, no. 45, pp. 18042–18045, 2011. DOI: <https://doi.org/10.1021/ja207367t>
- [93] J. Burschka, F. Kessler, M. K. Nazeeruddin, and M. Grätzel, "Co(III) Complexes as p-Dopants in Solid-State Dye-Sensitized Solar Cells", *Chem. Mater.*, vol. 25, no. 15, pp. 2986–2990, 2013. DOI: <https://doi.org/10.1021/cm400796u>
- [94] J. Ye *et al.*, "Bipyridine type Co-complexes as hole-transporting material dopants in perovskite solar cells", *RSC Adv.*, vol. 6, no. 21, pp. 17354–17359, 2016. DOI: <https://doi.org/10.1039/C5RA25753K>
- [95] L. Badia, E. Mas-Marzá, R. S. Sánchez, E. M. Barea, J. Bisquert, and I. Mora-Seró, "New iridium complex as additive to the spiro-OMeTAD in perovskite solar cells with enhanced stability", *APL Mater.*, vol. 2, no. 8, p. 81507, 2014. DOI: <https://doi.org/10.1063/1.4890545>
- [96] W. H. Nguyen, C. D. Bailie, E. L. Unger, and M. D. McGehee, "Enhancing the Hole-Conductivity of Spiro-OMeTAD without Oxygen or Lithium Salts by Using Spiro(TFSI)₂ in Perovskite and Dye-Sensitized Solar Cells", *J. Am. Chem. Soc.*, vol. 136, no. 31, pp. 10996–11001, 2014. DOI: <https://doi.org/10.1021/ja504539w>
- [97] Z. Yu and L. Sun, "Recent Progress on Hole-Transporting Materials for Emerging Organometal Halide Perovskite Solar Cells", *Adv. Energy Mater.*, vol. 5, no. 12, p. 1500213, 2015. DOI: <https://doi.org/10.1002/aenm.201500213>
- [98] S. Ameen *et al.*, "Perovskite Solar Cells: Influence of Hole Transporting Materials on Power Conversion Efficiency", *ChemSusChem*, vol. 9, no. 1, pp. 10–27, 2016. DOI: <https://doi.org/10.1002/cssc.201501228>
- [99] N. J. Jeon *et al.*, "o-Methoxy Substituents in Spiro-OMeTAD for Efficient Inorganic–Organic Hybrid Perovskite Solar Cells", *J. Am. Chem. Soc.*, vol. 136, no. 22, pp. 7837–7840, 2014. DOI: <https://doi.org/10.1021/ja502824c>
- [100] Z. Hu *et al.*, "Effects of heteroatom substitution in spiro-bifluorene hole transport materials", *Chem. Sci.*, vol. 7, no. 8, pp. 5007–5012, 2016. DOI: <https://doi.org/10.1039/C6SC00973E>
- [101] S. Ma *et al.*, "Spiro-thiophene derivatives as hole-transport materials for perovskite solar cells", *J. Mater. Chem. A*, vol. 3, no. 23, pp. 12139–12144, 2015. DOI: <https://doi.org/10.1039/C5TA01155H>
- [102] M. Franckevičius, A. Mishra, F. Kreuzer, J. Luo, S. M. Zakeeruddin, and M. Grätzel, "A dopant-free spirobi[cyclopenta[2,1-b:3,4-b']dithiophene] based hole-transport material for efficient perovskite solar cells", *Mater. Horiz.*, vol. 2, no. 6, pp. 613–618, 2015. DOI: <https://doi.org/10.1039/C5MH00154D>
- [103] M. Maciejczyk, A. Ivaturi, and N. Robertson, "SFX as a low-cost 'Spiro' hole-transport material for efficient perovskite solar cells", *J. Mater. Chem. A*, vol. 4, no. 13, pp. 4855–4863, 2016. DOI: <https://doi.org/10.1039/C6TA00110F>
- [104] P. Ganesan *et al.*, "A simple spiro-type hole transporting material for efficient perovskite solar cells", *Energy Environ. Sci.*, vol. 8, no. 7, pp. 1986–1991, 2015. DOI: <https://doi.org/10.1039/C4EE03773A>
- [105] M. Saliba *et al.*, "A molecularly engineered hole-transporting material for efficient perovskite solar cells", *Nat. Energy*, vol. 1, no. 2, p. 15017, 2016. DOI: <https://doi.org/10.1038/nenergy.2015.17>

- [106] Y.-K. Wang *et al.*, “Dopant-Free Spiro-Triphenylamine/Fluorene as Hole-Transporting Material for Perovskite Solar Cells with Enhanced Efficiency and Stability”, *Adv. Funct. Mater.*, vol. 26, no. 9, pp. 1375–1381, 2016. DOI: <https://doi.org/10.1002/adfm.201504245>
- [107] M.-H. Li *et al.*, “Novel spiro-based hole transporting materials for efficient perovskite solar cells”, *Chem. Commun.*, vol. 51, no. 85, pp. 15518–15521, 2015. DOI: <https://doi.org/10.1039/C5CC04405G>
- [108] S. Trasatti, “The Absolute Electrode Potential: an Explanatory Note (Recommendations 1986)”, *Pure & App. Chem.*, vol. 58, no. 7, pp. 955–966, 1986.
- [109] D. Bi *et al.*, “Efficient luminescent solar cells based on tailored mixed-cation perovskites”, *Sci. Adv.*, vol. 2, no. 1, p. e1501170, 2016. DOI: <https://doi.org/10.1126/sciadv.1501170>
- [110] M. K. R. Fischer *et al.*, “D- π -A Sensitizers for Dye-Sensitized Solar Cells: Linear vs Branched Oligothiophenes”, *Chem. Mater.*, vol. 22, no. 5, pp. 1836–1845, 2010. DOI: <https://doi.org/10.1021/cm903542v>
- [111] H. Li, K. Fu, A. Hagfeldt, M. Grätzel, S. G. Mhaisalkar, and A. C. Grimsdale, “A Simple 3,4-Ethylenedioxythiophene Based Hole-Transporting Material for Perovskite Solar Cells”, *Angew. Chem. Int. Ed.*, vol. 53, no. 16, pp. 4085–4088, 2014. DOI: <https://doi.org/10.1002/anie.201310877>
- [112] T. Krishnamoorthy *et al.*, “A swivel-cruciform thiophene based hole-transporting material for efficient perovskite solar cells”, *J. Mater. Chem. A*, vol. 2, no. 18, p. 6305, 2014. DOI: <https://doi.org/10.1039/c4ta00486h>
- [113] H. Li *et al.*, “Hole-Transporting Small Molecules Based on Thiophene Cores for High Efficiency Perovskite Solar Cells”, *ChemSusChem*, vol. 7, no. 12, pp. 3420–3425, 2014. DOI: <https://doi.org/10.1002/cssc.201402587>
- [114] J. Liu *et al.*, “A dopant-free hole-transporting material for efficient and stable perovskite solar cells”, *Energy Environ. Sci.*, vol. 7, no. 9, pp. 2963–2967, 2014. DOI: <https://doi.org/10.1039/C4EE01589D>
- [115] J.-S. Ni *et al.*, “Near-Infrared-Absorbing and Dopant-Free Heterocyclic Quinoid-Based Hole-Transporting Materials for Efficient Perovskite Solar Cells”, *ChemSusChem*, vol. 9, no. 22, pp. 3139–3144, 2016. DOI: <https://doi.org/10.1002/cssc.201600923>
- [116] Y. Xue, Y. Wu, and Y. Li, “Readily synthesized dopant-free hole transport materials with phenol core for stabilized mixed perovskite solar cells”, *J. Power Sources*, vol. 344, pp. 160–169, 2017. DOI: <https://doi.org/10.1016/j.jpowsour.2017.01.121>
- [117] F. Zhang *et al.*, “A Novel Dopant-Free Triphenylamine Based Molecular ‘Butterfly’ Hole-Transport Material for Highly Efficient and Stable Perovskite Solar Cells”, *Adv. Energy Mater.*, vol. 6, no. 14, p. 1600401, 2016. DOI: <https://doi.org/10.1002/aenm.201600401>
- [118] Y. Liu *et al.*, “Perovskite Solar Cells Employing Dopant-Free Organic Hole Transport Materials with Tunable Energy Levels”, *Adv. Mater.*, vol. 28, no. 3, pp. 440–446, 2016. DOI: <https://doi.org/10.1002/adma.201504293>
- [119] F. Zhang *et al.*, “Dopant-free star-shaped hole-transport materials for efficient and stable perovskite solar cells”, *Dyes Pigments*, vol. 136, pp. 273–277, 2017. DOI: <https://doi.org/10.1016/j.dyepig.2016.08.002>
- [120] F. Zhang *et al.*, “Dopant-Free Donor (D)- π -D- π -D Conjugated Hole-Transport Materials for Efficient and Stable Perovskite Solar Cells”, *ChemSusChem*, vol. 9, no. 18, pp. 2578–2585, 2016. DOI: <https://doi.org/10.1002/cssc.201600905>
- [121] X. Zhao *et al.*, “A novel one-step synthesized and dopant-free hole transport material for efficient and stable perovskite solar cells”, *J. Mater. Chem. A*, vol. 4, no. 42, pp. 16330–16334, 2016. DOI: <https://doi.org/10.1039/C6TA05254A>
- [122] S. Kazim, F. J. Ramos, P. Gao, M. K. Nazeeruddin, M. Grätzel, and S. Ahmad, “A dopant free linear acene derivative as a hole transport material for perovskite pigmented solar cells”, *Energy Environ. Sci.*, vol. 8, no. 6, pp. 1816–1823, 2015. DOI: <https://doi.org/10.1039/C5EE00599J>
- [123] Y. Liu *et al.*, “A dopant-free organic hole transport material for efficient planar heterojunction perovskite solar cells”, *J. Mater. Chem. A*, vol. 3, no. 22, pp. 11940–11947, 2015. DOI: <https://doi.org/10.1039/C5TA02502H>
- [124] Z. Li *et al.*, “Rational Design of Dipolar Chromophore as an Efficient Dopant-Free Hole-Transporting Material for Perovskite Solar Cells”, *J. Am. Chem. Soc.*, vol. 138, no. 36, pp. 11833–11839, 2016. DOI: <https://doi.org/10.1021/jacs.6b06291>
- [125] N. J. Jeon, J. Lee, J. H. Noh, M. K. Nazeeruddin, M. Grätzel, and S. I. Seok, “Efficient Inorganic–Organic Hybrid Perovskite Solar Cells Based on Pyrene Arylamine Derivatives as Hole-Transporting Materials”, *J. Am. Chem. Soc.*, vol. 135, no. 51, pp. 19087–19090, 2013. DOI: <https://doi.org/10.1021/ja410659k>
- [126] A. Krishna *et al.*, “Novel hole transporting materials based on triptycene core for high efficiency mesoscopic perovskite solar cells”, *Chem. Sci.*, vol. 5, no. 7, pp. 2702–2709, 2014. DOI: <https://doi.org/10.1039/C4SC00814F>

- [127] S. Lv *et al.*, “Mesoscopic TiO₂/CH₃NH₃PbI₃ perovskite solar cells with new hole-transporting materials containing butadiene derivatives”, *Chem. Commun.*, vol. 50, no. 52, pp. 6931–6934, 2014. DOI: <https://doi.org/10.1039/C4CC02211D>
- [128] P. Qin *et al.*, “Perovskite Solar Cells with 12.8% Efficiency by Using Conjugated Quinolizino Acridine Based Hole Transporting Material”, *J. Am. Chem. Soc.*, vol. 136, no. 24, pp. 8516–8519, 2014. DOI: <https://doi.org/10.1021/ja503272q>
- [129] Y. Song *et al.*, “Energy level tuning of TPB-based hole-transporting materials for highly efficient perovskite solar cells”, *Chem. Commun.*, vol. 50, no. 96, pp. 15239–15242, 2014. DOI: <https://doi.org/10.1039/C4CC06493C>
- [130] J. Das, R. B. K. Siram, D. Cahen, B. Rybtchinski, and G. Hodes, “Thiophene-modified perylene diimide as hole transporting material in hybrid lead bromide perovskite solar cells”, *J. Mater. Chem. A*, vol. 3, no. 40, pp. 20305–20312, 2015. DOI: <https://doi.org/10.1039/C5TA04828A>
- [131] H. Nishimura *et al.*, “Hole-Transporting Materials with a Two-Dimensionally Expanded π -System around an Azulene Core for Efficient Perovskite Solar Cells”, *J. Am. Chem. Soc.*, vol. 137, no. 50, pp. 15656–15659, 2015. DOI: <https://doi.org/10.1021/jacs.5b11008>
- [132] S. Park, J. H. Heo, C. H. Cheon, H. Kim, S. H. Im, and H. J. Son, “A [2,2]paracyclophane triarylamine-based hole-transporting material for high performance perovskite solar cells”, *J. Mater. Chem. A*, vol. 3, no. 48, pp. 24215–24220, 2015. DOI: <https://doi.org/10.1039/C5TA08417B>
- [133] F. Zhang *et al.*, “Engineering of hole-selective contact for low temperature-processed carbon counter electrode-based perovskite solar cells”, *J. Mater. Chem. A*, vol. 3, no. 48, pp. 24272–24280, 2015. DOI: <https://doi.org/10.1039/C5TA07507F>
- [134] J. Zhang *et al.*, “The Role of 3D Molecular Structural Control in New Hole Transport Materials Outperforming Spiro-OMeTAD in Perovskite Solar Cells”, *Adv. Energy Mater.*, vol. 6, no. 19, p. 1601062, 2016. DOI: <https://doi.org/10.1002/aenm.201601062>
- [135] I. Lim *et al.*, “Indolocarbazole based small molecules: an efficient hole transporting material for perovskite solar cells”, *RSC Adv.*, vol. 5, no. 68, pp. 55321–55327, 2015. DOI: <https://doi.org/10.1039/C5RA10148D>
- [136] I. Cho *et al.*, “Indolo[3,2-b]indole-based crystalline hole-transporting material for highly efficient perovskite solar cells”, *Chem. Sci.*, 2016. DOI: <https://doi.org/10.1039/C6SC02832B>
- [137] T. Malinauskas *et al.*, “Branched methoxydiphenylamine-substituted fluorene derivatives as hole transporting materials for high-performance perovskite solar cells”, *Energy Environ. Sci.*, vol. 9, no. 5, pp. 1681–1686, 2016. DOI: <https://doi.org/10.1039/C5EE03911H>
- [138] A. Molina-Ontoria *et al.*, “Benzotrithiophene-Based Hole-Transporting Materials for 18.2% Perovskite Solar Cells”, *Angew. Chem. Int. Ed.*, vol. 55, no. 21, pp. 6270–6274, 2016. DOI: <https://doi.org/10.1002/anie.201511877>
- [139] Y. Shi *et al.*, “Molecular structure simplification of the most common hole transport materials in perovskite solar cells”, *RSC Adv.*, vol. 6, no. 99, pp. 96990–96996, 2016. DOI: <https://doi.org/10.1039/C6RA21448G>
- [140] F. Wu, J. Liu, G. Wang, Q. Song, and L. Zhu, “m-Methoxy Substituents in a Tetraphenylethylene-Based Hole-Transport Material for Efficient Perovskite Solar Cells”, *Chem. – Eur. J.*, vol. 22, no. 46, pp. 16636–16641, 2016. DOI: <https://doi.org/10.1002/chem.201603672>
- [141] I. Zimmermann *et al.*, “High-Efficiency Perovskite Solar Cells Using Molecularly Engineered, Thiophene-Rich, Hole-Transporting Materials: Influence of Alkyl Chain Length on Power Conversion Efficiency”, *Adv. Energy Mater.*, vol. 7, no. 6, p. 1601674, 2017. DOI: <https://doi.org/10.1002/aenm.201601674>
- [142] P. Liu *et al.*, “Design, synthesis and application of a π -conjugated, non-spiro molecular alternative as hole-transport material for highly efficient dye-sensitized solar cells and perovskite solar cells”, *J. Power Sources*, vol. 344, pp. 11–14, 2017. DOI: <https://doi.org/10.1016/j.jpowsour.2017.01.092>
- [143] L. Zhu *et al.*, “High-Efficiency Perovskite Solar Cells Based on New TPE Compounds as Hole Transport Materials: The Role of 2,7- and 3,6-Substituted Carbazole Derivatives”, *Chem. – Eur. J.*, vol. 23, no. 18, pp. 4373–4379, 2017. DOI: <https://doi.org/10.1002/chem.201605187>
- [144] G.-W. Kim *et al.*, “Dopant-free polymeric hole transport materials for highly efficient and stable perovskite solar cells”, *Energy Environ. Sci.*, vol. 9, no. 7, pp. 2326–2333, 2016. DOI: <https://doi.org/10.1039/C6EE00709K>
- [145] K.-G. Lim, H.-B. Kim, J. Jeong, H. Kim, J. Y. Kim, and T.-W. Lee, “Boosting the Power Conversion Efficiency of Perovskite Solar Cells Using Self-Organized Polymeric Hole Extraction Layers with High Work Function”, *Adv. Mater.*, vol. 26, no. 37, pp. 6461–6466, 2014. DOI: <https://doi.org/10.1002/adma.201401775>

- [146] S. Lv *et al.*, “One-step, solution-processed formamidinium lead trihalide (FAPbI_{3-x}Cl_x) for mesoscopic perovskite–polymer solar cells”, *Phys. Chem. Chem. Phys.*, vol. 16, no. 36, pp. 19206–19211, 2014. DOI: <https://doi.org/10.1039/C4CP02113D>
- [147] K. Neumann and M. Thelakkat, “Perovskite solar cells involving poly(tetraphenylbenzidine)s: investigation of hole carrier mobility, doping effects and photovoltaic properties”, *RSC Adv.*, vol. 4, no. 82, pp. 43550–43559, 2014. DOI: <https://doi.org/10.1039/C4RA05564K>
- [148] J. M. Marin-Beloqui, J. P. Hernández, and E. Palomares, “Photo-induced charge recombination kinetics in MAPbI_{3-x}Cl_x perovskite-like solar cells using low band-gap polymers as hole conductors”, *Chem. Commun.*, vol. 50, no. 93, pp. 14566–14569, 2014. DOI: <https://doi.org/10.1039/C4CC06338D>
- [149] W. Yan *et al.*, “High-performance hybrid perovskite solar cells with polythiophene as hole-transporting layer via electrochemical polymerization”, *RSC Adv.*, vol. 4, no. 62, pp. 33039–33046, 2014. DOI: <https://doi.org/10.1039/C4RA05578K>
- [150] W. Chen *et al.*, “Simple planar perovskite solar cells with a dopant-free benzodithiophene conjugated polymer as hole transporting material”, *J. Mater. Chem. C*, vol. 3, no. 39, pp. 10070–10073, 2015. DOI: <https://doi.org/10.1039/C5TC01856K>
- [151] H. Choi *et al.*, “Conjugated polyelectrolyte hole transport layer for inverted-type perovskite solar cells”, *Nat. Commun.*, vol. 6, p. 7348, 2015. DOI: <https://doi.org/10.1038/ncomms8348>
- [152] P. Nagarjuna, K. Narayanaswamy, T. Swetha, G. H. Rao, S. P. Singh, and G. D. Sharma, “CH₃NH₃PbI₃ Perovskite Sensitized Solar Cells Using a D-A Copolymer as Hole Transport Material”, *Electrochimica Acta*, vol. 151, pp. 21–26, 2015. DOI: <https://doi.org/10.1016/j.electacta.2014.11.003>
- [153] W. Li, M. Otsuka, T. Kato, Y. Wang, T. Mori, and T. Michinobu, “3,6-Carbazole vs 2,7-carbazole: A comparative study of hole-transporting polymeric materials for inorganic–organic hybrid perovskite solar cells”, *Beilstein J. Org. Chem.*, vol. 12, pp. 1401–1409, 2016. DOI: <https://doi.org/10.3762/bjoc.12.134>
- [154] T. Matsui *et al.*, “Additive-Free Transparent Triarylamine-Based Polymeric Hole-Transport Materials for Stable Perovskite Solar Cells”, *ChemSusChem*, vol. 9, no. 18, pp. 2567–2571, 2016. DOI: <https://doi.org/10.1002/cssc.201600762>
- [155] K. Lee *et al.*, “Low-cost and efficient perovskite solar cells using a surfactant-modified polyaniline:poly(styrenesulfonate) hole transport material”, *Electrochimica Acta*, vol. 224, pp. 600–607, 2017. DOI: <https://doi.org/10.1016/j.electacta.2016.12.103>
- [156] D. Zhao, M. Sexton, H.-Y. Park, G. Baure, J. C. Nino, and F. So, “High-Efficiency Solution-Processed Planar Perovskite Solar Cells with a Polymer Hole Transport Layer”, *Adv. Energy Mater.*, vol. 5, no. 6, p. 1401855, 2015. DOI: <https://doi.org/10.1002/aenm.201401855>
- [157] H.-C. Liao *et al.*, “Dopant-Free Hole Transporting Polymers for High Efficiency, Environmentally Stable Perovskite Solar Cells”, *Adv. Energy Mater.*, vol. 6, no. 16, p. 1600502, 2016. DOI: <https://doi.org/10.1002/aenm.201600502>
- [158] W. S. Yang *et al.*, “Iodide management in formamidinium-lead-halide–based perovskite layers for efficient solar cells”, *Science*, vol. 356, no. 6345, pp. 1376–1379, 2017. DOI: <https://doi.org/10.1126/science.aan2301>
- [159] S. N. Habisreutinger, T. Leijtens, G. E. Eperon, S. D. Stranks, R. J. Nicholas, and H. J. Snaith, “Carbon Nanotube/Polymer Composites as a Highly Stable Hole Collection Layer in Perovskite Solar Cells”, *Nano Lett.*, vol. 14, no. 10, pp. 5561–5568, 2014. DOI: <https://doi.org/10.1021/nl501982b>
- [160] M. Cai, V. T. Tiong, T. Hreid, J. Bell, and H. Wang, “An efficient hole transport material composite based on poly(3-hexylthiophene) and bamboo-structured carbon nanotubes for high performance perovskite solar cells”, *J. Mater. Chem. A*, vol. 3, no. 6, pp. 2784–2793, 2015. DOI: <https://doi.org/10.1039/C4TA04997G>
- [161] J. H. Heo and S. H. Im, “CH₃NH₃PbI₃/poly-3-hexylthiophen perovskite mesoscopic solar cells: Performance enhancement by Li-assisted hole conduction”, *Phys. Status Solidi RRL – Rapid Res. Lett.*, vol. 8, no. 10, pp. 816–821, 2014. DOI: <https://doi.org/10.1002/pssr.201409330>
- [162] X. Jiang *et al.*, “High-Performance Regular Perovskite Solar Cells Employing Low-Cost Poly(ethylenedioxythiophene) as a Hole-Transporting Material”, *Sci. Rep.*, vol. 7, p. 42564, 2017. DOI: <https://doi.org/10.1038/srep42564>
- [163] W. Yan *et al.*, “Stable high-performance hybrid perovskite solar cells with ultrathin polythiophene as hole-transporting layer”, *Nano Res.*, vol. 8, no. 8, pp. 2474–2480, 2015. DOI: <https://doi.org/10.1007/s12274-015-0755-5>
- [164] Z. Wang *et al.*, “Copolymers based on thiazolothiazole-dithienosilole as hole-transporting materials for high efficient perovskite solar cells”, *Org. Electron.*, vol. 33, pp. 142–149, 2016. DOI: <https://doi.org/10.1016/j.orgel.2016.03.020>
- [165] Z. Zhu *et al.*, “Polyfluorene Derivatives are High-Performance Organic Hole-Transporting Materials for Inorganic–Organic Hybrid Perovskite Solar Cells”, *Adv. Funct. Mater.*, vol. 24, no. 46, pp. 7357–7365, 2014. DOI: <https://doi.org/10.1002/adfm.201401557>

- [166] X. Li, X. Liu, X. Wang, L. Zhao, T. Jiu, and J. Fang, "Polyelectrolyte based hole-transporting materials for high performance solution processed planar perovskite solar cells", *J. Mater. Chem. A*, vol. 3, no. 29, pp. 15024–15029, 2015. DOI: <https://doi.org/10.1039/C5TA04712A>
- [167] J. W. Jo *et al.*, "Improving Performance and Stability of Flexible Planar-Heterojunction Perovskite Solar Cells Using Polymeric Hole-Transport Material", *Adv. Funct. Mater.*, vol. 26, no. 25, pp. 4464–4471, 2016. DOI: <https://doi.org/10.1002/adfm.201600746>
- [168] W. Zhang *et al.*, "Systematic Improvement in Charge Carrier Mobility of Air Stable Triarylamine Copolymers", *J. Am. Chem. Soc.*, vol. 131, no. 31, pp. 10814–10815, 2009. DOI: <https://doi.org/10.1021/ja9034818>
- [169] J. H. Park *et al.*, "Efficient CH₃NH₃PbI₃ Perovskite Solar Cells Employing Nanostructured p-Type NiO Electrode Formed by a Pulsed Laser Deposition", *Adv. Mater.*, vol. 27, no. 27, pp. 4013–4019, 2015. DOI: <https://doi.org/10.1002/adma.201500523>
- [170] J. W. Jung, C.-C. Chueh, and A. K.-Y. Jen, "A Low-Temperature, Solution-Processable, Cu-Doped Nickel Oxide Hole-Transporting Layer via the Combustion Method for High-Performance Thin-Film Perovskite Solar Cells", *Adv. Mater.*, vol. 27, no. 47, pp. 7874–7880, 2015. DOI: <https://doi.org/10.1002/adma.201503298>
- [171] W. Chen *et al.*, "Efficient and stable large-area perovskite solar cells with inorganic charge extraction layers", *Science*, vol. 350, no. 6263, pp. 944–948, 2015. DOI: <https://doi.org/10.1126/science.aad1015>
- [172] W. Sun *et al.*, "Room-temperature and solution-processed copper iodide as the hole transport layer for inverted planar perovskite solar cells", *Nanoscale*, vol. 8, no. 35, pp. 15954–15960, 2016. DOI: <https://doi.org/10.1039/C6NR04288K>
- [173] S. Ye *et al.*, "CuSCN-Based Inverted Planar Perovskite Solar Cell with an Average PCE of 15.6%", *Nano Lett.*, vol. 15, no. 6, pp. 3723–3728, 2015. DOI: <https://doi.org/10.1021/acs.nanolett.5b00116>
- [174] C. Zuo and L. Ding, "Solution-Processed Cu₂O and CuO as Hole Transport Materials for Efficient Perovskite Solar Cells", *Small*, vol. 11, no. 41, pp. 5528–5532, 2015. DOI: <https://doi.org/10.1002/sml.201501330>
- [175] Q. Wu *et al.*, "Kesterite Cu₂ZnSnS₄ as a Low-Cost Inorganic Hole-Transporting Material for High-Efficiency Perovskite Solar Cells", *ACS Appl. Mater. Interfaces*, vol. 7, no. 51, pp. 28466–28473, 2015. DOI: <https://doi.org/10.1021/acsami.5b09572>
- [176] A. J. Huckaba *et al.*, "Exceedingly Cheap Perovskite Solar Cells Using Iron Pyrite Hole Transport Materials", *ChemistrySelect*, vol. 1, no. 16, pp. 5316–5319, 2016. DOI: <https://doi.org/10.1002/slct.201601378>
- [177] K.-C. Wang *et al.*, "p-type Mesoscopic Nickel Oxide/Organometallic Perovskite Heterojunction Solar Cells", *Sci. Rep.*, vol. 4, p. 4756, 2014. DOI: <https://doi.org/10.1038/srep04756>
- [178] W. Chen *et al.*, "Hybrid interfacial layer leads to solid performance improvement of inverted perovskite solar cells", *Energy Environ. Sci.*, vol. 8, no. 2, pp. 629–640, 2015. DOI: <https://doi.org/10.1039/C4EE02833C>
- [179] J. Cui *et al.*, "CH₃NH₃PbI₃-Based Planar Solar Cells with Magnetron-Sputtered Nickel Oxide", *ACS Appl. Mater. Interfaces*, vol. 6, no. 24, pp. 22862–22870, 2014. DOI: <https://doi.org/10.1021/am507108u>
- [180] A. S. Subbiah, A. Halder, S. Ghosh, N. Mahuli, G. Hodes, and S. K. Sarkar, "Inorganic Hole Conducting Layers for Perovskite-Based Solar Cells", *J. Phys. Chem. Lett.*, vol. 5, pp. 1748–1753, 2014. DOI: <https://doi.org/10.1021/jz500645n>
- [181] K.-C. Wang *et al.*, "Low-Temperature Sputtered Nickel Oxide Compact Thin Film as Effective Electron Blocking Layer for Mesoscopic NiO/CH₃NH₃PbI₃ Perovskite Heterojunction Solar Cells", *ACS Appl. Mater. Interfaces*, vol. 6, no. 15, pp. 11851–11858, 2014. DOI: <https://doi.org/10.1021/am503610u>
- [182] Z. Zhu *et al.*, "High-Performance Hole-Extraction Layer of Sol-Gel-Processed NiO Nanocrystals for Inverted Planar Perovskite Solar Cells", *Angew. Chem. Int. Ed.*, vol. 53, no. 46, pp. 12571–12575, 2014. DOI: <https://doi.org/10.1002/anie.201405176>
- [183] M. Nachman, L. N. Cojocaru, and L. V. Ribco, "Electrical Properties of Non-Stoichiometric Nickel Oxide", *Phys. Status Solidi B*, vol. 8, no. 3, pp. 773–783, 1965. DOI: <https://doi.org/10.1002/pssb.19650080316>
- [184] J. H. Kim *et al.*, "High-Performance and Environmentally Stable Planar Heterojunction Perovskite Solar Cells Based on a Solution-Processed Copper-Doped Nickel Oxide Hole-Transporting Layer", *Adv. Mater.*, vol. 27, no. 4, pp. 695–701, 2015. DOI: <https://doi.org/10.1002/adma.201404189>
- [185] W.-Y. Chen *et al.*, "Low-cost solution-processed copper iodide as an alternative to PEDOT:PSS hole transport layer for efficient and stable inverted planar heterojunction perovskite solar cells", *J. Mater. Chem. A*, vol. 3, no. 38, pp. 19353–19359, 2015. DOI: <https://doi.org/10.1039/C5TA05286F>
- [186] J. A. Christians, R. C. M. Fung, and P. V. Kamat, "An Inorganic Hole Conductor for Organo-Lead Halide Perovskite Solar Cells. Improved Hole Conductivity with Copper Iodide", *J. Am. Chem. Soc.*, vol. 136, no. 2, pp. 758–764, 2014. DOI: <https://doi.org/10.1021/ja411014k>

- [187] S. Ito, S. Tanaka, and H. Nishino, "Lead-Halide Perovskite Solar Cells by CH₃NH₃I Dripping on PbI₂-CH₃NH₃I-DMSO Precursor Layer for Planar and Porous Structures Using CuSCN Hole-Transporting Material", *J. Phys. Chem. Lett.*, vol. 6, no. 5, pp. 881–886, 2015. DOI: <https://doi.org/10.1021/acs.jpcclett.5b00122>
- [188] P. Qin *et al.*, "Inorganic hole conductor-based lead halide perovskite solar cells with 12.4% conversion efficiency", *Nat. Commun.*, vol. 5, 2014. DOI: <https://doi.org/10.1038/ncomms4834>
- [189] S. Chavhan *et al.*, "Organo-metal halide perovskite-based solar cells with CuSCN as the inorganic hole selective contact", *J. Mater. Chem. A*, 2014. DOI: <https://doi.org/10.1039/C4TA01310G>
- [190] G. A. Sepalage *et al.*, "A facile deposition method for CuSCN: Exploring the influence of CuSCN on *J*-*V* hysteresis in planar perovskite solar cells", *Nano Energy*, vol. 32, pp. 310–319, 2017. DOI: <https://doi.org/10.1016/j.nanoen.2016.12.043>
- [191] C. V. Kumar, G. Sfyri, D. Raptis, E. Stathatos, and P. Lianos, "Perovskite solar cell with low cost Cu-phthalocyanine as hole transporting material", *RSC Adv.*, vol. 5, no. 5, pp. 3786–3791, 2014. DOI: <https://doi.org/10.1039/C4RA14321C>
- [192] H.-H. Chou *et al.*, "Zinc Porphyrin-Ethynylaniline Conjugates as Novel Hole-Transporting Materials for Perovskite Solar Cells with Power Conversion Efficiency of 16.6%", *ACS Energy Lett.*, vol. 1, no. 5, pp. 956–962, 2016. DOI: <https://doi.org/10.1021/acsenerylett.6b00432>
- [193] Y. Hua *et al.*, "High conductivity Ag-based metal organic complexes as dopant-free hole-transport materials for perovskite solar cells with high fill factors", *Chem. Sci.*, vol. 7, pp. 2633–2638, 2016. DOI: <https://doi.org/10.1039/C5SC03569D>
- [194] F. J. Ramos *et al.*, "Non-aggregated Zn(II)octa(2,6-diphenylphenoxy) phthalocyanine as a hole transporting material for efficient perovskite solar cells", *Dalton Trans.*, vol. 44, no. 23, pp. 10847–10851, 2015. DOI: <https://doi.org/10.1039/C5DT00396B>
- [195] G. Sfyri *et al.*, "Subphthalocyanine as hole transporting material for perovskite solar cells", *RSC Adv.*, vol. 5, no. 85, pp. 69813–69818, 2015. DOI: <https://doi.org/10.1039/C5RA12004G>
- [196] K. T. Cho, K. Rakstys, M. Cavazzini, S. Orlandi, G. Pozzi, and M. K. Nazeeruddin, "Perovskite Solar Cells Employing Molecularly Engineered Zn(II) Phthalocyanines as Hole-transporting Materials", *Nano Energy*, vol. 30, pp. 853–857, 2016. DOI: <https://doi.org/10.1016/j.nanoen.2016.09.008>
- [197] J.-J. Guo *et al.*, "A novel asymmetric phthalocyanine-based hole transporting material for perovskite solar cells with an open-circuit voltage above 1.0 V", *Synth. Met.*, vol. 220, pp. 462–468, 2016. DOI: <https://doi.org/10.1016/j.synthmet.2016.07.013>
- [198] E. Nouri *et al.*, "Soluble tetratriphenylamine Zn phthalocyanine as Hole Transporting Material for Perovskite Solar Cells", *Electrochimica Acta*, vol. 222, pp. 875–880, 2016. DOI: <https://doi.org/10.1016/j.electacta.2016.11.052>
- [199] G. Sfyri *et al.*, "Soluble butyl substituted copper phthalocyanine as alternative hole-transporting material for solution processed perovskite solar cells", *Electrochimica Acta*, vol. 212, pp. 929–933, 2016. DOI: <https://doi.org/10.1016/j.electacta.2016.07.047>
- [200] G. Sfyri, C. V. Kumar, Y.-L. Wang, Z.-X. Xu, C. A. Krontiras, and P. Lianos, "Tetra methyl substituted Cu(II) phthalocyanine as alternative hole transporting material for organometal halide perovskite solar cells", *Appl. Surf. Sci.*, vol. 360, Part B, pp. 767–771, 2016. DOI: <https://doi.org/10.1016/j.apsusc.2015.11.065>
- [201] G. Sfyri, N. Vamshikrishna, C. V. Kumar, L. Giribabu, and P. Lianos, "Synthesis and characterization of tetratriphenylamine Zn phthalocyanine as hole transporting material for perovskite solar cells", *Sol. Energy*, vol. 140, pp. 60–65, 2016. DOI: <https://doi.org/10.1016/j.solener.2016.10.050>
- [202] S. Wu, Y. Zheng, Q. Liu, R. Li, and T. Peng, "Low cost and solution-processable zinc phthalocyanine as alternative hole transport material for perovskite solar cells", *RSC Adv.*, vol. 6, no. 109, pp. 107723–107731, 2016. DOI: <https://doi.org/10.1039/C6RA22451B>
- [203] P. Qi, F. Zhang, X. Li, Y. Xiao, J. Guo, and S. Wang, "2,9,16,23-Tetrakis(7-coumarinoxy-4-methyl)-metallophtalocyanines -based hole transporting material for mixed-perovskite solar cells", *Synth. Met.*, vol. 226, pp. 1–6, 2017. DOI: <https://doi.org/10.1016/j.synthmet.2017.01.004>
- [204] Y. Wang *et al.*, "Tetra-alkyl-substituted copper (II) phthalocyanines as dopant-free hole-transport layers for planar perovskite solar cells with enhanced open circuit voltage and stability", *Dyes Pigments*, vol. 139, pp. 619–626, 2017. DOI: <https://doi.org/10.1016/j.dyepig.2016.12.067>
- [205] A. Suzuki, T. Kida, T. Takagi, and T. Oku, "Effects of hole-transporting layers of perovskite-based solar cells", *Jpn. J. Appl. Phys.*, vol. 55, no. 2S, p. 02BF01, 2015. DOI: <https://doi.org/10.7567/JJAP.55.02BF01>
- [206] M. Sun, S. Wang, Y. Xiao, Z. Song, and X. Li, "Titanylphthalocyanine as hole transporting material for perovskite solar cells", *J. Energy Chem.*, vol. 24, no. 6, pp. 756–761, 2015. DOI: <https://doi.org/10.1016/j.jechem.2015.10.020>

- [207] K. T. Cho *et al.*, “Molecularly Engineered Phthalocyanines as Hole-Transporting Materials in Perovskite Solar Cells Reaching Power Conversion Efficiency of 17.5%”, *Adv. Energy Mater.*, vol. 7, no. 7, p. 1601733, 2017. DOI: <https://doi.org/10.1002/aenm.201601733>
- [208] G. Yang *et al.*, “A facile molecularly engineered copper (II) phthalocyanine as hole transport material for planar perovskite solar cells with enhanced performance and stability”, *Nano Energy*, vol. 31, pp. 322–330, 2017. DOI: <https://doi.org/10.1016/j.nanoen.2016.11.039>
- [209] X. Jiang *et al.*, “Efficient perovskite solar cells employing a solution-processable copper phthalocyanine as a hole-transporting material”, *Sci. China Chem.*, vol. 60, no. 3, pp. 423–430, 2017. DOI: <https://doi.org/10.1007/s11426-016-0393-5>
- [210] Q.-D. Dao, A. Fujii, R. Tsuji, Y. Takeoka, and M. Ozaki, “Efficiency enhancement in perovskite solar cell utilizing solution-processable phthalocyanine hole transport layer with thermal annealing”, *Org. Electron.*, vol. 43, pp. 156–161, 2017. DOI: <https://doi.org/10.1016/j.orgel.2017.01.027>
- [211] M. K. Kashif *et al.*, “Cobalt Polypyridyl Complexes as Transparent Solution-Processable Solid-State Charge Transport Materials”, *Adv. Energy Mater.*, vol. 6, no. 24, p. 1600874, 2016. DOI: <https://doi.org/10.1002/aenm.201600874>
- [212] M. Freitag *et al.*, “High-efficiency dye-sensitized solar cells with molecular copper phenanthroline as solid hole conductor”, *Energy Environ. Sci.*, vol. 8, no. 9, pp. 2634–2637, 2015. DOI: <https://doi.org/10.1039/C5EE01204J>
- [213] M. K. Kashif *et al.*, “Stable Dye-Sensitized Solar Cell Electrolytes Based on Cobalt(II)/(III) Complexes of a Hexadentate Pyridyl Ligand”, *Angew. Chem. Int. Ed.*, vol. 52, no. 21, pp. 5527–5531, 2013. DOI: <https://doi.org/10.1002/anie.201300070>
- [214] R. Sheng *et al.*, “Methylammonium Lead Bromide Perovskite-Based Solar Cells by Vapor-Assisted Deposition”, *J. Phys. Chem. C*, vol. 119, no. 7, pp. 3545–3549, 2015. DOI: <https://doi.org/10.1021/jp512936z>
- [215] F. C. Hanusch *et al.*, “Efficient Planar Heterojunction Perovskite Solar Cells Based on Formamidinium Lead Bromide”, *J. Phys. Chem. Lett.*, vol. 5, no. 16, pp. 2791–2795, 2014. DOI: <https://doi.org/10.1021/jz501237m>
- [216] H. Bakkali *et al.*, “Functionalized 2,5-Dipyridinylpyrroles by Electrochemical Reduction of 3,6-Dipyridinylpyridazine Precursors”, *Eur. J. Org. Chem.*, vol. 2008, no. 12, pp. 2156–2166, 2008. DOI: <https://doi.org/10.1002/ejoc.200701115>
- [217] M. K. Kashif *et al.*, “Polypyridyl Iron Complex as a Hole-Transporting Material for Formamidinium Lead Bromide Perovskite Solar Cells”, *ACS Energy Lett.*, vol. 2, pp. 1855–1859, 2017. DOI: <https://doi.org/10.1021/acsenerylett.7b00522>
- [218] J. W. Ciszek *et al.*, “Neutral Complexes of First Row Transition Metals Bearing Unbound Thiocyanates and Their Assembly on Metallic Surfaces”, *J. Am. Chem. Soc.*, vol. 128, no. 10, pp. 3179–3189, 2006. DOI: <https://doi.org/10.1021/ja055459d>
- [219] M. Saliba *et al.*, “Incorporation of rubidium cations into perovskite solar cells improves photovoltaic performance”, *Science*, vol. 354, no. 6309, pp. 206–209, 2016. DOI: <https://doi.org/10.1126/science.aah5557>
- [220] C. M. Cardona, W. Li, A. E. Kaifer, D. Stockdale, and G. C. Bazan, “Electrochemical Considerations for Determining Absolute Frontier Orbital Energy Levels of Conjugated Polymers for Solar Cell Applications”, *Adv. Mater.*, vol. 23, no. 20, pp. 2367–2371, 2011. DOI: <https://doi.org/10.1002/adma.201004554>
- [221] J. Zhang *et al.*, “Strategy to Boost the Efficiency of Mixed-Ion Perovskite Solar Cells: Changing Geometry of the Hole Transporting Material”, *ACS Nano*, vol. 10, no. 7, pp. 6816–6825, 2016. DOI: <https://doi.org/10.1021/acsnano.6b02442>
- [222] J. J. P. Stewart, *MOPAC2012*. Colorado Springs, CO, USA: Stewart Computational Chemistry, 2012
- [223] J. J. P. Stewart, *MOPAC2016*. Colorado Springs, CO, USA: Stewart Computational Chemistry, 2016
- [224] J. J. P. Stewart, “Optimization of parameters for semiempirical methods VI: more modifications to the NDDO approximations and re-optimization of parameters”, *J. Mol. Model.*, vol. 19, no. 1, pp. 1–32, 2013. DOI: <https://doi.org/10.1007/s00894-012-1667-x>
- [225] M. J. Frisch *et al.*, *Gaussian 09*. Wallingford, CT, USA: Gaussian, Inc., 2009
- [226] W.-J. Chi, Q.-S. Li, and Z.-S. Li, “Effects of Molecular Configuration on Charge Diffusion Kinetics within Hole-Transporting Materials for Perovskites Solar Cells”, *J. Phys. Chem. C*, vol. 119, no. 16, pp. 8584–8590, 2015. DOI: <https://doi.org/10.1021/acs.jpcc.5b02401>
- [227] O. V. Mazurin and V. Y. Gankin, “Glass transition temperature: problems of measurements and analysis of the existing data”, in *Proceedings, International Congress on Glass*, Strasbourg, France, 2007
- [228] O. V. Mazurin, “Problems of compatibility of the values of glass transition temperatures published in the world literature”, *Glass Phys. Chem.*, vol. 33, no. 1, pp. 22–36, 2007. DOI: <https://doi.org/10.1134/S108765960701004X>

- [229] Z. Hawash, L. K. Ono, S. R. Raga, M. V. Lee, and Y. Qi, "Air-Exposure Induced Dopant Redistribution and Energy Level Shifts in Spin-Coated Spiro-MeOTAD Films", *Chem. Mater.*, vol. 27, no. 2, pp. 562–569, 2015. DOI: <https://doi.org/10.1021/cm504022q>
- [230] H. Wohltjen, W. R. Barger, A. W. Snow, and N. L. Jarvis, "A vapor-sensitive chemiresistor fabricated with planar microelectrodes and a Langmuir-Blodgett organic semiconductor film", *IEEE Trans. Electron Devices*, vol. 32, no. 7, pp. 1170–1174, 1985. DOI: <https://doi.org/10.1109/T-ED.1985.22095>
- [231] A. Abate *et al.*, "Lithium salts as 'redox active' p-type dopants for organic semiconductors and their impact in solid-state dye-sensitized solar cells", *Phys. Chem. Chem. Phys.*, vol. 15, no. 7, pp. 2572–2579, 2013. DOI: <https://doi.org/10.1039/C2CP44397J>
- [232] *CrysAlisPro v. 1.171.38.43d*. Yarnton, England: Rigaku Oxford Diffraction, 2015
- [233] G. M. Sheldrick, *SHELX-2014*. Universität Göttingen, 2014
- [234] E44.09 Subcommittee, "Standard Specification for Solar Simulation for Photovoltaic Testing", *ASTM International*, 2015. URL: <https://doi.org/10.1520/E0927-10R15>
- [235] "Terrestrial photovoltaic (PV) modules - Design qualification and type approval", *International Electrotechnical Commission*, 2016. URL: <https://web.archive.org/web/20170625062742/https://webstore.iec.ch/publication/24312>
- [236] R. B. Dunbar *et al.*, "Device pre-conditioning and steady-state temperature dependence of CH₃NH₃PbI₃ perovskite solar cells", *Prog. Photovolt. Res. Appl.*, vol. 25, no. 7, pp. 533–544, 2017. DOI: <https://doi.org/10.1002/pip.2839>